Stony Brook University

Characteristics of Two Gravity Wave Sources in the US High Vertical-resolution Radiosonde Data

A Dissertation Presented

by

Jie Gong

to

The Graduate School

In Partial Fulfillment of the

Requirements

For the Degree of

Doctor of Philosophy

in

Marine and Atmospheric Science

Stony Brook University

December 2009

Stony Brook University

The Graduate School

Jie Gong

We, the dissertation committee for the above candidate for the
Doctor of Philosophy degree, hereby recommend
acceptance of this dissertation.

Marvin A. Geller - Dissertation Advisor
Professor, School of Marine and Atmospheric Sciences

Minghua Zhang – Chair of Defense
Professor, School of Marine and Atmospheric Sciences

Brian A. Colle
Associate Professor, School of Marine and Atmospheric Sciences

Xiaolin Li
Professor, Department of Applied Mathematics and Statistics

Stephen D. Eckermann
Head, Middle Atmosphere Dynamics Section
Naval Research Laboratory

This dissertation is accepted by the Graduate School

Lawrence Martin
Dean of the Graduate School

Abstract of the Dissertation

Characteristics of Two Gravity Wave Sources in the US High Vertical-resolution Radiosonde Data

by

Jie Gong

Doctor of Philosophy

in

Marine and Atmospheric Science

Stony Brook University

2009

Understanding gravity wave sources is essential to gravity wave research, and has profound effect on improving general circulation models (GCMs). My Ph.D. work is to analyze, diagnose and simulate the source behaviors of gravity waves that are observed in the US high vertical-resolution radiosonde data. Two sources - convection and jet imbalance - are of the major interest.

I used a ray-tracing gravity wave model GROGRAT to characterize the "mean" source spectrum of gravity waves in the lower stratosphere that are observed from US high vertical-resolution radiosonde profiles on a monthly scale. With a fixed source spectral function, one can get "best-fits" for most of the stations. A universal source function is found to be most powerful in capturing the major features of the variations, while another, which represents the convection source, works better for tropical stations. "Fits" are generally better for winter than for summer, indicating possible jet-related sources.

I furthermore examined the perturbation field of the ascent rate that is likely to be representative of higher-frequency gravity waves that are generated from the convection sources. The newly defined variable, VE, as well as the apparent dominant vertical wavelength analyzed from the ascent rate fluctuations turned out to be collocated very well with moist convection in the troposphere, especially during warm seasons. The waves tend to have higher frequencies, and this seems consistent with theory.

Forcing terms associated with the jet imbalance source are analyzed on a climatological basis. The derived forcings reveal some characteristics of the jet imbalance source, which we can sometimes see in the radiosonde profiles. GROGRAT and a linear forcing-response model are used to study a specific case, which sheds some light on parameterizations of gravity wave drag associated with the jet imbalance.

Table of Contents

List of Figures

List of Tables

Acknowledgements

I would like to acknowledge the faculty, staff and fellow students of the School of Marine and Atmospheric Sciences for their help and contributions to the research presented below. I would especially express my great gratitude to my advisor, Prof. Marvin A. Geller, for directing me step by step on the research and changing me from a student to a researcher. I would also like to thank the committee members – Dr. Stephen Eckermann, Prof. Brian Colle, Prof. Xiaolin Li, and Prof. Minghua Zhang – for the insights and questions that make this research stricter and the presentation clearer. In addition, I appreciate the great help from Dr. Ling Wang for useful discussions, and Dr. Shuguang wang for generously offering me his model. Finally, I would like to thank my parents, Xiangfang Gong and Mei Li, my husband, Lin Li, my mother-in-law, Guizhen Xin, and my son, Daniel Gong Li, for their everlasting love and supports for me in pursuing my Ph.D. degree.

This work is supported by NSF grant ATM-0413747.

Chapter 1 Introduction

Atmospheric gravity waves exist by virtue of the buoyancy force acting as the restoring force on parcels vertically displaced in a stable layer. Compared with baroclinic waves and planetary waves, gravity waves typically have with short periods and small amplitudes, and hence their importance in determining the large-scale atmospheric structure had been neglected for a long time until the 1980s when *Lindzen (1981)* and *Holton (1982)* proposed ideas of wave breaking and the induced stress on the mean flow. With the rapid development of observational techniques and theories, gravity waves are now recognized as one of the primary dynamic components of the atmosphere by virtue of "*their myriad effects and major contributions to atmospheric circulation, structure and variability*" (Fritts and Alexander, 2003). Gravity waves serve as a major coupling mechanism between the lower atmosphere (troposphere and lower stratosphere) and the upper atmosphere (upper stratosphere and above) through their momentum and heat fluxes. Because atmospheric density decreases approximately exponentially with height, the amount of energy in the lower atmosphere overwhelmingly exceeds that in the upper atmosphere, and therefore, this mechanism is particularly important to the latter, in the sense that the small portion of the energy/momentum transported from the lower atmosphere has profound effects on the upper atmosphere. Hence, gravity waves are one important dynamic process to redistribute the energies/momentums in the atmosphere.

The first Eliassen and Palm theorem can be written as eqn. (1) (Lindzen, 1990, eqn. 8.14). p is pressure, w is vertical velocity, u is zonal wind, ρ is density, and c is the wave phase speed. The overbars indicate averages over a wavelength, and primes indicate

departures from that average. Eqn. (1) states that when gravity waves dissipate because of meeting critical levels or becoming unstable, their momentum deposition always tends to drag the mean flow toward their phase speeds at the source level, and hence they have the effect of accelerating/decelerating the mean flow. This is usually called gravity wave drag (GWD).

$$\overline{p'w'} = -\bar{\rho}(\bar{u} - c)\overline{u'w'} \tag{1.1}$$

This mechanism is extremely important for explaining the mesosphere wind reversal. Gravity wave momentum deposition at the mesosphere induces a residual meridional circulation from summer pole to winter pole, driving the summer pole 90*K* away from radiative equilibrium (Garcia, 1989; Fritts and Alexander, 2003). *Plumb (2002)* believed that this is also true in the stratosphere giving rise to the so-called "Brewer-Dobson Circulation", although planetary waves and baroclinic waves are probably more important there. Another good example which shows how gravity waves couple the stratosphere and the mesosphere is the sudden stratospheric warming (SSW). When SSW occur, the weaker westerly jet in the polar stratosphere allows more gravity waves with eastward phase speed propagating into the mesosphere, and blocks the waves with westward phase speed. The eastward forcing associated with the breaking gravity waves in the mesosphere will eventually replace the former westward forcing, and reverse the mean meridional circulation in the upper mesosphere (Liu and Roble, 2002). The importance of GWD on helping to determine the observed mean zonal wind structure could be summarized in Fig. 1.1 (adapted from Kim et al., 2003, Fig. 1), which will be further discussed in the future.

In the tropics, because of the negligible Coriolis force, GWD induces a direct forcing on zonal wind, which in turn affects the propagation of gravity waves. This would create a zonal mean oscillation, which is believed to be essential in driving quasi-biennual oscillation (QBO) in the lower stratosphere and semi-annual oscillation (SAO) in the upper stratosphere (Dunkerton, 1997; Baldwin et al, 2001).

Gravity waves are not only an effective remote transmitter, but can also have local effects. They induce turbulence when they break, and this process is nontrivial for the mixing of chemical species and water vapor. This mesoscale process can cause clear-air turbulence (e.g., Clark et al., 2000) and trigger the formation of clouds (e.g., Haag and Karcher, 2004). As an example, Carslaw et al. (1998) presented a field experiment where they found mountain-wave-induced mesoscale polar stratospheric clouds (PSCs), and confirmed their impact on ozone depletion. The radiative effect associated with this can further influence the configurations of the atmosphere structure. Recently, *Xu et al. (2003)* showed that the distribution and variation of chemical species are largely influenced by the passage of gravity waves even when they do not break.

Gravity waves are also found to be able to modulate or even initiate synoptic weather. The vertical motion associated with large amplitude gravity waves can directly lead to an increase or decrease of local precipitation (e.g., Colle and Yuter, 2007). Gravity waves occurring near the surface can induce large pressure perturbation and strong gusts. Gravity waves can also modulate weather systems. For example, *Yang and Houze (1995)* found that convectively generated trapped gravity waves may determine the multicellular structure of the storm.

It is critical to incorporate GWD in general circulation models (GCMs) and some weather prediction models for realistic simulations and predictions, particularly in the middle atmosphere. Although there has been several attempts to explicitly resolve gravity waves in GCMs (e.g., Sato et al., 1999; Berger, 2008), most state-of-the-art GCMs need to parameterize gravity wave drag (GWD) in them. That's mainly because the scales of the gravity waves are so small that the current practical GCMs cannot resolve most of them. The typical horizontal wavelength of gravity waves ranges from tens to several hundred kilometers, and the vertical wavelength is from several meters to tens of kilometers, neither of which is longer than four times of the typical grid scales (i.e., the smallest wavelength that could be distinguished). Fig. 1.1 clearly states that the westerlies (easterlies) would become excessively strong without a parameterization of sub-grid scale GWD during hemisphere winter (summer). The GWD parameterization schemes can be categorized into three classes. The first class builds a spectrum of waves with amplitudes hopefully constrained by observations. Then they let the waves saturate one by one with single-wave physics in order to closely follow the observed spectra (Fritts and VanZandt, 1993). Another class tries to involve wave-wave interactions and to build up model-dependent spectra (Hines, 1997a, 1997b). The third class incorporates a distribution function into wave spectra, and let the waves propagate successively through the atmosphere (Alexander and Dunkerton, 1999). A detailed review of GWD parameterization can be found in Kim et al. (2003). In Chapter 3, I use the third class of GWD parameterization schemes, and will show the strong capability they have in replicating the observed real atmosphere.

No matter how complicated the schemes are, they consist of two components – source and sink. Most of the schemes in the past have been focused on the sink part, i.e., the dissipation process when waves are breaking. However, *McLandress and Scinocca (2005)* implemented three types of GWD parameterization schemes in a GCM sensitivity study, and achieved nearly identical responses, suggesting that "*GCM response is largely insensitive to the precise details of the dissipation mechanisms*", but "*potentially benefit more from the refinement of other aspects of the parameterization problem, such as the properties of the launch spectrum*". As a matter of fact, current GWD parameterization schemes employed in GCMs has large uncertainties. Since some of the parameters such as wave intermittency are tunable variables, people can achieve almost any solutions by "tuning" the free parameters without the knowledge of the gravity wave source properties. Most GCMs use oversimplified assumptions about gravity wave sources, such as uniform nonorgraphic source distribution in space and time, or arbitrary source spectra with little physical meanings. On the other hand, the spectrum of phase speed of gravity waves at the source level is especially important based on the aforementioned Eliassen-Palm theorem. Overall, to solve this dilemma in the foreseeable future, it is necessary to investigate gravity wave sources.

In principle, anything that can vertically displace the air parcels in a stable layer could emit gravity waves. In practice, there are mainly four gravity wave sources that are important for the atmosphere: orography, convection, spoutaneous adjustment associated with jet stream/streak and frontal systems, and shear instability. The orographic source is probably the most studied and the best understood source. Since mountains are stationary, they generate gravity waves with phase speed equal to zero, which always tend to

decelerate the mean background flow. Mountain generated gravity waves are important for the atmosphere in all altitudes, and the orographic GWD parameterization has been studied for more than three decades (e.g., Palmer et al., 1986; McFarlane, 1987), and it has been implemented in all GCMs. However, as the ground-based phase speed is zero for the mountain source, the gravity waves generated by orography can never change the sign of the wind, which apparently is not the case in real atmosphere as shown in Fig. 1.1. Besides, McFarlane (1987) showed that including orographic GWD in the GCM significantly improved the large-scale flow in the Northern hemisphere, but had little effect on the Southern hemisphere. The reason is that nonorographic gravity wave sources are much more important for some regions, including those without a significant topography, and the tropics and high latitudes.

Convection is one of the most important non-stationary gravity wave sources, in that it is present almost everywhere with irregular temporal behavior. Convection generates gravity waves covering a broad phase speed range, which varies from case to case. Convection is especially important in the tropics, where other major sources are generally weak or barely exist. Indeed, the gravity waves emitted by convection in the tropics contribute about one fourth of the total momentum flux that generates the QBO in the tropical stratosphere (Alexander and Holton, 1997). Currently three physical generation mechanisms for gravity waves from convective clouds have been proposed: the "mechanical oscillator" mechanism (Fovell et al., 1992), the "moving mountain" mechanism (Pfister et al., 1993) and the "thermal forcing" mechanism (Chun and Baik, 1998; Beres et al., 2004). Only the last mechanism has been successfully parameterized in the current GCMs. They will be further discussed in detail in Chapter 4.

Jet imbalance is another important source emitting non-stationary gravity waves. The atmosphere always tends to adjust itself back to balanced state once it's been driven away, during which gravity waves are radiated away from the source. For large-scale flow, the balanced state is quasi-geostrophic, and for mesoscale system, the balanced state is likely to be cyclonic flow or even gradient flow for smaller scale systems such as tornado. Although there has been much work done on trying to understand this spontaneous adjustment mechanism for generating gravity waves from baroclinic waves and frontal systems (e.g. O'Sullivan and Dunkerton, 1995; Plougonven and Snyder, 2007), this source is less studied in the sense of implementing it into the GCMs, than is the case for the convective source, and none of the popular GCMs in use nowadays have specified this source in them. *Wang and Zhang (2007)* declared that the dominant wave frequencies were related with the residual of the nonlinear balanced equation, and in Chapter 5, we will explore this more. Despite the discrepancy in parameterizing this source, jet imbalance is indeed a very unique source in the sense that it emits gravity waves both up and down. Besides, it's the only primary source located high into the stratosphere and mesosphere (Sato and Yoshiki, 2008) if we don't consider secondary wave generations such as wave-wave interactions, and hence has more close effect on the middle and upper atmosphere (e.g., Sato et al., 1997). More details can be found in Chapter 5.

Shear instability is one of the most complicated sources, and involves quite a lot of nonlinear dynamics. It's beyond the scope of my thesis, and will not be discussed further.

Without observational constraints on the gravity wave source spectra, we can never completely understand the source properties, nor characterize a spectrum that is properly based on physics instead of intuitions or ploys. Observational techniques have been

developing rapidly for the past several decades, providing opportunities to depict a global picture of gravity wave climatologies. A variety of observational techniques have been used, including remote sensors on satellites, GPS, rocket sounding, radiosonde, radar, superpressure balloons and so on. Remote sensing measurements on satellites can get global coverage throughout the atmosphere at frequent temporal scanning (Preusse et al., 2000). However, they are in general sensitive to long vertical wavelength waves, leaving the low end of the gravity wave spectrum unobserved. GPS occultation, strictly speaking belongs to remote sensing measurements, can also give temperature variations along the path, and they are more sensitive to low frequency, short vertical wavelength gravity waves for measurements are most accurate within an altitude range of about 15 km (Steiner and Kirchengast, 2000). However, both of the above techniques give only temperature information. As the dispersion relationship indicates that we need at least two variables (e.g., vertical wavelength, horizontal wavelength) to get the third one (e.g., frequency), the complete information of the gravity waves cannot be known without heavily depending on assumptions for these two techniques, which are, unfortunately, cannot be tested easily, although combining multi-scans together could partly solve this problem (Horinouchi and Tsuda, 2009).

Rocket soundings are very similar to radiosonde soundings in terms of measured variables and analysis methods, except it is sensitive to the vertical scale of the wave considered (Fritts and Alexander, 2003). Radar is a powerful instrument to measure gravity waves since they can directly measure the momentum fluxes with very high temporal resolution (Murayama et al., 1994). Superpressure balloon (Vincent et al., 2007) conquers the problem of background wind measurement, which needs little assumptions

to derive correct parameters. However, these instruments are too expensive to carry out a long-period observation, and are hence only used in field campaigns.

Compared with the above observational techniques, radiosonde plays a unique role in deriving the climatology of gravity waves. It is cheap, and hence can cover great range of latitudes and longitudes, as well as span a long time period. For example, the US high-vertical resolution radiosonde data that we use in this study has 94 stations, covering the whole US territory, and the time-span is from 1998 to 2007. It can measure the horizontal winds and temperature simultaneously, and hence frequency and vertical wavelength can be derived independently with fewer assumptions. It takes measurements in the troposphere and the lower stratosphere, and only a few techniques measure tropospheric gravity waves directly. This is particularly important in the sense that the majority of gravity wave sources are located within this layer. It is sensitive to low-frequency inertia gravity waves, as shown in Fig. 1.2, with large overlap with GPS (Wu et al., 2006). However, as will be shown in Chapter 4, utilizing ascent rate information in the radiosonde data could yield a broader "observational window".

The term "observational window" is first proposed by *Alexander (1998)*, where she presented results from multi observational techniques. Then, she used a linear ray-tracing model to prove that the background fields and the observational filters can lead to different "preference" for different techniques in "seeing" the gravity waves in the spectrum. In other words, each technique has its unique "observational window", and the ultimate goal for us is to put the jigsaw puzzle together. This is vividly shown in Fig. 1.2, which is modified from Fig. 8b of *Alexander et al. (2009)*.

With former researchers' works as the foundation, this study is going to investigate the source properties of gravity waves from radiosonde profiles, with emphasis on the convective source and the jet imbalance source. **The main objective of this work is to quantitatively evaluate the climatology of the sources, as well as the emitted gravity waves from the US high-vertical resolution radiosonde data, to qualitatively show the relationships between the characteristics of the sources and the generated gravity waves, and to offer useful implications to the study of GWD parameterizations in the GCMs.**

The thesis is organized as follows. Chapter 1 is the introduction. Chapter 2 briefly describes the data, models and methods used in this study. Chapter 3 presents "best-fit" experiments, demonstrating the effects of background fields on shaping the observed gravity wave spectra, and the necessity to use different source spectra in different regions. Chapter 4 shows the usefulness of ascent rate profiles in deriving higher frequency gravity waves, and their close relationship with the convective source. Jet streak cases study is performed in Chapter 5, where forcings and gravity waves are related together. Chapter 6 gives the final conclusions and future work plans.

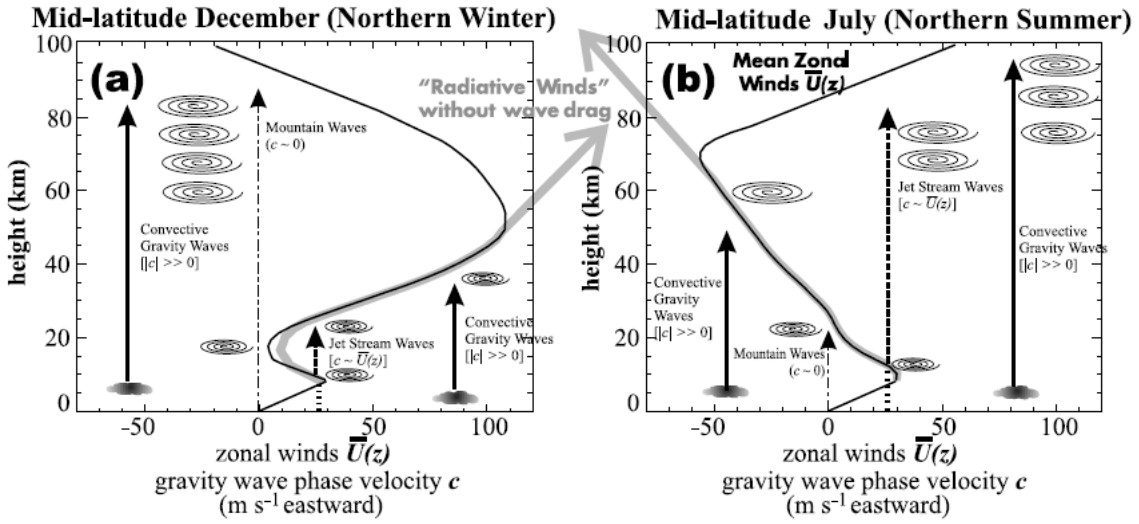

Figure 1.1: Typical mid-latitude zonal winds $\bar{U}(z)$ during northern hemisphere (a) winter and (b) summer. Black curves show observed winds, and grey curves give model "radiative" winds that result without a GWD parameterization. Source with various phase speeds c are also plotted, with suggested breaking levels. (adapted from Kim et al., 2003, Fig. 1)

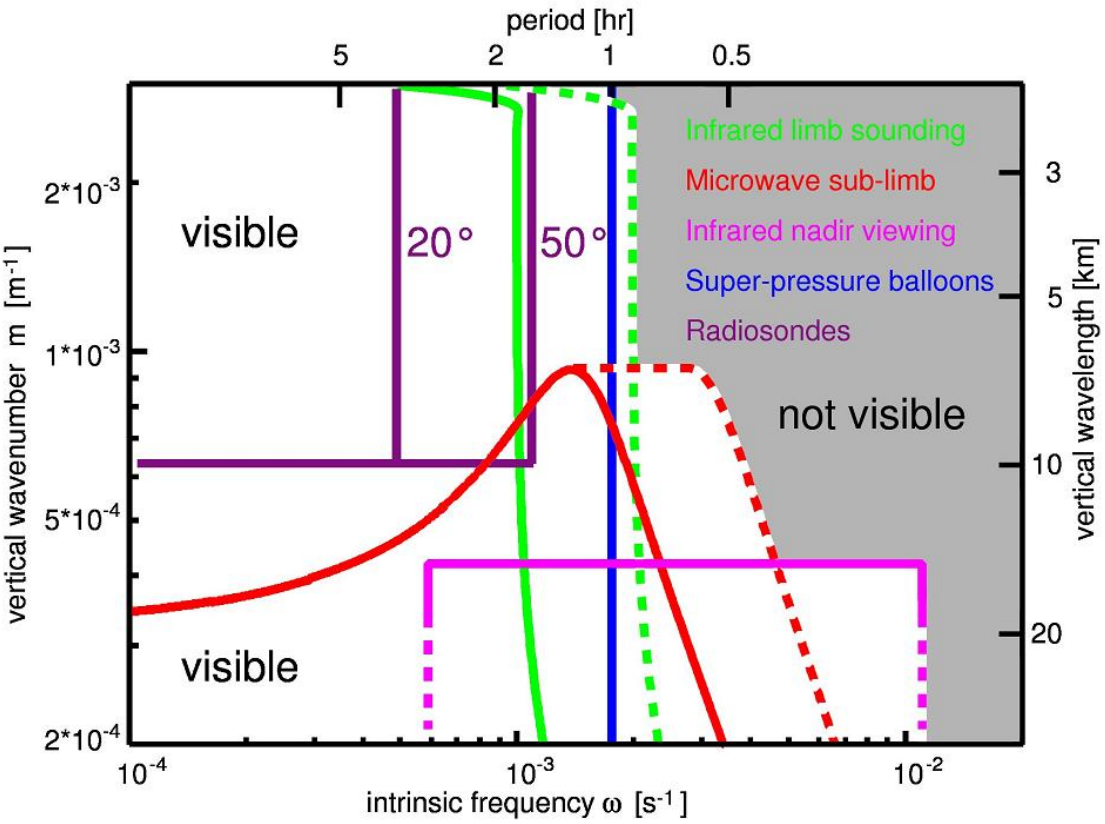

Figure 1.2: Schematic picture showing typical visibility limits as functions of frequency and vertical wavenumber for various observational techniques. Dashed lines indicate waves seen only at favorable viewing geometries. Shaded areas are not visible to any of these techniques. (adapted from Fig. 8b of Alexander et al., 2009).

Chapter 2 Description of Data, Models, and Methods

2.1 Data

The dataset used in this work is US high-vertical resolution radiosonde data from the National Oceanic and Atmospheric Administration (NOAA) National Climatic Data Center (NCDC). The data are available at http://www.sparc.sunysb.edu/html/hres.html for the year from 1998 to 2007. The first part of this work on source spectra investigation (Chapter 3) uses the time period of 1998 – 2005, and the rest of the thesis uses 9 years of data from 1998 to 2006.

There are in total 93 US stations in this dataset, covering a broad range of latitudes and longitudes, from 14.33 °S to 71.3 °N, and from 134.48 °E to 59.5 °W. The highest elevation of the stations is more than 2 kilometers, and the lowest one is only 2 meters above sea level, covering various landscapes including tropical islands, mountains, Great Plain, and the Arctic region. These features are shown in Table 2.1 and Fig. 2.1. Five of these stations (Seawell Apt, WA [300.5 °E, 13.07 °N]; Guam, Mariana Island [144.83 °E, 13.55 °N]; Belize Island [127.7 °E, 17.53 °N]; Grand Cayman [278.63 °E, 19.3 °N]; Charleston, SC [279.97 °E, 32.9 °N]) miss one or more years of data in the lower stratosphere, and hence are excluded from our study. Pago Pago International Airport [189.28 °E, 14.33 °S], is very isolated from the other stations, and is also discarded. The above stations are marked with red circles in Fig. 2.1. Norman, OK [262.53 °E, 35.23 °N] and Wilmington, OH [276.18 °E, 39.42 °N] were discarded by Wang et al. (2005) because of measurement problems, and they are also excluded in the study in Chapter 3 (green

triangles in Fig. 2.1). The investigation using ascent rate perturbations, which will be presented in Chapter 4, does not exclude these two stations.

The major variables we use in this study are zonal wind, meridional wind, temperature, and ascent rate. The horizontal winds are derived from raw 6 seconds resolution elevation and azimuth angle which were measured by tracking the position of the balloons with the Micro-ART system (Williams et al., 1993). To avoid large oscillations in winds due to less precise measurements in azimuth angles, especially at low elevation angles, a 9^{th} order polynomial fit is applied to the end of the sounding to remove the outliers (NWS 1991; NCDC 2002). The error in these winds is generally around $\pm 1 ms^{-1}$. Väisälä RS-80 series (~70% of the stations) and VIZ B2 series (~ 30% of the stations) radiosondes were used for the temperature measurements, which have an accuracy of $0.2^{\circ} K$ for the former, and $0.3^{\circ} K$ for the latter (Wang, 2003). The ascent rate is calculated based on the altitudes of the reference and previous levels derived from these two systems. The ascent rate accuracy is about $\pm 0.1 m/s$ (1%) near the surface, and $\pm 0.5 m/s$ (10%) above 100hpa (Reeder et al., 1999). The temporal resolution of temperature and the ascent rate is 6-sec, corresponding to a 30 m vertical resolution, given that the average ascent rate is approximately $5 m/s$. However, smoothing procedures have been applied to the wind fields during measurements, yielding a vertical resolution of about 150 m.

For this study, we only analyze data at 0000 and 1200 UTC (Coordinated Universal Time), since the majority of the radiosondes are taken at 0000 (49.1%) and 1200 UTC (48.6%), and the rest of the soundings account for only about 2.3% of the total profiles. After quality control and preprocessing of the raw data, which will be described in detail in section 2.2, the qualified wind and temperature profiles account for more than 79.6%

of the total in the troposphere, and 73.2% in the lower stratosphere. For the qualified ascent rate profiles, the percentages are 84.4% in the troposphere and 90.6% in the lower stratosphere. The histograms of qualified profiles versus number of stations are plotted in Fig. 2.2, with the left two columns representing horizontal winds and temperatures, and right two columns representing the ascent rate. In general, stations have more qualified profiles in the troposphere than in the lower stratosphere. In all, with the various locations of the stations, as well as with the nine years of data available, the data are abundant and diverse enough to represent gravity wave climatologies throughout all latitudes as well as all longitudes over the US, with some coverage also in the western Pacific and Caribbean.

2.2 Data Analysis Methods

2.2.1 Gravity wave perturbations in horizontal winds and temperature

The analysis methods follow Vincent et al. (1997) and Wang (2003) closely. The gravity wave perturbations (u', v', T') are simply defined as the difference between the observed fields and the background fields, i.e.,

$$(u', v', T') = (u, v, T) - (\bar{u}, \bar{v}, \bar{T}) \qquad (2.1),$$

where u, v, T are the total zonal wind, meridional wind and the temperature. The overbars mean the background fields, and primes indicate the perturbation fields. The basic assumption made here is that the perturbations are caused by gravity waves. This assumption has demonstrated validity in previous investigations (Allen and Vincent, 1995; Vincent et al. 1997).

For each individual sounding, two vertical segments are defined for analysis. The tropospheric segment is defined as 2 - 8.9 km, except as 2 - 7.4 km for Alaska stations to account for the lower tropopause in high latitudes. The lower stratospheric section is defined as 18 – 24.9 km to be in the stratosphere at all latitudes. The Brunt - Väisälä frequencies (N) are almost constant in these two sections, making the interpretations of the results more straightforward (Allen and Vincent, 1995). The altitude ranges are the same as in Wang (2003), and very close to Allen and Vincent, 1995.

Quality control is performed before analysis. The profiles with missing data of more than 1 km altitude range are excluded. Also, profiles that have suspiciously large gradients in the winds or temperatures are also discarded. In principle, gravity waves cannot propagate through unstable layers, where $N^2 = \frac{g}{\theta}\frac{\partial \theta}{\partial z} < 0$. N is the Brunt - Väisälä frequency, θ is the background potential temperature, and $g = 9.81 ms^{-2}$ is the gravitational constant. In practice, since absolute instability rarely occurs, and even if it occurs, it occurs only over a very shallow layer, we set N^2 to an extremely small number in such regions, and the mean value of N throughout the segment is taken for further calculation. Fig. 2.3 shows two examples of each rejected profiles (panels a and b), with panel (c) representing a qualified profile. After the quality control, most of the stations have more than 400 profiles left for each year, as is shown in Fig. 2.2. The elevation of the station Flagstaff, AZ [248.2°E, 35.2°N] is over 2 km, and the boundary layer measurements seem to have suspicious values or large gaps (Wang, 2003), and therefore this station is excluded from troposphere analysis.

After the quality control, the background fields ($\bar{u},\bar{v},\bar{T}$) are obtained from second-order polynomial fits, which were also used by Vincent and Alexander (2000). Vincent et al. (1997) used third - order polynomials to retrieve background fields over stations at Australia and Antarctica. Sato and Yoshiki (2008) used a band-pass filter with vertical wavelength of 2 – 8 km to derive the gravity wave perturbations. Wang (2003) tested 3rd – polynomial and 4th-polynomial fits, and the results seem not to be so sensitive to these changes in terms of climatologies. Even with diverse approaches, they all basically assume the sounding is an instantaneous profile instead of a time series. This assumption is only valid when the waves are low frequency inertia - gravity waves ($f < \omega < 10f$, where ω is the wave frequency, and f is the Coriolis parameter) to avoid phase change during the time of measurement. This is also one of the basic assumptions for the hodograph method.

With the assumption that all perturbations are caused by gravity waves, the kinetic energy density *KE* of horizontal motions can be written as:

$$KE = \frac{1}{2}(\overline{u'^2} + \overline{v'^2}) \tag{2.2}$$

Note that the vertical component of *KE* is not included in the definition here, simply because that it's too small compared with the horizontal components for inertia-gravity waves. However, it still has physically meaning, and for higher frequency waves, they give useful information. They will be discussed in the section 2.2.2.

The gravity wave potential energy density *PE* is defined as:

$$PE = \frac{g^2}{2\bar{N}^2}\overline{\left(\frac{T'}{\bar{T}}\right)^2} \tag{2.3},$$

and the total energy density E_t is defined as the combination of KE and PE.

Wave parameters and momentum fluxes are derived using the hodograph analysis method (Sawyer, 1961). This method is based on linear gravity wave theory for monochromatic gravity waves in a resting or uniform flow. The axial-ratio (AXR) of the wind hodograph is used to determine the intrinsic wave frequency ($\hat{\omega}$), from the relationship:

$$AXR = \left| \frac{\hat{\omega}}{f} - \frac{1}{\bar{N}} \frac{dV_T}{dz} \right| \tag{2.4},$$

where V_T is the mean wind velocity component perpendicular to the direction of wave propagation (Vincent et al., 1997).

The AXR is determined by Stokes parameters. This was first introduced by Vincent and Fritts (1987) for gravity wave research. The Stokes parameters are:

$$I = 2(\hat{u}'\hat{u}'^{*} + \hat{v}'\hat{v}'^{*}) \tag{2.5},$$

$$D = 2(\hat{u}'\hat{u}'^{*} - \hat{v}'\hat{v}'^{*}) \tag{2.6},$$

$$P = 4\,\mathrm{Re}(\hat{u}'^{*}\hat{v}') \tag{2.7},$$

$$Q = 4\,\mathrm{Im}(\hat{u}'^{*}\hat{v}') \tag{2.8},$$

and the degree of polarization (d) is equal to:

$$d = \frac{D^2 + P^2 + Q^2}{I^2} \tag{2.9}.$$

The symbol "^" means the Fourier transformed field. The symbol "*" means the harmonic conjugate. Re (Im) means the real (imaginary) part. Then,

$$AXR = \frac{1}{\tan(\xi)} \tag{2.10},$$

where

$$\xi = \frac{1}{2}\sin^{-1}\left(\frac{|Q|}{d \times I}\right) \tag{2.11}.$$

The most dominant vertical wavenumber (m) is derived from the energy-weighted vertical wavenumber of the Fourier spectrum of the temperature perturbation. The most dominant horizontal wavenumber (K) can then be inferred from the dispersion relationship:

$$m^2 = \frac{(N^2 - \hat{\omega}^2)K^2 + (f^2 - \hat{\omega}^2)\alpha^2}{\hat{\omega}^2 - f^2} \tag{2.12},$$

where $\alpha = 1/4 H_\rho^{\ 2}$, and H_ρ is the density scale height. $\hat{\omega} = \omega - \bar{u}k - \bar{v}l$ is the intrinsic frequency.

Although radiosonde measurements do not directly give information on vertical velocity, w, gravity wave polarization relationships can be used to derive some vertical fluxes, given appropriate assumptions. For instance, for a monochromatic wave, the zonal pseudo momentum flux[1] (M_x) can be estimated as:

$$M_x = \rho\overline{u'w'}\delta\_ = -\frac{\rho\hat{\omega}g}{\bar{N}^2}\overline{u'\hat{T}'_{+90}}\delta\_(\hat{\omega}) \tag{2.13},$$

Where ρ is the air density, $\hat{T}_{+90}$ is the Hilbert transformation of the normalized temperature perturbation $\hat{T} = T'/\bar{T}$, and then take the reverse form to produce a 90° phase shift, since U' should be 90° out of phase from T' for monochromatic waves.

[1] Referred as momentum flux hereinafter for convenience.

$\delta(\hat{\omega}) = \left(1 - f^2 / \hat{\omega}^2\right)$ is a weighting function that accounts for the fact that high-frequency waves are more effective in transporting momentum (Fritts and Vincent, 1985).

In practice, we are dealing with a spectrum of waves instead of monochromatic wave, and we can replace $\hat{\omega}\delta\_(\hat{\omega})$ with a spectral average $\bar{\hat{\omega}}$, where for $p \neq 2$,

$$\bar{\hat{\omega}} = \hat{\omega}\delta\_(\hat{\omega}) = \bar{N}\frac{(p-1)}{(2-p)}\hat{f}^{p-1}\left(1 - \hat{f}^{2-p}\right) \quad (2.14),$$

and for $p = 2$,

$$\bar{\hat{\omega}} = -f\ln(\hat{f}) \quad (2.15).$$

$\hat{f} = f / \bar{N}$, where p is the frequency spectrum index. The above relationship assumes the intrinsic frequency spectrum has the form of $B(\omega) = B_0\omega^{-p}$ (Vincent et al., 1997; Vincent and Alexander, 2000).

From eqn. (2.7) and (2.8), the upward momentum flux is seen to be strongly dependent on p. In practice, the value of p can be determined from the relationship $p = KE/PE$, and it is found to vary geographically, and temporally. However, we take $p = 5/3$ as is conventional (e.g., Vincent et al., 1997; Wang et al., 2005) to facilitate comparisons with earlier works.

The hodograph method is valid only if three assumptions are true. First, the waves should be approximately stationary relative to the sounding, so we can treat the sounding as an instantaneous profile instead of a time series. This assumption is only valid for obtaining information about low-frequency gravity waves from radiosonde data if we use

this method. Secondly, the hodograph method is heavily dependent on gravity wave polarization and dispersion relationships for monochromatic waves. Hen it will give correct results only if there is a predominant gravity wave existing in the profile. Last, the horizontal wavelengths of the observed gravity waves must be much larger than the slantwise drift of the balloon in order to treat the sounding as a vertical profile. Again, this assumption is valid only for low frequency gravity waves. Zhang et al. (2004) discussed the uncertainties inherent in this method. Wang (2003) has demonstrated that, climatological information is seldom affected by these limitations although analyzing single soundings might lead to invalid results without proper care.

The wave propagation properties are calculated using rotary spectral analysis (Vincent, 1984). This is related to Stokes parameter analysis, which has been extensively used in analyzing the degree of polarization in optics. The rotary spectral approach decomposes the vertical motion into superposition of upward and downward propagating waves which are assumed to be circularly polarized. In the Northern Hemisphere, the upward (downward) propagation corresponds to clockwise (anticlockwise) rotation of the hodograph, and vice versa in the southern hemisphere. Therefore, the fraction of upward propagation in the Northern hemisphere can be easily calculated from the spectral decomposition:

$$f_{up} = \frac{C}{C+A} = \frac{\sum C_m}{\sum C_m + \sum A_m} = \frac{\sum \frac{1}{2}\left\langle V_{-m} V_{-m}^{*} \right\rangle}{\sum \frac{1}{2}\left\langle V_{-m} V_{-m}^{*} \right\rangle + \sum \frac{1}{2}\left\langle V_{+m} V_{+m}^{*} \right\rangle} \qquad (2.16),$$

and

$$f_{down} = \frac{\sum \frac{1}{2}\left\langle V_{+m} V_{+m}^{*} \right\rangle}{\sum \frac{1}{2}\left\langle V_{-m} V_{-m}^{*} \right\rangle + \sum \frac{1}{2}\left\langle V_{+m} V_{+m}^{*} \right\rangle} \qquad (2.17),$$

where f_{up} (f_{down}) is the fraction of upward (downward) propagation, C (A) is the clockwise(anticlockwise) component, V is the horizontal velocity, and V_{+m} (V_{-m}) are the complex values of V at wavenumber $+m$ ($-m$). This method tends to underestimate the upward propagation fraction, especially for high frequency waves (Eckermann and Vincent, 1989). Since as mentioned before, radiosondes mainly observe low-frequency gravity waves, this issue is not a serious issue. A spectrum of waves may also impact the results (Eckermann and Hocking, 1989).

The horizontal wave phase propagation direction is determined using both wind and temperature information. Theoretically speaking, V' should be parallel to the major axis of the ellipse of the hodograph, while T' is parallel to the minor axis. Therefore, the propagation angle (measured clockwise from the north) is:

$$\varphi = \tan^{-1}\left(\frac{\overline{\rho u' T'_{+90}}}{\overline{\rho v' T'_{+90}}} \right) \qquad (2.18).$$

2.2.2 Gravity wave perturbations in the ascent rate

There have been some attempts to use radiosonde ascent rate profiles for gravity wave analysis. Reeder et al. (1999) and Lane et al. (1999) used ascent rate profiles from radiosonde soundings to study two lee – wave cases, and obtained the horizontal wavelength from the ascent rate perturbations in their analyses. Lane et al. (2003) analyzed the balloon ascent rates during a field campaign, and found that the gravity

wave signature in the ascent rate over a tropical island was closely associated with the occurrence of convection.

In this work, the perturbations in the derived ascent rate profiles are studied thoroughly. The vertical perturbation energy density (VE) is defined as

$$VE = \frac{1}{2}\left(\overline{w'^2}\right) \tag{2.19},$$

where w' is the ascent rate perturbation, defined as the deviations from the 2nd – order polynomial fit to the total profile. Although Zhang et al. (2004) pointed out the uncertainties inherent in this procedure, 2nd-order polynomial fitting is much more reliable here in retrieving the background ascent rate simply because it is near constant, and doesn't possess the large gradients or curvatures due to jet and tropopause features, for example. The quality control processes are the same as those mentioned before. The basic assumption here is that these ascent rate fluctuations are produced by gravity waves. This is believed to be a reasonable assumption after certain procedures are applied.

The estimated w' is only trustworthy for large – amplitude gravity waves (Zink and Vincent, 2001b), so a low-pass filter has been applied to the ascent rate perturbations with a cut-off wavelength of 300 m to remove fluctuations that may be due to smaller scale effects such as measurement errors, turbulence, variation of drag coefficients of the balloon, etc. (e.g., thin solid lines in Fig. 2.4 (a), (d), and (g)). Since w' should contain the signature of balloon oscillations, the frequencies associated with balloon oscillations (ω_B) are removed from the spectrum, where

$$\omega_B = \frac{g}{T_{00}}\left(\frac{g}{R} - \gamma\right) \tag{2.20}.$$

In Eqn. (2.20), T_{00} is the reference temperature, $R = 287.1$ is the gas constant for dry air, γ is the lapse rate of the chosen section with the hypothesis that background temperature T can be written as a function of height: $T = T_{00} - \gamma z$. This is a reasonable assumption for both the troposphere and the lower stratosphere segments. In practice, the powers of the two closest frequencies to ω_B are set to 0 before the frequency spectrum is reconstructed back to the altered w' field. One example is given in Fig. 2.4 (b), (e) and (h), where the ω_B is marked as dash-dot line, and the Brunt - Vaisälä frequency is marked as a dashed line. The reason for removing the balloon oscillation component is discussed in more detail in Chapter 4.

Two assumptions must be satisfied here to assure that vertical wavelength calculations are meaningful. First,

$$\left| \frac{kU + lV}{m\overline{W}} \right| << 1 \qquad \text{(2.21a)},$$

$$\left| \frac{\omega}{m\overline{W}} \right| << 1 \qquad \text{(2.21b; Lane et al., 2003)},$$

where *k, l* and *m* are zonal, meridional and vertical wavenumbers, respectively. ω is the ground-based frequency, U and V, are the magnitudes of the zonal and meridional background wind fields, and $\overline{W}$ is the mean ascent rate. Eqn. (2.21a) indicates that the horizontal wavelength must be much longer than the slantwise drift of the trajectory from the local vertical direction in order to properly treat the trajectory as a vertical profile. Furthermore, the period must be long enough for the balloon to rise through one vertical wavelength in order to treat it as a quasi-instantaneous profile (Eqn. 2.21b). With a zonal

wind speed of $20 m/s$ and a mean ascent rate of $5 m/s$, eqn. 1a is satisfied so long as $4k << m$ (assume $l = 0$), which roughly holds for gravity waves with intrinsic frequencies such that $\hat{\omega} << N/4$. Since the typical vertical phase speed of a medium frequency gravity wave is on the order of $\sim 1 m/s$, while the mean ascent rate of the balloon is $\sim 5 m/s$, it is reasonable to assume the wave is effectively stationary while a balloon rises through it, i.e., eqn. (2.21b) is satisfied. Therefore, our calculated values for the dominant vertical wavelength are trustworthy for low – mid frequency waves, though they may be questionable for mid – high frequency gravity waves. We will show later through further analyses that the characteristics of the dominant vertical wavelength calculated from w' profiles are physically reasonable.

The second assumption is that the vertical wavelength is constant throughout the whole altitude. As pointed out by Reeder et al. (1999), this is not the case when the wave is trapped or becomes evanescent. Therefore, in mountain regions, we excluded those days that were favorable for trapped lee – wave or evanescent wave situations using the horizontal projection method of Reeder et al. (1999) and Lane et al. (1999).

The horizontal projection method treats the sounding profile as a time series instead of an instantaneous profile. It then maps the measured time series of w' onto a space section of w' such that the peak in its power spectrum can be used to estimate *k*. If we assume the background flow is a function of height only, for the vertically trapped wave, *m* varies with height, while *k* is a constant. Here *k* is taken to be transverse to the mountain ridge direction. Monochromatic stationary waves have the expression $w'(x,z) = A\cos\alpha$, where A is the amplitude and $\alpha = kx + mz + \alpha_0$ is the phase

of the wave. A new coordinate D_p is then calculated from the following method, such that $\cos(\alpha) = \cos(kD_p)$ is along the radiosonde trajectory.

The angle between the wavenumber vector (k, m) and the projected horizontal direction is:

$$\chi = \tan^{-1}\left(m(z)/k\right) \qquad (2.22\text{ a}).$$

Similarly, as shown in the schematic picture Fig. 2.5, the angle between the horizontal movement of the radiosonde and the projected horizontal direction is: $\phi(z) = \tan^{-1}\left(W(z)/U(z)\right)$, where $W = \bar{W} + w'$ is the total ascent rate, and $U = \bar{U} + u'$ is the horizontal wind transverse to the mountain. Considering the major mountains across US territory are roughly oriented north-south, for simplicity, we take U as the zonal wind. $\bar{W}$ and $\bar{U}$ are the background fields, and w' and u' are the gravity wave perturbations.

For trapped mountain waves, the phase speed is 0 relative to the ground, and the dispersion relationship is:

$$k^2 + m^2(z) = l_s^{\,2}(z) = \frac{N^2(z)}{\bar{U}^2(z)} - \left(\frac{\bar{U}_{zz}(z) + \bar{U}_z(z)/H_s}{\bar{U}(z)}\right) - \frac{1}{4H_s^{\,2}} \qquad (2.22\text{ b}),$$

Where $l_s^{\,2}$ is the Scorer parameter, and H_s is the density-scale height. If the derived horizontal wavenumber *k* satisfies $k^2 > l_s^{\,2}$, the wave is evanescent within that region, i.e., the wave amplitude grows with height, but virtually not vertically progresses.

The last step is to get an expression for ΔD_p. Assume the background flow varies slowly enough that it can be treated as a constant over a small distance ΔD that the

balloon travels within time interval Δt between two consecutive measurements, where by definition, $\Delta D = \sqrt{U^2(z) + W^2(z)}\Delta t$, now the hypothetical horizontal distance that the balloon travels is:

$$\Delta D_p \equiv k\Delta D\cos\phi + m\Delta D\sin\phi \qquad (2.22\text{ c}).$$

Now with an initial guess of *k*, we can solve for Eqn. (2.22 a-c) to obtain $\chi(z), m(z)$ and $\Delta D_p(z)$. χ is set to 0 where $k^2 > l_s^2$. Let D_p be the new projected horizontal coordinate, and the new *k* is the peak of the power spectrum of the Fourier transformed w' with respect to D_p . This procedure is iterated on and on until the difference of *k* between two consecutive steps is smaller than the resolution of the frequency spectrum of w' . As an example, Fig. 2.6 gives the ΔD_p and ΔD as functions of time after the loop converges for one specific trapped-wave case, from which we can find they differ more when the balloon enters the lower stratosphere, where the horizontal wind is larger. Fig. 2.6 b (c) gives the scorer number (vertical wavelength) as a function of height for this case. The waves are seen to be trapped below 14 km, and above 19 km, where the vertical wavelength goes to infinity. They are virtually evanescent within these two segments there, since $k^2 > l_s^2$. The waves can vertically propagate within 14 – 19 km altitude range. In practice, in the troposphere segment, if $k^2 \le l_s^2$ always hold, and the vertical wavelength is finite throughout all altitudes, or the iteration diverges, we consider the trapped waves are with not likely to occur, and hence the corresponding ascent rate profile is retained for further analysis. Besides, since the mountain generated lee-wave situation should not be present at the subtropical and tropical stations in that they are all islands stations, and no big topographies present there, we do not apply the horizontal

projection method to stations south of $25^{\circ} N$, and assume the lee-waves do not occur over these stations. Also, the balloon generally drifts less horizontal distance in the tropics due to weak wind there, and hence our assumption that we can derive vertical wavelength directly from the ascent rate perturbations is more reliable there.

We have compared our results with and without including trapped lee – wave case, using these criteria, and we found that this caused very little difference to our monthly mean values, even though this is apparently very important for single event analysis. About 1/3 – 2/3 of the profiles in the mountain stations have been eliminated by this procedure, as shown in Fig. 2.7 (see the caption for details), where summer seems to be the most affected season. However, the numbers of the remaining profiles are still sufficient enough (the worst situation is about 60 profiles left for one season) for us to make conclusions on climatologies.

2.3 Models

In this study, two numerical models are employed. These models are used together with the observations. The first model is a gravity wave ray-tracing model, called GROGRAT. This model is used to trace the waves backward in time to the source, as well as forward in time to study the propagation properties. The second model is a linear forcing – response model, developed by Dr. Shuguang Wang[2] based on the theory developed in Plougonven and Zhang (2007). I will describe these two models briefly in the following two sections. The detailed procedures for employing these models will be presented in later chapters.

[2] S. Wang's paper about this model is in revision.

2.3.1 GROGRAT – A gravity wave ray-tracing model

Gravity-wave Regional Or Global Ray Tracer (GROGRAT) (Marks and Eckermann, 1995) is a four-dimensional nonhydrostatic ray-tracing wave model, which can trace nonhydrostatic gravity waves globally through a given background atmosphere. The version used in this work is v2.9.

Under the WKB approximation in both time and space, we can define a ray as the trajectory of a point moving with the group velocity:

$$\frac{d_g \vec{x}}{dt} = \vec{C}_g[\vec{k}(\vec{x}(t),t);\vec{x}(t),t] \qquad (2.23),$$

where $\frac{d_g}{dt} \equiv \frac{\partial}{\partial t} + \vec{C}_g \bullet \vec{\nabla}$, $\vec{x} \equiv (x,y,z)$ is the position vector of the point, $\vec{k} \equiv (k,l,m)$ is the wavenumber vector, and $\vec{C}_g = (C_{gx}, C_{gy}, C_{gz}) = \left(\frac{\partial \omega}{\partial k}, \frac{\partial \omega}{\partial l}, \frac{\partial \omega}{\partial m}\right)$ is the group vector velocity. The variation of local wavenumbers and the frequency along the ray then satisfy the following relations:

$$\frac{d_g k}{dt} = -\frac{\partial \omega}{\partial x},\ \frac{d_g l}{dt} = -\frac{\partial \omega}{\partial y},\ \frac{d_g m}{dt} = -\frac{\partial \omega}{\partial z},\ \frac{d_g \omega}{dt} = \frac{\partial \omega}{\partial t} \qquad (2.24\ \text{a,b,c,d}).$$

Given the dispersion relationship Eqn. (2.12) and initial conditions for $\bar{x}$ and $\vec{k}$, Eqn. (2.23) and (2.24) can be solved for the ray paths, as well as the wavenumber and the frequency along the rays (refer to Andrews et al. [1987] for details).

The ray-tracing equations do not give information about the wave amplitude. To solve for this, a wave action equation is introduced:

$$\frac{\partial A}{\partial t} + \nabla \bullet (\vec{C}_g A) = -\frac{2A}{\tau} \qquad (2.25),$$

where $A = E/\hat{\omega}$ is the so-called "wave action density", τ is the damping time scale, and E is defined as $E = \frac{1}{2}\rho_0(\overline{u'^2} + \overline{v'^2} + \overline{w'^2} + N^2\overline{\varsigma'^2})$, where ς' is the vertical displacement. In GROGRAT, Eqn. (2.25) is transformed into:

$$\frac{\partial F}{\partial t} + \overrightarrow{C_g} \bullet \nabla F = -\frac{2}{\tau}F - FC_{gz}\nabla \bullet \vec{j} \qquad (2.26),$$

where $F = C_{gz}A$, and $\vec{j}$ is defined such that $\vec{C}_g = C_{gz}\vec{j}$. $\nabla \bullet \vec{j}$ is omitted because several experiments suggested that its contribution is small (Marks and Eckermann, 1995). In practice, an initial rms velocity $(\overline{u'^2} + \overline{v'^2})^{1/2}$ is given at the source level in GROGRAT, as well as the horizontal wavenumbers *k* and *l*, and the source-level based frequency ω. Eqns. (2.23), (2.24) and (2.26) can then be integrated step by step using a given (and possibly time-varying) background flow. After each time step, $(\overline{u'^2} + \overline{v'^2})^{1/2}$ (hence *F*) is calculated by tracking $\hat{\omega}/N$ and $f/\hat{\omega}$ along the ray.

Since the above theory is based on WKB assumptions, a parameter (δ) is used to evaluate whether this assumption is valid or not at each time step, where

$$\delta = \frac{1}{m^2}\left|\frac{\partial m}{\partial z}\right| = \left|\frac{1}{C_g m^2}\frac{d_g m}{dt}\right| \qquad (2.27).$$

A ray is terminated once $\delta \geq 1$ to save computational time, which usually occurs when $m \to 0$ (wave reflection) or the wave meets a critical level (where the background wind

speed equals the wave phase speed). Hence, this model does not deal with the wave ducting and absorption.

A saturation algorithm is introduced to avoid very large wave amplitudes resulting from the exponential increase[3]. The timescale associated for these instabilities can be written as:

$$\hat{\tau}^{-2} = \frac{\hat{\delta}}{4}\left|\frac{\partial \vec{u}}{\partial s}\right|^2 - \left(\frac{g}{\theta}\right)\frac{\partial \theta}{\partial s}\cos\varsigma \qquad (2.28),$$

where $\vec{u}$ is the total wind vector, ς is the angle between the wave progressing direction and the vertical axis, and $\hat{\delta}$ is a switching function to either use vertical dynamic instability (VDI) or saturation via dynamic instability (SDI). When wind shear is negligible ($\hat{\delta} = 0$) and the air parcel only moves vertically ($\varsigma = 0^\circ$), VDI is applied, and $\hat{\tau} = (2\pi\beta)^{-1} \bullet 2\pi/\hat{\omega}$. Otherwise, $\hat{\delta} = 1$, and the criterion for SDI is:

$$\hat{\tau}^{-2} - \beta^2\hat{\omega}^2 = \frac{\hat{\delta}}{4}\left|\frac{\partial \vec{u}}{\partial s}\right|^2 - \left(\frac{g}{\theta}\right)\frac{\partial \theta}{\partial s}\cos\varsigma - \beta^2\hat{\omega}^2 = 0 \qquad (2.29).$$

β is a tunable parameter, and is set to 1 in GROGRAT. The saturation amplitude can then be inferred from Eqn. (2.28). Detailed procedures can be found in Marks and Eckermann (1995).

Besides saturation, other physical processes, such as infrared radiative damping, photochemical damping, and turbulent damping, can also damp the wave amplitudes. In GROGRAT, photochemical damping due to ozone is neglected because it's generally small compared to other processes for relatively small time intervals. The radiative

[3] Strictly speaking, the wave amplitude grows as $e^{z/2H}$.

damping used is Zhu (1993)'s scheme, and for turbulent damping, a scheme similar to that used in Pitteway and Hines (1963) is implemented into the model.

In GROGRAT, a fourth-order Runge-Kutta algorithm is used to adaptively adjust the time step δt (Press et al., 1992, section 16.1-16.2). This algorithm uses a fourth-order Runge-Kutta scheme to choose the largest possible δt for computational efficiency while ensuring a truncation error less than 1%.

Detailed information about GROGRAT can be found in Mark and Eckermann (1995), and Eckermann and Marks (1997)[4].

2.3.2 A linear forcing-response model

The linear forcing-response model we use in this work was developed by S. Wang at 2008 based on the theory proposed by Plougonven and Zhang (2007). They basically separate the primary flow and the secondary flow by several scaling parameters in both the time and space, and assume that the secondary flow is generated from the forcings associated with the primary flow.

The adiabatic, inviscid and hydrostatic primitive equations using the Boussinesq approximation on a β-plane are:

$$\frac{\partial \vec{u}_H^*}{\partial t} + \vec{u}^* \nabla \vec{u}_H^* + f\bar{k} \times \vec{u}_H^* + \nabla_H \Phi^* = 0 \qquad (2.30\text{ a}),$$

$$-\frac{g}{\Theta}\theta^* + \frac{\partial \Phi^*}{\partial z} = 0 \qquad (2.30\text{ b}),$$

$$\frac{\partial \theta^*}{\partial t} + \vec{u}^* \nabla \theta^* = 0 \qquad (2.30\text{ c}),$$

[4] The website for GROGRAT is http://uap-www.nrl.navy.mil/dynamics/html/grograt.html

$$\nabla \bullet \vec{u}^* = 0 \qquad (2.30\ d)$$

Where * designates the dimensional variables, $f = f_0 + \beta y$ is the Coriolis parameter, Θ is the reference potential temperature, while θ^* is the potential temperature, and Φ^* is the geopotential height. Subscript *H* denotes the horizontal component, and $\vec{k}$ is a unit vertical vector. Since most of the research in this dissertation deals with low-frequency hydrostatic gravity waves, the Boussinesq approximation is reasonable.

Now, every field can be written into primary (denoted by overbars) and secondary (denoted by primes) flows, e.g., $A^* = \overline{A}^* + A'^*$. A scale analysis is then applied to separate these two fields. The detailed procedure can be found in Plougonven and Zhang (2007), and the scale factors are listed in Table 2.2. The final formula for the vertical perturbation velocity *w'* derived by this method is:

$$[(D_\gamma^2 + f^2)\partial_{zz} + N^2\Delta_H]w^{*\prime} = D_\gamma \partial_z \Delta_{NBE} - f\partial_z A_{1,\zeta^*} - \frac{g}{\Theta}\Delta_H A_{0,\theta^*} \qquad (2.31),$$

where
$$\Delta_{NBE} = -f\overline{\zeta^*} + \Delta_H \overline{\Phi^*} + \beta\overline{u^*} + 2J(\overline{v^*}, \overline{u^*}), \qquad (2.32\ a)$$

$$A_{1,\zeta^*} = -\partial_t \overline{\zeta^*} - \overline{\vec{u}_H^*}\nabla\overline{\zeta^*} - f\overline{\delta^*} - \beta\overline{v^*}, \qquad (2.32\ b)$$

$$A_{0,\theta^*} = (\partial_t + \overline{\vec{u}_H^*}\nabla)\overline{\theta^*} + \overline{w^*}\partial_z\Theta^* \qquad (2.32\ c)$$

where $D_\gamma = \partial_t$ ($D_\gamma = \partial_t + \overline{\vec{u}_H^*}\nabla$) if $\gamma = 1$ ($\gamma = \varepsilon \ll 1$), where γ is the ratio between the horizontal scale of the primary flow and the horizontal scale of the secondary flow, and ε is the Rossby number. ζ is the vertical component of the vorticity, δ is the divergence of horizontal ???, and $\theta_{total} = \Theta^* + \overline{\theta}^* + \theta'^*$. ∂_z and ∂_{zz} are the first and second order

derivatives with respect to z, $\Delta_H = \partial_{xx} + \partial_{yy}$ is the horizontal Laplacian operator, and J is the Jacobian operator.

Eqn. (2.31) states that the secondary flow (gravity wave fields) is generated from the residuals of the divergence, vorticity and thermodynamic equations for the primary flow. In other words, during the spontaneous adjustment process of the primary flow, it emits gravity waves which act to reduce these residuals to adjust the primary flow back to a balanced state. Eqn. (2.31) and (2.32) together also supply a way to directly compare the importance of each forcing for a specific case as well as for the climatologies since the left hand side of Eqn. (2.31) is a linear operator.

The residual from nonlinear balance equation (Δ_{NBE}) has been documented before in Zhang et al. (2000). Other similar parameters to evaluate the degree of imbalance include the Lagrangian Rossby number (Van Tuyl and Young, 1982), cross-stream Lagrangian Rossby number (Koch and Dorian, 1988), psi vector (Keyser et al., 1989), etc.. Plougonven and Zhang (2007) demonstrates that not only the Δ_{NBE} term is an important forcing, but the residuals invoked from thermal and vorticity equations are also important, even more significant for some specific cases, as will be presented in Chapter 5.

In practice, the primary flow is derived from piecewise PV inversion approach (Davis and Emanuel, 1991). The Ertel PV (q) can be expressed as a nonlinear function of the geopotential height (Φ) and the streamfunction (Ψ):

$$q = \mathcal{N}_1(\Phi, \Psi) \qquad (2.33\text{ a}),$$

and the relationship between Φ and Ψ can be expressed as:

$$\Phi = \mathcal{N}_2(\Psi) \qquad \text{(2.33 b)},$$

where $\mathcal{N}_1$ and $\mathcal{N}_2$ are two nonlinear operators. With lateral boundary conditions in Φ and Ψ (either Dirichlet or Neumann conditions), and specified potential temperature at the top and the bottom, we can invert q to solve for Φ and Ψ, giving both the flow field information and the forcing terms.

It's difficult to solve Eqn.(2.31) directly. On the other hand, the intermediate steps are much easier to solve with proper initial and boundary conditions. With this, S. Wang developed a linear forcing-response model to solve for the time evolution of the emitted gravity waves.

The primitive equation set for the secondary flow (nonhydrostatic, compressible, Boussinesq approximation, *f*-plane) is written as:

$$(\partial_t + \vec{\bar{u}}_H \nabla)\delta' + \vec{u}'\nabla\bar{\delta} + \Delta_H \Phi' - f \cdot \zeta' + [...] = F_\delta \qquad (2.34a)$$

$$(\partial_t + \vec{\bar{u}}_H \nabla)\zeta' + f \cdot \delta' + [...] = A_{1,\zeta} \qquad (2.34b)$$

$$(\partial_t + \vec{\bar{u}}_H \nabla)\theta' + w' \frac{\partial \bar{\theta}}{\partial z} + [...] = A_{0,\theta} \qquad (2.34c)$$

$$(\partial_t + \vec{\bar{u}}_H \nabla)w' = -\Phi'_z + \frac{g}{\bar{\theta}}\theta' \qquad (\Phi'_z = \frac{g}{\bar{\theta}}\theta') \qquad (2.34d)$$

$$(\partial_t + \vec{\bar{u}}_H \nabla)\Phi' + \delta' + \partial_z w' = 0 \qquad \left(\partial_x u' + \partial_y v' + \partial_z w' = 0\right) \qquad (2.34e)$$

where […] indicates higher order diffusive terms. $F_\delta = -(\partial_t + \vec{\bar{u}}_H \nabla)\bar{\delta} + \Delta_{NBE}$, and the other two forcing terms $A_{1,\zeta}$ and $A_{0,\theta}$ are the same as in Eqn. (2.32b,c). Similarly, we can define G_δ, G_ζ and G_θ such that:

$$\mathcal{L}(w') = G_\delta + G_\zeta + G_\theta \qquad (2.35)$$

where $\mathcal{L}$ is a linear operator with the same left-hand-side of Eqn. (2.31), and

$$G_\delta = D_\gamma \frac{\partial F_\delta}{\partial z}, \qquad G_\zeta = -f \frac{\partial A_{1,\zeta}}{\partial z}, \qquad G_\theta = -\frac{g}{\Theta}\Delta_H A_{0,\theta} \qquad \text{(2.36 a,b,c)}$$

Again, G_δ, G_ζ and G_θ can be compared directly to see their relative importance for specific cases.

The prognostic variables in Eqns. (2.34 a-e) are $\delta', \zeta', w', \theta'$ and Φ'. The equation set (2.34) is solved by a time split-explicit method which was first introduced by Klemp and Wilhelmson (1978) and Skamarock and Klemp (1992)[5], where they used Euler's method for the slow modes, using a large time step (Δt), and a forward-backward scheme for the fast modes, advancing in small time steps (δt). Here, the advection, horizontal and vertical diffusion, Coriolis, and forcing terms are slow modes, and are integrated with time steps of Δt with a 3rd-order Runge-Kutta scheme[6], and all other terms (marked in bold in Eqn. 2.34) are updated every δt using the forward and backward scheme since they are fast modes, and need to be integrated with acoustic time steps. Δt and δt are specified at the very beginning. The vertical velocity eqn. (2.34d) is solved implicitly.

RK3 can be described as follows:

$$\begin{aligned} Q^* &= Q_0 + \frac{\Delta t}{3} f(Q_0) \\ Q^{**} &= Q_0 + \frac{\Delta t}{2} f(Q^*) \\ Q_1 &= Q_0 + \Delta t \cdot f(Q^{**}) \end{aligned} \qquad \text{(2.35)},$$

[5] Referred to as KW78 and SK92 hereinafter.
[6] Referred to as RK3 hereinafter.

where Q_0 and Q_1 are the current and forward time steps, Q^* and Q^{**} are intermediate steps, and $f(Q)$ describes the function of the variable Q. Compared with an explicit forward scheme (Euler's method), RK3 can use larger time step by a fraction of about 10^4, while keeping the errors on the order of $o(\Delta t^3)$ for linear equations (Wicker and Skamarock, 2002). This procedure saves a great deal of computational cost. It has been widely used for explicit (slow-mode) terms in other models (e.g., for the Advanced Research WRF model, refer to Skamarock and Klemp [2008] for details).

In each small time step δt, a simple forward scheme is used. Assuming $\Delta t / \delta t = n_s$, we need $n_s / 3$ small steps to advance to time $t + \Delta t / 3$, where the large time step is recomputed, and is substituted again into the loop of the small time step to integrate to time $t + \Delta t / 2$. Replacing the slow mode values with the most updated values at this time, we can loop again, and eventually reach the next time step $t + \Delta t$. The central scheme is used for spatial derivatives. Since for small time steps, the slow-modes are not updated for each time, it is backward in time in terms of the fast mode. Therefore, it's called a "forward-backward scheme". Wicker and Skamarock (2002) thoroughly investigated the stability and computational efficiency of the combined RK3 and forward-backward scheme.

The Wang model uses 4th-order advection scheme in the inner domain. This scheme is noisy, so a bi-harmonic diffusion scheme is implemented also to diffuse away noise while keep the gradients well resolved. At the boundaries, simple outflow is used as lateral boundary conditions, and the top and bottom boundary conditions are rigid lids.

To avoid spurious wave reflections at the boundaries, sponge layers are added at the top, bottom and lateral boundaries.

The detailed model setup will be discussed later on in Chapter 5.

WBAN	NAME	STATE	LAT	LON	ELV.(m)
03020*	SANTA TERESA	NM	31.9	-106.7	1257
03160*	DESERT ROCK/MERCURY	NV	36.62	-116.02	1007
03190	MIRAMAR NAS	CA	32.85	-117.15	134
03198*	RENO	NV	39.57	-119.8	1516
03937	LAKE CHARLES	LA	30.12	-93.22	5
03940	JACKSON/THOMPSON FLD	MS	32.32	-90.07	91
03948	NORMAN	OK	35.23	-97.47	362
03952	N LITTLE ROCK	AR	34.83	-92.27	172
03990	FT WORTH	TX	32.8	-97.3	196
04102*	GREATFALLS	MT	47.45	-111.38	1130
04105*	ELKO	NV	40.85	-115.73	1608
04106	SPOKANE INTNL APT	WA	47.68	-117.63	728
04830	DETROIT/PONTIAC	MI	42.7	-83.47	329
04833	LINCOLN-LOGAN COUNTY AP	IL	40.15	-89.33	178
04837	GAYLORD/ ALPENA	MI	44.90	-84.70	448
11501	SEAWELL APT	99	13.07	-59.5	47
11641	SAN JUAN/ISLA VERDE	PR	18.43	-66	3
11813	GRAND CAYMAN	99	19.3	-81.37	3
11818	BELIZE	99	17.53	-88.3	5
12842	TAMPA BAY/RUSKIN	FL	27.7	-82.4	13
12850	KEY WEST	FL	24.5	-81.8	13
12919	BROWNSVILLE	TX	25.9	-97.43	7
12924	CORPUS CHRISTI	TX	27.77	-97.5	14
13723	GREENSBORO	NC	36.08	-79.95	277
13841	WILMINGTON	OH	39.42	-83.82	317
13880	CHARLESTON	SC	32.9	-80.03	15
13889	JACKSONVILLE	FL	30.43	-81.7	10
13897	NASHVILLE	TN	36.25	-86.57	180
13957	SHREVEPORT REGIONAL AP	LA	32.45	-93.83	84
13985*	DODGE CITY	KS	37.77	-99.97	791
13995	SPRINGFIELD REGIONAL AP	MO	37.23	-93.4	394
13996	TOPEKA	KS	39.07	-95.62	268
14607	CARIBOU	ME	46.85	-68.02	191
14684	CHATHAM	MA	41.67	-69.97	16
14733	BUFFALO/GRTR ARPT	NY	42.93	-78.73	218
14898	GREEN BAY	WI	44.48	-88.13	210
14918	INTERNATIONALFALLS	MN	48.57	-93.38	359
14929	ABERDEEN	SD	45.45	-98.42	397
21504	HILO	HI	19.72	-155.07	10
22010	DELRIO	TX	29.37	-100.92	313
22536	LIHUE/KAUAI	HI	21.98	-159.35	36
23023*	MIDLAND	TX	31.93	-102.2	873
23047*	AMARILLO	TX	35.23	-101.7	1095
23050*	ALBUQUERQUE	NM	35.05	-106.62	1619
23062*	DENVER/STAPLETON ARPT	CO	39.77	-104.88	1611
23066*	GRAND JUNCTION	CO	39.12	-108.53	1472
23160*	TUSCON	AZ	32.12	-110.93	788
23230	OAKLAND INT AP	CA	37.75	-122.22	6

24011	BISMARCK	ND	46.77	-100.75	503
24023*	NORTH PLATTE	NE	41.13	-100.68	847
24061*	RIVERTON	WY	43.06	-108.47	1688
24127*	SALT LAKE	UT	40.77	-111.97	1288
24131*	BOISE	ID	43.57	-116.22	871
24225	MEDFORD	OR	42.37	-122.85	397
24232	SALEM	OR	44.92	-123.02	61
25308	ANNETTE ISLAND	AK	55.03	-131.57	37
25339	YAKUTAT	AK	59.52	-139.67	10
25501	KODIAK	AK	57.75	-152.48	4
25503	KING SALMON	AK	58.68	-156.65	15
25624	COLD BAY	AK	55.2	-162.72	30
25713	ST PAUL ISLAND	AK	57.15	-170.22	10
26409	ANCHORAGE IAP/PT CAMPBE	AK	61.17	-150.02	45
26411	FAIRBANKS	AK	64.82	-147.85	135
26510	MCGRATH	AK	62.97	-155.62	103
26615	BETHEL	AK	60.78	-161.8	36
26616	KOTZEBUE	AK	66.85	-162.63	5
26617	NOME AP	AK	64.5	-165.43	5
27502	POINT BARROW	AK	71.3	-156.78	12
40308	YAP ISLAND	99	9.48	138.08	17
40309	KOROR/PALAU ISLAND	99	7.33	134.48	33
40504	PONAPE ISLAND	99	6.97	158.22	46
40505	TRUK INTL/MOEN ISL	99	7.47	151.85	2
40710	MAJURO/MARSHALL ISL	99	7.08	171.38	3
41415	GUAM MARIANA ISL	99	13.55	144.83	111
53103*	FLAGSTAFF/BELLEMT (ARMY)	AZ	35.23	-111.82	2179
53813	SLIDELL	US	30.33	-89.82	8
53819	PEACHTREE CITY	GA	33.35	-84.56	246
53823	BIRMINGHAM (SHELBY APT)	AL	33.1	-86.7	178
53829	ROANOKE/BLACKSBURG	VA	37.2	-80.41	648
54762	GRAY	ME	43.89	-70.25	125
61705	PAGO PAGO INTL ARPT	99	-14.33	-170.72	3
92803	MIAMI/FL INTL UNIV	FL	25.75	-80.38	4
93734	STERLING(WASH DULLES)	VA	38.98	-77.47	85
93768	MOREHEAD CITY/NEWPORT	NC	34.7	-76.8	11
93805	TALLAHASEE	FL	30.38	-84.37	25
94008*	GLASGOW	MT	48.2	-106.62	693
94043*	RAPID CITY	SD	44.07	-103.21	1037
94240	QUILLAYUTE	WA	47.95	-124.55	56
94703	BROOKHAVEN	NY	40.85	-72.85	20
94823	PITTSBURGH/MOON TOWNSHIP	PA	40.53	-80.23	360
94980	OMAHA/VALLEY	NE	41.32	-96.37	350
94982	DAVENPORT MUNICIPAL AP	IA	41.6	-90.57	229
94983	MINNEAPOLIS	MN	44.83	-93.55	287

Table 2.1: List of stations of US high-vertical resolution radiosonde data, 99 in the column of state means island station.

variables	$\bar{u},\bar{v}$	$\bar{w}$	$\bar{x},\bar{y}$	$\bar{z}$	x',y'	z'	Φ'	w'	τ
Scale factor	U	$\frac{\varepsilon UH}{L}$	L	H	γL	γH	$\alpha f U \gamma L$	$\frac{\alpha UH}{L}$	f^{-1}

Table 2.2: Scale factors for primary flows (indicated by overbars) and the secondary flow (indicated by primes). τ is the time scale. $\varepsilon = \frac{U}{fL} \ll 1$ is the Rossby number, $\alpha \ll 1$ and $\gamma \leq 1$. $\alpha / \gamma = \varepsilon$.

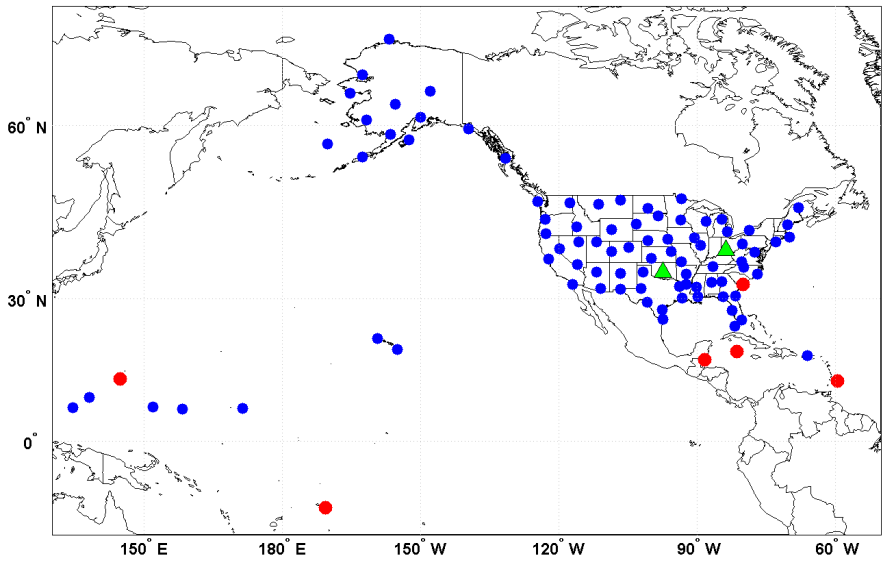

Figure 2.1: Geographical distribution of US high-vertical resolution radiosonde stations (blue filled circles). The stations excluded from the entire study are marked as red filled circles, and the stations excluded from the research in Chapter 3 are marked as green filled triangles. See text for details.

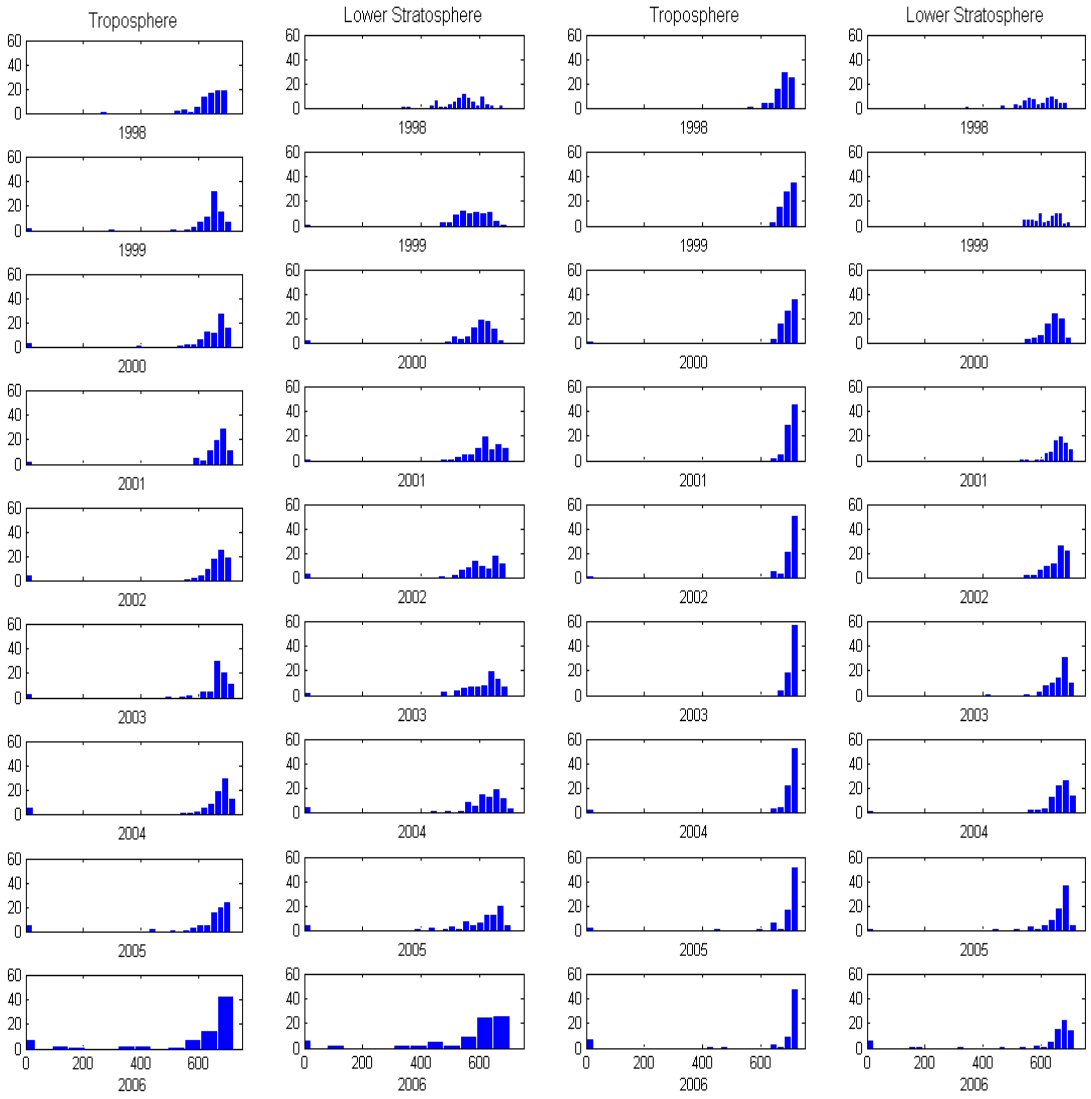

Figure 2.2: Histogram of qualified profiles for the troposphere (columns 1 and 3) and the lower stratosphere (columns 2 and 4) of the winds and temperature (left two columns) and the ascent rate (right two columns) for year 1998 - 2006. The abscissa gives the number of valid profiles, while the ordinate gives the number of stations.

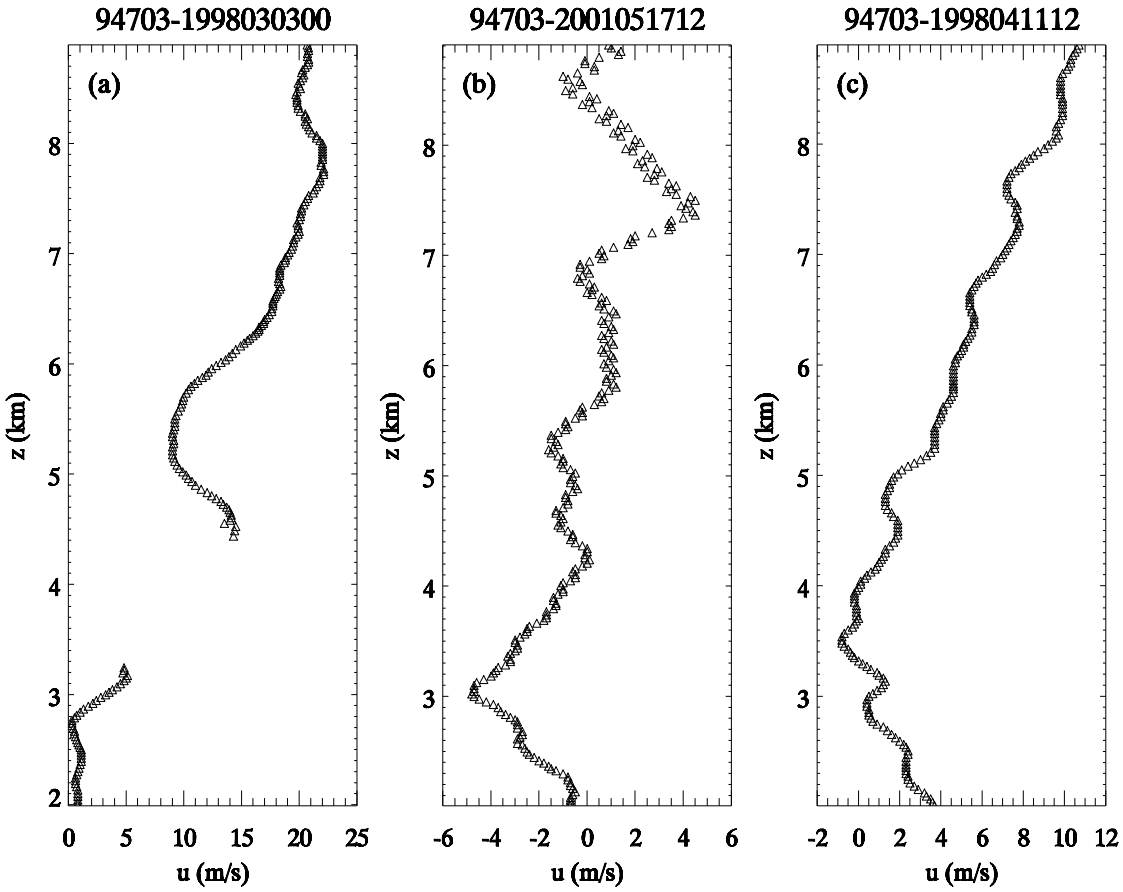

Figure 2.3: Three cases of disposable profiles, where the observation gap between two consecutive measurements is larger than 1 km altitude range (a), there are suspiciously large gradients in the measurements (b), and one case of a good profile (c). Note the small-scale oscillations in panel (b). The title of each panel gives the WBAN number of the station and the measured time in the format of yyyymmddZZ, where ZZ=00UTC or 12UTC.

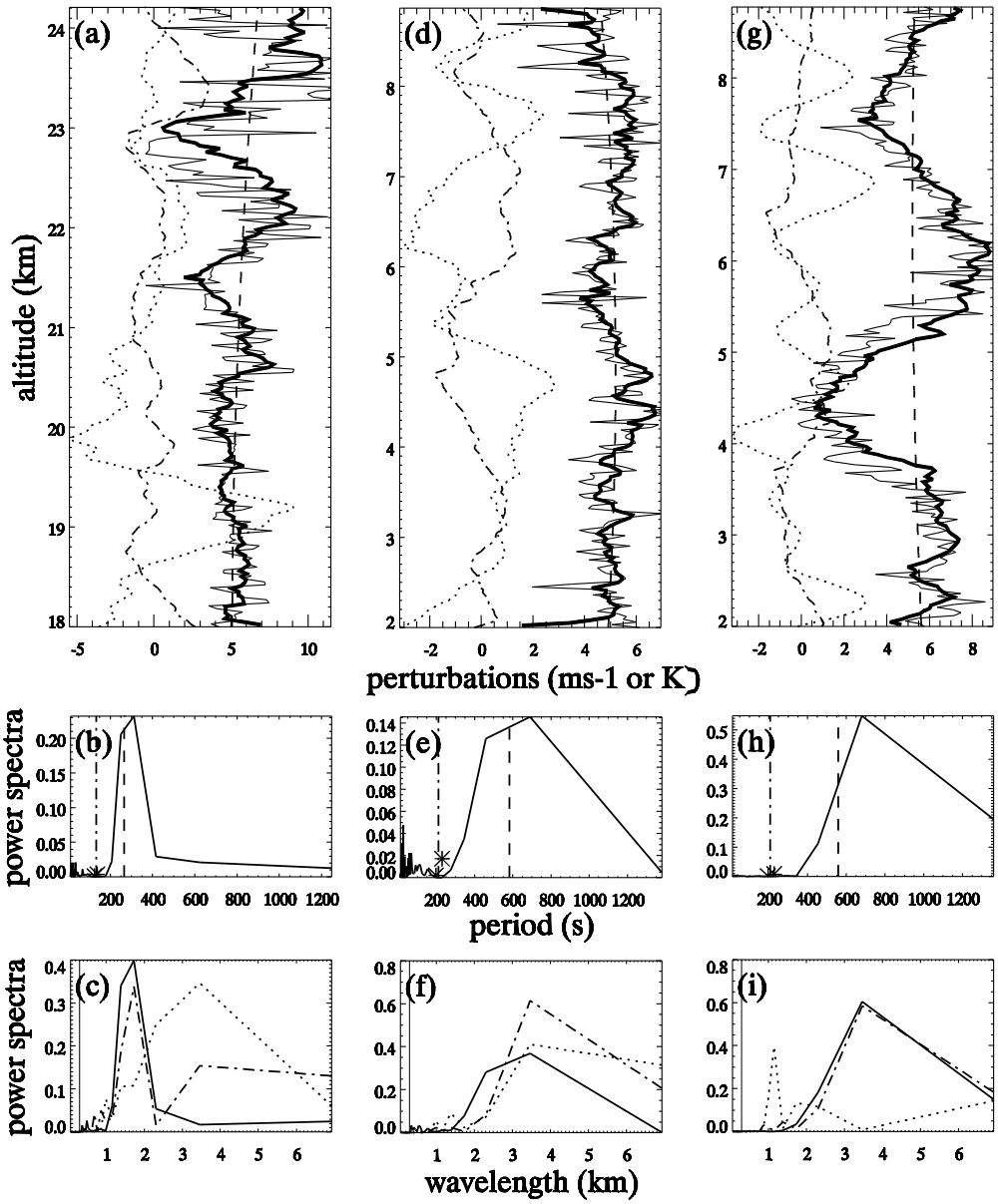

Figure 2.4: Vertical profiles of zonal wind perturbation (dotted), temperature perturbation (dash - dotted) and ascent rate (thin solid, with perturbation part multiplied by a factor of 2 and then added onto mean ascent rate) (a, c, d, f, g, and i). Mean and the low-pass filtered ascent rates are drawn in dashed and bold solid lines, respectively. Top panels are profiles and bottom panels are corresponding normalized vertical - wavelength power spectra. The middle panels give Fourier transformed power spectra of *w'* with respect to time, with dash-dotted lines representing balloon oscillation frequencies, dash lines representing Brunt - Vasäla frequencies, and stars corresponding to the two closet frequencies associated with balloon oscillation frequency. (a) (b) and (c) are taken on 00Z July 05, 2003, Lincoln-logan county airport, IL in lower stratosphere; (d) (e) and (f) are on the same time, at the same location, but in troposphere; (g) (h) and (i) are on 12Z January 4, 2000, Roanoke/Blacksburg, VA in troposphere. (a) - (f) correspond to a squall line case, while (g) - (i) correspond to a jet-front case.

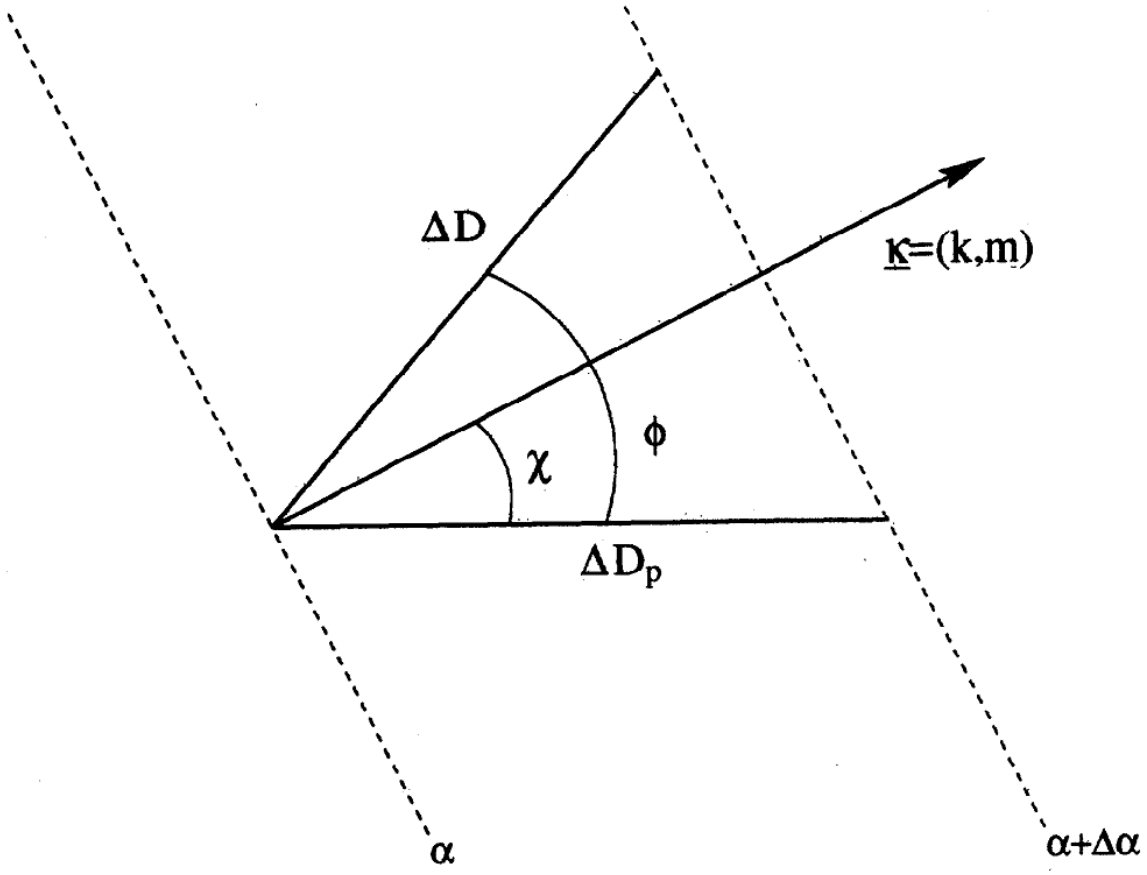

Figure 2.5: Schematic plot showing the geometric relationships among various variables. See the text for details (Adapted from Reeder et al., 1999).

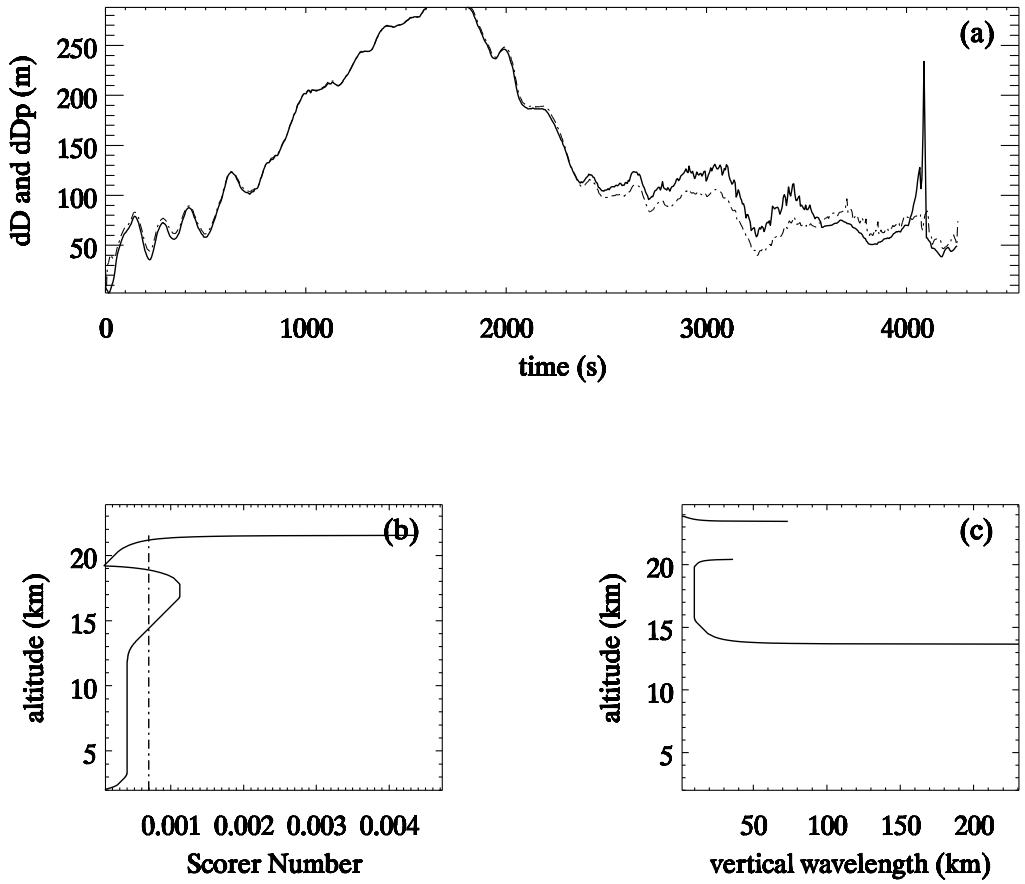

Figure 2.6: One example of a trapped wave case at 12 UTC on Jan. 23, 2000 at station 04105 (Elko, NV). The observed space interval (*dD*, dash-dotted) and horizontal projected space interval (*dDp*, solid) as functions of time (a); The Scorer number (solid) and the derived horizontal wavenumber (dash-dotted) as functions of height (b); and the derived vertical wavelength as a function of height (c).

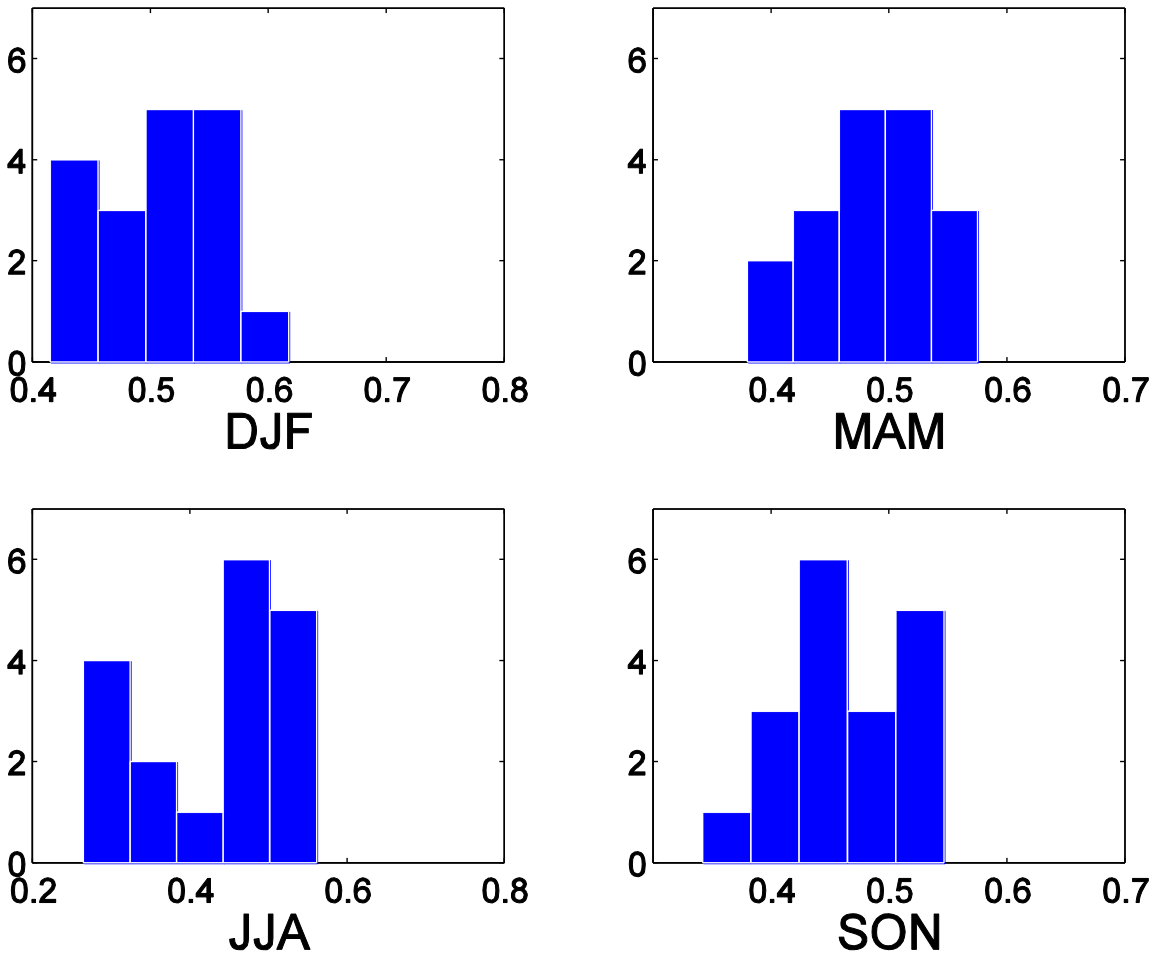

Figure 2.7: Histogram of the number of retained profiles (with trapped-wave profiles and evanescent-wave profiles removed) divided by the total number of qualified profiles for Rocky Mountain stations for four seasons, averaged over 1998 - 2006. The mountain stations are marked as "*" at the corner of WBAN in Table 2.1.

Chapter 3 Spatial and Temporal Variations of Source Spectra

3.1. Introduction

In Chapter 1 there was some discussion of the importance and necessity of incorporating observational constraints to parameterize GWD in a physically justified manner in GCMs, but this is in practice quite difficult. The main reasons are two manifolds. Firstly, each observational technique only sees part of the gravity waves spectrum (Alexander, 1998), some of which overlap what is observed by other methods. Secondly, observations often neglect the fact that waves are sometimes refracted in and out of the "observational window", making it challenging to assess the full nature of gravity waves.

Currently there are two possible paths to incorporate observational information into the parameterizations of GWDs. One is to trace back to the specific source for each observed event, particularly large ones, and then to assess source models by comparison to observations (e.g., Wu et al., 2006; Alexander and Barnet, 2007). This approach will likely lead to improvement in parameterizations of GWDs in GCMs, and Chapter 4 and 5 will present this dissertation's research achievements along this path. The other approach is to try to find proper source expressions to generate waves that are observed by specific techniques. This has associated uncertainties, but the advantage over the first method is that this approach is simpler to implement. As will be shown in this chapter, our results do have physical implications, which give information on the first approach.

In this chapter, we use eight years (1998-2005) of data to get information on both gravity wave horizontal propagation direction and source spectra. Our goal in this

investigation is to give some observational guidance for gravity wave parameters that can be used to improve parameterizations of unresolved gravity waves in GCMs in the near future.

Following *Alexander and Vincent (2000, AV00 hereinafter)*, we apply similar gravity wave source spectra as were used in AV00. We use the GROGRAT gravity wave ray-tracing program (Marks and Eckermann, 1995) for 85 U.S. high resolution radiosonde stations, and then compare certain simulated wave parameters with those derived from high-vertical resolution radiosonde observations to determine the characteristics of the "best-fit" source spectra. In this way, we are able to derive the climatology for gravity wave source information on a continental scale.

Section 2 describes the procedures of analyzing data and the experiment setups. Section 3 gives results for "best-fit" gravity wave source spectra. Several features of the source spectra and their relationships to propagation are further described and explained in detail in section 4, and finally section 5 gives a summary and the principal conclusions of this study. Our observational results are basically derived using the methods of Wang (2003), but we extend the data length from four years (1998 - 2001) to eight years (1998 - 2005), so the results should be statistically more robust, and also we use the observational results a bit differently than he did.

3.2. Data Analysis Method and Experiment Setups

3.2.1 Analysis methods of characteristics of gravity waves from the radiosonde

US high-vertical resolution data have been previously described in Chapter 2. For this study, we use eight years (1998 - 2005) of data.

We calculate the total gravity wave energy density E_t and the vertical flux of the zonal momentum M . The calculation of E_t is identical to the methods used by Wang and Geller (2003):

$$E_t = KE + PE = \frac{1}{2}\left(\overline{u'^2} + \overline{v'^2} + \frac{g^2}{N^2}\overline{\hat{T}'^2}\right) \tag{3.1}$$

Since the energy associated with the vertical velocity is significantly smaller than that associated with the horizontal velocities, the vertical velocity term is not included in this energy calculation.

The vertical flux of the zonal momentum $M = \rho_0 \overline{u'w'\delta\_}$ [1] is calculated based on Eqns. (2.13) - (2.15). We choose $p = 5/3$ as is conventional (e.g., Vincent et al. (1997), Wang et al. (2005)) to facilitate comparisons with these earlier works. One needs to be cautious that this value might be too small for gravity waves in the lower stratosphere (generally around 2 - 4, Wang, 2003), however, since this tends to overestimate the momentum flux.

The mean orientation of the perturbation velocity ellipse is used to determine the direction of propagation with a $180°$ ambiguity. This ambiguity is then resolved by examining the phase difference between the perturbation wind velocity parallel to the major axis of this ellipse *u'* and the perturbation temperature *T'*. The wave horizontal directions of propagation are then binned into twelve $30°$ segments. The energy-weighted horizontal direction of propagation is calculated by weighting the direction of each wave by the associated total wave energy density within each bin. This variable gives

[1] Another equivalent name is the "zonal component of the vertical momentum flux", and we use "zonal momentum flux M " hereinafter for simplicity.

information on those wave propagation directions associated with the most energetic gravity waves.

3.2.2 Experiment Procedures

We use methods similar to those used in AV00 to better understand the climatological properties of gravity wave sources. *Vincent and Alexander (2000)* used the methods described above to calculate time series of the vertical flux of westerly momentum M, and the kinetic energy density KE in the lower stratosphere for six years of high vertical-resolution radiosonde data at Cocos Island ($12^{\circ}S, 97^{\circ}E$). AV00 then used ray tracing techniques for various source gravity wave spectra (Eqns. (6)-(9) in their paper) to obtain a "best-fit" to the observationally derived time series for gravity wave kinetic energy density and zonal momentum flux, where the source spectral shape($B_1 - B_4$), the source spectral width(c_w), the horizontal wavelength (λ), the spectral amplitude(B_m) and the source altitude (z_0) were all varied until a "best-fit" was obtained. Their "best-fit" had correlation coefficients between the observationally derived and the "best-fit" modeled KE of 0.66 and between the observationally derived and "best-fit" modeled M of 0.57. We apply these methods to all of the 85 US high vertical-resolution radiosonde stations that have sufficient quality lower stratosphere data records using the different parameter values shown in Table 3.1. Our simulations differ from AV00 in the following respects. First, we use GROGRAT instead of their ray-tracing model, but we would not expect this difference to cause serious divergence in the results since the fundamental theory for both models are the same. Secondly, we slightly lower the "best-fit" criteria for the correlation coefficients since we are analyzing eight years of data instead of six. For a "best-fit" to exist, both these correlation coefficients must be at

least 0.30 (The 95% significant level is 0.25. But with consideration of missing months for some stations, we take 0.3 as a uniform standard for all stations). Thirdly, apart from $B_1 - B_4$, we add B_5 (Eqn. (3.6)) as the simplest functional form with anisotropic momentum fluxes. Fourthly, we test a wider range of model parameters (compare our Table 3.1 with Table 1 in AV00).

$$B_1(c) = \pm B_m \exp[-(c/c_w)^2 \ln 2] \tag{3.2}$$

$$B_2(c) = \pm B_m \exp[-(\frac{c-U_0}{c_w})^2 \ln 2] \tag{3.3}$$

$$B_3(c) = \pm B_m \left(\frac{c-U_0}{c_w} \right) \exp\left(1 - \left| \frac{c-U_0}{c_w} \right| \right) \tag{3.4}$$

$$B_4(c) = B_m \left(\frac{c-U_0}{c_w} \right) \exp\left(1 - \frac{\pm U_0}{12} - \left| \frac{c-U_0}{c_w} \right| \right) \tag{3.5}$$

$$B_5(c) = \pm const \tag{3.6}$$

where c is the source-based phase speed; U_0 is the background zonal wind at the source altitude z_0. The + (-) sign is chosen when $c \geq U_0$ ($c < U_0$). The constant for B_5 equals $\frac{1}{200} \sum_{-100}^{100} |B_3(c)| \cdot \Delta c$, where $\Delta c = 2ms^{-1}$ is our chosen interval of phase speed. Note that for B_3 and B_4, c_w also determines the intrinsic phase speed where the source momentum flux peaks at the source level.

As an example, Fig. 3.1 shows the source spectra of Eqns. (3.2) - (3.6) with $u_0 = 10ms^{-1}$, $c_w = 10ms^{-1}$ and $B_m = 0.03m^2s^{-2}$. Among these sources, B_1, B_4 and B_5 are anisotropic, with most of the momentum flux being westward (eastward) if the zonal wind at the launch level is eastward (westward). B_1 always peaks at $c = 0$, while B_4 peaks

at its intrinsic phase speed. B_2 and B_3 are both isotropic. With the same c_w value, B_3 and B_4 are broader in width compared to B_1 and B_2. AV00 suggested B_4 is a reasonable representative of a convection source with the "transient mountain" mechanism. With the monthly-based calculations here, Eqns. (3.2) - (3.6) represent monthly mean "sources" that are in fact combinations of both "physical" sources launching at various altitudes and other factors such as propagation, intermittency, etc.. We also neglect the temporal variations of the background fields when performing ray-tracing for each month.

For this work, we only consider vertical propagation of gravity waves in GROGRAT, which is a limitation in simulating real three - dimensional propagation. We will study 3-D propagation in Chapter 4 and 5 later on. The simulations here are performed with a vertical resolution of 300m and time steps of 0.1 hour. Sensitivity tests (150m and 600m vertical resolutions; 0.05hr and 0.2hr time steps) have been carried out for several stations and the results are robust.

Four things deserve some discussion before we present our results. First, although it is total energy that is transported by gravity waves during propagation, we still choose to compare observed and simulated kinetic energy density KE, since GROGRAT cannot directly output potential energy density PE (same as in AV00). However, more than 60% of the stations have correlation coefficients between observed E_t and KE larger than 0.9. The correlation between observed KE and momentum flux M from observations, which turns out to be a key factor in determining our result, is also high if the correlation coefficient of E_t and momentum flux is high, except for a few stations, (see Table 3.2). Therefore, this choice does not significantly affect our results. Secondly, the analysis of radiosonde data by our method is known to be most sensitive to low intrinsic frequency

($\omega \sim 1-10f$) gravity waves (Vincent et al., 1997; Alexander, 1998; Wang et al., 2005), so the simulation is expected to reveal source information only within this part of the gravity wave spectrum (ω typically around *1-10f*). In other words, the source information that we can get is "biased" to inertia-gravity waves. Thirdly, although $B_1 - B_5$ possess some characteristics of different sources (e.g., B_4 is the so-called "transient-mountain" representation of convection, Pfister et al., 1993), they are not representative of any specific physical sources nor do they represent any particular event, but rather a climatological picture of mixed source and propagation information at a certain altitude for the gravity waves we see in the lower stratosphere in the radiosonde profiles. This is of special importance for gravity wave parameterization in GCMs since it gives certain observational constraints on climatological spectral source representations. Finally, our simulations and comparisons are done on a monthly basis.

3.3. "Best-fit" Gravity Wave Source Spectra

Gravity Waves carry energy and momentum flux during their propagation. The energy and momentum flux at a certain time and at a certain place are determined by two factors: characteristics of the source, and the propagation that is determined by the background fields. In this section, we basically follow the methodology of AV00 to determine the "best-fit" gravity wave source spectra that are implied by the US high vertical-resolution radiosonde analyses for the time series of both the gravity wave kinetic energy density KE and zonal momentum flux M in the lower stratosphere.

We analyze the monthly mean kinetic energy density KE, total energy density E_t and zonal momentum flux M within the lower stratosphere for the 85 stations that are

listed in Table 3.2, and carry out simulations for these stations for 96 months (1998-2005) since this work has been done prior to the year 2006 data becoming available. For each simulation, we release 101 rays with phase speed c varying between -100 and 100 with a uniform resolution of $2\,ms^{-1}$ for each combination of values of the parameters that are listed in Table 3.1 into the background atmosphere fields (obtained from NCEP/NCAR monthly reanalysis), and trace each wave ray until it breaks down within the altitude interval of 18 - 24.9 km or penetrates through the top of this lower stratosphere region. The collective kinetic energy density and momentum flux of the 101 rays are then calculated from the sum of these rays. A scale factor, which is determined by the ratio between the maximum value of the modeled *KE* and the observed one, is introduced here considering the dependence of the simulated energy densities and momentum fluxes on the numerical details such as the resolution of the phase speed. In reality, these scale factors ε can be interpreted in terms of the so-called "wave intermittency" of the wave forcing (ε obviously has a purely mathematical component in that its magnitude is dependent on the number of rays, but its relative value is an indicator of the frequency with which the waves are launched from their sources, hence the term "intermittency."). NCEP/NCAR monthly reanalysis data are interpolated to the location of each station as the background atmosphere instead of directly using the background values from the radiosonde soundings. The interpolated NCEP/NCAR reanalysis fields are very similar to the mean fields derived directly from the radiosonde profiles (see Fig. 3.2). One reason for using reanalysis fields stems from the fact that the reanalysis data should be in general more accurate than the balloon measurements since they are the ensemble of diverse observations. The other consideration is that it's hard to separate the background winds

from the waves throughout the troposphere and the lower stratosphere. In Fig. 3.2, we use 5^{th}-order polynomial fit to extract the background fields from 2.1 *km* to 24.9 *km*. However, the abrupt changes at the tropopause still cannot be captured sometimes, and the fit procedures have large uncertainties at the boundaries. This gives the largest differences at the upper and lower boundaries as well as the tropopause regions between the reanalysis and the balloon measured background fields.

Our definition of "best-fit" is as follows. First, the value of the correlation coefficient between the observed and simulated momentum flux must be equal to or larger than 0.3 with the same being true for the kinetic energy. Second, by dividing by the same scale factor ε, the simulated time series must reproduce the observed kinetic energy density *KE* and momentum flux *M* "well" simultaneously. Practically speaking, this is defined as the regression coefficient being within the range of 1 ± 0.2, and the relative intercept, which is defined as the absolute value of the ratio of the intercept to the maximum value in the time series (Wang, 2003), being less than or equal to 0.4. If more than two sets of parameter values satisfy the above two criteria, the one with the largest absolute value for the correlation coefficient of momentum flux is taken. The reason for this is that it is easier to obtain a good simulation for *KE* than for the momentum flux. Once we find the "best-fit", the magnitude of the momentum flux at the source level for the determined "best-fit" combination of parameters is calculated by $F_0 = \sum_c (\rho_0 |B_0(c)|) \Big/ \varepsilon$.

Out of these 85 stations, we find that 68 have observed zonal momentum flux M well correlated with kinetic energy density KE ($|r| \geq 0.3$), among which we get "best-fit" for 59 of these stations. For the remaining 17 stations, we find "best-fits" for only 2

stations. The source momentum fluxes calculated from the "best-fit" spectra and the simulated zonal momentum fluxes within the lower stratosphere section are significantly correlated ($|r| \geq 0.3$) for 54 of the "best-fit" stations out of the total of 61 "best-fit" stations. The 61 stations for which we find "best-fit" sources are designated by filled circles (B_1) and filled squares (B_4) in Fig. 3.3. Fig. 3.4 (Fig. 3.5) gives two station time series of the "best-fitted" KE, M and F_0 with higher (lower) correlations, and Table 3.2 gives all the results numerically. One notices that even for the lower correlated cases, simulations with a constant source spectrum can still capture the major characteristics of the observed time series (e.g., Fig. 3.5). For the mid-high latitude stations, the seasonal variations of the lower stratospheric kinetic energy density are reasonably reproduced. Furthermore, the modeled zonal momentum flux is generally negative (westward) for the mid-high latitude stations while positive (eastward) for the tropical stations. The simulations are generally underestimated during summer (shown in the cross symbol in Fig. 3.6), implying a smaller value of ε and hence less wave events during summer, which agrees well with previous studies (Wang, 2003).

Fig 3.3 also shows the spatial distribution of the "best-fit" stations and the horizontal wavelength λ values. λ generally increases with decreasing latitude. Both this trend and the values agree well with the analysis by Wang et al., (2005), as shown in Fig. 3.7. In this figure, the black crosses represent eight-year averaged horizontal wavelengths derived from observations at each station, and the black line is a linear fit taken within every 5° latitudinal bin. For each latitudinal bin, an "averaged best-fit" experiment is employed with the background fields taken to be the mean values of all stations within that latitudinal bin, and with the same procedures of "best-fit" experiment for the

individual station. The reference observations are the means of the observed *KE* and M within each latitudinal bin. The horizontal wavelengths for "averaged best-fit" are marked as red squares, and the linear fit is drawn as the red line. We can see from this figure that the overall decreasing trend is well-represented in the "best-fit" horizontal wavelengths, except the simulations seem to prefer longer horizontal wavelength (~200 km longer) than those observed.

Different from λ, the amplitude B_m, and the wave intermittency ε do not show a clear latitudinal dependence. The results are not very sensitive to small changes of any parameter values. For example, if we double the value of B_m, it's likely that ε should also be doubled to reach a "good-fit". In other words, the model results are not so sensitive to the strength of the input source. Interestingly, only sources B_1 and B_4 work, and B_4 works only in low-latitudes while B_1 works for all latitudes. AV00 found their "best-fit" for Cocos Island to be a B_1 spectrum, but the B_4 spectrum is the "best-fit" in our simulation for most tropical stations, though one can find a B_1 spectrum that very closely resembles it and gives almost as good a fit. Although B_4 doesn't represent any "real" source, it seems that B_4 captures the character of real convective sources on a monthly basis, while B_1 is the most general one in resembling the mean situation for various sources. As mentioned in section 2.2, the westward momentum flux is larger (smaller) than the eastward momentum flux for both B_1 and B_4 if the source level zonal wind is eastward (westward). This agrees with the SGWDC simulations of *Song et al. (2007)*. Although we only tried three altitudes to release these rays, only 17.75 km, which is right at the bottom of the analyzed section, gives the best results. This will be discussed

later in section 4. The spectral width c_w doesn't seem to have a latitudinal nor geographical dependence, although narrow spectral width (e.g. $5ms^{-1}$) seem to work only for lower latitudes.

While our individual station "best-fits" give useful information for gravity wave parameterizations in global models, it is clearly impractical and undesirable to specify parameterization parameters grid point by grid point. Therefore, we performed the following experiment to see how this information might be used over large areas. In this experiment, we divided the entire region over which we have the observations into three regions: one north of 30 °N (including Alaska stations); one 10 °N to 30 °N (including the Caribbean stations); and another south of 10 °N (the Pacific island stations). The choice of 30 °N as a dividing line is motivated by the fact that the sign of the momentum flux changes sign around 30 °N (Fig. 3.10a). For each of the three regions, we construct a synthetic time series of the averages of KE and M from all stations within each region. Furthermore, we take the background field from the average location within each region. The "best fit" parameters from this experiment are listed at the end of Table 3.2 in bold. B_1 again is the most universal source spectral type, but B_4 also gives a comparable "best-fit" result over the tropics. The "best-fit" horizontal wavelengths agree reasonably with those derived by Wang et al. (2005). This relatively crude experiment illustrates how the "best-fit' information in this paper can provide some guidance for global modelers.

The same procedures are employed again for every 5° latitudinal bin. We perform these extra simulations not only to try to give more hints on GWD parameterizations in GCMs, but also to disclose the similarities and diversities between observations and model results. The eight-year averaged zonal kinetic energy density KE_x and zonal

momentum flux M are compared at Fig. 3.8, and the composite maps of both temporal and latitudinal variations are shown in Fig. 3.9 and 3.10. From Fig. 3.8a and 3.9 we can see that the KE_x agree very well between observations and simulations both in time and latitude, with the simulated KE_x slightly smaller overall. Even the interannual variabilities in the tropics are captured very well in the model results. If we compare the M, however, the weak positive zonal momentum fluxes (~ 2mpa) during summer do not appear in the simulations for mid-high latitudes. We attribute this to the deficiency of representing summer gravity wave sources in certain regions over the mid-high latitudes, which will be discussed in the next section.

Interestingly, the stations for which we can not find "best-fit" occur over well-defined regions; that is to say, over the central contiguous US as well as the North American summer monsoon region (California, Utah region), where the energy-weighted horizontal propagation directions of waves within the lower stratosphere differ most from winter to summer, and are quite isotropic most of the time (as will be shown later in Fig 3.14). To further evaluate the situation over those areas, we applied source spectra separately for different seasons for those stations. The relative best results are shown in Table 3.3. Sensitivity tests are also carried out for these stations. If the absolute value of the largest correlation coefficient we get is smaller than 0.45 (95% significant level), or the regression coefficient is out of the range of 1 ± 0.2, or the relative intercept is greater than 1.0, we consider that no "best-fit" is found for this station. Using this approach, we can get a relative good fit for at least one season for 9 stations out of the 26 stations for which we couldn't get "best-fit" previously, all of which have a high correlation between KE and M in the observations. This season is preferentially a cold season (winter or

fall). All the general conclusions agree with the other "best-fit" stations, except that the relative intercept is generally higher. From those stations where we can find a "good fit" for two seasons, the source properties are different. That is to say, for the stations in those two areas, dominant physical sources are probably different, and the differences are strong enough to cause the failure of one fixed source spectrum throughout the year. No "good fits" are obtained with the B_2, B_3 and B_5 spectra. These results will be discussed further in section 4.

Another feature deserves further attentions is the boundary between "B_1-only" stations and "B_1-B_4" stations. If we draw a line on Fig. 3.3a to separate the west and the Rockies away from the east of the Rockies, we see that only B_1 works for the Rockies and the Western US, while B_1 and B_4 work equally well in the east of the Rockies regions. We explore this interesting feature from the source point of view in the next section.

3.4. Discussions of The Results

The simulation results reveal some important features of gravity wave sources. First, It is necessary for the KE and M derived from observations to be significantly correlated (higher than 95% confidence level) to get a "best-fit" simulation with fixed source spectra. The reason is that GROGRAT is designed based on "ray-tracing" theory, where simulated E_t and M are related by

$$\frac{M}{E_t} = \rho_0 k \frac{C_{gz}}{\hat{\omega}} \qquad (3.7),$$

$$\text{where } C_{gz} = -\frac{\hat{\omega}^2 - f^2}{\hat{\omega} m (1 + \frac{\hat{\omega}^2 - f^2}{N^2 - \hat{\omega}^2})} \qquad (3.8).$$

Both the necessity of these high correlations and this explanation were given earlier by Wang (2003).

Eqn. 3.7 is an alternative way to write Eqn. 1.1, which is only valid if there is no dissipation and if the background atmosphere varies only in the vertical. By setting up a fixed zonal wavenumber k, if $\frac{C_{gz}}{\hat{\omega}}$ and ρ_0 don't vary greatly, the variation of M is dominated by the variation of E_t. From Table 3.2 we can find that only 3 "best-fit" stations have a significantly lower correlation between E_t and M, compared with that between KE and M. Careful reexamination shows that $\frac{C_{gz}}{\hat{\omega}}$ varies by about 20-30% annually, and ρ_0 varies by less than 10% from winter to summer. However, KE varies over 200% annually. Therefore, for those stations with low correlation between KE and M, horizontal wavelength can vary significantly between summer and winter if we choose only one source type. Actually, the assumption here that we fix the zonal wavenumber k (i.e., wavelength λ) is quite arbitrary. In fact, if we give freedom to all the parameters for different seasons, 9 more stations have "best-fits" for at least one season (Table 3.3), all of which have high correlations between KE and M in the observations. This again confirms that high correlation between KE and M derived from observations is a necessary condition to get a "best-fit", and the fixed horizontal wavelength might be a cause for the failure of some simulations.

The simulation results indicate that the source must be anisotropic if we fix the source during the 8-year period. Both B_1 and B_4 are anisotropic source spectra so long as the wind at the source level is not zero while B_2 and B_3 are isotropic (Fig. 3.1). For comparison, results for the computed energy-weighted gravity wave horizontal propagation directions (see Vincent et al., 1997, Eqns. 6 and 7 for definition) are shown in Fig. 3.11 for the contiguous United States, Fig. 3.12 for Alaska, and Fig. 3.13 for the western Pacific stations. These results are shown separately for the winter (DJF) and summer (JJA) for both the lower stratosphere and troposphere. Note that in winter, spring and fall (the latter two are not shown here), the computed energy-weighted horizontal propagation directions are predominantly westward for most stations in the western and eastern parts of the US, though the directions are more mixed over the eastern half. Florida is the exception, where eastward and westward directions are about equal during the equinox seasons in the lower stratosphere. In the summer, much more southeastward propagation is seen over the southeastern United States, with about equal eastward and westward energy-weighted propagation direction over the remainder of the eastern two-thirds of the country, and with predominant westward propagation direction over the western third of the contiguous US. For Alaska stations, westward energy-weighted propagation is predominant during winter and fall, while equally distributed into eastward and westward for most stations during the other two seasons. The tropical Pacific island stations exhibit eastward energy-weighted propagation direction during the whole year in the lower stratosphere. The central contiguous US is the only region where eastward and westward energy-weighted propagation directions are equally distributed during both winter and summer.

Comparing our results with *Vincent et al. (1997)* and *Chun et al. (2006)*, we see clearly the strong latitudinal as well as geographical dependences of the energy-weighted gravity wave horizontal propagation. As for latitudinal dependence, background wind filtering seems to be the major factor to determine the propagation direction in the lower stratosphere (18 - 24.9 km). In mid-high latitudes, westerlies during winter filter out those waves that propagate downstream, similarly for tropical easterlies. During the summer, the much weaker westerlies allow for a more even split of gravity wave propagation between eastward and westward directions for most of the central and eastern stations. The limited and stable range of energy-weighted propagation directions for the western US, Alaska and the island stations imply a dominant anisotropic wave source, whereas the large variations over central to southeast contiguous US may be caused by mixed sources. Fig 3.14 further substantiates this viewpoint. The change in the averaged propagation direction from summer to winter over the central contiguous US likely indicates different wave sources, which are thus quite difficult for the fixed-source ray-tracing method to capture, consistent with our results in section 3, where we found that this is the most difficult region to determine the "best-fit" spectra by our methods. Both B_1 and B_4 have most of their momentum flux being directed upstream (Fig. 3.1) at the source level, which coincides with the upstream energy-weighted propagation direction from the observations.

We also found that the source altitude for a "best-fit" must be located at 17.75 km height. It should be pointed out that for considerations of computation time, we only tested three source altitudes (11.75, 14.75 and 17.75km), but our results indicate that the source altitude should be located in the altitude range of 14.75-17.75 km. Examining this

result more closely, however, we note that gravity wave sources and propagations are inherently intertwined together in determining our "observed" gravity waves. As stated above, the source spectra are highly anisotropic and wind filtering is very important. This may indicate the location and anisotropic character of the physical sources themselves, but there is also a possibility that wave propagation is the underlying real reason. Since the wind-filtering effect within the lower stratosphere prevents those downstream-propagating waves from traveling upward, those waves that propagate upstream are the predominant ones that carry energy and momentum upward. That is to say, the physical sources might be isotropic, but the wind-filtering effect during the propagation (both below and above the source level) determines the preferential wave propagation direction, and hence helps in leading to the appearance of an anisotropic source spectrum. Alaska winter (left panels of Fig 3.12) and tropical summer (right panels of Fig 3.13) results substantiate this. The fact that all of the "best-fit" sources are at 17.75 km is likely also caused by propagation rather than the physical source locations. Physical source locations are different from case to case. Note that our simulations are on a monthly scale, which tries to represent monthly mean gravity wave characteristics by a monthly mean source propagating through a monthly mean wind and temperature state. Hence the 17.75 km source altitude likely gives a mathematical wave source spectral type at that level on a monthly averaged basis rather than the physical source location. Also, the correlation between momentum flux at the source and that calculated for the whole lower stratosphere section is generally high (54 out of 61), but far below unity. Therefore, the determination of anisotropic source spectra with most of momentum flux directed upstream is at least partly caused (shaped) by propagation effects rather than the

characterization of the sources. This might be important for gravity wave parameterizations in climate models, since the details of sources may not be so important on long-time scales.

The most likely sources for low-frequency, long-horizontal-wavelength gravity waves in the lower stratosphere are jet stream imbalances (Guest et al., 2000) and mountains (Sato, 1994), especially during winter, and mesoscale-organized systems during summer (Tsuda et al., 1994; Alexander et al., 1995; Vincent and Alexander, 2000). Note that the difficult regions for obtaining "best-fits" are where organized convective systems are known to frequently occur during summer, especially for the central US (McAnelly and Cotton, 1989). Besides, the weak positive zonal momentum fluxes that are observed in the mid-latitudes (Fig. 3.10a) do not appear in the simulations (Fig. 3.10b). These motivate us to propose the following hypothesis to explain the inertia-gravity wave activity seen over the US in high vertical-resolution radiosonde data. As shown in Fig. 3.15b, where the geographical distributions of the zonal momentum flux are contoured for the contiguous US for different seasons in the lower stratosphere, the mountain source clearly shows up. This can explain why only B_1 works for the mountain region. Jet stream imbalance adjustment, as a stable inertia gravity wave source, is the other dominant source for the generation of inertia gravity waves over the western and eastern US in the lower stratosphere during all seasons except summer. In fact, jet imbalance source is probably the cause of the negative momentum fluxes that are observed outside mountain regions during cold seasons (Fig. 3.15b, and Chapter 5). Although convective activity frequently occurs during summer, it often appears in isolated convective outbreaks, and gravity waves probably are Doppler shifted out of the

"observational window" because of their high frequencies or refract back to the troposphere (especially important for waves that are going to be investigated in Chapter 4) or have large vertical wavelengths to which our analysis techniques are not sensitive. Having said that, large organized convections can still generate gravity waves that are visible in the radiosonde data, and they are probably responsible for the positive zonal momentum flux seen east of the mountain regions during summer, as shown in JJA panel of Fig. 3.15b. Therefore, the summer sources for lower stratospheric inertia-gravity waves are difficult to represent with a seasonal uniform source. This is likely the reason that cross symbols in Fig. 3.6 are the major ones deviating from the regression line, and are likely the cause of the lack of positive momentum flux signals in Fig. 3.10b in the simulations. A fixed source that represents the Jet stream source/mountain source could work for stations over western and eastern US. A similar explanation can be applied to Alaska and islands stations, except that the dominant source for the island stations are likely not jet stream imbalances nor mountain sources, but should be dominant and stable with time. When we try to extend the simulation season by season for the "no-best-fit" stations (Table 3.3) we find that there seems to be one stable summer source for only one tropical station, but winter/fall sources for the other seven stations. Over the other regions, especially over the central US, mesoscale-organized convective systems can be a strong source for inertia-gravity waves in the lower stratosphere (Alexander et al., 1995). The clear difference between summer and winter gravity wave sources in the central US is likely the main reason that causes our failure to obtain a "best-fit" with a source fixed during the whole time period.

The lack of validity of some of the assumptions that are made for the ray-tracing model (e.g., slowly and vertically varying background wind field) and other methods used in this paper can cause failure to simulate the gravity wave time series for some stations. For instance, in GROGRAT, background fields are the only factors that determine the development of rays, and we only take into account the zonal momentum flux associated with source. We also omit the meridional propagation in the simulations. In reality, however, background fields within the 18-24.9 km altitude interval might generate new gravity waves, and the meridional source momentum flux and/or the meridional wave propagation can be very important under some circumstances. Hence, the gravity waves characteristics derived by our methods can deviate from reality significantly under complicated situations.

3.5. Summary and Conclusions

In this chapter we use the GROGRAT gravity wave ray-tracing model to study the climatological source spectral properties for gravity waves that are seen in the lower stratosphere for eight years of US high-resolution radiosonde data. 85 stations with sufficient data completeness and quality are analyzed using this method. For each station, we apply 5 different types of source spectra with different combinations of parameter values. We examine two derived quantities – the kinetic energy density *KE* and the zonal momentum flux *M* within the lower stratosphere (18-24.9 km). If we find a high correlation ($|r| \geq 0.3$) between simulated values and those derived from observations for both parameters with the same source properties, with the same wave intermittency, with

1 ± 0.2 regression coefficients and low relative intercepts (≤ 0.4), this we call a "best-fit" for this station.

By using this method, we find "best-fit" for 61 stations out of the total 85 with fixed source spectra throughout the eight years. The "best-fit" stations show the following common characteristics:

1. 59 out of 61 "best-fit" stations have high correlation between KE and M derived from the observations. Theoretical analysis shows that this is a necessary condition if we fix the horizontal wavelength. However, it is still not known why we can obtain "best-fits" for the other two stations.

2. Another necessary condition is that the source must be just below the region of consideration. This is probably caused by the climatological nature of both the real physical sources and wave propagations. Since we use monthly averages for comparison, the source does not represent any detailed physical source, but rather a stable climatological source wave spectrum at a particular altitude. Wind-filtering effects below that altitude could largely modify the original wave source spectra, which eventually lead to our results.

3. With the previous two necessary conditions, we find that all the sources are anisotropic, and most of the momentum flux is directed upstream of the dominant wind direction. 54 "best-fit" stations have high correlation between source momentum flux and M within the lower stratosphere ($|r| \geq 0.3$). Propagation effects above the source level lead to M deviations from the source flux. Propagation effects below the source level, however, likely cause the anisotropy of the sources.

4. A source spectrum representing a "mean" convection source (B_4), works better for most of the tropical – subtropical stations, while the most general source (B_1) works for almost all stations, but better for mid-high latitude stations. The "best-fit" horizontal wavelength decreases from the tropics to high latitudes, which agrees well with that derived from observations by different methods, but using the same dataset (Wang et al., 2005). Recommended "best-fit" parameter sets for GCM modelers are also provided for three regions.

5. It is difficult for us to find "best-fits" for two regions in the contiguous US. One is the central US, and the other is the North American monsoon region. We propose two different reasons for the central US region. By evaluating the energy-weighted gravity wave propagation directions within the lower stratosphere from the observations, we find that the they are almost evenly split between westward and eastward and the mean direction switches sign (westward to eastward) from winter to summer for the central US region. The other possible reason, which is more related to physical sources, is that summer mesoscale-organized convective systems act as inertia-gravity wave sources, and such systems are known to occur frequently in these two regions. Our results show, however, that B_1 is good at capturing the stable winter sources (e.g., Jet stream imbalances, mountain source), which are believed to be major sources of such waves. For the North American summer monsoon region, the second reason might also apply, but since the meridional wind maximizes in this region during summer, the lack of consideration of meridional propagation might be another reason.

There have been several attempts to explicitly take into account individual sources of gravity waves and the resultant momentum fluxes for gravity wave parameterization (e.g.,

Beres, 2004; Song and Chun, 2005) and to investigate the impact of these parameterizations in GCMs (Beres et al., 2005; Song et al., 2007). Despite the different sections of the atmosphere and different parts of the spectrum of gravity waves of interest, the fundamental differences between this work and the works mentioned above are: (1) they studied a single source (convection) with single generation mechanism (thermal forcing), while this work implicitly includes all sources of gravity waves that are visible to radiosonde observations; (2) Since they specified the source momentum flux from the information on the structure of the thermal forcing, the parameterizations are largely dependent on the quality of specifications of the convections. Our results, however, do not depend on any specific sources, but rather a proper source spectra right beneath the layer of interest; (3) *Beres [2004]* and *Song and Chun [2005]* consider propagation through idealized atmospheres, while we use realistic atmospheres as background states.

This is the first large-scale calculation of "best-fit" gravity wave source spectra for lower stratosphere gravity waves derived from high-resolution radiosonde data, in the sense of AV00. Some caveats in our fundamental assumptions should be pointed out, however. (1) The whole simulation is carried out using monthly means, so the source spectra are not "physical". Twice-daily simulations (00Z and 12Z) are also carried out for one station (Blacksburg, VA [$37.2^{\circ}N$, $80.41^{\circ}W$]) for one year to test this assumption, and we found that although the "best-fit" source spectra have difficulty in capturing single events, they agree reasonably well with the monthly averages of the twice-daily experiments (Fig. 3.16). This means that our monthly-mean assumption appears to reasonably represents the climatology of the "physical" source spectra. Single large-amplitude events, however, are unavoidably even out by weak events and "noises", as

indicated by *Alexander and Barnet (2007)*. Our source spectra are a combination of both "monthly averaged" real sources and propagation effects, and they may have important implications for GCM gravity wave parameterization. For example, we can infer from this work that the details of the sources at levels below the regions of interest might not be so important, but rather a proper specification of parameters at the bottom of this region might suffice, in a climatological sense. (2) We only consider the vertical propagation. Inertia-gravity waves propagate slantwise, so this is a poor assumption. Since this is the only propagation direction currently implemented in GCMs, however, the results are still quite informative to most state-of-the-art parameterization of gravity waves in GCMs. (3) We only fit part of the GW spectrum, which is inherently unavoidable for any single observation technique. This work gives some observational constraints for radiosonde data for low-frequency gravity waves in the lower stratosphere. Other limitations of this study include lack of consideration of the meridional wind as well as meridional momentum fluxes, etc.. Other source spectral functions (e.g., Beres, 2004; Song and Chun, 2005) can also be considered.

PARAMETERS	VALUES
Source Spectral Shape	B1, B2, B3, B4, B5
c_w (ms^{-1})	1, 5, 10, 15, 20
$B_m (m^2 s^{-2})$	0.01, 0.03, 0.1, 0.3
λ (km)	300, 400, 600, 800, 1000, 1200, 1400, 1600
	1800, 2000
z_0 (km)	17.75, 14.75, 11.75

Table 3.1: Simulation parameters and values considered. See text for details.

WBAN	NAME	STATE	LAT	LON	CORR (Et, M)	CORR (Ke, M)	CORR (Ke)	CORR (M)	CORR (S)	ε	GOOD-FIT
~~61705~~	~~PAGO PAGO INTL ARPT~~	~~99~~	~~-14.33~~	~~-170.72~~	—	—	—	—	—	—	—
40504	PONAPE ISLAND	99	6.97	158.22	0.429	0.577					NO, ④
40710	MAJURO/MARSHALL ISL	99	7.08	171.38	0.604	0.547	0.372	0.334	0.607	60.54	B4-0.1-5-1400
40309	KOROR/PALAU ISLAND	99	7.33	134.48	0.555	0.739					NO, ①
40505	TRUK INTL/MOEN ISL	99	7.47	151.85	0.440	0.715	0.471	0.368	0.776	80.1	B4-0.1-5-1200
40308	YAP ISLAND	99	9.48	138.08	0.272	0.672	0.335	0.301	0.748	244	B4-0.03-15-1800
~~11501~~	~~SEAWELL APT~~	~~99~~	~~13.07~~	~~-59.5~~	~~-0.391~~	~~-0.319~~	—	—	—	—	—
~~41415~~	~~GUAM MARIANA ISL~~	~~99~~	~~13.55~~	~~144.83~~	~~-0.378~~	~~-0.392~~	—	—	—	—	—
~~11818~~	~~BELIZE~~	~~99~~	~~17.53~~	~~-88.3~~	~~-0.218~~	~~0.057~~	—	—	—	—	—
11641	SAN JUAN/ISLA VERDE	PR	18.43	-66	0.068	0.112					NO, ④
~~11813~~	~~GRAND CAYMAN~~	~~99~~	~~19.3~~	~~-81.37~~	~~-0.030~~	~~-0.143~~	—	—	—	—	—
21504	HILO	HI	19.72	-155.07	-0.084	-0.001					NO, ④
22536	LIHUE/KAUAI	HI	21.98	-159.35	-0.104	-0.050					NO, ①
12850	KEY WEST	FL	24.5	-81.8	-0.272	-0.317	0.496	0.475	0.125	500.5	B1-0.1-20-1200
92803	MIAMI/FL INTL UNIV	FL	25.75	-80.38	-0.349	-0.406	0.408	0.490	-0.709	517.4	B4-0.1-20-1600
12919	BROWNSVILLE	TX	25.9	-97.43	-0.335	-0.462	0.652	0.321	-0.954	129.3	B4-0.1-5-1000
12842	TAMPA BAY/RUSKIN	FL	27.7	-82.4	-0.356	-0.536	0.516	0.505	0.609	571	B1-0.1-20-1000
12924	CORPUS CHRISTI	TX	27.77	-97.5	-0.416	-0.423	0.768	0.453	-0.763	119.5	B4-0.03-15-1800
22010	DELRIO	TX	29.37	-100.92	-0.529	-0.524	0.493	0.473	0.686	405.4	B1-0.1-20-1000
03937	LAKE CHARLES	LA	30.12	-93.22	-0.428	-0.461	0.561	0.429	-0.966	65	B4-0.03-5-1000
53813	SLIDELL	US	30.33	-89.82	-0.422	-0.532	0.552	0.300	0.582	75.6	B1-0.03-20-1400
93805	TALLAHASEE	FL	30.38	-84.37	-0.246	-0.453	0.473	0.459	0.765	328	B1-0.1-20-1200
13889	JACKSONVILLE	FL	30.43	-81.7	-0.334	-0.307	0.618	0.436	-0.947	73	B4-0.1-5-1200
03020	SANTA TERESA	NM	31.9	-106.7	-0.351	-0.635	0.522	0.582	0.708	368	B1-0.1-10-600
23023	MIDLAND	TX	31.93	-102.2	-0.219	-0.424	0.470	0.401	-0.849	478.1	B4-0.03-15-1000
23160	TUSCON	AZ	32.12	-110.93	-0.251	-0.371	0.466	0.373	0.548	308.1	B1-0.1-20-1000
03940	JACKSON/THOMPSON FLD	MS	32.32	-90.07	-0.445	-0.427	0.564	0.365	-0.859	74.3	B4-0.1-5-1200
13957	SHREVEPORT REGIONAL AP	LA	32.45	-93.83	-0.335	-0.330	0.532	0.344	0.52	94.2	B1-0.1-20-1600

03990	FT WORTH	TX	32.8	-97.3	-0.559	-0.452	0.614	0.313	-0.801	98	B4-0.3-5-1400
03190	MIRAMAR NAS	CA	32.85	-117.15	-0.453	-0.448	0.509	0.504	0.632	247.1	B1-0.03-20-600
~~13880~~	~~CHARLESTON~~	~~SC~~	~~32.9~~	~~-80.03~~	~~-0.581~~	~~-0.580~~	—	—	—	—	—
53823	BIRMINGHAM (SHELBY APT)	AL	33.1	-86.7	-0.447	-0.455	0.538	0.445	0.438	614	B4-0.1-20-1200
53819	PEACHTREE CITY	GA	33.35	-84.56	-0.359	-0.358					NO, ④
93768	MOREHEAD CITY/NEWPORT	NC	34.7	-76.8	-0.114	-0.071	0.709	0.326	-0.792	42.86	B4-0.3-5-1600
03952	N LITTLE ROCK	AR	34.83	-92.27	-0.368	-0.433	0.529	0.296	0.643	71	B1-0.1-10-1600
23050	ALBUQUERQUE	NM	35.05	-106.62	-0.736	-0.683	0.572	0.601	0.710	289.8	B1-0.1-15-600
~~03948~~	~~NORMAN~~	~~OK~~	~~35.23~~	~~-97.47~~	~~-0.220~~	~~-0.265~~	—	—	—	—	—
23047	AMARILLO	TX	35.23	-101.7	-0.295	-0.350	0.456	0.314	-0.782	72.1	B4-0.1-5-1000
53103	FLAGSTAFF/BELLE MT (ARMY)	AZ	35.23	-111.82	-0.054	-0.164					NO, ①
13723	GREENSBORO	NC	36.08	-79.95	-0.406	-0.529	0.764	0.397	0.656	77	B1-0.1-15-1500
13897	NASHVILLE	TN	36.25	-86.57	-0.485	-0.425	0.321	0.470	-0.855	886.7	B4-0.1-10-1000
03160	DESERT ROCK/MERCURY	NV	36.62	-116.02	-0.105	-0.062					NO, ①
53829	ROANOKE/BLACKSBURG	VA	37.2	-80.41	-0.641	-0.613	0.743	0.620	0.623	54.2	B1-0.03-20-1000
13995	SPRINGFIELD REGIONAL AP	MO	37.23	-93.4	-0.247	-0.253					NO, ③
23230	OAKLAND INT AP	CA	37.75	-122.22	-0.062	-0.165					NO, ①
13985	DODGE CITY	KS	37.77	-99.97	-0.423	-0.424					NO, ④
93734	STERLING(WASH DULLES)	VA	38.98	-77.47	-0.513	-0.488	0.586	0.323	0.357	61.8	B1-0.1-20-1600
13996	TOPEKA	KS	39.07	-95.62	-0.296	-0.273					NO, ③
23066	GRAND JUNCTION	CO	39.12	-108.53	-0.105	-0.529	0.459	0.577	0.578	244	B1-0.1-10-600
~~13841~~	~~WILMINGTON~~	~~OH~~	~~39.42~~	~~-83.82~~	~~-0.448~~	~~-0.440~~	—	—	—	—	—
03198	RENO	NV	39.57	-119.8	-0.533	-0.474					NO, ②
23062	DENVER/STAPLETON ARPT	CO	39.77	-104.88	-0.466	-0.466	0.523	0.574	0.636	149.7	B1-0.03-15-400
04833	LINCOLN-LOGAN COUNTY AP	IL	40.15	-89.33	-0.123	-0.217					NO, ①
94823	PITTSBURGH/MOON TOWNSHIP	PA	40.53	-80.23	-0.752	-0.649	0.651	0.604	-0.896	219.5	B4-0.03-10-800
24127	SALT LAKE	UT	40.77	-111.97	-0.654	-0.470					NO, ④
04105	ELKO	NV	40.85	-115.73	-0.395	-0.378					NO, ④
94703	BROOKHAVEN	NY	40.85	-72.85	-0.443	-0.596	0.683	0.355	0.517	17.1	B1-0.03-10-1400
24023	NORTH PLATTE	NE	41.13	-100.68	0.062	0.024					NO, ①

94980	OMAHA/VALLEY	NE	41.32	-96.37	-0.149	-0.158					NO, ①③
94982	DAVENPORT MUNICIPAL AP	IA	41.6	-90.57	0.010	-0.390	0.585	0.354	0.621	77	B1-0.1-10-1200
14684	CHATHAM	MA	41.67	-69.97	-0.352	-0.699	0.640	0.486	0.607	340	B1-0.1-5-800
24225	MEDFORD	OR	42.37	-122.85	-0.547	-0.472	0.479	0.433	0.203	441.4	B1-0.1-15-600
04830	DETROIT/PONTIAC	MI	42.7	-83.47	-0.374	-0.494	0.585	0.437	0.648	185.8	B1-0.1-10-1000
14733	BUFFALO/GRTR ARPT	NY	42.93	-78.73	-0.083	-0.602	0.793	0.573	0.725	238	B1-0.1-10-800
24061	RIVERTON	WY	43.06	-108.47	-0.549	-0.600	0.515	0.506	0.264	72.1	B1-0.03-15-600
24131	BOISE	ID	43.57	-116.22	-0.485	-0.479	0.427	0.412	-0.158	183.8	B1-0.03-20-400
54762	GRAY	ME	43.89	-70.25	-0.662	-0.669	0.686	0.500	0.575	76.3	B1-0.03-15-800
94043	RAPID CITY	SD	44.07	-103.21	-0.244	-0.134					NO, ①③
14898	GREEN BAY	WI	44.48	-88.13	-0.483	-0.426	0.520	0.358	0.341	139.1	B1-0.1-15-1200
94983	MINNEAPOLIS	MN	44.83	-93.55	-0.152	-0.331	0.562	0.372	0.328	194	B1-0.1-15-1000
04837	GAYLORD/ ALPENA	MI	44.90	-84.70	-0.288	-0.274	0.638	0.425	0.303	43.2	B1-0.03-15-1000
24232	SALEM	OR	44.92	-123.02	-0.785	-0.679	0.606	0.708	0.059	104.7	B1-0.03-15-400
14929	ABERDEEN	SD	45.45	-98.42	-0.125	-0.078					NO, ④
24011	BISMARCK	ND	46.77	-100.75	-0.313	-0.305	0.343	0.295	-0.411	327	B1-0.1-20-800
14607	CARIBOU	ME	46.85	-68.02	-0.767	-0.727	0.707	0.619	0.613	151.6	B1-0.1-10-800
04102	GREATFALLS	MT	47.45	-111.38	-0.437	-0.410					NO, ④
04106	SPOKANE INTNL APT	WA	47.68	-117.63	-0.537	-0.504					NO, ③
94240	QUILLAYUTE	WA	47.95	-124.55	-0.810	-0.731	0.686	0.669	0.164	127.1	B1-0.03-10-400
94008	GLASGOW	MT	48.2	-106.62	-0.047	-0.055					NO, ①
14918	INTERNATIONALF ALLS	MN	48.57	-93.38	-0.263	-0.215					NO, ②
25308	ANNETTE ISLAND	AK	55.03	-131.57	-0.759	-0.720	0.631	0.699	0.138	153.8	B1-0.03-15-400
25624	COLD BAY	AK	55.2	-162.72	-0.309	-0.690	0.709	0.560	0.266	78.4	B1-0.1-10-800
25713	ST PAUL ISLAND	AK	57.15	-170.22	-0.770	-0.732	0.611	0.627	0.316	80.3	B1-0.1-10-800
25501	KODIAK	AK	57.75	-152.48	-0.542	-0.518	0.803	0.453	0.373	74	B1-0.1-10-800
25503	KING SALMON	AK	58.68	-156.65	-0.843	-0.854	0.773	0.829	0.382	52.2	B1-0.03-10-400
25339	YAKUTAT	AK	59.52	-139.67	-0.830	-0.794	0.740	0.706	0.450	180.6	B1-0.1-10-400
26615	BETHEL	AK	60.78	-161.8	-0.790	-0.808	0.624	0.693	0.441	280.2	B1-0.3-10-600
26409	ANCHORAGE IAP/PT CAMPBE	AK	61.17	-150.02	-0.815	-0.815	0.699	0.679	0.499	206.3	B1-0.3-10-600
26510	MCGRATH	AK	62.97	-155.62	-0.680	-0.742	0.653	0.550	0.485	100.6	B1-0.1-10-600
26617	NOME AP	AK	64.5	-165.43	-0.543	-0.685	0.483	0.280	0.435	74.6	B1-0.1-10-800
26411	FAIRBANKS	AK	64.82	-147.85	-0.476	-0.667	0.548	0.474	0.546	138.5	B1-0.1-10-600

26616	KOTZEBUE	AK	66.85	-162.63	-0.788	-0.734	0.559	0.590	0.470	179	B1-0.1-10-400
27502	POINT BARROW	AK	71.3	-156.78	-0.680	-0.651	0.589	0.440	0.701	65.6	B1-0.1-10-800
—	**N. of 30N**	**—**	**43.19**	**-107.10**	**—**	**—**	**0.685**	**0.714**	**0.406**	**48.2**	**B1-0.03-10-800**
—	**S. of 30N**	**—**	**22.89**	**-97.15**	**—**	**—**	**0.838**	**0.574**	**0.172**	**193**	**B1-0.03-20-1000**
—	**Pacific Islands**	**—**	**7.66**	**150.8**	**—**	**—**	**0.493**	**0.373**	**0.492**	**158.6**	**B1-0.1-15-1600**
							0.478	**0.365**	**0.65**	**60.1**	**B4-0.1-5-1600**

Note:① means the failure of obtaining a "best-fit" is caused by low correlation coefficient ($r < 0.3$), but the correlation of observed and simulated kinetic energy density is in general much better than that of momentum flux for all the combinations of parameters that we tested. At least one of the correlation coefficient of observed and simulated Ke is larger than 0.3.

② means the same with ①, except for momentum flux.

③ means the failure of obtaining a "best-fit" is caused by the disagreement of wave intermittency. That is to say, with the same wave intermittency, the slope of regression of either Ke or M or both is out of the range of 1 ± 0.2.

④ means the failure of obtaining a "best-fit" is caused by the relative intercept of either Ke or M or both of them is larger than 0.4 with the same wave intermittency.

Table 3.2: Simulation Results. Column 6 and 7 give the correlations between E_t and M , KE and M based on observations, respectively. Column 8 and 9 give the correlations between observed and simulated KE , M , respectively. Column 10 gives the correlation between source momentum flux and corresponding M calculated from the simulation result for the "best-fit" combinations. Column 11 gives the wave intermittency. The parameters in the last column are type-B_m-c_w-λ. The last three lines marked in bold give the "best-fits" for three regions (see text for details).

WBAN	NAME	STATE	CORR (Ke)	CORR (M)	CORR (S)	ε	Inter E	Inter M	GOOD-FIT
40504	PONAPE ISLAND	99	0.452	0.478	0.519	501.2	0.57	0.00	B4-0.1-10-120 (JJA)
40309	KOROR/PALAU ISLAND	99	0.557	0.465	0.085	18.4	0.65	0.00	B1-0.1-5-1600 (DJF)
			0.558	0.563	0.223	123.9	0.66	0.00	B1-0.1-10-1000 (MAM)
53819	PEACHTREE CITY	GA	0.704	0.504	-0.756	73.2	0.45	0.04	B4-0.3-5-1600 (MAM)
13985	DODGE CITY	KS	0.530	0.470	0.881	423.5	0.63	0.59	B4-0.03-10-800 (DJF)
			0.739	0.514	0.521	120.5	0.67	0.09	B1-0.3-5-800 (SON)
03198	RENO	NV	0.543	0.578	0.362	154.9	0.33	0.21	B1-0.1-15-800 (SON)
24127	SALT LAKE	UT	0.461	0.597	-0.210	1192	0.57	0.00	B1-0.3-10-400 (DJF)
			0.580	0.636	0.457	1335	0.46	0.00	B1-0.3-15-400 (SON)
04105	ELKO	NV	0.553	0.578	0.432	75.69	0.58	0.00	B1-0.03-10-600 (DJF)
			0.479	0.450	0.024	104.3	0.69	0.00	B1-0.1-5-600 (SON)
04102	GREATFALLS	MT	0.669	0.521	0.155	79.8	0.24	0.09	B1-0.1-15-800 (MAM)
			0.564	0.545	0.821	43.3	0.16	0.68	B4-0.03-5-400 (SON)
04106	SPOKANE INTNL APT	WA	0.643	0.494	-0.197	4.74	0.44	0.00	B1-0.03-10-1200 (DJF)

Table 3.3: Simulation results of "no-best-fit" stations which have high correlations between observed kinetic energy density and zonal momentum flux ($|r| \geq 0.3$) with separated four seasons. Only the "best-fits" are shown here. Columns 1-7 share the same meaning with those columns in Table 2. Column 8 and 9 give the corresponding relative intercept for KE and M . See text for details about the "best-fit" criteria.

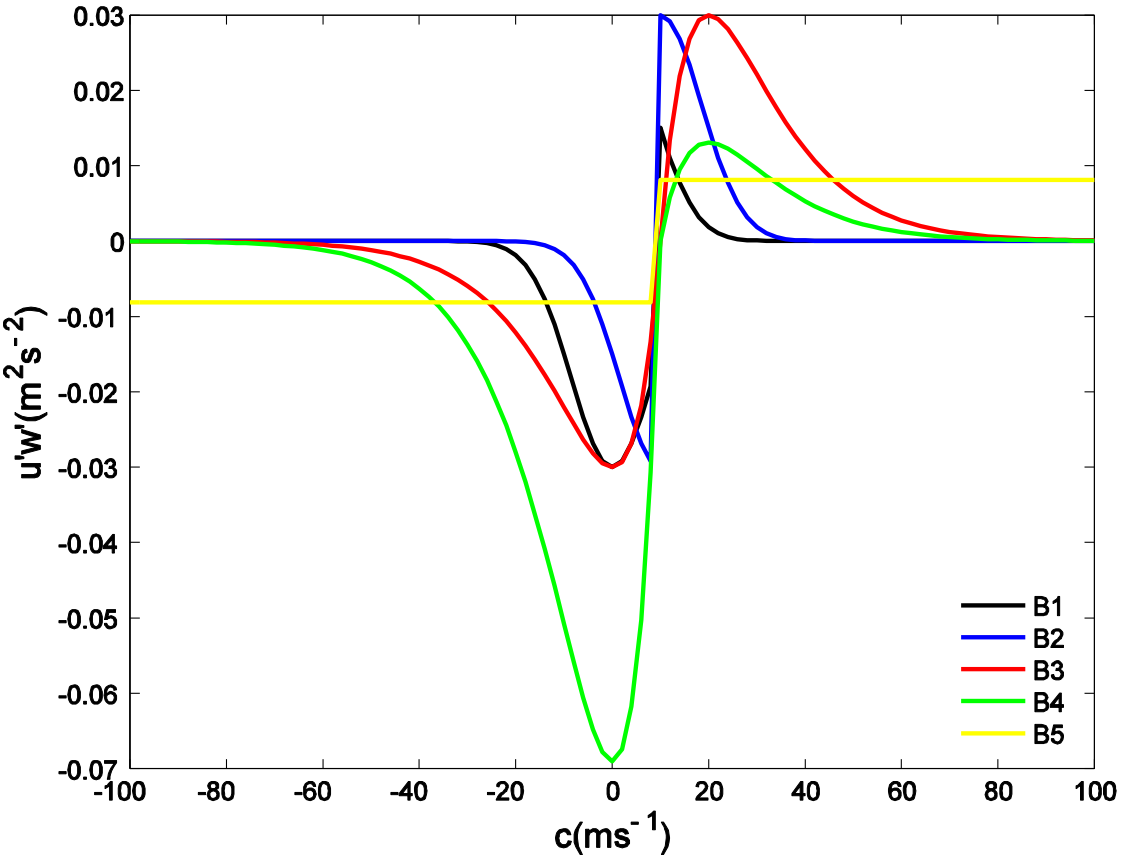

Figure 3.1: Examples of the source spectrum shapes of described by Eqn 3.2 (B1, black), Eqn. 3.3 (B2, blue), Eqn. 3.4 (B3, red), Eqn. 3.5 (B4, green) and Eqn. 3.6 (B5, yellow). This is for the case of $u_0 = 10ms^{-1}$, $c_w = 10ms^{-1}$ and $B_m = 0.03m^2s^{-2}$. Modified after Alexander and Vincent (2000) and Wang (2003).

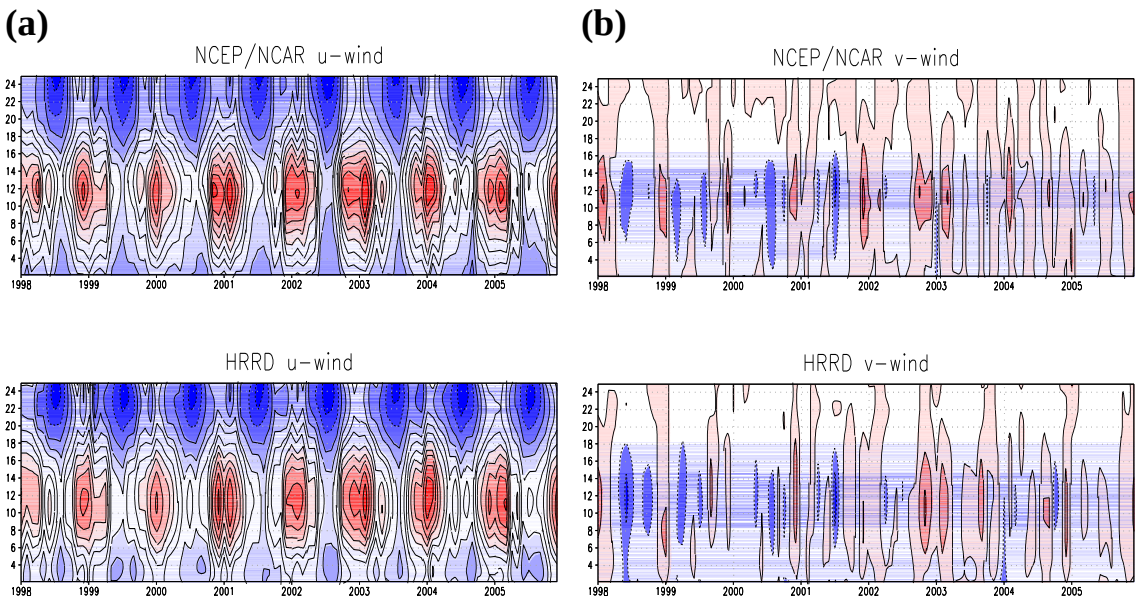

Figure 3.2: background zonal wind (a) and meridional wind (b) derived from NCEP/NCAR monthly mean reanalysis (top), and the monthly mean of the 5th-order polynomial fits of the high-resolution radiosonde data (bottom) for 1998 - 2005 at station 53829 (Blacksburg, VA [37.2$^{\circ}N$, 80.41$^{\circ}W$]).

(a)

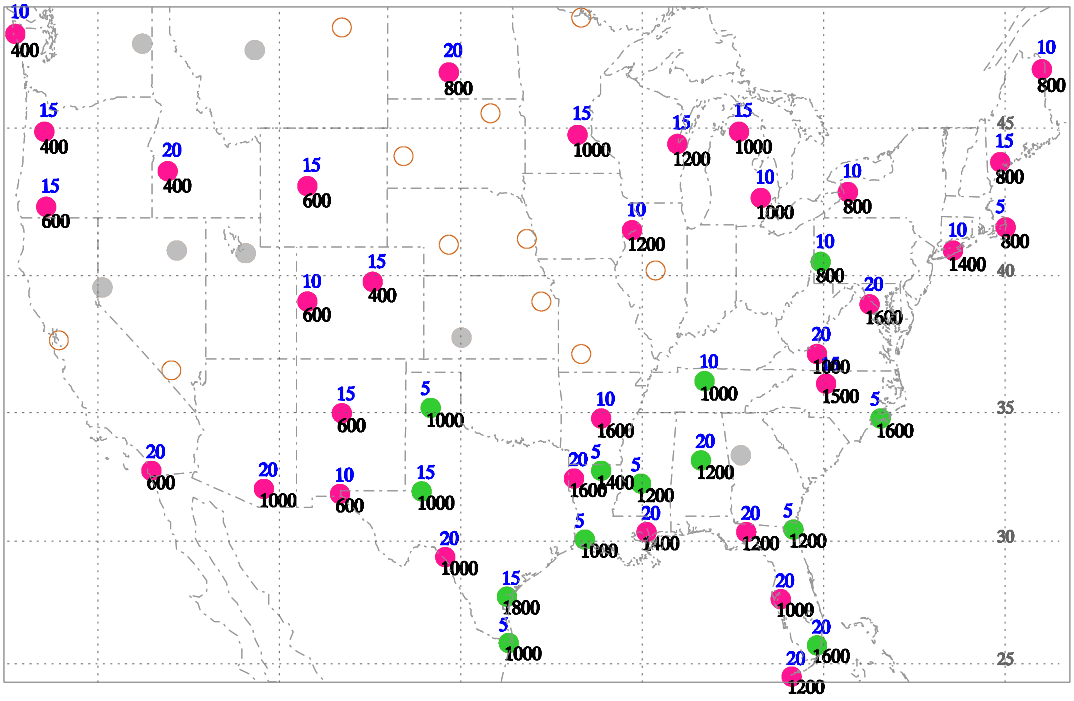
10 400
15 400
15 600
20 400
15 600
20 800
15 400
10 600
15 600
5 1000
20 600
20 1000
10 600
15 1000
20 1000
15 1800
5 1000
15 1000
10 1200
10 1600
20 1600
5 1400
5 1200
5 1000
20 1400
20 1200
15 1200
1000
10 1000
10 800
10 800
20 1600
20 1000
1500
5 1600
10 1400
15 800
5 800
10 800
45
40
35
30
25

(b)

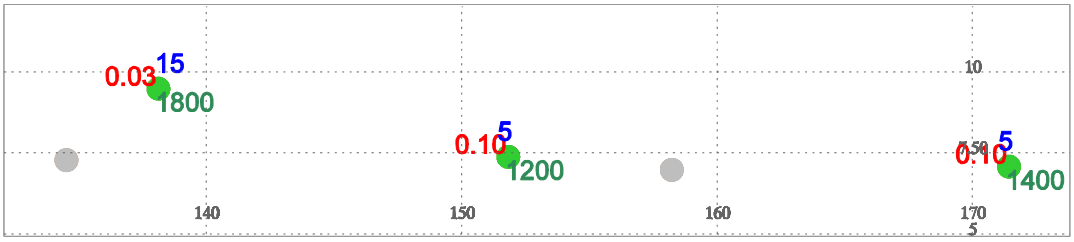
0.03
15
1800
0.10
5
1200
0.10
5
1400
10
140
150
160
170
5

(c)

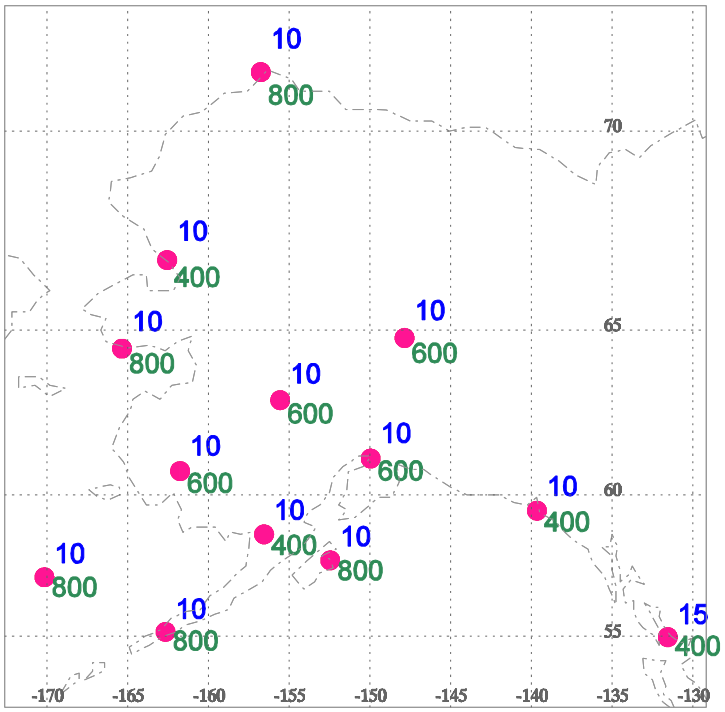

Figure 3.3: Spatial distribution of "best-fit" stations. From top to bottom: Contiguous USA (a), Pacific Islands (b) and Alaska (c). Red filled circles are stations for which we obtain a "best-fit" using B_1, while green filled circles indicate a B_4 source spectrum. Grey filled circles are stations that have high correlation coefficients of total energy and momentum derived from observations ($|r| \geq 0.3$) but no "best-fit" is obtained. Open brown circles are stations where observed energy and momentum are insignificantly correlated and where we cannot find a "best-fit". Numbers on the top-right of each station are the $c_w(m/s)$, and numbers on the bottom-right are the horizontal wave length (km) values for the "best-fit".

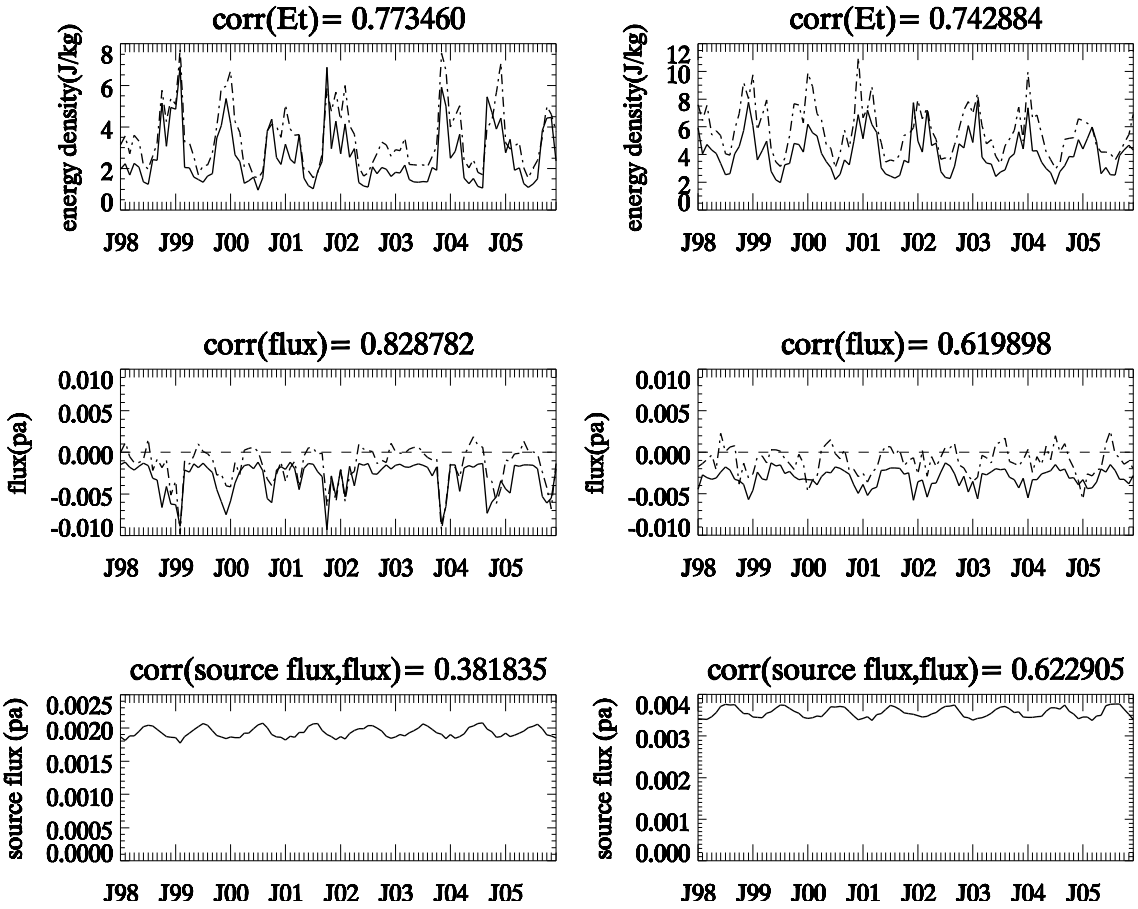

Figure 3.4: Two stations that have high correlation values ($r > 0.6$). From top to bottom: time series of KE, M and source momentum flux divided by wave intermittency. Solid lines represent the model simulation result while dashed lines are calculated from radiosonde data. The two stations are 25503 (King Salmon, AK [$58.68^\circ N$, $156.65^\circ W$], left panels) and 53829 (Blacksburg, VA [$37.2^\circ N$, $80.41^\circ W$], right panels).

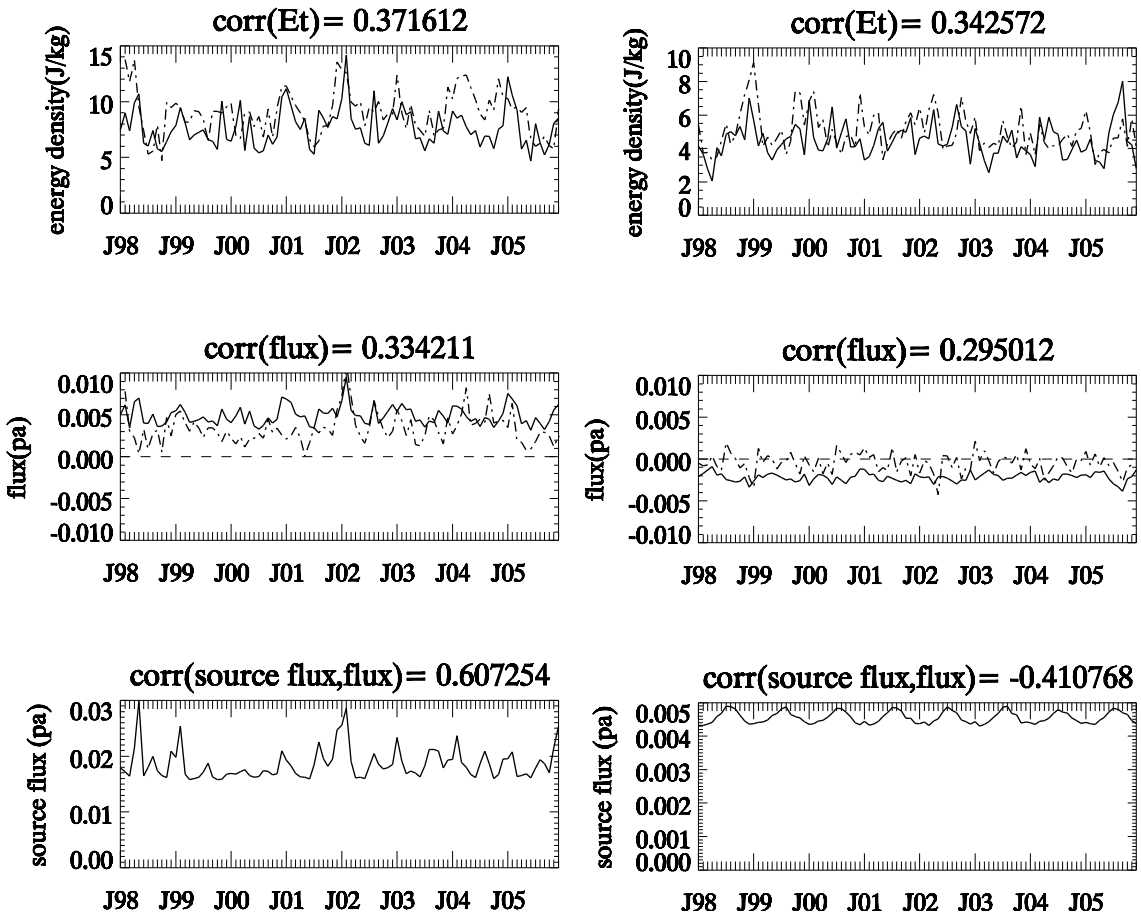

Figure 3.5: Same as Fig. 3.4, but for two low-correlation stations ($r < 0.4$) – 40710 (Majuro/Marshall Island [$7.08^{\circ}N$, $171.38^{\circ}E$], left panels) and 24011 (Bismarck, ND [$46.77^{\circ}N$, $100.75^{\circ}W$], right panels)

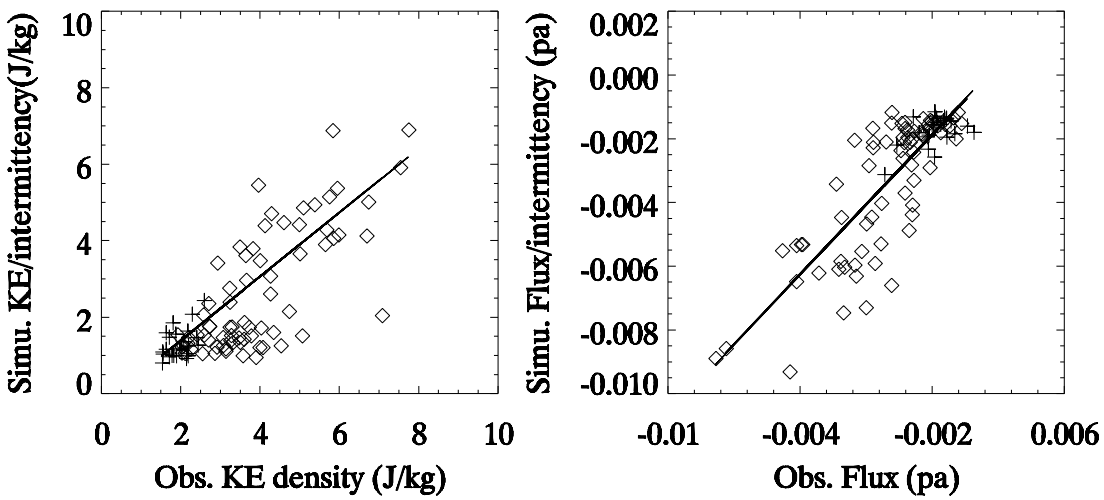

Figure 3.6: Regressions of observed kinetic energy density and zonal momentum flux to the simulated results (scaled by ε) for King Salmon, AK[58.68$^\circ N$, 156.65$^\circ W$]. The solid lines give the regression lines. Cross symbols represent summer values while diamond symbols give values for the other three seasons.

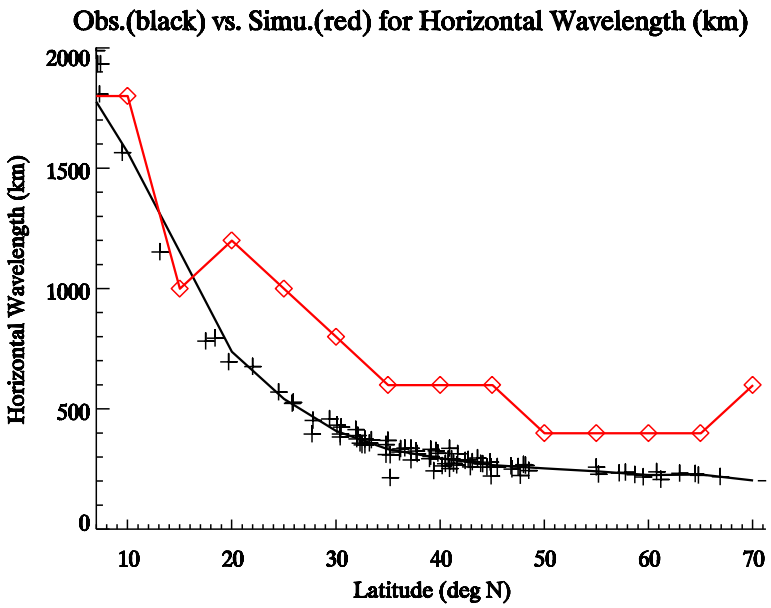

Figure 3.7: The horizontal wavelength (*km*) calculated from the observations (black) and taken from the "best-fit" parameters (red). Black crosses represent observations at stations, while red squares are simulations with 5° latitude interval. Black lines and crosses are reproduced from Wang (2003) with extended data length (1998 - 2005).

(a)

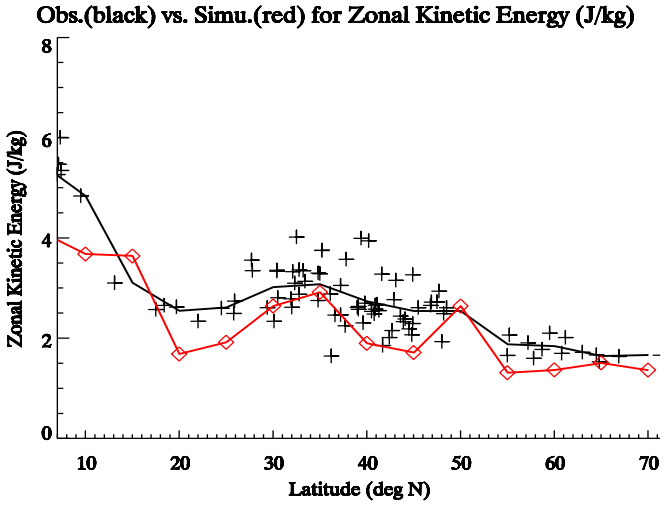

(b)

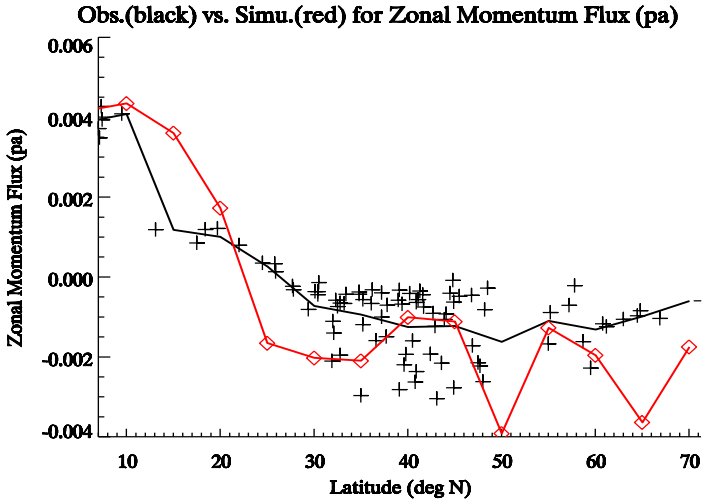

Figure 3.8: The observed (black) and simulated (red) zonal kinetic energy density (J/kg) (a) and the zonal momentum flux (*pa*) (b) in the lower stratosphere. Symbols have the same meaning with Fig. 3.7. Black lines and crosses are reproduced from Wang (2003) with extended data length (1998 - 2005).

(a)

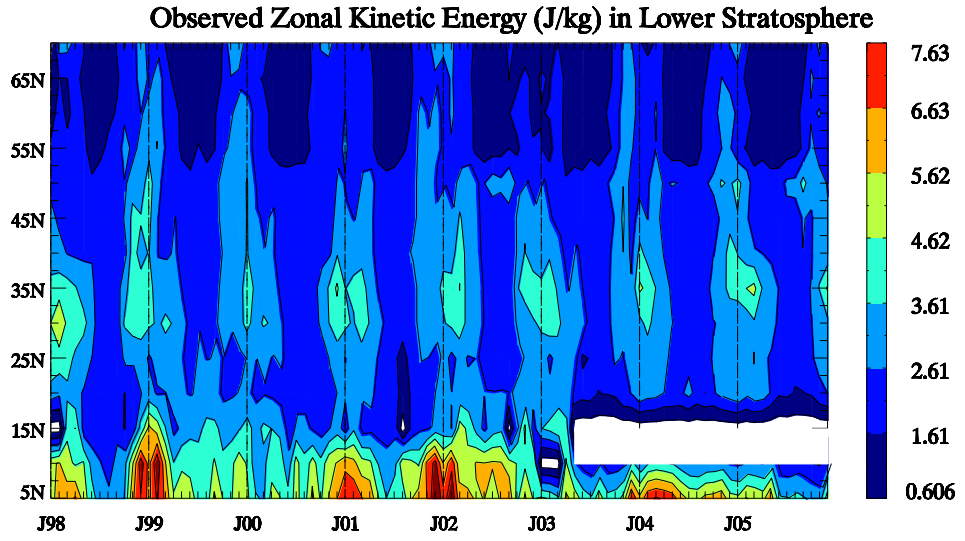

(b)

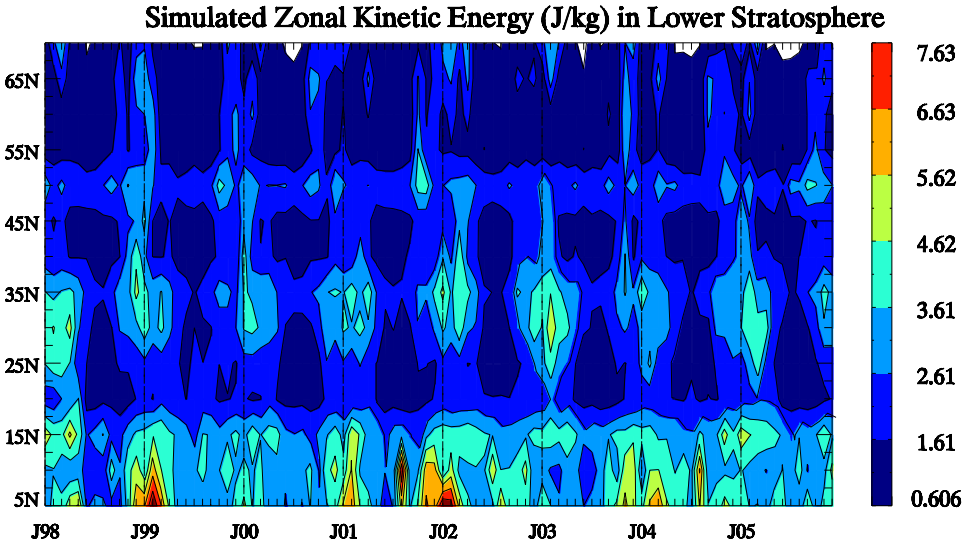

Figure 3.9: Temporal-latitudinal variations of zonal kinetic energy (J/kg) from the observations (a) and the simulations in the lower stratosphere. See text for details on how to achieve the results. Panel (a) are reproduced from Wang (2003) with extended data length (1998 - 2005).

(a)

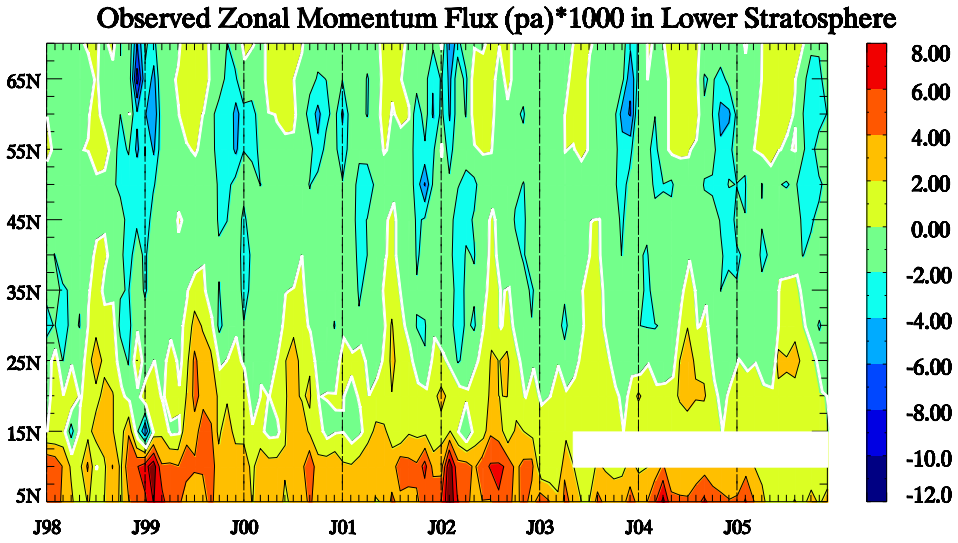

(b)

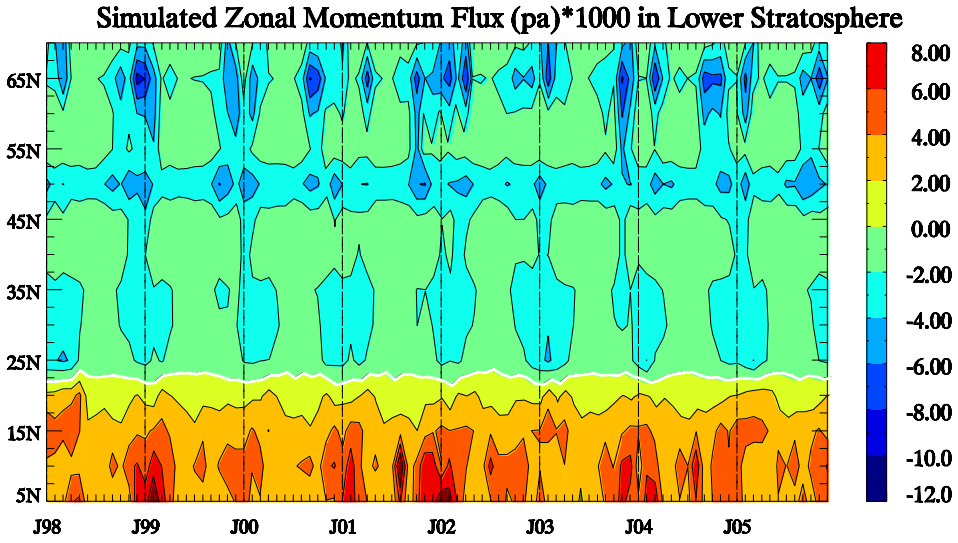

Figure 3.10: Same with Fig. 3.9, except for the vertical flux of zonal momentum (*mpa*).

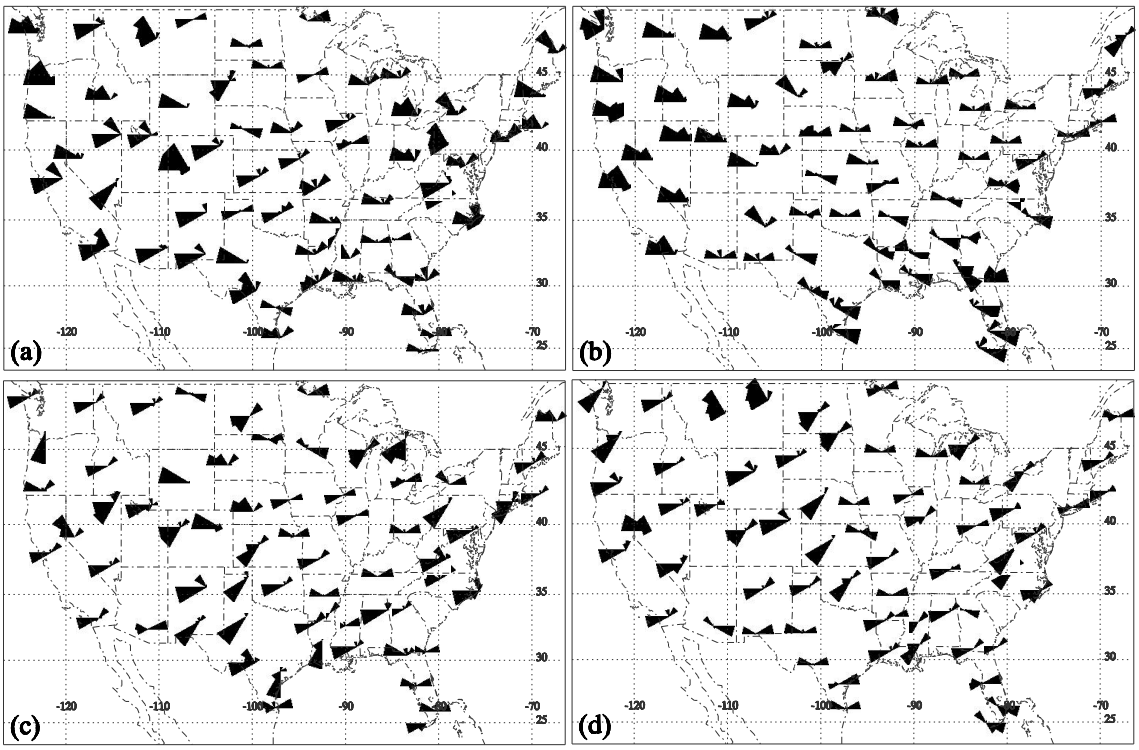

Figure 3.11: 1998-2005 averaged energy-weighted horizontal wave propagation directions for contiguous US for (a) winter, lower stratosphere, (b) summer, lower stratosphere, (c) winter, troposphere, (d) summer, troposphere.

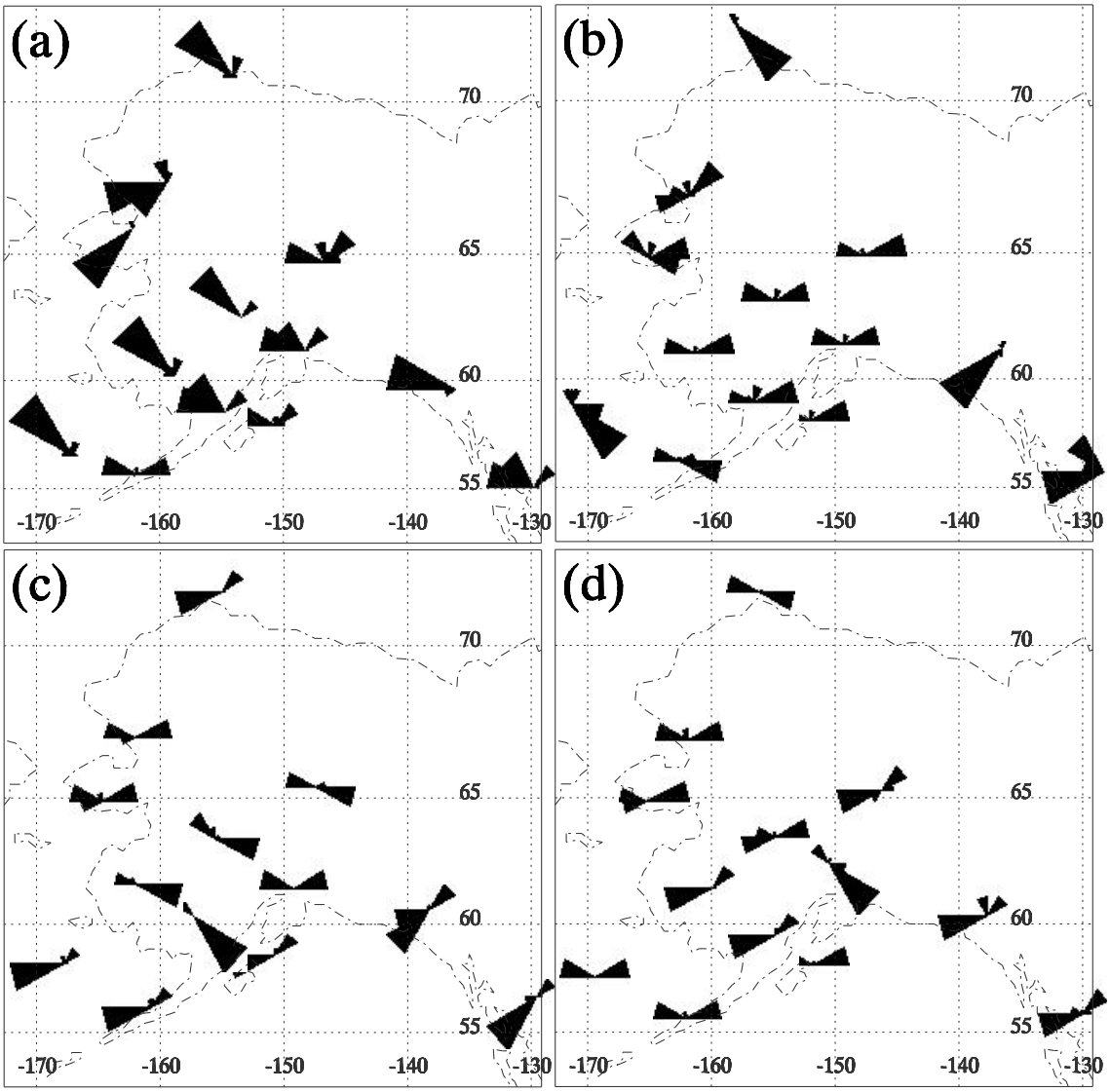

Figure 3.12: Same with Fig. 3.11, except for Alaska stations

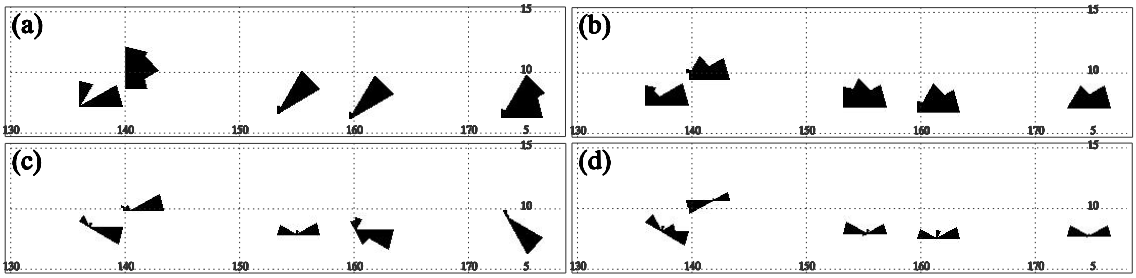

Figure 3.13: Same with Fig. 3.11, except for Western Pacific island stations

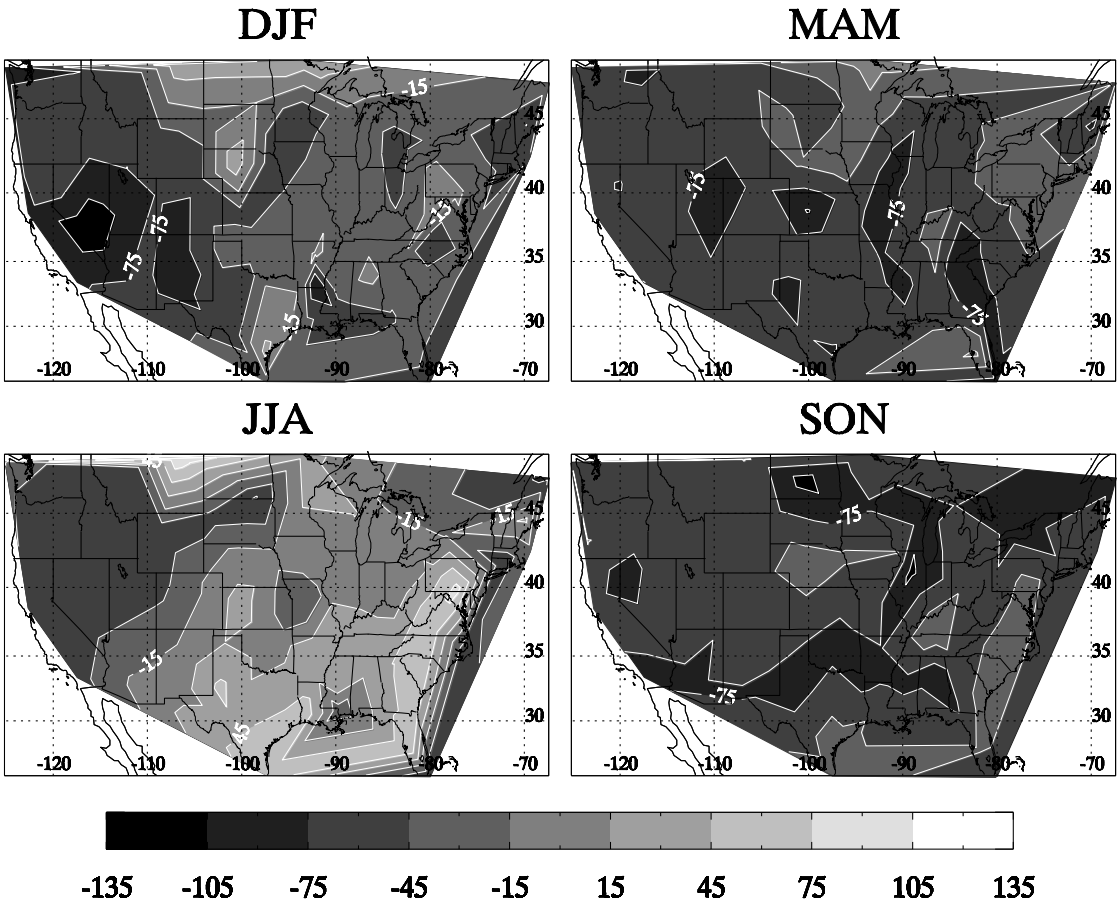

Figure 3.14: Spatial pattern of Energy-weighted horizontal propagation direction (deg.) for contiguous US during four seasons.

(a)

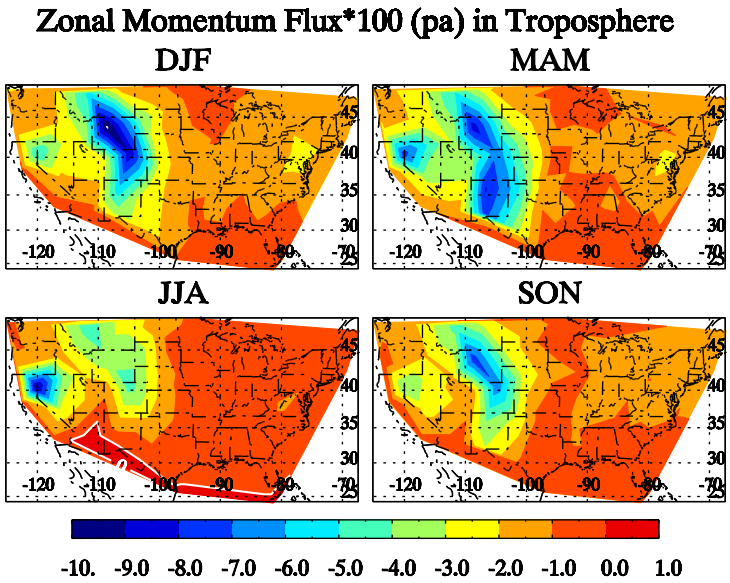

(b)

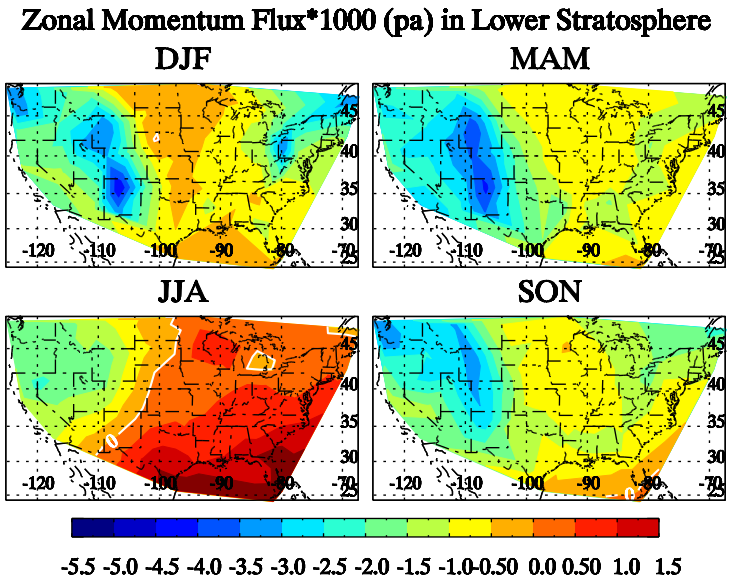

Figure 3.15: Geographical distributions of the zonal momentum flux over the contiguous US for four seasons in the troposphere (a) and the lower stratosphere (b). Adapted from Wang (2003) with extended data length (1998 - 2005).

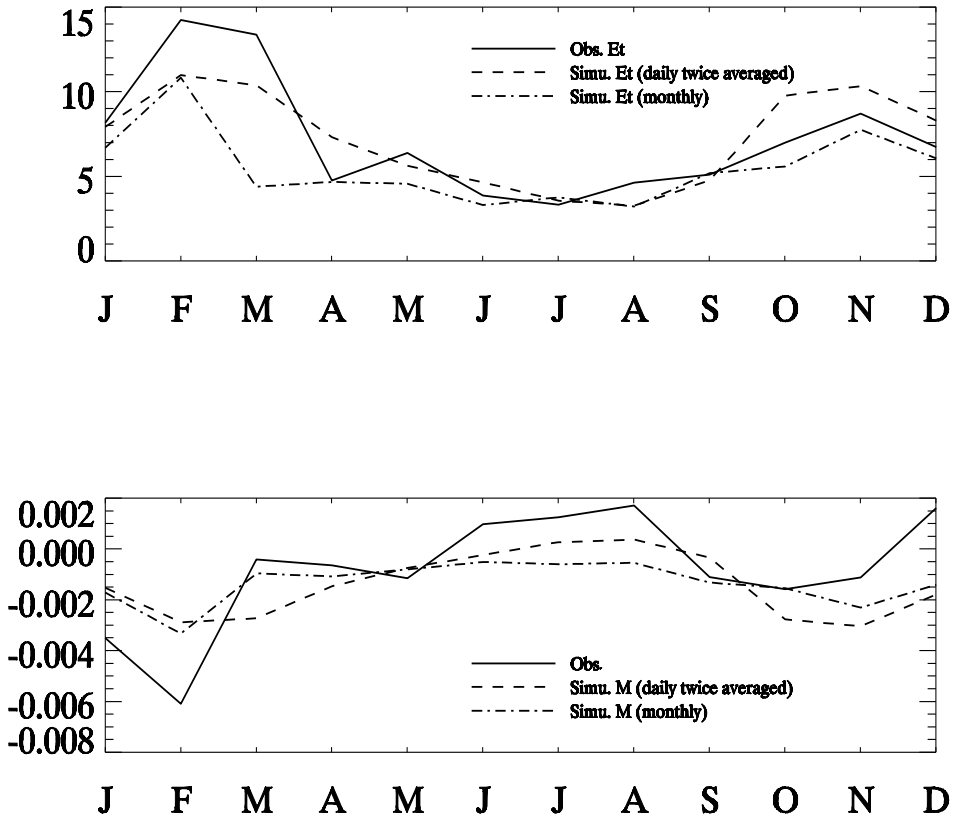

Figure 3.16: Comparisons of E_t (top panel) and zonal momentum flux M (bottom panel) among the observations (solid), the simulations which are carried out twice-daily and averaged monthly (dashed) and the simulations that are carried out monthly (dash-dotted) for one station 53829 (Blacksburg, VA [$37.2^\circ N$, $80.41^\circ W$]).

Chapter 4 Vertical Fluctuation Energy as a measure of Higher-frequency Gravity Waves and as an Indicator of Convective Gravity Wave Sources

4.1.Introduction

Convection is one of the most important gravity wave sources. While the orographic (stationary) source for gravity waves gives rise to decelerations of both easterly and westerly flows, non-stationary sources tend to preferentially drive the flow in a specific direction. As shown in Fig. 1.1, non-stationary gravity waves are essential in driving the mean zonal flow in a given direction, and thus are crucial for the zonal circulations in the mesosphere and the lower thermosphere (MLT). Convective gravity wave sources are particularly important for the Southern Hemisphere and the tropics, where orographic sources are not so dominant compared with the Northern Hemisphere (Chun et al., 2001). Compared with other non-stationary gravity wave sources, convection has been investigated the most. Three physical generation mechanisms for gravity waves from convective clouds have been proposed in the existing literature: the "mechanical oscillator" mechanism, the "moving mountain" mechanism and the "thermal forcing" mechanism. The "mechanical oscillation" mechanism depicts convective systems as oscillatory drivers of vertical motions at the tropopause and generate gravity waves above the clouds (Fovell et al., 1992). The "moving mountain" mechanism treats convection as a moving mountain, where gravity waves are generated by flow over the convective obstacles (Pfister et al., 1993). The "thermal forcings" mechanism considers the latent

heat release in convective clouds as thermal forcings, which radiate gravity waves into the stable layer above the clouds (Garcia, 2000). It has been argued through this last mechanism that the vertical wavelengths are approximately twice the heating depth (Alexander et al., 1995; Garcia, 2000). The last mechanism has been incorporated into physically-based parameterizations and has been implemented into GCMs (Chun and Baik, 1998; Beres et al., 2004). Convective sources have large seasonal variation, being strongest in summer, and weakest during winter, when jet imbalances, frontal systems and mountains dominate gravity wave emissions.

There have been several attempts to use radiosonde ascent rate profiles for gravity wave analyses (e.g., Shutts, 1992; Shutts et al., 1994). *Reeder et al. [1999] and Lane et al. [1999]* used the ascent rate profiles from radiosonde soundings to study two lee – wave cases, respectively, and obtained horizontal wavelength from the ascent rate perturbations in their analyses. *Lane et al. [2003]* analyzed the ascent rate of the balloon during a field campaign, and found that the gravity wave signature in the ascent rate over a tropical island was closely associated with the occurrence of convection.

Gravity wave theory implies that horizontal winds, temperature and ascent rate perturbations should be sensitive to different parts of the frequency spectrum of gravity waves (Geller and Gong, 2009). Motivated by this, we investigate the ascent rate information from radiosonde profiles over the US in this chapter. We analyze the climatology of the so-called "vertical fluctuation energy"[1] (VE) in a similar fashion to *Lane et al. (2003)*, and the apparent dominant vertical wavelengths that are derived from ascent rate profiles from US high vertical-resolution radiosonde data, which cover a

[1] Strictly speaking, VE is vertical fluctuation energy density.

broad latitudinal range. The VE climatology is then compared with climatologies of the kinetic energy density (KE), potential energy density (PE) and vertical wavelength derived from temperature and wind observations to prove that different analyses indeed "see" different gravity waves. The theoretical derivations will be presented in section 2. The results of diurnal and seasonal variations of VE and vertical wavelength are given in section 3 with comparisons to KE and PE. A small numerical experiment is carried for interpretive purposes. The frequency information derived from ratios between KE and VE, KE and PE are discussed in section 4, together with frequency spectra derived from a very simple model. Final conclusions and remarks are made in section 5.

4.2.Description of Theories

This section is taken from Geller and Gong (2009), where details can be found.

Starting from the dispersion and polarization relationships for hydrostatic gravity waves, we obtain the following expressions:

$$KE = \frac{1}{2}\left(\overline{u'^2} + \overline{v'^2}\right) = \frac{1+\left(f/\hat{\omega}^2\right)^2}{1-\left(f/\hat{\omega}^2\right)^2}\frac{m^2}{N^2}\frac{\hat{p}^2}{4} \tag{4.1}$$

$$PE = \frac{1}{2}\frac{g^2}{N^2}\overline{\left(\frac{T'}{T_0}\right)^2} = \frac{m^2}{N^2}\frac{\hat{p}^2}{4}, \text{ and} \tag{4.2}$$

$$VE = \frac{1}{2}\overline{w'^2} = \frac{\hat{\omega}^2 m^2}{N^4}\frac{\hat{p}^2}{4}, \tag{4.3}$$

where the overbar indicates averaging over wave phase. $\hat{p}$ is a complex amplitude, defined as $\frac{p'}{\rho_0} = \mathrm{Re}\left[\hat{p}e^{i(kx+ly+mz-\omega t)}\right]$. Re indicates the real part of the bracketed expression. Variables with a 0-subscript represent the basic state. Other symbols have been introduced previously in Chapter 2.

From Eqns. (4.1)-(4.3), one sees that each of the gravity wave energies has different frequency dependence. *KE* is the most sensitive to low-frequency waves, while, as *Lane et al. (2003)* has previously pointed out, *VE* is the most sensitive to relatively higher-frequency waves.

Now the ratio between two energies are:

$$\frac{\overline{KE}}{\overline{PE}} = \frac{1+\left(\frac{f}{\hat{\omega}}\right)^2}{1-\left(\frac{f}{\hat{\omega}}\right)^2} \tag{4.4}$$

$$\frac{\overline{VE}}{\overline{PE}} = \frac{\hat{\omega}^2}{N^2} \tag{4.5}$$

Thus we can derive the intrinsic frequency $\hat{\omega}$ from (4.4) and (4.5) independently. Since different energies emphasize different parts of the frequency spectrum, the derived $\hat{\omega}$'s are not expected to have the "correct" value, but are rather a compromise between two frequency spectra. The impact is discussed in *Geller and Gong (2009)*. $\hat{\omega}$ derived here is still physically meaningful, which will be presented in section 4.

Analogous procedures can be carried out for non-hydrostatic gravity waves. With the full dispersion relationship Eqn. (2.12), considering equations in Hines (1960) for an

incompressible fluid ($c_s^2 \to \infty$), we can derive the energy expressions for non-hydrostatic gravity waves:

$$\overline{KE} = \left(\frac{1+\left(\frac{f}{\hat{\omega}}\right)^2}{\hat{\omega}^2\left[1-\left(\frac{f}{\hat{\omega}}\right)^2\right]\left[\left(\frac{N}{\hat{\omega}}\right)^2-1\right]} \right)\left(m^2+\frac{1}{4H^2}\right)\frac{g^2H^2}{4N^2}\,\tilde{p}^2 \tag{4.6}$$

$$\overline{PE} = \left\{1-\frac{N^2}{\hat{\omega}^2\left[\left(\frac{N}{\hat{\omega}^2}\right)^2-1\right]}+\frac{H^2N^4\left(m^2+\frac{1}{4H^2}\right)}{\hat{\omega}^4\left[\left(\frac{N}{\hat{\omega}}\right)^2-1\right]^2}\right\}\frac{g^2\tilde{p}^2}{4N^2} \tag{4.7}$$

$$\overline{VE} = \frac{\left(m^2+\frac{1}{4H^2}\right)}{\hat{\omega}^2\left[\left(\frac{N}{\hat{\omega}}\right)^2-1\right]^2}\frac{g^2H^2}{4}\,\tilde{p}^2 \tag{4.8}$$

where $\tilde{p} = \dfrac{\hat{p}}{gH_s}$.

Similarly, the ratios are:

$$\frac{\overline{KE}}{\overline{PE}} = \left[\frac{1+\left(\frac{f}{\hat{\omega}}\right)^2}{1-\left(\frac{f}{\hat{\omega}}\right)^2}\right]\frac{\left[m^2+\frac{1}{4H^2}\right]N^2H^2}{\left(N^2-\hat{\omega}^2\right)\left[1-\frac{N^2}{N^2-\hat{\omega}^2}+\frac{H^2\left(m^2+\frac{1}{4H^2}\right)N^4}{\left(N^2-\hat{\omega}^2\right)}\right]} \tag{4.9}$$

$$\frac{\overline{VE}}{\overline{PE}} = \frac{\left(m^2 + \frac{1}{4H^2}\right) N^2 H^2}{\hat{\omega}^2 \left[\left(\frac{N}{\hat{\omega}}\right)^2 - 1\right]^2 \left[1 - \frac{N^2}{\hat{\omega}^2 \left[\left(\frac{N}{\hat{\omega}}\right)^2 - 1\right]} + \frac{H^2 N^4 \left(m^2 + \frac{1}{4H^2}\right)}{\hat{\omega}^4 \left[\left(\frac{N}{\hat{\omega}}\right)^2 - 1\right]^2}\right]} \tag{4.10}$$

Note that the asymptotic behaviors of Eqns. (4.9) and (4.10) are the same with those of Eqns. (4.5) and (4.6). When $\hat{\omega} \to f$, $\overline{KE}/\overline{PE} \to \infty$, since the wave becomes pure inertial oscillations with no vertical component. As $\hat{\omega} \to N$, $\overline{KE}/\overline{PE} \to 0$ as expected since it corresponds to a pure buoyancy oscillation. $\overline{VE}/\overline{PE} \to f^2/N^2 \left(\hat{\omega}^2/N^2\right)$ as $\hat{\omega} \to f(N)$. These relationships are important in interpreting results in section 4.

The US high-vertical resolution radiosonde data has been described in Chapter 2, as well as the method we use to extract gravity wave information from the ascent rate perturbations. Since a fair amount of profiles indicate trapped gravity waves generated by mountain sources, it is necessary for us to exclude these trapped wave cases in order to study convective source and other potential gravity wave sources. Besides, trapped waves carry zero vertical momentum flux into the lower stratosphere, so the exclusion procedure keeps only the vertically propagating waves, and hence the results are expected to be more meaningful for the lower stratosphere.

As two examples, Fig. 2.4 gives the vertical profile of perturbation fields for the cases of a squall line event and a jet streak event. At 00Z July 5, 2003, a squall line was fully developed over Illinois and Ohio (Bosart et al., 2005), and the perturbed ascent rate

profiles over Lincoln-Logan county airport [270.67 °E, 40.15 °N], IL show strong wave-type structures in both the troposphere and the lower stratosphere (Fig. 2.4a, d), implying the plausibility of relating them to real physical sources. At 12Z Jan. 4, 2000, an upper level jet streak passed by Blacksburg, VA [279.59 °E, 37.2 °N], which had similar structure to the one discussed by *Zhang and Koch [2000]*, and we also see large wave-type structures in the perturbation ascent rate profile in the troposphere at that station (Fig. 2.4g). w' shown in Fig. 2.4 has been multiplied by a factor of 2 for better comparisons. The power spectra of the Fourier transformed w' with respect to time are given in the second row, where the dominant periods are all greater than the buoyancy oscillation periods. The power spectra of the Fourier transformed u', T' and w' with respect to height are given in the panels at the last row. The apparent dominant vertical wavelengths estimated from u', T' and w' profiles are quite different, indicating that, as we expect, the different variables are indeed sensitive to different gravity waves (Geller and Gong, 2009). For two of them (Fig. 2.4c and i), the most dominant wavelengths of T' overlap with those derived from w', suggesting that we may be able to obtain useful information from analysis of both the temperature and vertical velocity perturbations. It is easy to understand why this is the case since the temperature perturbations are partly caused by vertical motion. Furthermore, even for the same squall line case, if we compare Fig. 2.4a with d for the w' field, the waves are likely different since the most dominant vertical wavelengths are different (Fig. 2.4c and f). One thing to notice here is that here we mainly deal with relatively shallow convection in the troposphere. This is easy to be understood since gravity waves cannot survive in deep unstable convective layers, and

we also find this is true from examining individual profiles with large ascent rate perturbations.

4.3.Climatologies of VE and the dominant vertical wavelength from the observations

In this section, we first present our results for tropical stations, since these are more straightforward. In the second part, diurnal, seasonal and interannual variations of VE as well as the apparent dominant vertical wavelength are studied, with emphasis on the mid-high latitudes. In the last part, a simple simulation is presented to further interpret the different behaviors of the tropics and extratropics.

4.3.1 Results for the tropics

It is easier to relate VE and vertical wavelength variations to convective activity in the tropics than is the case at mid-high latitudes. Fig. 4.1 gives the normalized time series of 3-month running averaged anomalies of VE in both the troposphere and lower stratosphere at one tropical western Pacific island (Majuro/Marshall Island [171.38°E, 7.08°N]) together with the Outgoing Longwave Radiation (OLR) and the Convective Precipitation Rate at the Surface (CPR) from NCEP/NCAR reanalysis. We see that the VEs in the troposphere and lower stratosphere are largely coherent with each other (R = 0.813). Furthermore, both are significantly (at the 95% level) anti - correlated with the OLR (R = -0.513 and -0.358, respectively), and positively correlated with CPR (R = 0.291 and 0.330, respectively). Thus, high values of VE in both the troposphere and lower stratosphere are highly correlated with indications of convective activity. The correlation coefficients are listed in Table 4.1 for the five western Pacific tropical stations

available in the dataset, with values that pass 95% significance test marked in bold. We can find from Table 4.1 that these relationships hold for all the stations by looking at those significant correlation coefficients, except that VE in the lower stratosphere and OLR are significantly positively correlated for station Truk Intl./ Moen Island [151.85°E, 7.47°N], the reason for which is unclear. An inverse relationship between KE and OLR has also been found in certain studies for some tropical stations (e.g., Tsuda et al., 1994 and Vincent and Alexander, 2000), but this correlation is low in our data.

4.3.2 Results for mid-latitudes

4.3.2.1 Diurnal variations

The relation between VE and convective activity is more complicated at mid-latitudes, so we use quite a different analysis for this. A diurnal cycle of convective activity exists throughout the year over most of the United States, but is much more pronounced during the summer since the overall frequency of convective occurrence is the highest then (Wallace, 1975). For the contiguous US, 00Z corresponds to local afternoon to early evening, while 12Z corresponds to early morning. Therefore, the VE differences for these times should reflect the diurnal variation of gravity waves from convective sources. Fig. 4.2a (the 1st and 2nd rows) gives VE at 00Z minus that at 12Z for four seasons over the contiguous US in the troposphere. The white-line shaded areas are regions where these diurnal variations are significant at the 95% level. We can clearly see from Fig. 4.2a that the diurnal variation of VE is pronounced over almost the whole country during summer except for the Great Plains and eastern Texas. It's also significant for the other three seasons over the Rockies. The late afternoon and early evening convective activity maxima for the western US and eastern US, respectively, have been well documented

(e.g., Easterling and Robinson, 1985; Winkler et al., 1988). The strong diurnal cycle of boundary-layer heating typically has its largest amplitude during local afternoon (1600 LST) in the western US and early evening (1800 LST) in the eastern US, as suggested by *Easterling and Robinson (1985)*, when convective activity is easily triggered. Convective activity over the central US has a different character. Eastward propagating convective systems from the Mountains, interacting with the nocturnal low level jet over the central US, determines the preferred conditions for convection during the nighttime in summer (Winkler et al., 1988; Weisman and Rotunno, 2004), and that is likely the reason why we do not see a diurnal cycle of VE in this region in the 00Z and 12Z VE differences. The mid-noon convective activity maximum over southern Texas (Easterling and Robinson, 1985) possibly causes the absence of this signature over that region in Fig. 4.2a for similar reasons. The overall diurnal variation of VE fits the rhythm of the occurrence of convection almost perfectly, especially during summer. We adapted Fig. 3b of *Easterling and Robinson (1985)* here as Fig. 4.2b for easier comparison, where they composite the summer pattern of the time of maximum activity derived from the 1st harmonic of hourly thunderstorm activity in the US. The two centers of maximum diurnal difference coincide with the Rockies and Florida regions, which are the most favorable places for convective activity during the summer. We would not expect to see as large diurnal variation signatures in VE during the winter since the dominant gravity wave sources at that time are likely not convection but topography, spontaneous emission from jets, frontal systems, etc. VE does exhibit a similar diurnal variation in the lower stratosphere that we see in the troposphere, but with much weaker amplitudes (Fig. 4.2c). We will further investigate this later in this paper.

The diurnal variations of the most dominant vertical wavelength for *w'* exhibit similar patterns to those of VE, but with larger areas at the 95% significant level (Fig. 4.3a). Since the intrinsic frequency is proportional to vertical wavelength for internal gravity waves, other things being equal, the local afternoon maxima of vertical wavelength of *w'* likely correspond to higher – frequency gravity waves. The spatial distribution of the diurnal difference of PE and the most dominant vertical wavelength of *T'* pretty much resemble the diurnal variations of VE in both layers, but the area of 95% significance is smaller (Fig. 4.4 and 4.5). That is likely due to the fact that temperature perturbations are not only caused by vertical motions, but also caused by other processes such as horizontal temperature advection, etc. KE barely exhibits any signature of a diurnal cycle in both the troposphere and lower stratosphere except for the western US in the troposphere, which has opposite phase to that of VE. The close correlation between KE and background wind has been pointed out by previous researchers (e.g., Wang and Geller, 2003). We computed the diurnal variation of the zonal wind from the NCEP/NCAR reanalysis dataset for the contiguous US during the summer of 2003, and found it's closely related to the diurnal pattern of KE.

To prove that the diurnal signals are really robust, the VE and the apparent dominant vertical wavelength derived from *w'* calculated with the low-pass filtered ascent rate perturbations but without removing the balloon oscillation component nor the trapped-wave profiles are plotted in Fig. 4.6 and 4.7, respectively. One can see that the diurnal variations in the troposphere are in general more apparent with the raw data with only the band-pass filter, and less apparent in the lower stratosphere, compared with Fig. 4.2 and 4.3. Later we will demonstrate this is likely not caused by including the trapped-wave

profiles in section 3.2.2, but caused by not removing the balloon oscillation component. As suggested in Chapter 2, the balloon oscillation frequency tends to be smaller (i.e., period becomes longer) when the atmosphere is less stable, which easily occurs during summer and late afternoon in the troposphere when convection is favored. Therefore, it adds a positive component to the diurnal variations if the balloon oscillation component is not excluded. In the stratosphere, the upper part is heated up by direct solar radiation, which indicates that the atmosphere is more stable during summer and in the afternoon. Hence, the balloon oscillation component acts in the opposite direction to the diurnal patterns of and the apparent dominant vertical wavelength derived from *w'*, and that is likely the reason that the signals are even weaker in the lower stratosphere if we include the balloon oscillation component, as shown in Fig. 4.6a and 4.7a.

4.3.2.2 Seasonal variations

Wang and Geller (2003) presented climatologies for E_t, the total gravity wave energy, which they defined as being $KE + PE$. They showed that E_t maximized during winter in both the troposphere and the lower stratosphere. In fact, there was no indication of any signature of energy maxima due to convectively forced gravity waves in summer except in the tropics. This was at variance with some other works that showed signatures of convectively forced gravity waves (e. g., Allen and Vincent, 1995, and Lane et al., 2003). To evaluate the latitude dependence of the seasonal variation of VE, KE, and PE, we applied a 5^o latitudinal binning from 5^oN to 70^oN. After assigning every station to its designated bin, we calculate the average for each bin. The time series of the monthly values of VE, KE, and PE as a function of latitude are plotted in Fig. 4.8, 4.11 and 4.12, respectively, with top (bottom) panels showing results for the troposphere (lower

stratosphere). The stations binning into the 5^o-10^oN, 25^o-50^oN, and 55^o-70^oN bins roughly correspond to the tropical western Pacific islands, the contiguous US, and the Alaska stations, respectively.

VE , *KE* , and *PE* show quite different variations in time and latitude. In the troposphere, *KE* and *PE* have winter maxima, occurring at mid-latitudes, while *VE* has summer maxima, again occurring at mid-latitudes, with secondary maxima at high latitudes occurring mainly in winter, which may be indicative of spontaneous emission srouces. This is consistent with *VE* in the troposphere showing higher frequency gravity wave response to convection during summer. The situation is different in the lower stratosphere, especially for *VE* . As can be found in Fig. 4.8b, *VE* in the lower stratosphere shows winter maxima at middle and high latitudes, with strong maxima in some years at around 20 ^{0}N. The dominant mid-latitude summer maxima seen in the troposphere are not as prominent in the lower stratosphere, although some signatures of secondary maxima still persist. We will investigate the inconsistency of diurnal and seasonal variabilities of *VE* in the troposphere and lower stratosphere at the end of this section and further in section 3.3. *KE* and *PE* still maximize in winter, but the magnitudes decrease with latitude, while *VE* doesn't show a clear latitudinal dependence.

It is interesting to further examine the time series for the apparent dominant vertical wavelength of *w'* and $\frac{T'}{\overline{T}}$ as functions of latitudes, also (Fig. 4.9 and 4.10). In the troposphere, the apparent dominant vertical wavelength derived from *w'* has very similar pattern to that of *VE* (Fig. 4.9a). In the lower stratosphere, however, it is somewhat different from *VE*, as shown in Fig. 4.9b. The summer maxima of vertical wavelength

extends to around 40 ℃N, and the regime suddenly shifts to winter maxima to the north of 40 ℃N, with no significant latitudinal dependence in its magnitude. Similar features are presented in the dominant vertical wavelength of $\frac{T'}{\overline{T}}$ (Fig. 4.10b). The annual variation of the apparent dominant vertical wavelength of *w'* is about 100%, roughly corresponds to 100% variation of the intrinsic frequency if we consider the simplified dispersion relationship $\frac{\hat{\omega}}{N} \approx \frac{\lambda_z}{\lambda_x}$ and assume N and λ_x being equal, where λ_x is the horizontal wavelength. The patterns of the vertical wavelength derived from the horizontal wind fields are quite different, however, with peaks in the tropics and decreasing with latitude in both the troposphere and lower stratosphere, and they peak in winter throughout the whole latitudinal range in the troposphere as well as in the lower stratosphere (Wang et al., 2005). These differences again indicate the ascent rate perturbations and horizontal wind perturbations are "seeing" different gravity waves.

Even within the troposphere, the seasonal variation patterns for VE and apparent vertical wavelength from *w'* differ from station to station. Fig. 4.13 gives five examples, representing different locations, with the 1st row for a Western coast station (Spokane Intnl. Apt., WA [242.37 ℃E, 47.68 ℃N]), the 2nd row for a Rocky Mountain station (Elko, NV [244.27 ℃E, 40.87 ℃N]), the 3rd row for a Great Plains station (North Platte, NE [259.32 ℃E, 41.13 ℃N]), and the 4th row for an eastern US station (Peachtree City, GA [275.44 ℃E, 33.35 ℃N]), and the last row for another eastern US station (Blacksburg, VA [279.59 ℃E, 37.2 ℃N]). For the Western coast and mountain stations (Fig. 4.13a-d), results at 00Z contribute most to the seasonal variations for both VE and the most dominant vertical wavelength, while values at 12Z are much smaller than those at 00Z, which do

not show a clear seasonal variation. For the central and one eastern US stations (Fig. 4.13e-h), 00Z and 12Z values are comparable. Both of them contribute to the seasonal variation of VE and the most dominant vertical wavelength, where the latter seems to have more clearly-defined seasonal patterns. For the other eastern US station (Fig. 4.13i, j), the time series of VE has some indications of winter maximum, and the time series of the dominant vertical wavelength, however, barely shows any marked seasonal variation.

VE is expected to be much more sensitive to relatively higher frequency waves. Since convective events are most active during summer, and have larger interannual variability compared with stable orographic sources, this likely leads to the peak of *VE* in summer at mid-latitudes, and can explain the large interannual variations of *VE* compared to those of *KE* and *PE* in the troposphere. This interpretation also works to explain the seasonal cycle of the apparent dominant vertical wavelength since more vertically propagating gravity waves with higher-frequency tend to have longer vertical wavelength. At high latitudes, *VE* maximize in winter in the troposphere, probably indicating jet imbalance as the primary source there during winter seasons. In the lower stratosphere, *Eckermann [1995]* attributed the annual cycle of *KE* and *PE* to the seasonal variation of the density scale height, which also likely explains the dominant winter maxima of *VE* in the lower stratosphere. The secondary summer maxima of *VE*, however, can not be explained by this theory. It can be attributed to the convective source since some of the vertically propagating gravity waves do propagate into the lower stratosphere. The apparent summer peak in the dominant vertical wavelength in the lower stratosphere at mid-latitudes supports this conclusion.

It is noticeable that *VE* does have one of the peaks located at the Rockies in the troposphere during warm seasons. However, this peak becomes less prominent in winter (Fig. 4.14), consistent with the fact that they are not purely related with the orographic source. Another evidence is that all the summer peak signals still exist after removing the trapped-wave profiles in the pre-processing procedures. As a matter of fact, we evaluated the difference between the ones with/without excluding trapped-wave profiles for mountain stations, and the results, as shown in Fig. 4.15, show little difference. The geographical dependence of the seasonal variations of *VE* might imply the importance of the Rockies in generating medium frequency gravity waves. During the summer, the Sun heats the surface of the mountains, and triggers convection in the local afternoon as the air becomes convectively unstable. This occurs almost everyday in the mountain region, but the convective systems have much more complicated origins than simple local generation in the eastern US. The different behaviors of convection at different locations likely cause the diversities in VE and dominant vertical wavelength from station to station, as shown in Fig. 4.13. With respect to the jet streak (or spontaneous emission) source, it doesn't have a strong diurnal dependence. Secondly, cyclone systems usually experience rapidly intensifications in the lee of the mountains (Eichler and Higgins, 2006) and in the eastern US when they pass under upper level jet streaks (Uccellini and Kocin, 1987) or merge with surface frontal systems. That may be responsible for the winter maximum at some eastern US stations (e.g., Fig. 4.13i, j) with no clear distinction between 00Z and 12Z.

Alexander, Tsuda and Vincent [2002] proposed a theory to explain the latitudinal dependence of *KE* and *PE* in the lower stratosphere. They argue that as $f \to 0$

approaching the equator, the frequency spectrum of gravity waves becomes wider since the lower bound of $\hat{\omega}$ decreases as decreasing the latitude. That is the reason why larger *KE* and *PE* are seen closer to the equator (Fig. 4.11b and 4.12b). *VE* measures relatively high-frequency gravity waves, and hence it should not be so sensitive to the variation of f , in both the troposphere and the lower stratosphere. That is probably the reason why we don't see a clear latitudinal dependence of VE in Fig. 4.8.

4.3.3 Difference between the tropics and the extratropics

It is interesting that Lane et al. (2003) found a clear relation between the occurrence of deep convection at their analyzed tropical station and increased balloon ascent rate fluctuations (essentially our VE) in the lower stratosphere. Thus, the occurrence of deep convection showed a clear relation to shorter period gravity waves in the lower stratosphere. Our results agree with this point at tropical stations. But the results also indicate that, while there is an apparent relation between deep convection at mid-latitudes with VE in the troposphere, such a relation is much less apparent in the lower stratosphere. In this section, we explore a likely cause for this.

We studied the propagation dependence on the background fields by using the GROGRAT (Marks and Eckermann, 1995). In this experiment, we take NCEP/NCAR four times per day reanalysis data as the background fields for the whole month of July, 2000, and release gravity wave rays at $5\,km$ with a source spectrum that represents the "moving mountain" mechanism (Eqn. 3.5), which has been suggested as being a representation of convective sources (Alexander and Vincent, 2000; Gong et al., 2008). The $5\,km$ source altitude choice is arbitrary. We also tested source heights at $4\,km$ and $6\,km$, respectively, the results vary little, and the major features still hold.

The background properties are updated every 6 hours, and the rays are terminated after 4 days. To investigate the relationship between gravity wave propagation and the background fields, the source spectrum is fixed during the whole month with $B_m = 0.1 m^2 s^{-2}$, $c_w = 5\, m/s$ and $\lambda_x = 20 km$ in order to assure the majority of the rays released at the source level have the intrinsic frequency on the order of *10f* for mid-latitudes. The source spectra with respect to intrinsic frequencies at the source levels for two specific cases are plotted in Fig. 4.17c and d. These values are typically observed or found in simulations of convective sources (e.g., Alexander and Vincent, 2000). As a heuristic experiment, we choose these parameter values to generate a spectrum of middle-frequency gravity waves with a realistic convective source, rather than for the purpose of comparing with observations directly.

Two stations (Ponape Island, [158.22 ºE, 6.97 ºN]; Denver, CO, [255.12 ºE, 39.77 ºN]) are arbitrarily chosen to represent tropical and extratropical conditions, respectively. We carry out the simulations every six hours for the entire month of July, 2000. In Fig. 4.16, the typical ray-paths over these two stations are plotted, and Fig. 4.17 gives the corresponding vertical distribution of zonal momentum flux as a function of intrinsic phase speed as well as the mean background zonal wind profiles. Fig. 4.17 also gives corresponding source spectrum for each case. The most distinct feature at the tropical station is that many of the rays ascend into the lower stratosphere, with some of them propagating almost vertically and even penetrating through the top of the lower stratosphere. Compared to the tropical station, essentially all of the rays over the midlatitude station are terminated before reaching the lower stratosphere for this particular time. As a matter of fact, the time series of the whole month give a significant

correlation of VE in the troposphere and lower stratosphere layers at the tropical station ($r = 0.25$, 95% significant), but basically no correlation at the midlatitude station ($r = 0.035$). Several other combinations of parameters ($c_w = 15\,m/s$ and $\lambda_x = 100km$; $c_w = 20\,m/s$ and $\lambda_x = 200km$) are tested, and we still get high (low) correlations of VE between the troposphere and the lower stratosphere at the tropical (mid-latitude) stations, indicating the robustness of this result.

Close examination on Fig. 4.17 reveals the reason for this dissimilarity. The mean zonal easterlies increase steadily with height above $20\,km$ in Fig. 4.17a, so the gravity waves with negative intrinsic frequencies are refracted (or "Doppler shifted") toward long vertical wavelength (Alexander, 1998). Since the vertical group velocity C_{gz} has the following form:

$$C_{gz} = \frac{-m(\hat{\omega}^2 - f^2)}{\hat{\omega}(k^2 + m^2 + \alpha^2)} \qquad (5),$$

$C_{gz} \to 0$ when the vertical wavelength is extremely long. Here k and m are the horizontal and vertical wavenumbers, respectively, and $\alpha = 1/2H_s$, where H_s is the density scale height. Waves with positive intrinsic frequencies do not suffer from this refraction effect, and can therefore penetrate the top of the lower stratosphere. At the midlatitude station, as seen in Fig. 4.17b, the "dissipated" waves are removed by critical-level filtering, while "vertically stalled" waves are eliminated by wave refraction. During summer time, the structure of westerlies in the troposphere and easterlies in the lower stratosphere in the extratropics effectively removes gravity waves generated below. In the tropics, however, easterlies with weak vertical shear dominate the whole troposphere through the bottom of

the lower stratosphere. Although modulated by the QBO, the lower stratosphere wind shear usually only removes one sign of the phase velocity spectrum by refracting the waves horizontally, and leaving the other gravity waves to propagate freely upward.

These results are in agreement with the consistency of VE in the troposphere and lower stratosphere in the tropics, and the relative lack of similarity at mid-latitudes. Hence, it provides a plausible explanation for the much weaker diurnal cycle of VE in the lower stratosphere at mid-latitudes compared with that in the troposphere. However, this feature can also be caused by other reasons. For example, it takes a finite time for gravity waves generated in the troposphere to propagate into the lower stratosphere and this time varies with changing background values. Therefore, we may miss the diurnal cycle in the lower stratosphere from twice daily measurements. The vertical wavelengths of convectively generated gravity waves (6.9 km is the upper limit in our study) in the lower stratosphere might be too long and fall out of our "observational window". Careful examination shows that many of balloons get lost or stop working before they enter the lower stratosphere during severe weather events, which imposes an "observational bias" onto our observations.

It seems that the convection signal becomes very weak in the lower stratosphere in VE as well as the vertical wavelength time series except for the vertical wavelength south of 40 ºN. We think that the "observational window", "measurement bias" and the "ducting" effects might also help to explain this feature. Compared to VE, the apparent dominant vertical wavelength is not that sensitive to these effects as long as there are some gravity waves propagating vertically into the lower stratosphere, and that might be

the reason why we can still see summer peaks of vertical wavelength in the lower stratosphere south of 40 ℕ, though this signature is largely suppressed north of 40 ℕ.

4.4. Gravity wave frequency spectra

Wang et al. (2005) derived the intrinsic frequency $\hat{\omega}$ from the axial-ratio of the wind hodograph (Eqn. 2.4). Here, by applying Eqns. (4.4) and (4.5), we can independently obtain information of $\hat{\omega}$ through the ratio of $\overline{KE}/\overline{PE}$ and $\overline{VE}/\overline{PE}$. The nine-year (1998-2006) averaged values of $\hat{\omega}$ as a function of latitude are given in Fig. 1 of *Geller and Gong (2009)*, where $\hat{\omega}$ derived from $\overline{KE}/\overline{PE}$ is near constant throughout the latitude in the troposphere, but decreases with the increasing latitude in the lower stratosphere. This latitudinal dependence is crucial for us to achieve good results from a simple model. The $\hat{\omega}$ derived from $\overline{VE}/\overline{PE}$ are significantly larger than the ones derived from the ratio of $\overline{KE}/\overline{PE}$.

Closer inspections of the $\hat{\omega}$ derived from $\overline{VE}/\overline{PE}$ (Fig. 4.18) reveals that the temporal variations of $\hat{\omega}$ is largely dependent on $\bar{N}^2$ (not shown), as expected from Eqn. (4.5). However, the temporal-latitudinal variations of $\overline{VE}/\overline{PE}$ also gives summer peaks in both the troposphere and the lower stratosphere, as shown in Fig. 4.19. Besides, $\bar{N}^2$ barely shows a diurnal variation in the troposphere but $\overline{VE}/\overline{PE}$ does. Hence, we have even more

confidence that *VE* is indeed more sensitive to convectively generated relatively higher frequency gravity waves.

It is interesting to further investigate the correlations among the three energies, which are shown in the top panels of Fig. 4.20 and 4.21. In the troposphere, the observed correlation coefficient of $\overline{KE}$ and $\overline{VE}$ (*corr(KE,VE)* hereinafter and so forth) is low (centered at around 0.1) as expected, and *corr(KE,PE)* is relatively high (centered around 0.4). *Corr(PE,VE)* is relatively low also, centered at around 0.1. Compared to the troposphere, the correlation coefficients are much wider spread. This can be explained by the fact that $\hat{\omega}$ derived from $\overline{KE}/\overline{PE}$ has a marked latitudinal dependence in the lower stratosphere but not in the troposphere (Fig. 1 of Geller and Gong, 2009).

A simple model is implemented here to study the frequency spectra information that lies behind the correlations. We compute 500 cases, each of which has 60 superposed gravity waves where the $\hat{\omega}$ is randomly chosen from *2f* to *20f*, the latitude of each case is also randomly chosen from $5^{\circ} N$ to $70^{\circ} N$. To further closely represent the observational conditions, the vertical wavenumber *m* is selected according to the observed probability density function, and the horizontal wavelength is constrained to be within $10-2000km$. We then use both the hydrostatic equations (4.1) - (4.3) and non-hydrostatic equations (4.6) - (4.8) to get the energy information for each wave, and calculate the histogram of the correlation coefficients among the three energy forms.

Different spectra of wave amplitude with respect to $\hat{\omega}$ are tried to reach the frequency spectra that gives the best-fit to the three correlation distributions. In the troposphere, the "best-fit" spectrum has a constant amplitude when $\hat{\omega} < 8f$, and the amplitude is scaled

by $\hat{\omega}^{-1.2}$ when $\hat{\omega} \geq 8f$. If we use constant amplitude spectrum, the *Corr (PE, VE)* would be much larger than the observed ones. This can be understood since this spectrum amplifies the high frequency waves. In the extreme situation, if $\hat{\omega} \to N$, the wave becomes a pure buoyancy oscillation, and *VE* and *PE* should be perfectly correlated. If we use a spectrum where the amplitude decreases linearly with the increase of $\hat{\omega}$ (i.e., scaled by $\hat{\omega}^{-1}$) , the *Corr (PE, VE)* is compared reasonably with observations, but *Corr (KE, PE)* is much larger than the observations. For this case, the low frequency gravity waves become too dominant, if we consider $\hat{\omega} \to f$, *KE* and *PE* are both large since the waves become essentially inertial oscillations, and $m \to 0$ also. These two extreme situations motivate us to try the "best-fit" spectrum. We also tried other exponents (-0.8, -1.0, -1.5, -2.0), and it turns out -1.2 gives the best results that are comparable to the observations. The "best-fit" frequency spectrum coincides with the frequency spectra in *VanZandt (1982)* and *Fritts and VanZandt (1987)*, and the exponent -1.2 is consistent with what has been found in *Wang (2003)*, where he used the same dataset, but with completely different methods.

In the lower stratosphere, the simulated distributions are too narrow for all the spectra we tested. However, as suggested by the observed $\hat{\omega}$ derived from $\overline{KE} \big/ \overline{PE}$, which has a marked latitudinal dependence in the lower stratosphere, it's reasonable for us to add this factor into consideration. The "best-fit" spectrum we get has similar properties with the one in the troposphere, but the high frequency part is scaled by $\hat{\omega}^{-2}$. The separation point is now not fixed at $8f$, but changes as a linear function with latitude. This set of spectra simulates comparable results to the observations in terms of both the centers and the

spreads. *Wang (2003)* showed that the exponent in the lower stratosphere ranges from -2 to -4 in the observations. Our simulation exponent again falls into this region. The non-hydrostatic relationships yield very similar results for both the troposphere and the lower stratosphere.

4.5. Conclusions and discussions

The "vertical fluctuation energy" is defined in a similar fashion to the definition of kinetic and potential energy densities. The apparent dominant vertical wavelength, derived from the low-pass filtered perturbation field of the ascent rate with balloon oscillation frequency removed, is also analyzed. The diurnal, seasonal and interannual variations of both variables are studied and compared with $\overline{KE}$ and $\overline{PE}$. The new variable $\overline{VE}$ is quite sensitive to relatively high-frequency gravity waves, as is the apparent dominant vertical wavelength. We believe these waves are significantly excited by convective sources during warm seasons.

The time series of $\overline{VE}$ do not show comparable features in the tropics to those in the mid-latitudes in terms of the diurnal and seasonal variations, but they are closely related to convective clouds and precipitations (Fig. 4.1) in both the troposphere and lower stratosphere. *Lane et al. [2003]* found local-afternoon maxima in the lower stratosphere at one tropical station with extensive observations during a field campaign. With only 00Z and 12Z observations, we can not evaluate this feature here.

The diurnal variations of both $\overline{VE}$ and the dominant vertical wavelength of w' in the troposphere peak at times when local convection is favored (Fig. 4.2 and 4.3), but the

signatures are much weaker in the lower stratosphere over the contiguous US. The possible reasons for the difference between *Lane et al. [2003]* and ours are as follows. First, they have much more frequent observations during the campaign, and secondly, their campaign was taken at a tropical station, while section 3.3 explains the different propagation properties between tropics and the mid-latitudes that would cause different results.

$\overline{VE}$ peaks during summer for most of the contiguous US stations in the troposphere, again suggesting the convection as the major source, but dominantly peaks in the winter time in the lower stratosphere (Fig. 4.8), with some indications of secondary maxima in summer. The apparent dominant vertical wavelength shows a similar pattern, but also peaks in summer time in the lower stratosphere south of 40 ºN (Fig. 4.9). Moreover, the vertical wavelengths derived from the ascent rate fluctuations have a much larger latitudinal dependence with maxima at mid-latitudes in the troposphere. Several possible reasons to explain the differences between the two layers for both diurnal and seasonal cycles are proposed, which relate to the "observational window", "measurement bias" and "ducting effect". Our numerical experiments suggest the "ducting effect" as a major candidate. From observations, we find that $\overline{PE}$ shows a similar diurnal signature to $\overline{VE}$, and the vertical wavelength derived from $T'/\overline{T}$ agrees well with that of w' in the lower stratosphere. This indicates that the gravity wave spectrum in the T' field at least partly overlaps with that in the w' field.

A numerical experiment is carried out to try to elucidate the dissimilarities of $\overline{VE}$ in the lower stratosphere at different latitudes. The model results imply that it is mainly the

background wind and wind shear that causes waves propagating differently in the tropics versus the extratropics (Fig. 4.16 and 4.17). In our experiment, gravity waves with the zonal momentum flux peaking at an intrinsic phase speed of $10-20ms^{-1}$ propagates the highest, and this feature is also documented by others (e.g., Beres et al., 2002). This result has important implications for parameterizations of convectively generated gravity waves in that the source spectrum in the tropics is essentially more important than that in the mid-latitudes. That means the parameterization of convective sources needs to be more robust and representative of the true spectrum in the tropics, while it may be a less important issue in the mid-latitudes since the mean flow shapes the spectrum during the gravity wave propagations.

Both theories and the radiosonde observations indicate that $\overline{KE}$ is most sensitive to low frequency inertial gravity waves, $\overline{VE}$ is most sensitive to higher frequency waves, and $\overline{PE}$ is in between. Furthermore, the ratio between $\overline{KE}$ and $\overline{PE}$, and $\overline{VE}$ and $\overline{PE}$ can be used to derive the intrinsic frequency information. Although the values of $\hat{\omega}$ derived from VE/PE seems to be too high ($1/4 - 1/2\,N$), this is because the high frequency waves dominate the averaging process of the ratio inherently, the spatial and temporal patterns coincide with convective activities, again demonstrates convection as a source for these higher-frequency waves (see details in Geller and Gong, 2009). A simple model is implemented to simulate the observed correlations among three types of energies. Various types of frequency spectra are tested, and the "best-fit" frequency spectra coincide well with those derived from other independent techniques (e.g., Wang, 2003) or dataset (e.g., VanZandt, 1987).

This chapter indicates convection as one source for generating gravity waves that are seen in ascent rate perturbations from radiosonde profiles. It is likely that some of the features seen might also be related to spontaneous emission from jet streaks, especially during winter time. Thus, radiosonde measurements being already widespread over the US gives a convenient way to analyze the characteristics of convectively generated gravity waves, as well as those emitted through spontaneous emissions from jet streaks.

WBAN	*Corr (VE_tropo, VE_strato)*	*Corr (VE_tropo, OLR)*	*Corr (VE_strato, OLR)*	*Corr (VE_tropo, CPR)*	*Corr (VE_strato, CPR)*
40308	**0.325**	**-0.342**	0.052	0.115	**0.355**
40309	**0.392**	-0.126	**-0.351**	-0.021	-0.214
40504	**0.375**	**-0.530**	**-0.286**	**0.375**	0.010
40505	**0.308**	-0.233	**0.370**	-0.009	-0.197
40710	**0.813**	**-0.513**	**-0.358**	**0.291**	**0.330**

Table 4.1: Correlation coefficients between VEs in the troposphere (VE_tropo) and the lower stratosphere (VE_strato), VE and outgoing long-wave radiation (OLR), and VE and convective precipitation anomaly (CPR) for five tropical stations. Values with confidence level greater than 95% are in bold.

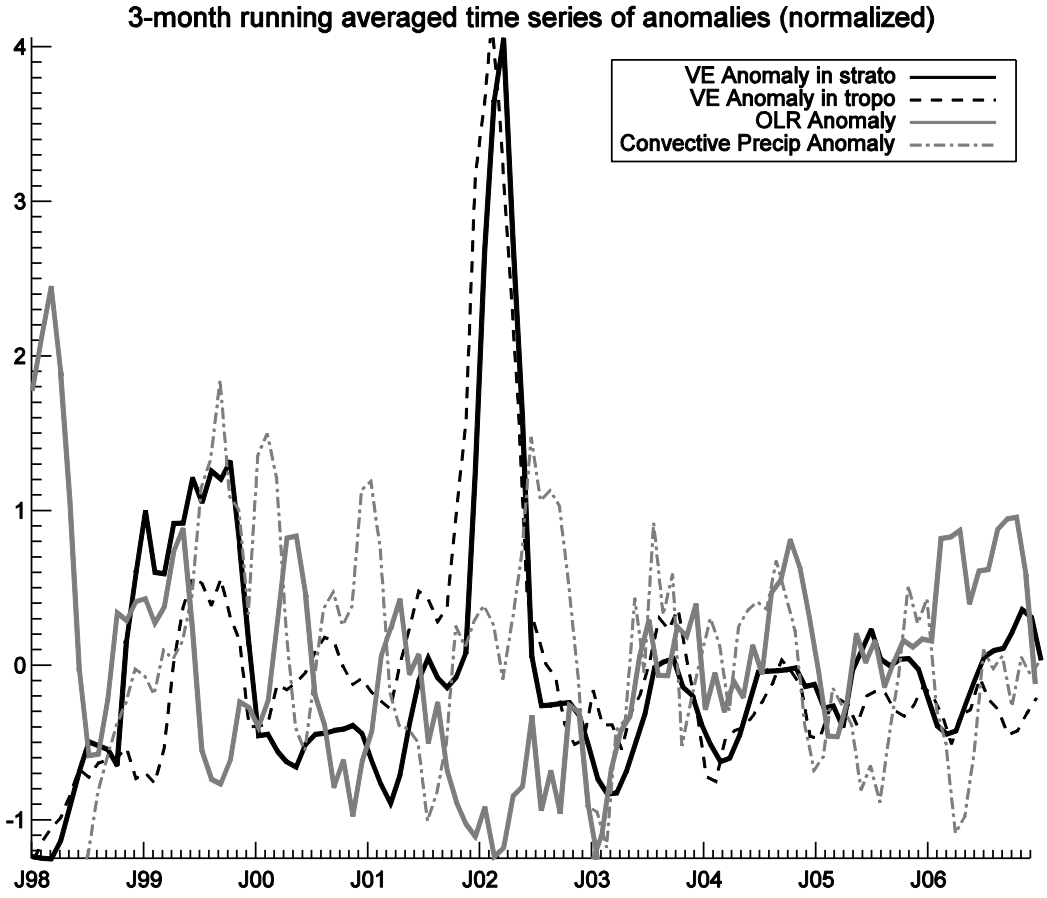

Figure 4.1: Normalized monthly mean of anomalies of VE in lower stratosphere (black solid), troposphere (black dashed), OLR (grey solid) and convective precipitation at the surface (grey dash-dotted) over Majuro/Marshall Island [171.38 ºE, 7.08 ºN]. A 3-month running window has been applied to the time series.

Troposphere

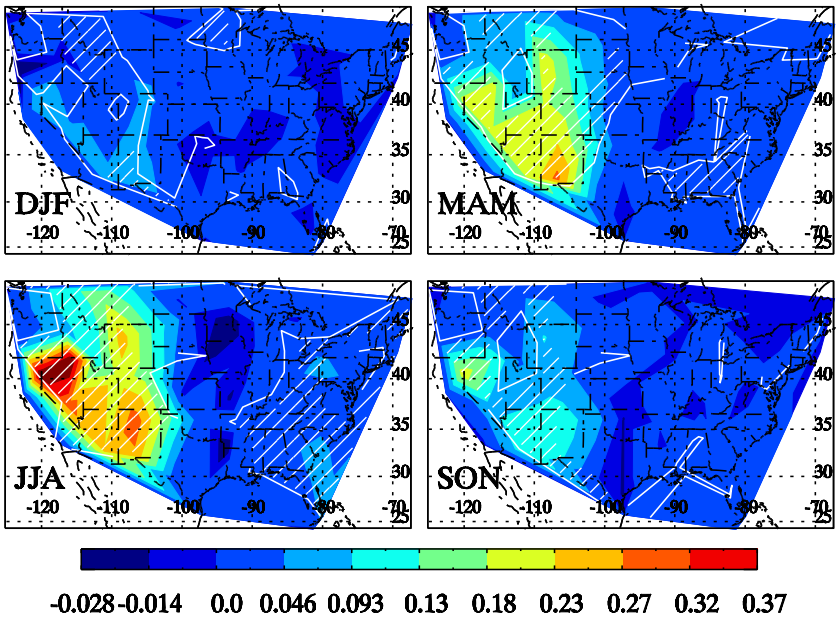

a

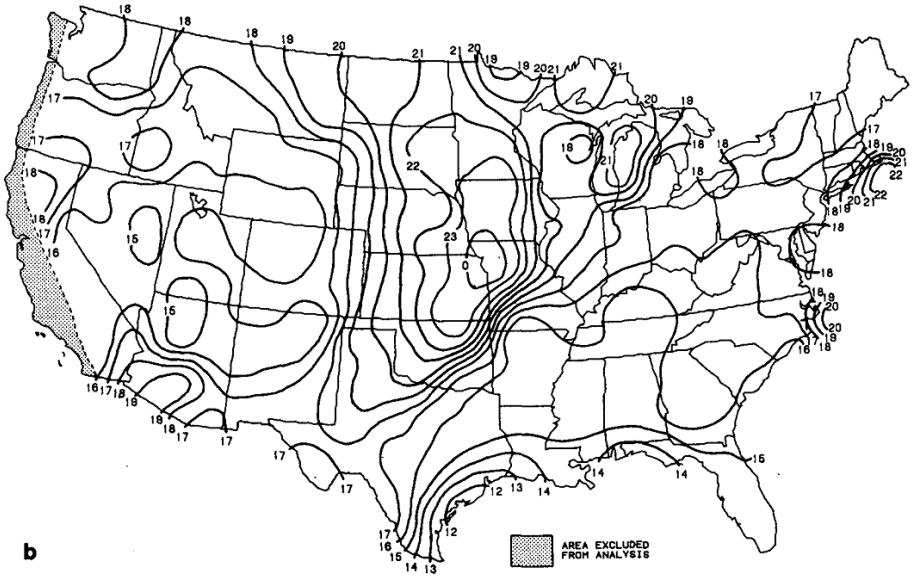

b

Lower Stratosphere

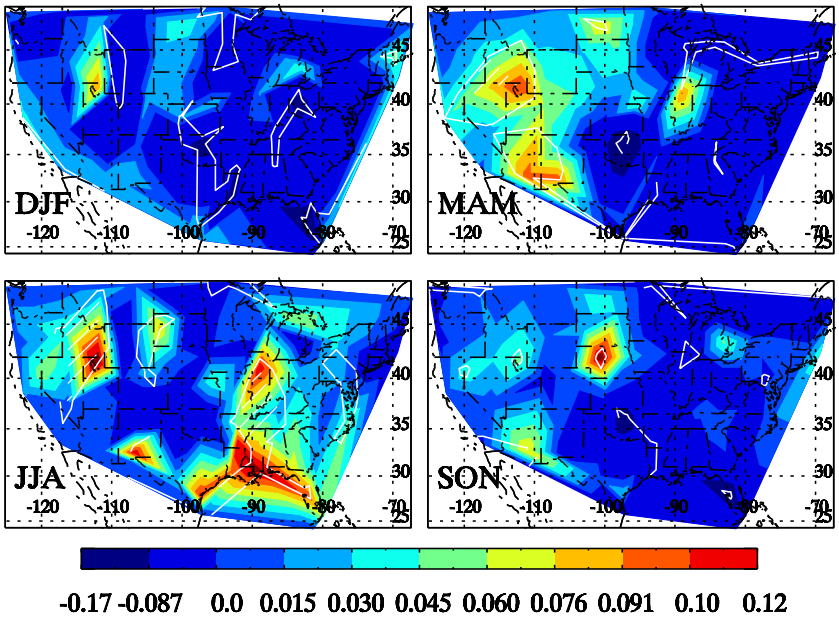

c

Figure 4.2: Diurnal variation (00Z – 12Z) of vertical energy density over contiguous US during four seasons averaged over 1998 – 2006 for the troposphere (a) and the lower stratosphere (c). The white-line shaded area passed the 95% significant test. Panel (b) is Fig. 3b adapted from *Easterling and Robinson (1985)*, where they contoured the summer pattern of the time of maximum activity derived from the 1st harmonic of hourly thunderstorm activity in the contiguous US.

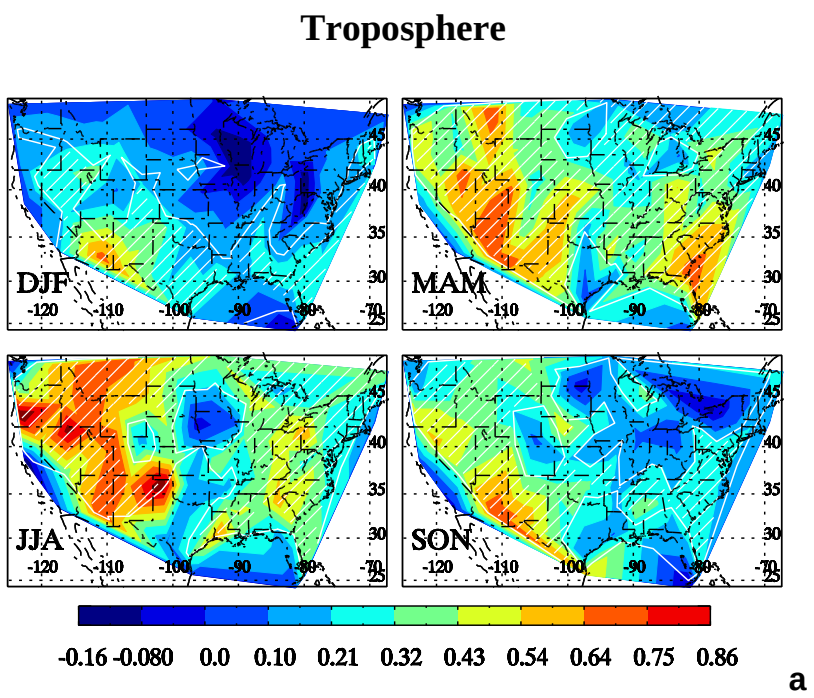

Figure 4.3: Same with Fig. 4.2 (a) (c), except for the most dominant vertical wavelength in the troposphere (a) and the lower stratosphere (b).

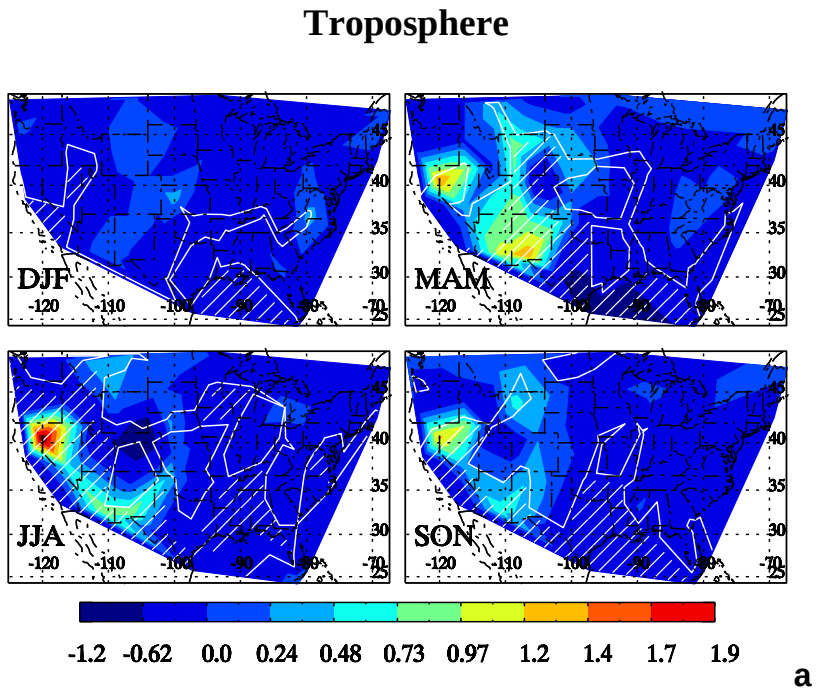

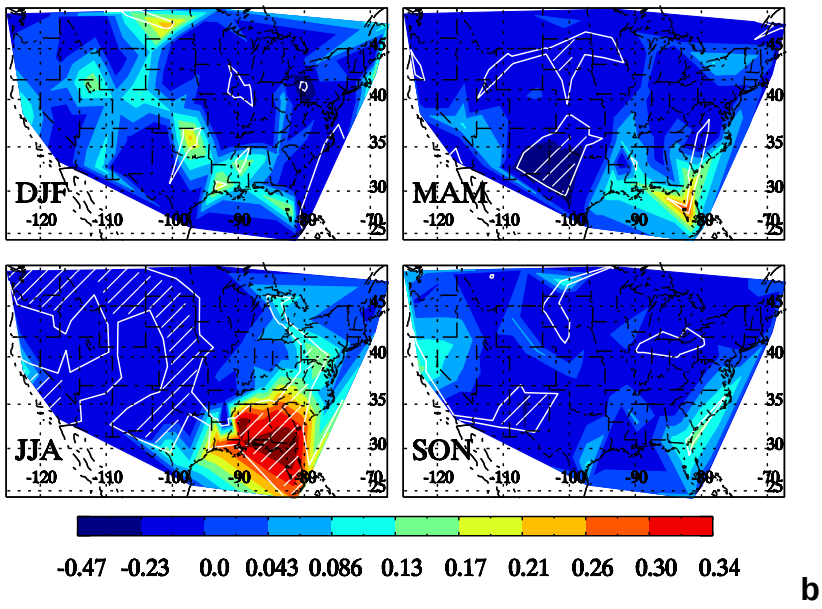

Figure 4.4: Same with Fig. 4.3, except for PE.

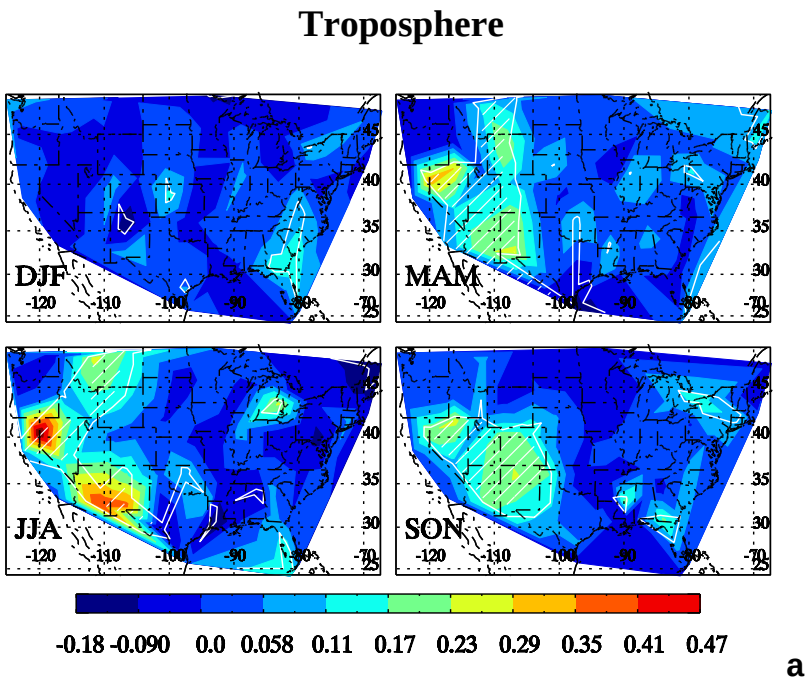

Figure 4.5: Same with Fig. 4.3, except for the most dominant vertical wavelength derived from $T'/\overline{T}$.

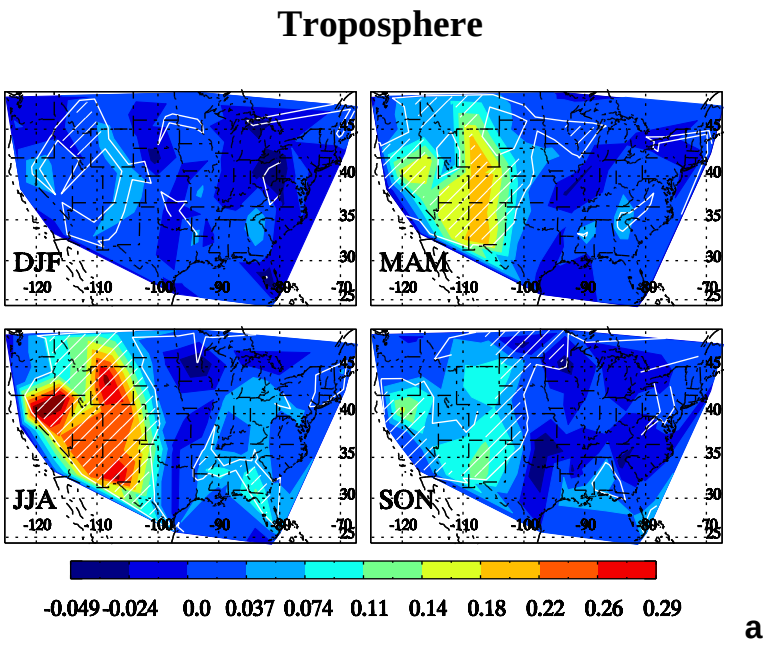

Figure 4.6: Same with Fig. 4.2 (a) (c), except the band-passed ascent rate perturbations are used, without removing balloon oscillation component, and without excluding the trapped-wave profiles.

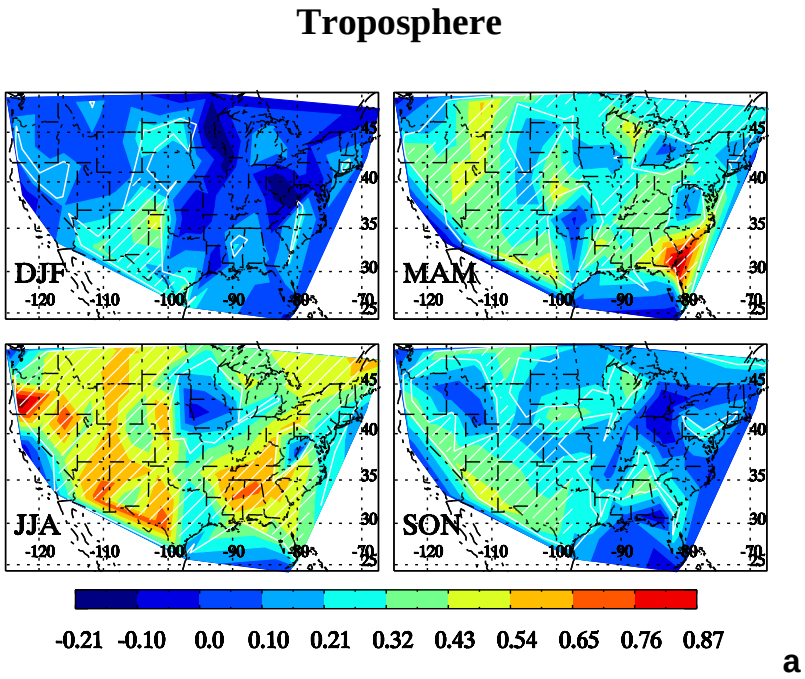

Figure 4.7: Same with Fig. 4.6, except for the apparent dominant vertical wavelength.

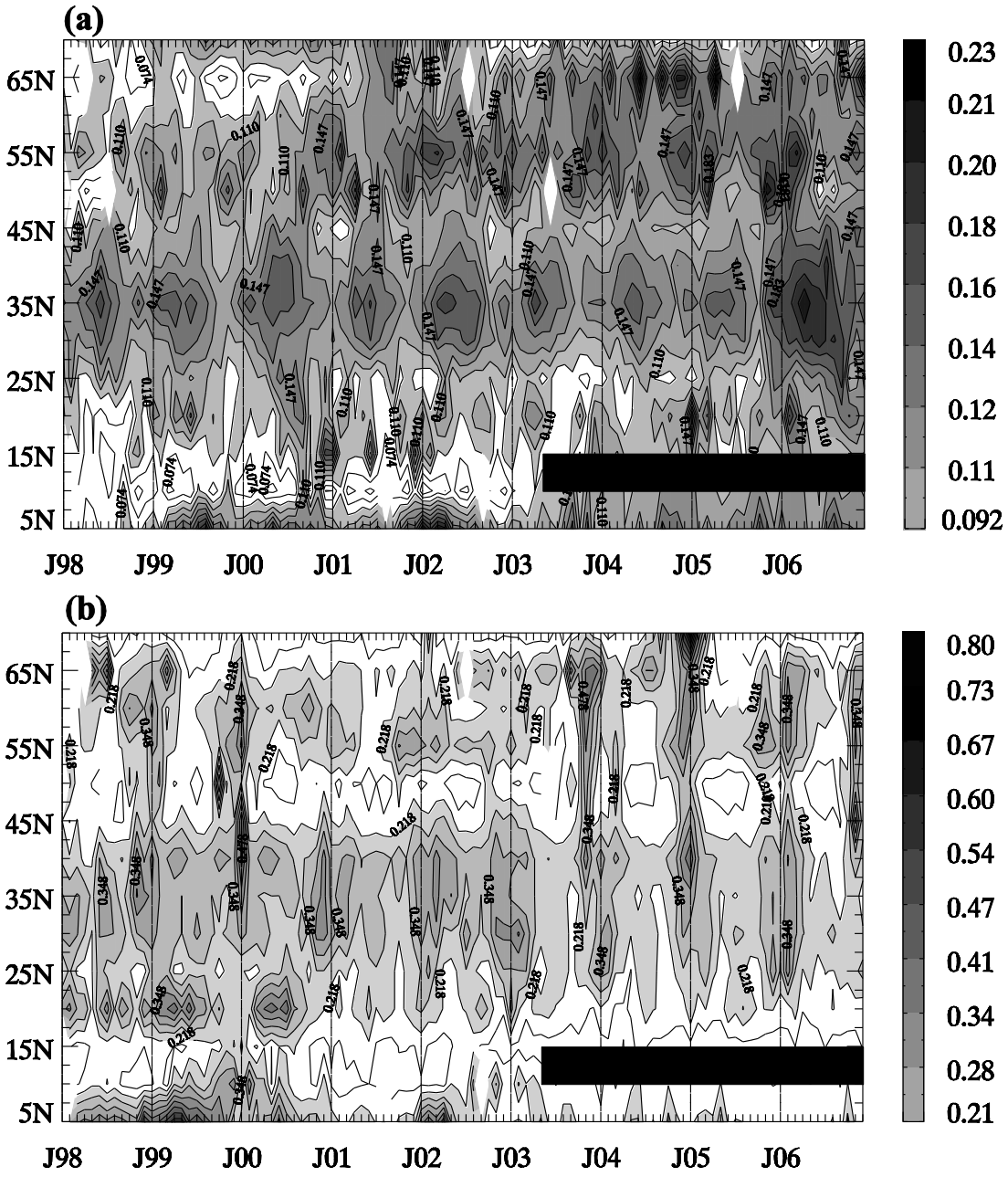

Figure 4.8: Time series of VE (J/kg) in the troposphere (a) and the lower stratosphere (b). The values are averaged within 5 °bins from 5 ℃N to 70 ℃N. The 5 °- 10 ℃N, 25 °- 50 ℃N and 55 °- 70 ℃N bins roughly correspond to tropical western Pacific islands, contiguous US and Alaska stations, respectively. Values below 0.092 J/kg and 0.21 J/kg are not shaded for (a) and (b), respectively. Missing value area is marked with black.

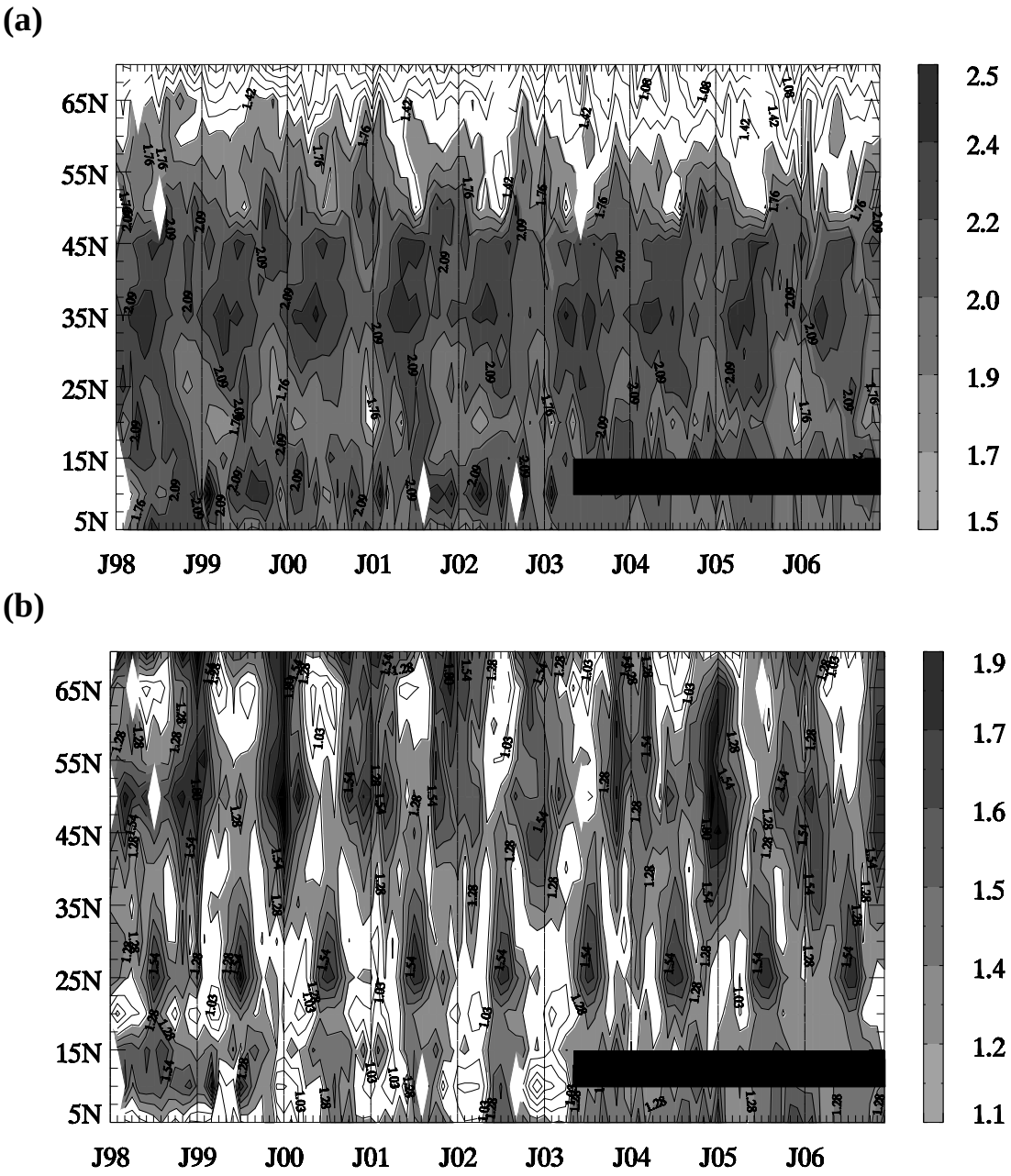

Figure 4.9: Same with Fig. 4.8, except for the apparent dominant vertical wavelength derived from *w'*. The values are processed in the same way of Fig. 4. Values below $1.5\,km$ and $1.1\,km$ are not shaded for (a) and (b), respectively.

(a)

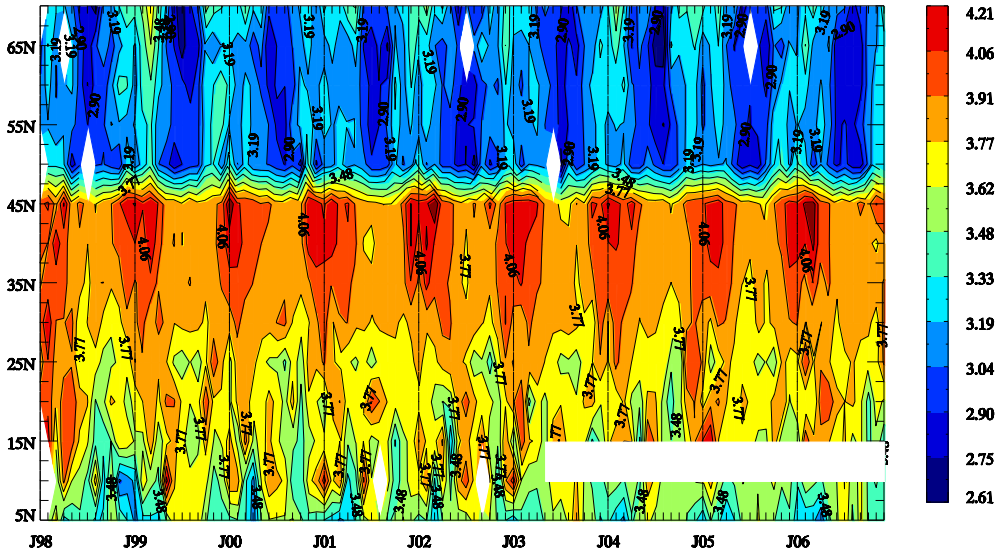

(b)

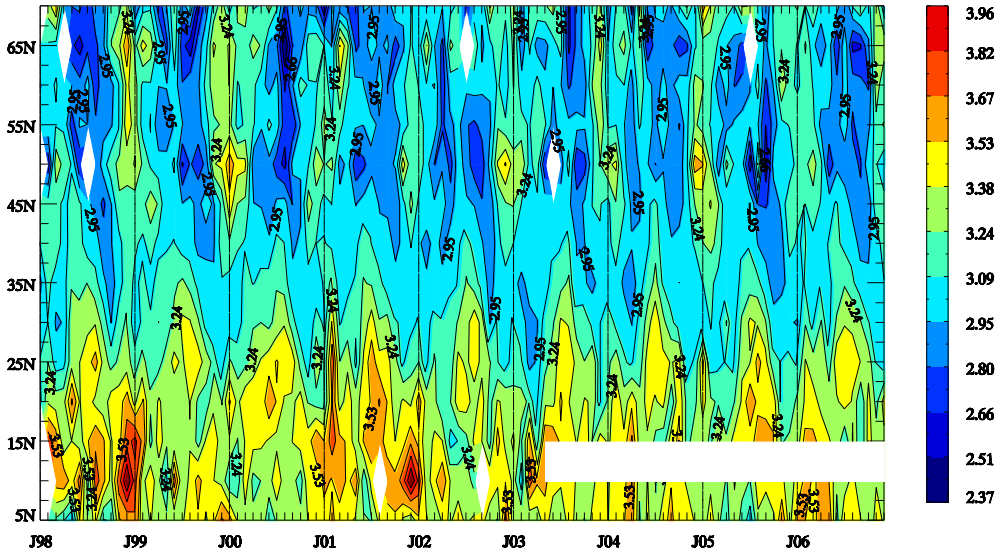

Figure 4.10: Same with Fig. 4.9, except for the dominant vertical wavelength derived from $T'/\overline{T}$.

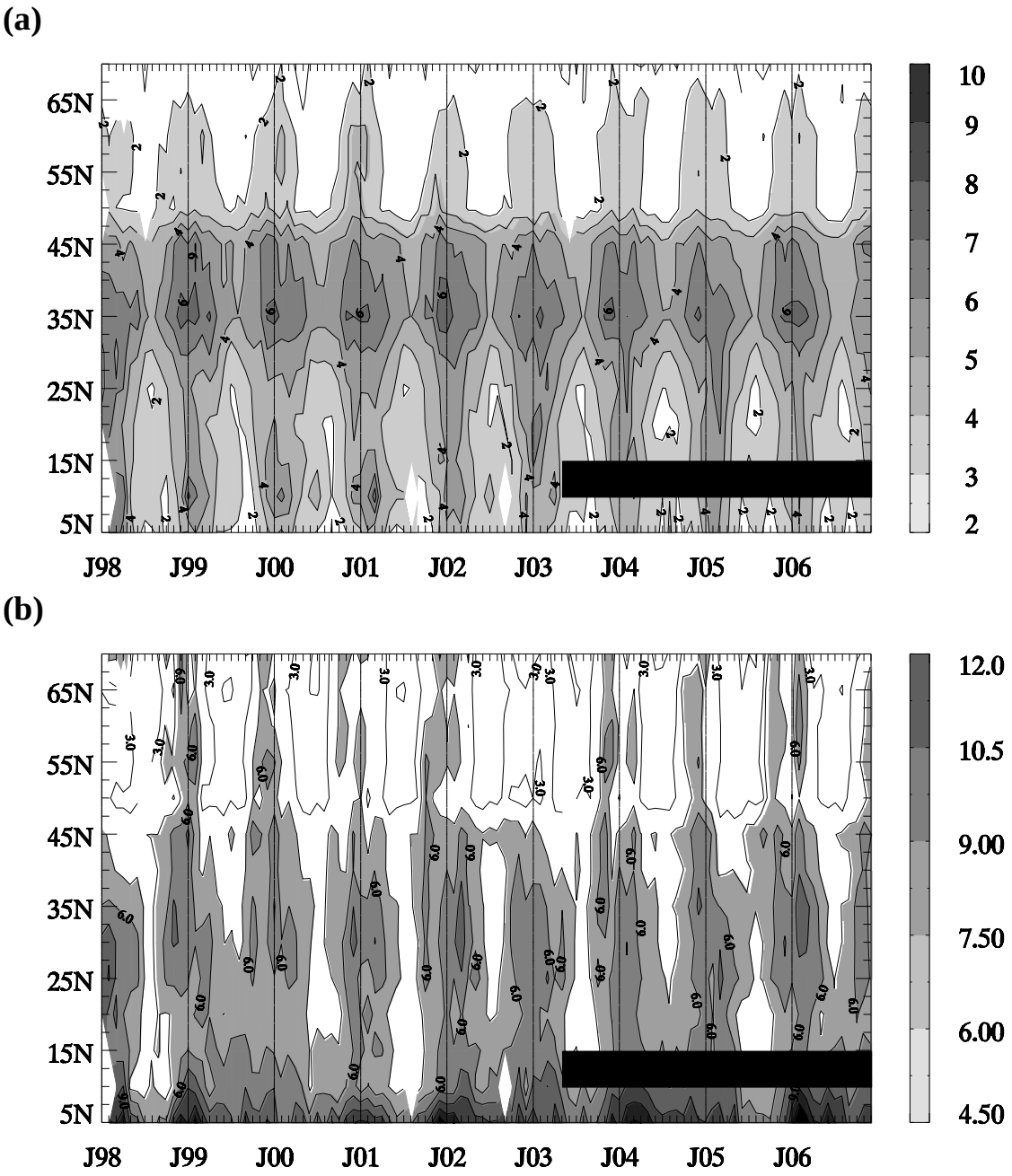

Figure 4.11: Same with Fig. 4.8, except for KE. Values below 2 J/kg and 4.5 J/kg are not shaded for (a) and (b), respectively.

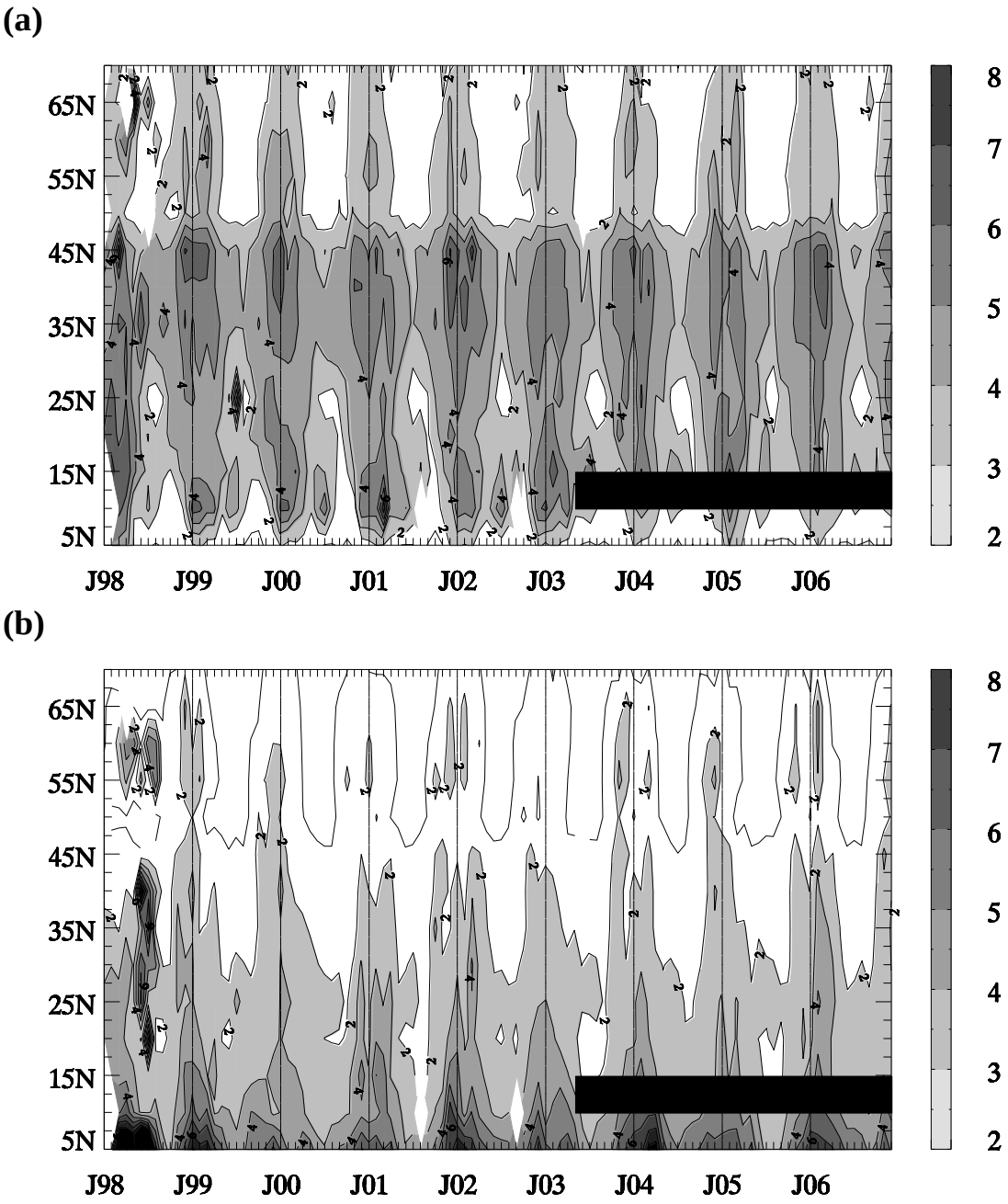

Figure 4.12: Same with Fig. 4.8, except for PE. Values below 2 J/kg are not shaded.

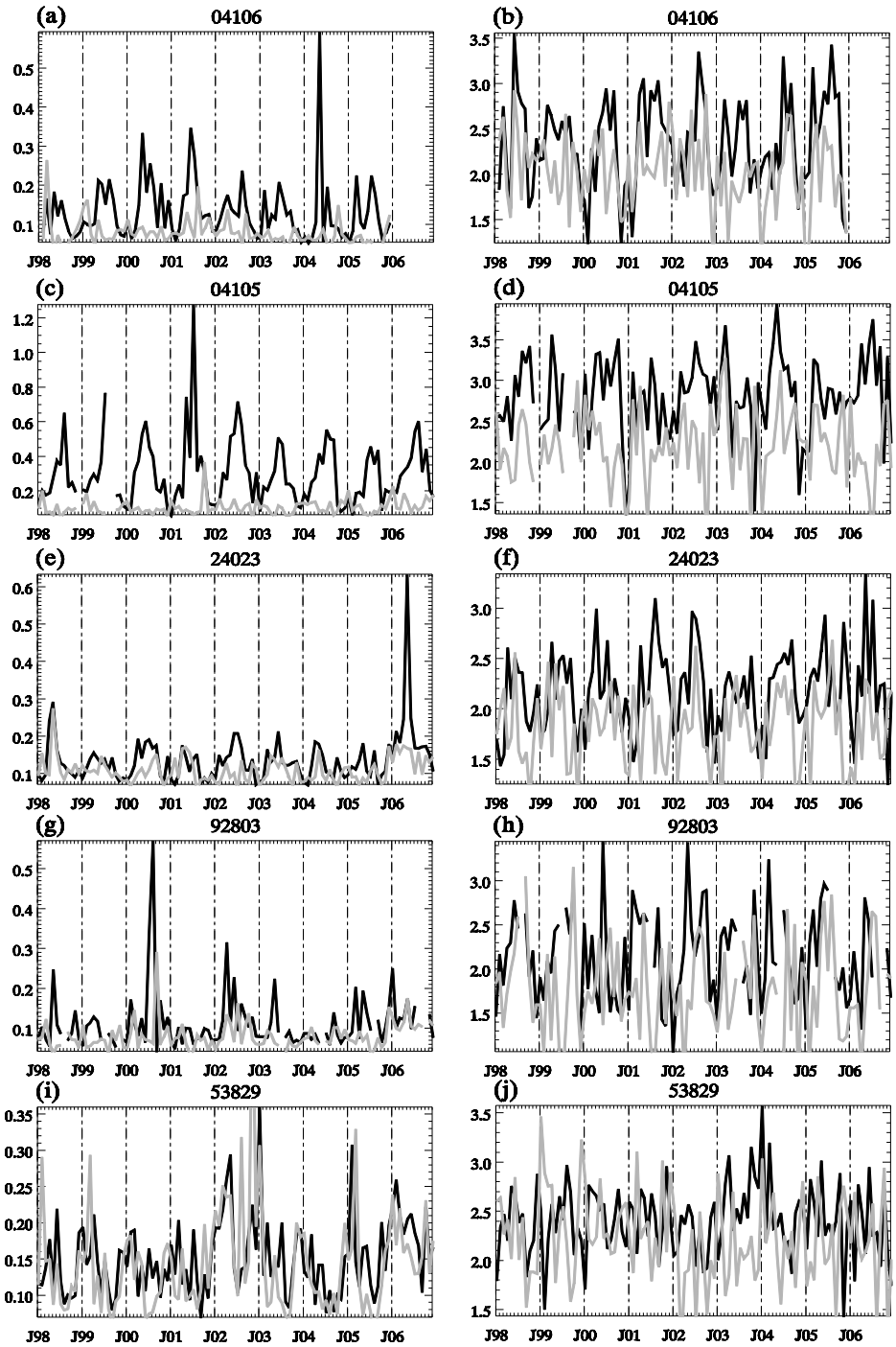

Figure 4.13: Time series of vertical energy (left) and apparent dominant vertical wavelength derived from *w'* (right) at 00Z (black) and 12Z (grey) for a Western coast station Spokane Intnl. Apt., WA [242.37 ºE, 47.68 ºN] (a, b), a Rocky Mountain station Elko, NV [244.27 ºE, 40.87 ºN] (c, d), a Great plain station North Platte, NE [259.32 ºE, 41.13 ºN] (e, f), an eastern US station Peachtree City, GA [275.44 ºE, 33.35 ºN] (g, h), and another eastern US station Blacksburg, VA [279.59 ºE, 37.2 ºN] (i, j).

(a)

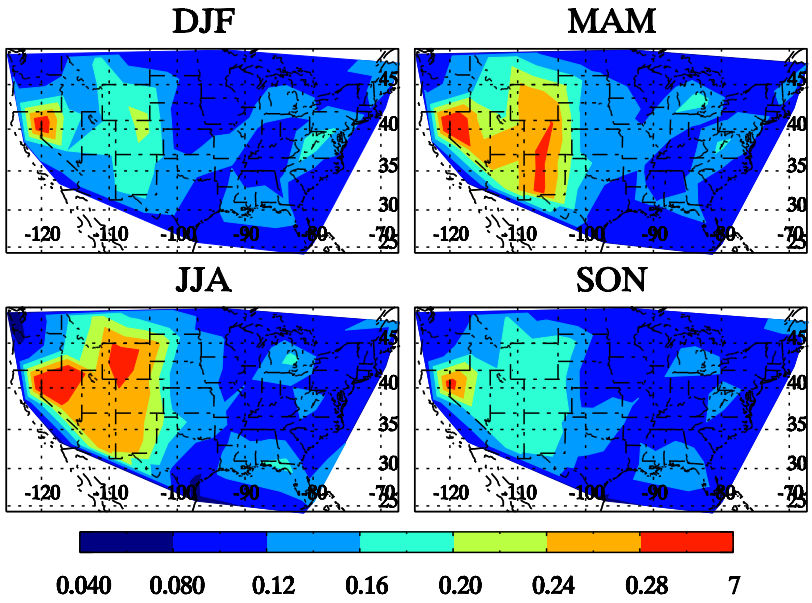

(b)

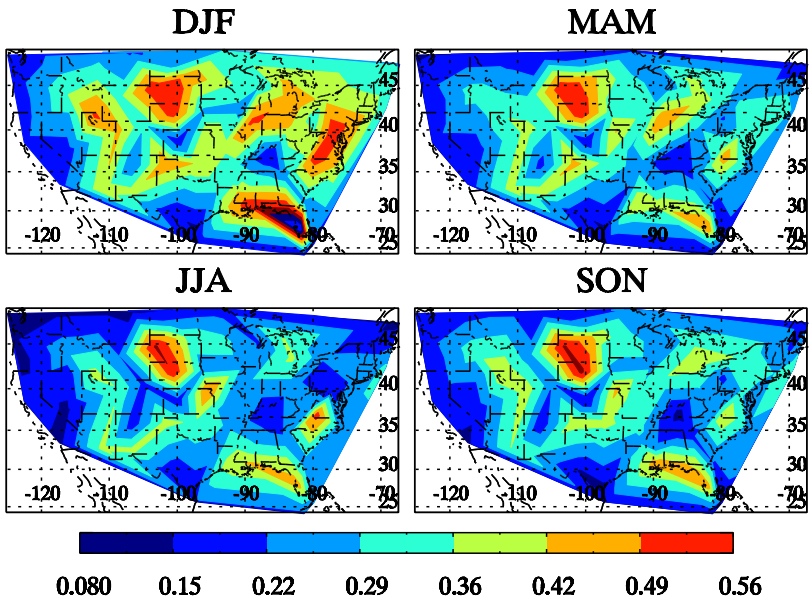

Figure 4.14: Spatial variations of VE in different seasons in the troposphere (a) and the lower stratosphere (b).

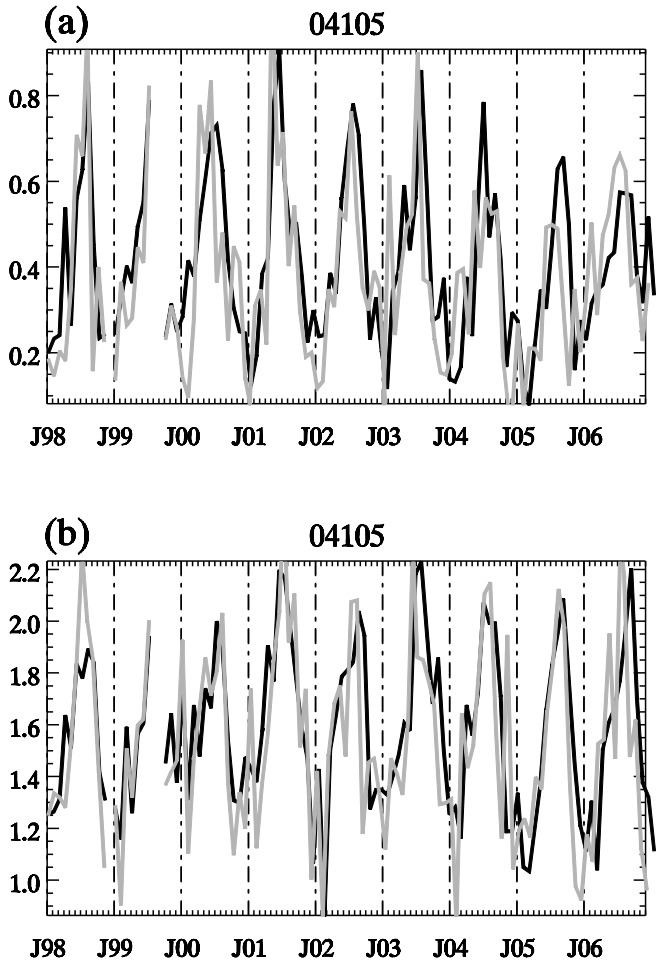

Figure 4.15: Time series of VE (a) and the apparent dominant vertical wavelength for the station Elko, NV [244.27 ºE, 40.87 ºN] in the troposphere with (black) and without (grey) removing the trapped-wave profiles.

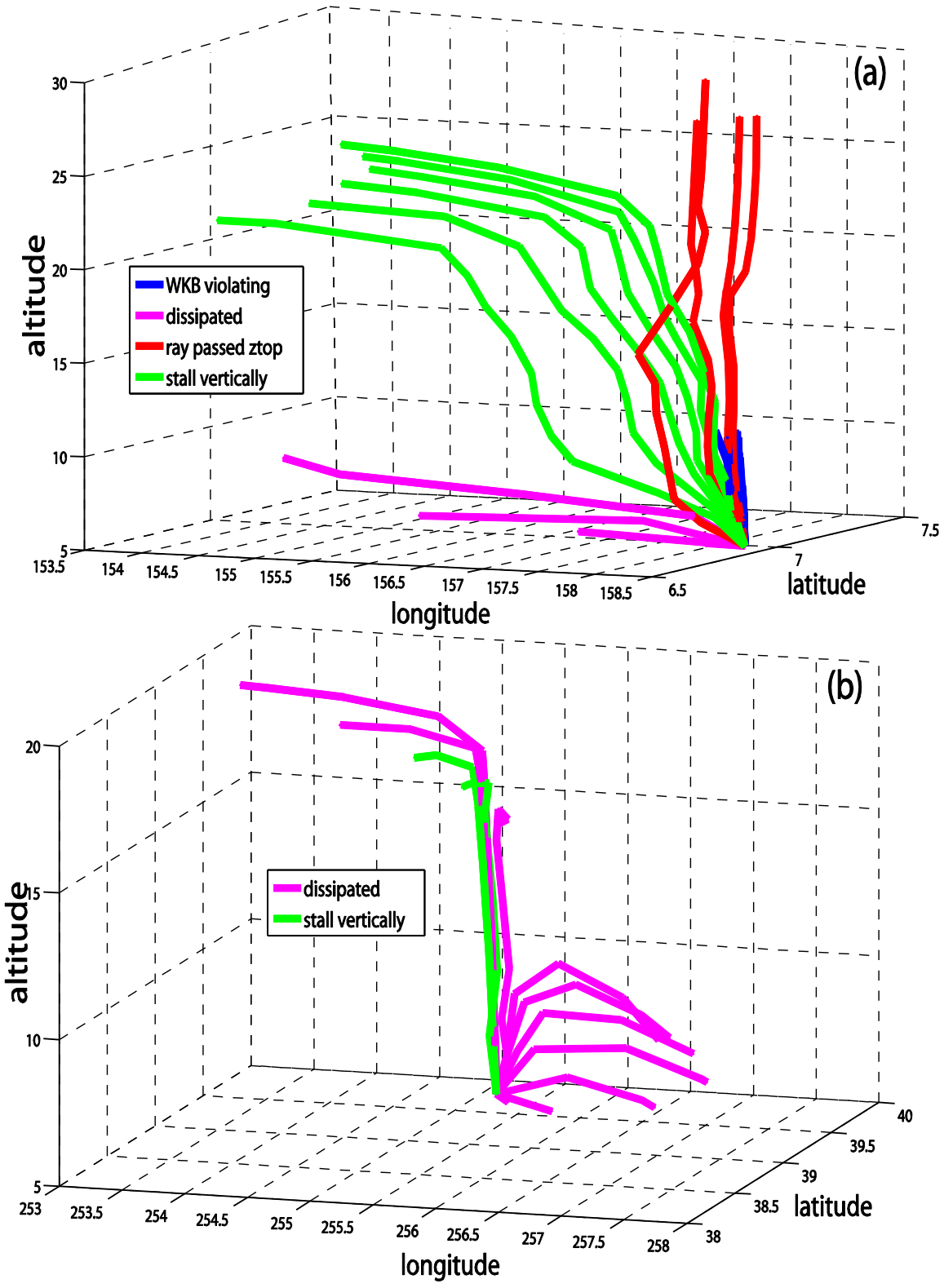

Figure 4.16: Typical ray paths during July, 2000 experiments over (a) Ponape Island, [158.22 ℃E, 6.97 ℃N] and (b) Denver, CO [255.12 ℃E, 39.77 ℃N].

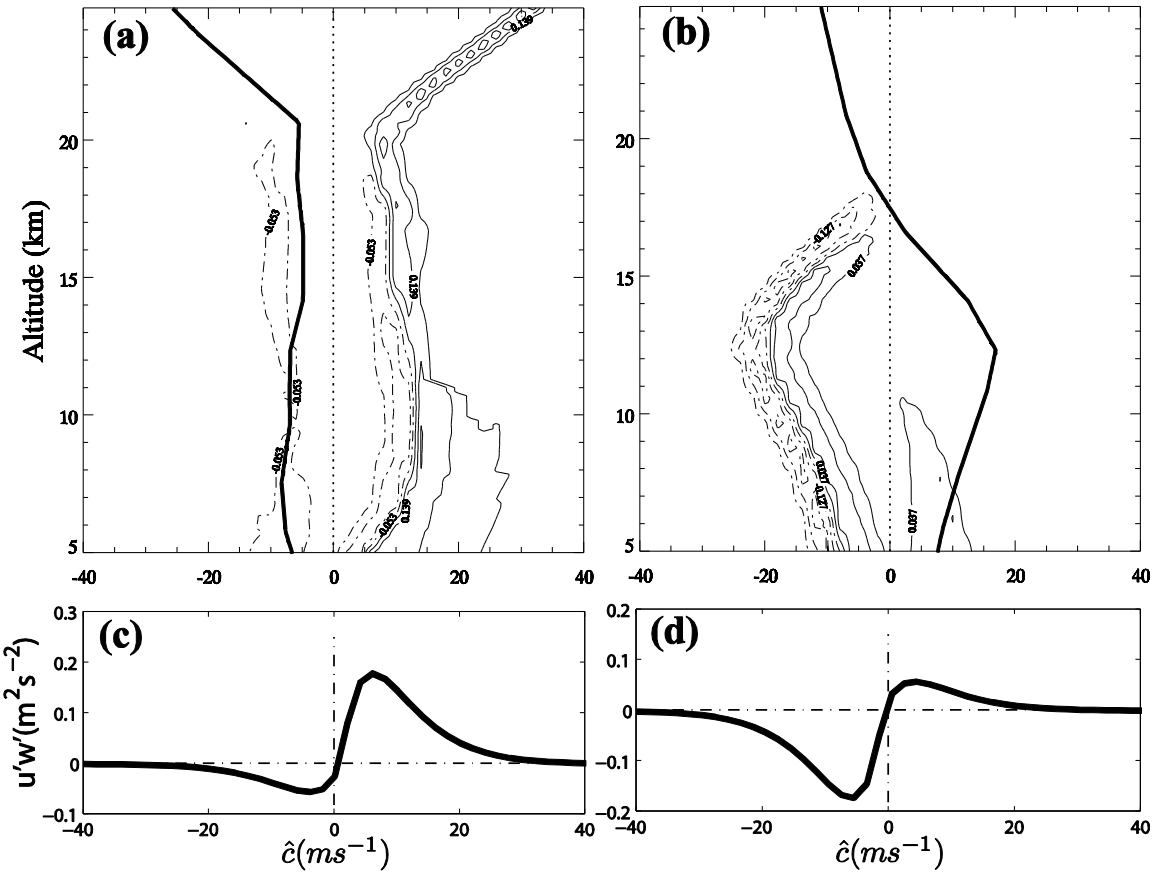

Figure 4.17: Zonal momentum flux (dash-dot: negative; solid: positive) spectra and mean background zonal winds (bold solid) for the cases in Fig. 7 of Ponape Island (a) and Denver, CO (b). The contour range and the interval are [-0.244, 0.330] m^2/s^2 and 0.096 for (a), and [-0.292, -.202] m^2/s^2 and 0.082 for (b). (c) and (d) give the corresponding source spectrum for each case.

(a)

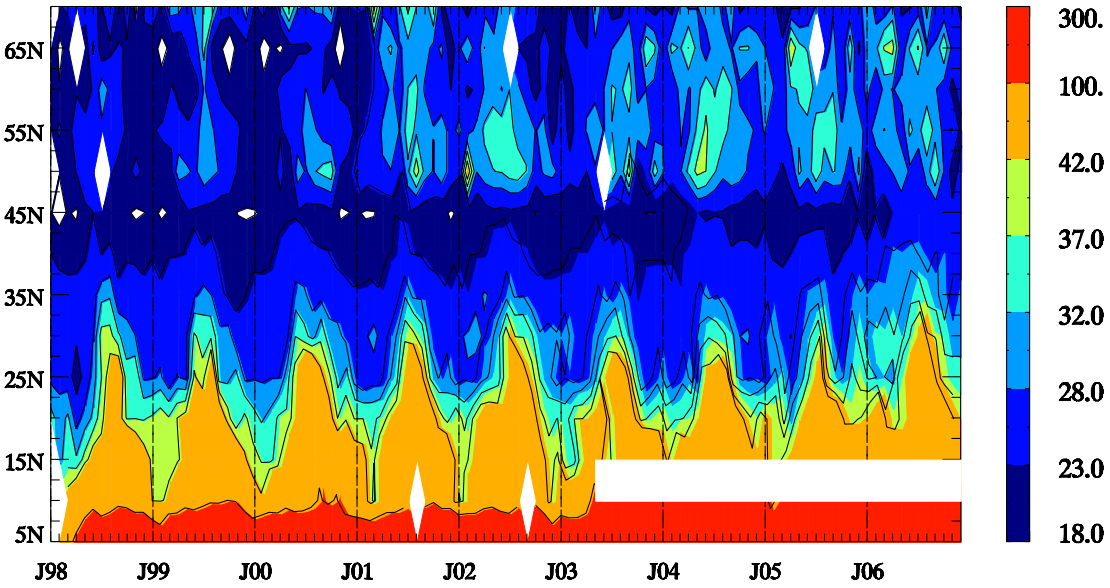

(b)

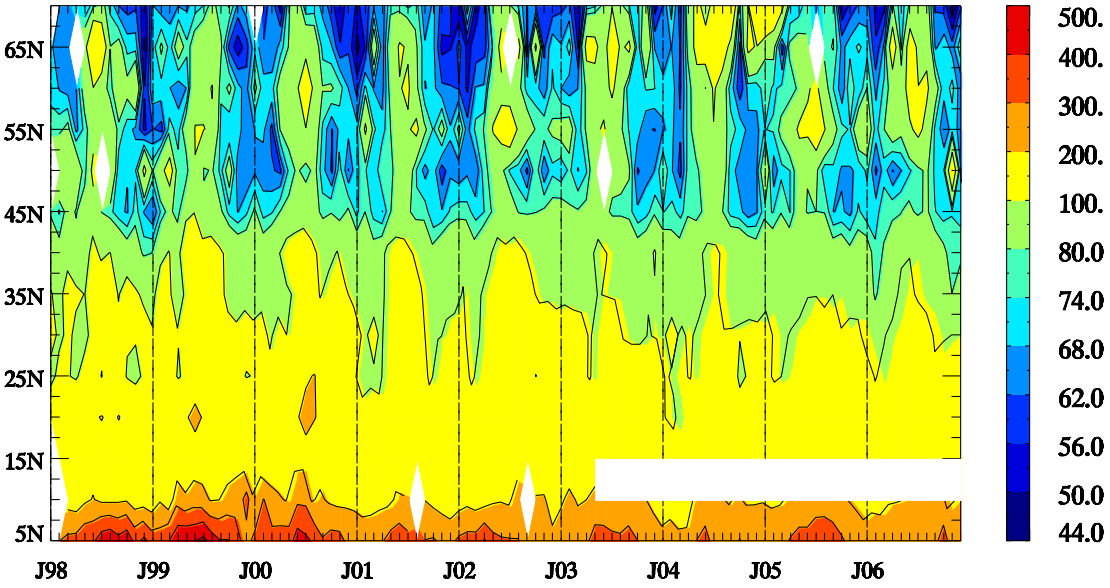

Figure 4.18: Same with Fig. 4.8, except for the $\hat{\omega}/f$ derived from $\overline{VE}/\overline{PE}$.

(a)

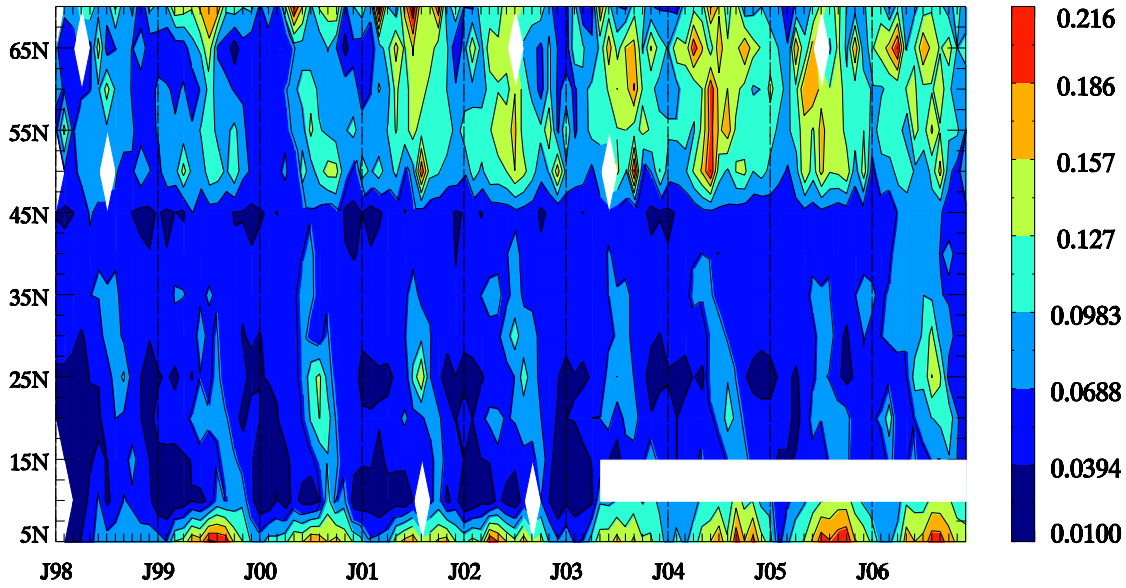

(b)

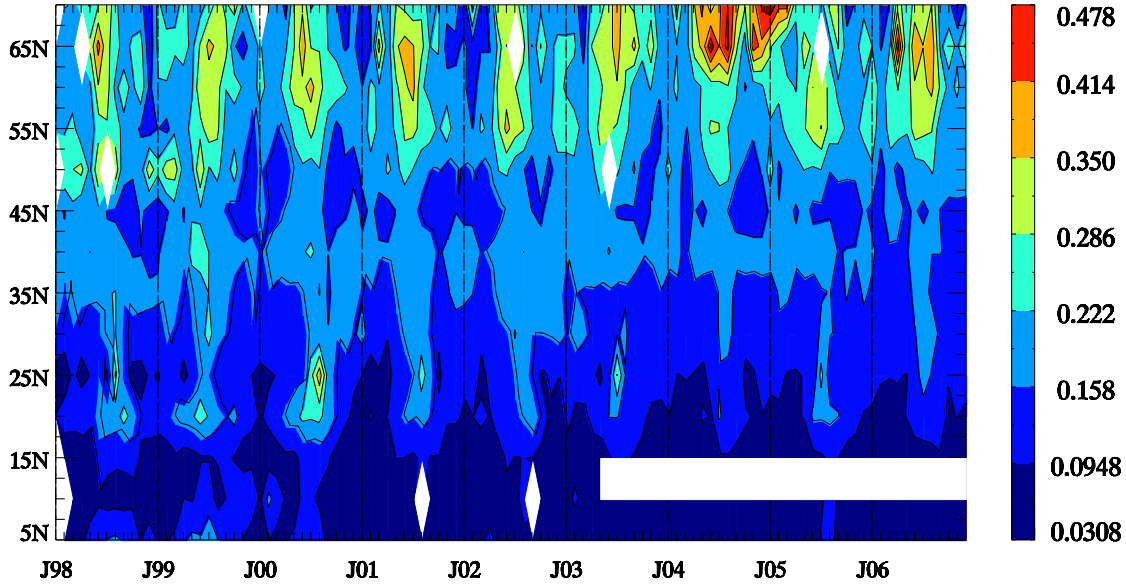

Figure 4.19: Same with Fig. 4.8, except for $\overline{VE}/\overline{PE}$.

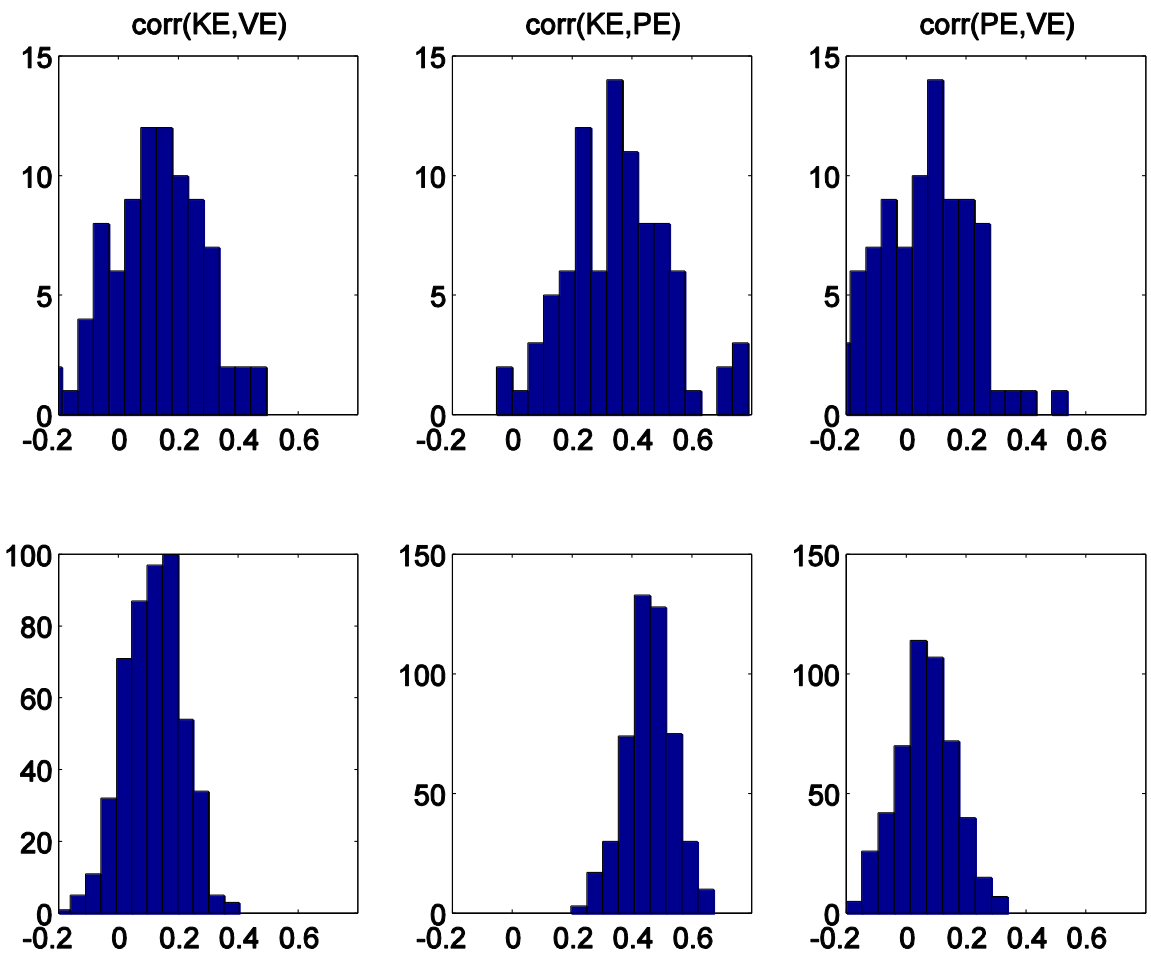

Figure 4.20: Histograms for correlation coefficients between two energies calculated from the nine-year (1998-2006) observations in the troposphere (top panels), and the simple model results (bottom panels). Details can be found in the text.

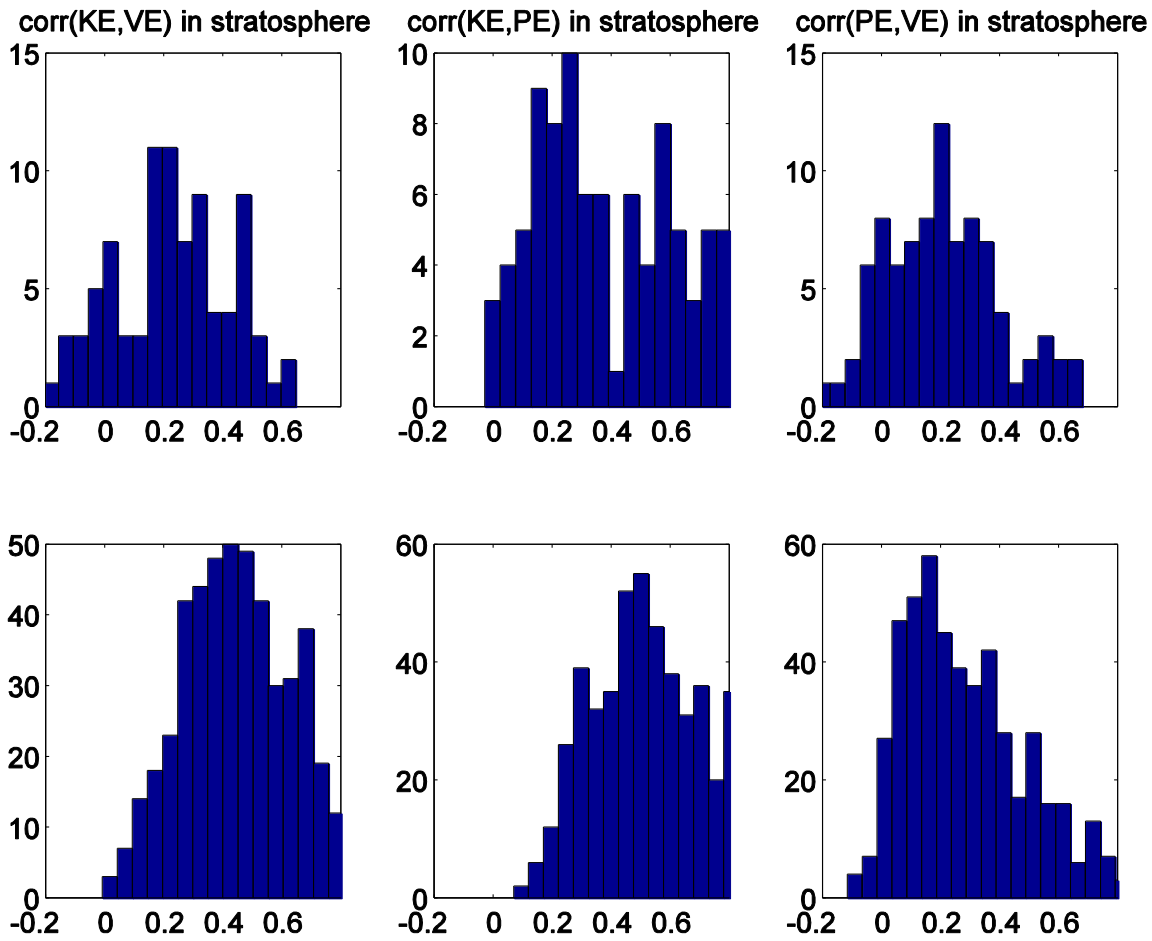

Figure 4.21: Same with Fig. 4.20, except for the lower stratosphere.

Chapter 5 Gravity Waves generated by Jet Imbalance Sources

5.1 Introduction

Rind et al. (1988) was the first to develop parameterizations of non-stationary gravity waves in terms of real physical sources – convection, wind shear, etc.. Since little was known about wind shear generated gravity waves at that time, *Rind et al. (1988)* used a simple mathematical relationship between wave momentum flux and vertical wind shear above the jet stream level.

Since then, there have been observational, theoretical and modeling attempts to better understand gravity wave generation from baroclinic waves, jets and frontal systems. Some observational evidences show that gravity wave generation favors the jet exit region of an upper level ridge (e.g., Uccellini and Koch, 1987; Guest et al., 2000) and/or an upper level trough (e.g., Plougonven et al., 2003). These two situations are shown in the schematic picture Fig. 5.1. *Plougonven et al. (2003)* also noted upward propagation of gravity waves into the lower stratosphere and downward propagation into the mid-troposphere from the jet level in a synoptic case, indicating the jet as the source for these waves. *Wang et al. (2005)* found from radiosonde data that the upward propagation fraction of gravity waves in the lower stratosphere is about 25% higher than that in the troposphere, and the upward propagation fraction in the lower stratosphere is significantly correlated with the wind speeds for high-latitudes, indicating some of the gravity waves in the lower stratosphere might be generated in the upper troposphere. Some other studies highlight surface fronts as the source of gravity waves (Eckermann

and Vincent, 1993), though it's difficult to unambiguously identify single sources such as surface fronts since, for example, there may be wave emission from deep convection associated with the front.

The theoretical study of the jet imbalance generation mechanism can be traced back to the seminal work of *Rossby (1938)*, although his primary focus was not on the gravity wave radiation from an unbalanced flow, he still pointed the direction for future investigators. *Medvedev and Gavrilov (1995)* proposed a method for separating the fast manifold from the slow manifold using the Rossby number, and they derived similar results to those of *Plougonven and Zhang (2007)*, which we briefly introduced in Chapter 2.

Most numerical studies on this topic have focused on idealized cases. For example, *O'Sullivan and Dunkerton (1995)* simulated inertia-gravity waves generated in the stratosphere above and downstream of the upper-level ridge of a baroclinic wave. *Reeder and Griffiths (1996)* investigated the wave emission from two-dimensional frontogenesis, and they demonstrated that wave emissions become much more pronounced when the frontogenesis varies rapidly. *Plougonven and Snyder (2007)* found out that the wave generation depends strongly on the details of the baroclinic wave developments in that spontaneous emission from the upper-level jet tends to excite gravity waves in the cyclonic sector, while surface fronts seems to be a strong candidate for gravity wave emissions in anticyclonic flow.

Quantitative analyses of wave characteristics have been carried out for some idealized simulations. For example, *Wang et al. (2007)* found out that the wave amplitude is proportional to the square of the Rossby number for small Rossby number cases.

However, two issues conspicuously remain. Firstly, spontaneous adjustment has often been invoked to explain the generation mechanism from jets, but fronts, jets, convection and shear instabilities associated with strong wind shears are often interwoven together in the model simulations, and it's difficult to separate the various causes from the response. Secondly, the information modelers have discovered so far do not provide sufficient guidelines for parameterization in GCMs. Even though several attempts have been made to implement frontogenesis into GCMs using diagnostics for frontal systems (e.g., Charron and Manzini, 2002; Richter et al., 2009), large uncertainties still exist. For example, *Richter et al. (2009)* arbitrarily choose 600 hPa as the source level for the frontogenesis source. More importantly, the spontaneous emission from jet mechanism has not yet been implemented in any GCMs so far.

Using the theory proposed by *Plougonven and Zhang (2007),* one can, in principle, solve for the resulting gravity waves from forcings resulted from the residuals in unbalanced flow. Furthermore, we should be able to compare the modeled gravity wave fields directly to observations, since the theory is not restricted to idealized cases.

In this chapter, the analysis methods and the models used are introduced in section 5.2. A study of a baroclinic wave event with several specific cases identified in this event will be investigated in section 5.3 with comparisons between observations and models. The climatologies of various forcings are studied in section 5.4, and potential implications on future parameterizations for the jet imbalance source into GCMs are discussed in the conclusion section.

5.2 Data Analysis Methods and Model Experiment Setups

In this chapter, we study a relatively clean case, which hopefully can shed light on further investigations of more complicated cases. Our approaches are as follows.

First of all, the synoptic situation is diagnosed. Several embedded jet streaks and their development are identified on the 300 hPa isotach map. Furthermore, we use isentropes on the tropopause surface to diagnose diabatic/adiabatic processes, as well as upper level front. This technique has been widely used by others (e.g., Morgan and Nielsen-Gammon, 1998). Since potential temperature increases with height, small values of potential temperature indicate a depression of the tropopause towards the surface, and small centers of high potential temperature suggest possible deep convection. A sharp gradient of the isentropes indicates the position of possible upper-level fronts, where stratospheric air and the accompanying positive PV anomalies "leak" into the troposphere and lead to a deepening of the trough (Morgan and Nielsen-Gammon, 1998).

Secondly, several radiosonde profiles are selected where there isone dominant gravity wave in each profile. All of these show clear upward (downward) propagating gravity wave signal in the lower stratosphere (troposphere), with only one exception. The wave parameters are derived using the methods described in Chapter 2. In this case study, we define the tropospheric segment as 3 – 7.2 *km* and the stratospheric segment as 10 – 18 *km* to make sure the boundaries of each altitude segment are close enough to the jet level to hopefully eliminate complicated propagation issues. To test the robustness of the derived gravity wave parameter values, 1^{st}-order and 3^{rd}-order polynomial fits are also applied to separate the mean background flow from the gravity wave perturbations. Since the next step involves carrying out GROGRAT ray-tracing experiments to trace gravity wave rays back to their sources, and this requires the RMS wave amplitude (i.e., the

square root of *KE*); the intrinsic frequency $\hat{\omega}$; and the zonal wavenumber k and meridional wavenumber l as inputs; these parameters should be insensitive to the orders of polynomial fits for our methods to be robust. Thereby only those profiles with consistencies in the derived parameter values are analyzed. Consistency here is defined such that the value of $\hat{\omega}$ derived from 1st, 2nd and the 3rd polynomial fits deviate by less than 20% of its mean value, and the k and l should be roughly of the same order and have consistent signs. Since there are large uncertainties in the horizontal wavelength (Zhang et al., 2004), as will be shown in Table 5.1, the latter requirements are rather loose. The value of *KE* doesn't impact the comparisons since we do not directly compare the simulated wave amplitudes with the observations.

Gravity wave rays with combinations of mean values $\pm$ 20% for $\hat{\omega}$, k and l are then released in GROGRAT at the top of the stratospheric segment and the bottom of the tropospheric segment. These combinations create a bundle of 27 rays. They are released in a 4D atmosphere and are traced back in time. By these means, we can trace these rays back to their sources. If the bundle diverges in different directions, we consider the result to be not robust. All the GROGRAT experiments are carried out with 0.3 *km* vertical resolution, and $2.5^{\circ} \times 2.5^{\circ}$ horizontal resolution. Different vertical resolutions (0.2 *km* and 0.6 *km*) are tested, and results are insensitive to the vertical resolution.

The last step is to simulate the response gravity wave fields, with the identified forcings, in the linear forcing response model that was introduced in Chapter 2. The forcings are centered where the rays end in the back-tracing experiments, and we find that the forcings can be identified with the unbalanced residuals of the flow associated with the jet streaks. The wave forcings are then calculated from the residuals of the PV

inverted balanced flows. NCEP/NCAR four times daily reanalysis data are used to calculate these forcings and are used as the background flow for the GROGRAT back-tracing experiments. The generated gravity waves are compared with those observed in the radiosonde data in terms of location, horizontal wavelength, vertical wavelength and wave frequency. Since the model starts from an assumed initial condition with no gravity waves nor mean circulations, a spin-up time is required and hence the results are not compared in their time dependence.

Strictly speaking, both the input forcings and the background flow should evolve in time. Besides, the "primary" flow (i. e., the mean background fields) is affected by the "secondary flow" (i. e., the emitted gravity waves), also altering the forcings (Medevedev and Gavrilov, 1995). In this experiment, since the selected case is quasi-stationary, we do not consider the evolution of the forcings nor the background flow, and do not take the wave - mean flow interactions into account. This is a shortcoming of this experiment.

Since the analyzed case is in the contiguous US, a large model domain of [$20^{\circ}N$, $65^{\circ}N$] and [$205^{\circ}E$, $335^{\circ}E$] is chosen to avoid boundary effects. Thick sponge layers are put at the latitudinal boundaries (200 *km*) and the upper boundary (3 *km*) to avoid wave reflection. The longitudinal boundary condition is periodic. A Rayleigh damping scheme is also applied at the top to further clean up some weak reflected waves. The horizontal resolution is 60 *km* by 60 *km*, and the vertical resolution is 0.2 *m* from the surface up to 20 *km*. The resolution is moderate for typical numerical simulations of gravity waves, but it's fine enough to resolve large-scale inertial gravity waves (Plougonven and Snyder, 2007).

In the next section, a control run (CTRL) is first presented with solitary centers for each of the F_δ, $A_{1,\zeta}$ and $A_{0,\theta}$ forcings. A sensitivity run with a halved grid-size is also carried out. Another run (noA0) with only the F_δ and the $A_{1,\zeta}$ forcings is performed to evaluate the impact of the residual for the thermal forcing. To assess the effects of solitary forcing, a run with dipole forcings (DIPOLE) is performed. All of the above experiments are designed to investigate the spontaneous emission from a jet streak located at the anticyclonic sector. The other two jet streaks, one at the trough of the baroclinic wave and the other at the cyclonic sector can also generate waves. The simulations of these two jets are named "CURVE" and "CYCLONE", respectively.

5.3 A baroclinic wave case study

A pilot case study of a baroclinic wave event that occurred during the week of Dec. 16th, 2003 has been investigated by *Bell (2006)*, where he focused on the first stage of its development over the Rockies (Dec. 14th-17th, 2003) in order to study the characteristics of tropopause evolution. Here, I concentrate on its redevelopment over the central and eastern part of the contiguous US after the 17th, and will study the gravity wave emissions from the jet streaks embedded in this baroclinic wave.

5.3.1 Synoptic setup

Beginning from Dec. 14th, 2003, a short wave trough dives from the Alaska Gulf into the Western US and amplifies as it propagates eastward through the central and eastern US in the later half of the period (after Dec. 17th). As one can see from the synoptic map on 300 hPa in Fig. 5.2, it reaches its maximum amplitude at around 00UTC on the 17th,

when the flow is largely meridional, and a ridge begins to develop over the western half of the US. Another jet streak comes in afterwards, substituting for the original one at the anticyclonic sector, and deepens the wave again. The wave stays pretty much stationary in terms of its amplitude, its location, and the relative positions of its wind maxima from 00UTC, 18th to 12UTC, 19th, as shown in Fig. 5.2.

This case was chosen mainly for three reasons. Firstly, the case is relatively dry, with most regions receiving less than 0.2 inches of rain during the whole event (Bell, 2006). Since convection is one of the major sources for gravity waves, and it often evolves together with the jet/frontal systems during cold seasons, it is much easier for us to eliminate this source from the possibilities by choosing a relatively dry case. As can be seen from Fig. 5.3, deep convections only occur in the warm sector of the upper level front before 06UTC, 18th, and appear again at 18UTC, 18th, but they are already far away from the land at that time. Surface diagnostic maps with precipitations and analyzed fronts also confirm this point (Fig. 5.4). Another merit about this case is that diabatic processes are not prominent, especially in the anticyclonic sector. The dynamic tropopause minima, enclosed by the 300K isentrope, slowly moves and elongates along the anticyclonic sector from 06UTC, 18th to 12UTC, 19th, validates that the large scale diabatic processes are not playing a major role here. This is confirmed again through Fig. 5.4. Since the *Plougonven and Zhang (2007)* derivations are only valid for a dry atmosphere, this case roughly satisfies this requirement. Last but not least, the baroclinic wave stays quasi-stationary from 12UTC, 18th to 12UTC, 19th, and thus is expected to have relative stationary forcings for gravity waves. This case is expected to generate and to reinforce strong, identifiable gravity wave fields. Although the high-vertical resolution

radiosonde stations are relatively sparsely distributed over the contiguous US, the spatial maximum centers of *KE* in both the lower stratosphere and the troposphere at 12UTC, 18th, 00UTC, 19th and 12UTC 19th collocate roughly at the jet exit regions, one in the southeast US, and the other in the northeast US, as predicted by theory. The maximum value reaches $46\,J/kg$, triple the maximum monthly mean values of *KE* (Fig. 4.11). Interestingly, a maximum center of *KE* persists along the jet streak in the anticyclonic sector, which has not been predicted by theory before.

5.3.2 Radiosonde profiles

Two stations are picked for special interest. These are 04830 (Detroit, MI [$42.7^{\circ}N$, $83.47^{\circ}W$]) and 54762 (Grey, ME [$43.89^{\circ}N$, $70.25^{\circ}W$]). We choose these two stations not for the reason that KE is large, but rather because the hodographs at these two stations give a relatively clean and dominant gravity wave in both the lower stratosphere and the troposphere, and the upward propagation fraction is large (i.e., anticyclonic rotation) in the lower stratosphere and quite small (i.e., cyclonic rotation) in the troposphere in order to validate our hypothesis that the gravity waves are generated from jet spontaneous emission. The only exception is the hodograph in the troposphere of station 54762 at 12UTC, 19th, where a dominant upward propagating gravity wave is present, and we will discuss this later. The vertical profiles of total *u*, *v*, and *T* (solid) and $\bar{u}$, $\bar{v}$ and $\bar{T}$ (dashed) are given in Fig. 5.6, and the hodographs within the sections of 3 - 7*km* and 10 - 18*km* are shown in Fig. 5.7. The parameters derived from the profiles are listed in Table 5.1. As one can see, there are large uncertainties in the derived horizontal wavelengths. However, since the gravity waves generated from the model simulations are apparently a packet consisting of a combination of several waves, the estimation of

horizontal wavelength is expected to be quite rough. The results are acceptable as long as the wavelength is on the same order, and the key issue is the propagation direction.

5.3.3 Model results and comparisons with observations

(1) CTRL

A bundle of rays using the parameters derived from the profile at 00UTC, 19th over Detroit, MI are released in GROGRAT. The detailed procedures are described in section 5.2. The trajectories can be viewed in different angles in Fig. 5.8. As one can see from Fig. 5.8, the rays largely follow one trajectory in the lower stratosphere, descending back in time toward about $260^{\circ}E$, $40^{\circ}N$ at around 8 *km*, where they apparently suffer great refraction, and diverge afterward. It takes about 15 hours before the rays either violate the WKB condition or stall, which corresponds to 09UTC, 18th. The jet streak at the anticyclonic sector is located at about the same location, as is shown in the top panel of Fig. 5.9. The associated F_{δ}, $A_{1,\zeta}$ and $A_{0,\theta}$ forcings all have a large positive center to the east of the jet, and a negative center toward the west of the jet (not shown). Direct comparisons of the three forcings can be made through Eqn. (2.36). For this case, G_{θ}, G_{ζ}, G_{δ} and the sum of the three are shown in Fig. 5.10. For the jet streak located at the anticyclonic sector, G_{ζ} has the largest amplitude to the east of the jet, indicating the significance of the vorticity forcing. G_{θ} is in phase with G_{ζ}, but the amplitude is much weaker. G_{δ} is partly out of phase with G_{ζ}, and the total of the three give a large positive center to the east of the jet.

Only the positive part of the forcings associated with this jet streak are selected for the CTRL run. In practice, we only consider positive forcing values within the domain of $[30^{\circ}N\ ,\ 60^{\circ}N\ ],[110^{\circ}W\ ,80^{\circ}W\ ]$ at 09UTC, 18th, and run the simulation with frozen forcings and background fields at 09UTC, 18th until a stable solution is reached. The spatial distribution of the solitary forcings at 9 km (jet level) and cross-sections at $42.5^{\circ}N$ are given in Fig. 5.11. One can see that the nonlinear balanced residuals (F_{δ}) are located above and to the east of the jet maxima, indicating that the flow is the most unbalanced above and to the east of the jet maxima. This is consistent with previous findings (e. g., Plougonven et al., 2003; Zhang et al., 2000). The residual of the vorticity equation ($A_{1,\zeta}$) is the largest right at jet level, and to the east of the jet maxima. This forcing is very similar to the S_0 forcing proposed in *Medvedev and Gavrilov (1995)*, where they hypothesize that the large-scale inertial gravity waves should be generated mainly from the S_0 forcing. The waves we see in the sounding have intrinsic frequencies quite close to *f*, and the $A_{1,\zeta}$ forcing is the largest for this case if we evaluated the three forcing, G_{θ} , G_{ζ} and G_{δ} . The total advection of the potential temperature ($A_{0,\theta}$) is located below and behind the jet streak, and the divergence of the gradient of $A_{0,\theta}$ (i. e., G_{θ}) is in phase with G_{ζ} .

The simulated horizontal wind divergence field is contoured in Fig. 5.12 (spatial pattern) and Fig. 5.13 (cross-section taken at $42.5^{\circ}N$). Since the direct divergence field associated with the forcings is too large, we enlarge the responding gravity wave fields for clearer view. The station 04830 (Detroit, MI) is marked as a red triangle to the west in the horizontal map, which is right at the edge of the responding gravity wave field. This

is the reason why the amplitude of the wave we observe there is relatively small. The estimated horizontal wavelength is about 1000 *km*, longer than the observed value (~ 500 *km*). The waves firstly propagate toward northeast, and then toward northwest north of $40^\circ N$, hence with negative zonal wavenumber and positive meridional wavenumber north of $40^\circ N$. This is coherent with the observations. The vertical wavelength estimated from Fig. 5.13 is about 3 *km*, again longer than the observed value (~ 2 *km*). Interestingly, there seem to be two packets of waves that are generated vertically. One packet is more vertical and the other one is more tilted. The wave frequency inferred from the wavelengths using the dispersion relationship eqn. (2.12) is about 3.5*f* ($N^2 \approx 0.015 s^{-2}$ over the station 04830 at 14 *km* altitude), doubled the observed frequency.

Zhang (2004) suggested that the model resolution would impact the wave frequency by running a similar model simulation similar to that of *O'Sullivan and Dunkerton (1995)* but with a finer mesh-grid size. He found a higher frequency secondary wave packet above the jets, and he attributed the reason to the unresolved subgrid-scale processes. We therefore carried out a sensitivity experiment with half of the mesh-grid size, and found that the basic picture barely changed at all. That is probably simply because this model is a linear forcing-response model, involving no subgrid-scale processes.

All in all, the CTRL experiment result roughly agrees with the observations in terms of the location of the wave, and the wave propagation direction. The simulations have longer horizontal and vertical wavelength, and the waves, although still being inertial gravity waves, have a somewhat higher intrinsic frequency. The maximum gravity wave activity from the simulation appears at the jet exit region, which agrees well with other numerical simulation results (e.g., Zhang, 2004) as well as various other observations

(e.g., Plougonven et al., 2003), but the emitted gravity wave fields extend further downstream a greater distance than what's been observed. The trajectories of rays from the GROGRAT back-trace experiment show good similarity to the simulated gravity waves.

(2) noA0

Although the CTRL experiment shows pretty decent consistency between the observations and the simulations, the inferred wavelength and the frequency do not quite agree with those that are observed. Visual inspection of the evolution of the emitted gravity waves suggests that a small $A_{0,\theta}$ forcing centered at around [$31^{\circ}N$, 6000 *km*] (Fig. 5.11e, f) is suspiciously responsible for waves emitted downstream, and this may cause some of the inconsistency of the simulation result compared with the observations. To assess this issue, we run another case without $A_{0,\theta}$ forcing, and name that as "noA0".

The pattern of the resultant gravity wave fields are shown in Fig. 5.14. This time, a well-defined wave packet is generated, bending toward the northwest from $35^{\circ}N$. Only one major wave packet is seen in the cross-section, which corresponds to the more tilted one in Fig. 5.13. The estimated horizontal and vertical wavelengths are about 700 *km* and 2 *km*, resulting an intrinsic frequency of about 1.2*f*. These values are in good agreement with observations. One thing that deserves mention is that another wave packet is generated spontaneously from the jet downward toward the surface, as shown in Fig. 5.14 (b). This is expected from theory. Since the wave packet is far away from the station 04830 (Detroit, MI), however, it's hard to evaluate this point from the soundings taken at station 04830 (Detroit, MI).

Apparently for this specific case, the small $A_{0,\theta}$ forcing located at the jet exit region does have an unexpected impact on the emitted gravity wave fields. After removing that, the wave field is much more clearly defined, and is in high agreement with the observations. This suggests that the waves seen over station 04830 (Detroit, MI) is in fact generated from the jet located in the anticyclonic sector.

(3) DIPOLE

Fig. 5.10 suggests that there is a negative forcing center located at the west of the jet streak. An interesting test with dipole forcing can evaluate whether it's the solitary positive forcing or the dipole forcing that works better in terms of comparison with the observation.

Another radiosonde profile taken at 12UTC, 19th over station 04830 (Detroit, MI) has a strong upward propagating gravity wave present in the lower stratosphere. The vertical profiles and the hodographs are shown in Fig. 5.6 (c - d) and Fig. 5.7 (c - d) respectively, and the derived parameter values are listed in Table 5.1 for both the lower stratosphere and the troposphere segments.

The GROGRAT experiment gives very similar results to the wave trajectories found in the CTRL run in the lower stratosphere, as shown in Fig. 5.15. The waves are also traced back to the east of the jet streak, and the propagation time is about 15 hours (i. e., traced back to 18UTC, 18th). Minute differences still exist, though. For example, the rays propagate even further down to the bottom of the jet, which suggest they might be related to the surface frontal systems instead of to the jet itself. This feature has been previously reported in *Lin and Zhang (2008)*.

Direct comparison of G_θ, G_ζ and G_δ is made in Fig. 5.16, which is a snapshot at z = 6 km at the bottom of the jet. Since the altitudes are different, Fig. 5.16 is not directly comparable to Fig. 5.10, even though the jet configuration is more or less the same. We find that for this case, G_θ dominates at low levels. G_ζ (G_δ) is in (out of) phase with G_θ. This time we take the dipole forcings, shown in Fig. 5.16. Compared with Fig. 5.10, the positive forcings are about at the same locations. A large negative $A_{0,\theta}$ forcing extends into the lower stratosphere (Fig. 5.17f). This is likely due to the fact that the baroclinic wave is approaching its decay phase at 18UTC, 18th, and the tropopause behind the jet is higher.

The simulation results are shown in Fig. 5.18 and 5.19 for this case. The estimated horizontal wavelength and the vertical wavelength are about 1000 *km* and 2 *km*, resulting in an intrinsic frequency of 1.14*f*. The values are in general in agreement with the observations, despite the fact that great uncertainty exists in the horizontal wavelength. The horizontal propagation direction seems to be too zonal, compared with the observed northwestward propagation. The major wave packet extends further downstream to the east, but its amplitude is smaller than the CTRL run.

For both the CTRL and DIPOLE runs, large amplitude waves are also generated right above the forcing, as shown in Fig. 5.13 and 5.19. They may account for the large KE values observed right over the jet streak (Fig. 5.6). Hodograph analysis for two stations in this area (station 94982 and 94983) also show clear upward propagating waves. This feature has also been found by *Lin and Zhang (2008)* in an idealized mesoscale gravity wave case simulation. Another interesting thing to notice is seen in the wave fields in the

troposphere. Fig. 5.20 shows the results from a GROGRAT experiment in the troposphere starting from 12UTC, 19th for station 04830 (Detroit, MI). The rays diverge when traced back in time toward the jet source. Some of them seem to originate from the jet streak in the anticyclonic sector, but the trajectories do not follow the wave packet seen in the simulations. One trajectory goes toward another jet streak located at the trough of the baroclinic wave, which might suggest waves emitted from different sources.

The DIPOLE run does not significantly improve the simulation result. Together with the implications from the noA0 run, we conclude that it is important to find the correct forcing fields associated with a specific jet streak in order to simulate the gravity waves accurately.

(4) CURVE

No studies have looked at the problem of spontaneous emission from a jet streak located right at the trough of a baroclinic wave. In this case study, we were fortunate to see this at 12UTC, 18th (Fig. 5.2). A ray tracing experiment carried out from station 54762 (Grey, ME) at 12UTC, 19th points out the waves we see over this station are likely to be generated from the jet streak at the most curved region of the short wave (therefore, the case is named "CURVE"), although this station is actually located at the exit region of the jet streak in the cyclonic sector.

The trajectories of this GROGRAT experiment are shown in Fig. 5.21. The observed sounding profiles, hodograph and the parameter values are given in Fig. 5.6 (e-f), 5.7 (e-f) and Table 5.1, respectively. It takes about 24 hours for the trajectories to end at the trough of this baroclinic wave, when the jet streak is located right at the trough. The jet maximum center is shown in vertical cross-section at $30^{\circ}N$ in the bottom panel of Fig.

5.9. The jet is located at a relatively high altitude, the center of which is at about 12 *km*. The majority of the trajectories released at 18 *km* end at about 13.5 *km*.

The forcings associated with this jet streak show a negative (positive) center to the west (east) of the jet (Fig. 5.22). The forcing resulting from the residuals of the vorticity equation seems to play the least important role here, but still contribute to the total forcing. G_θ and G_δ act in opposition to each other, and G_θ seems to dominate the total forcing field. For simplicity, all the forcings within the domain of [$27.5^\circ N$, $40^\circ N$], [$90^\circ W$, $70^\circ W$] and between the altitude range of 10 *km* and 16 *km* are used to initiate the model run. They are shown in Fig. 5.23.

The simulated gravity wave fields are well-defined (Fig. 5.24). The estimated horizontal wavelength is about 1000 *km*, larger than the observed wavelength of about 400 *km*. The vertical wavelength is around 3 *km*, in agreement with the observations. The resultant intrinsic frequency is 1.2*f*, smaller than the observed one approximately 1.8*f*. The wave propagates northeastward with a large meridional component, which is in agreement with the observations. Even some detailed vertical structures coincide with the trajectories of the ray-tracing experiment in that the waves are almost purely vertically propagating right above the jet center (12 - 14 *km*).

For this CURVE run, although the initial forcings have relatively small values, and they are not well organized, the resulting gravity waves are quite impressive in their amplitudes. We suspect that is due to the reason that the large positive center of the three forcings are collocated with one another (Fig. 5.23), amplifying the wave patterns. Interestingly, we do not see a downward propagating gravity wave in the hodograph of soundings at station 54762 (Grey, ME) at this particular time, which is suggested to have

happened in the simulations. Note that a surface front is also located across the center of this jet streak at 12UTC, 18th (Fig. 5.4b), indicating that the observed upward propagating gravity wave in the tropospheric segment over this station might be due to the surface front.

(5) CYCLONE

The station 54762 (Grey, ME) is located at the exit region of the jet streak in the cyclonic sector. To demonstrate that waves we seen over this station are not likely to be generated from this jet imbalance source, a run named CYCLONE is carried out, with forcings within the domain of $[40^{\circ}N\ ,\ 60^{\circ}N\ ]$, $[90^{\circ}W\ ,\ 60^{\circ}W\ ]$ representing the forcings associated with this jet streak. We find that the three forcings are collocated together at 14 *km*, but the vertical structures are quite complicated (Fig. 5.25).

The simulation result is shown in Fig. 5.26. The waves are propagating northwestward before they curve back to northeastward at high latitudes. Both the horizontal and the vertical wavelengths are longer than those observed. As a matter of fact, the wave field over the station 54762 (Grey, ME) seems to be directly generated above the jet streak, like what was seen in the CTRL and the DIPOLE runs, instead of a far-field downstream development.

The comparisons between the CURVE and CYCLONE runs indicate that some waves we see at the exit region of a jet streak might not be able to be easily attributed to a jet streak source. Instead, they may come from a jet streak far away upstream. Another implication is that a strong jet does not necessarily correspond to a strong gravity wave field. The configuration of the forcings and/or the background flows might be more

important in determining whether the gravity waves can be generated, amplified, and propagated.

5.4 Climatology of the forcings

The monthly mean values of the F_δ, $A_{1,\zeta}$ and $A_{0,\theta}$ forcings are not quite indicative of their importance since jet streaks have large seasonal and interannual variability over the contiguous US. However, several interesting points can still be made from investigating the climatology of the forcings.

The G_δ forcing collocates well with the climatological patterns of the winter storm activity (Eichler and Higgins, 2006). This coincidence is not so evident in the residual of the thermal forcings, maybe because the *Plougonven and Zhang (2007)*'s theory works only for dry cases.

The spatial distribution map in January and July exhibits interesting patterns. As shown in Fig. 5.27, where G_θ, G_ζ and G_δ are directly compared with one another, G_θ has the largest overall amplitude, while G_δ is the smallest in January (note the difference in the contour intervals). G_θ and G_ζ largely overlap with each other, while G_δ seems to be completely out of phase with both G_θ and G_ζ over most of the contiguous US. This implies that the forcing from the residual of the divergence field tends to partly offset the effects from the other two forcings. This feature is also evident in the case studies presented above. This might be explained by the manner in which the divergence term enters into the vorticity equation as well as the way in which the divergence is connected

to the thermal response to vertical motions. As we expected, all three forcings are larger during January than during July. G_θ and G_ζ retreat northward during July, coinciding with the northward retreat of cyclone activity during summer. Compared to the DJF map of Fig. 3.15, where the estimated zonal momentum flux in the lower stratosphere is plotted, the relatively weak negative values over the central US collocate with the positions of the positive forcings of G_θ and G_ζ, indicating that jet imbalance source may have great impact over this region, especially during winter. Although the seasonal variation of *KE* cannot be totally explained by the jet imbalance source variations, Fig. 5.5 implies they can be at least partly attributed to the sources.

5.5 Conclusions

Spontaneous emission of gravity waves from jet imbalance sources has been recognized for a long time, but there lacks an effective way to bridge the gap between observations and numerical simulations. In this chapter, we use a linear forcing-response model, together with ray-tracing simulations, successfully identifying the forcings associated with the jet streak believed to be responsible for the waves seen from the US high-vertical resolution radiosonde data.

Although only one baroclinic wave case is studied, the investigations of several sub-cases involving different jet streaks embedded in this baroclinic wave give interesting results. Some of the major conclusions we make from this case study are as follows:

(1) Jet streak can emit gravity waves downstream for a long distance, not just at the exit region. The generated wave fields tend to follow the mean flow.

(2) The positive forcings associated with the jet streak seem to play a more important role in determining the resulting gravity wave fields than the negative forcings. This is consistent with other numerical results documented in the literature (e.g., Zhang, 2004). Though flows are typically mostly unbalanced at the jet exit region, this study suggests that the imbalance regions in the vicinity of the jet maxima account for most of the the wave generation.

(3) The details of the numerical simulation result might be sensitive to the specification of the forcings associated with the jet streak, but the overall features are largely insensitive to numerical details. We made a rather rough separation of the jet streaks located at the trough and the cyclonic side of the baroclinic wave, and the resulting gravity wave fields are indeed different from each other.

(4) The amplitude of the waves is not proportional to the strength or the size of the unbalanced forcings. However, the observed inertial gravity waves likely generated from the jet streak located at the most curved region of the wave seem to have larger intrinsic frequencies, indicating that the size of the jet streak might be related to the frequency of the waves. This point is rather tentative, and needs more numerical simulations to test this suggestion.

(5) The model simulations work rather well in the lower stratosphere, but are much more problematic in explaining waves seen in the troposphere. That is probably because other wave sources in the troposphere may play more significant roles, such as frontal systems, convection along the front, etc.

The case study supplies great support to possibly incorporating these forcings into GWD parameterizations in GCMs in the near future, as representation of jet imbalance

sources. They do not require to be specified at any particular leveling the manner of *Richter et al. (2009)* in parameterizing the frontal source. Furthermore, the wave intermittency doesn't need to be specified anymore since it inherently follows the jet activity. The resulting gravity waves seem to agree fairly well with observations in the lower stratosphere, which is encouraging for treating inertial gravity wave impacts on the middle to upper atmosphere. Before doing so though, several shortcomings of this case study need to be improved. The forcings and the background flow should evolve with time, as in the realistic situation. Furthermore, as suggested by *Zhang (2004)*, the resulting gravity waves can lead to more unbalance of the mean flow, so it is necessary to allow the gravity wave fields and the mean flow to interact with each other. In the model, we use thick sponge layers to avoid gravity wave reflections. Obviously, this needs to be modified if a similar approach is to be incorporated in GCMs. The model used is linear model, and nonlinearities occurring in GCMs may lead to instabilities.

Lower stratosphere

04830-2003121900	1st - order	2nd - order	3rd - order
$KE(J/kg)$	5.778	5.147	4.715
$\hat{\omega}/f$	1.213	1.399	1.7
$k(m^{-1})$	-5.4E-6	-1.35E-5	-2E-5
$l(m^{-1})$	8.453E-6	5.03E-6	9.35E-6
$up\_frac(\%)$	86.1	86	82.5
$\lambda_z(km)$	2.14	2.12	2.01
$\lambda_h(km)$	626.4	436.13	284.6

Lower stratosphere

04830-2003121912	1st - order	2nd - order	3rd - order
$KE(J/kg)$	3.1	2.69	2.43
$\hat{\omega}/f$	1.34	1.14	1.06
$k(m^{-1})$	-6.75E-6	-5.91E-6	-3.38E-6
$l(m^{-1})$	1.16E-5	6.78E-6	5.06E-6
$up\_frac(\%)$	79	87	90.3
$\lambda_z(km)$	2.1	1.92	1.82
$\lambda_h(km)$	468.16	698.58	1032.56

Troposphere

04830-2003121912	1st - order	2nd - order	3rd - order
$KE(J/kg)$	2.32	1.3	0.84
$\hat{\omega}/f$	2.18	2.065	2.37
$k(m^{-1})$	3.28E-5	3.07E-5	4.5E-5
$l(m^{-1})$	-2.06E-5	-2.78E-5	-4.36E-5
$up\_frac(\%)$	12.5	19	22.4
$\lambda_z(km)$	2.42	2.176	1.85
$\lambda_h(km)$	162.3	151.71	100.28

Lower stratosphere

54762-2003121912	1st - order	2nd - order	3rd - order
$KE(J/kg)$	6.96	6.457	6.15
$\hat{\omega}/f$	2.02	1.8	1.67
$k(m^{-1})$	1.82E-5	1.736E-5	1.46E-5
$l(m^{-1})$	7.68E-6	4.32E-6	4.26E-6
$up\_frac(\%)$	82.8	86.4	89.6
$\lambda_z(km)$	2.88	2.73	2.77
$\lambda_h(km)$	318.07	351.22	413.13

Table 5.1: The parameter values derived from each profile. The station and the time is listed in the first cell of each sub table in the format of STATION – YYYYMMDDMN, where STATION is the WBAN number, YYYY is the year, MM is the month, DD is the date, and MN = 00UTC or 12UTC[1]. The corresponding hodographs are in Fig. 5.6.

[1] This format holds for all the station plots below, if not particularly mentioned.

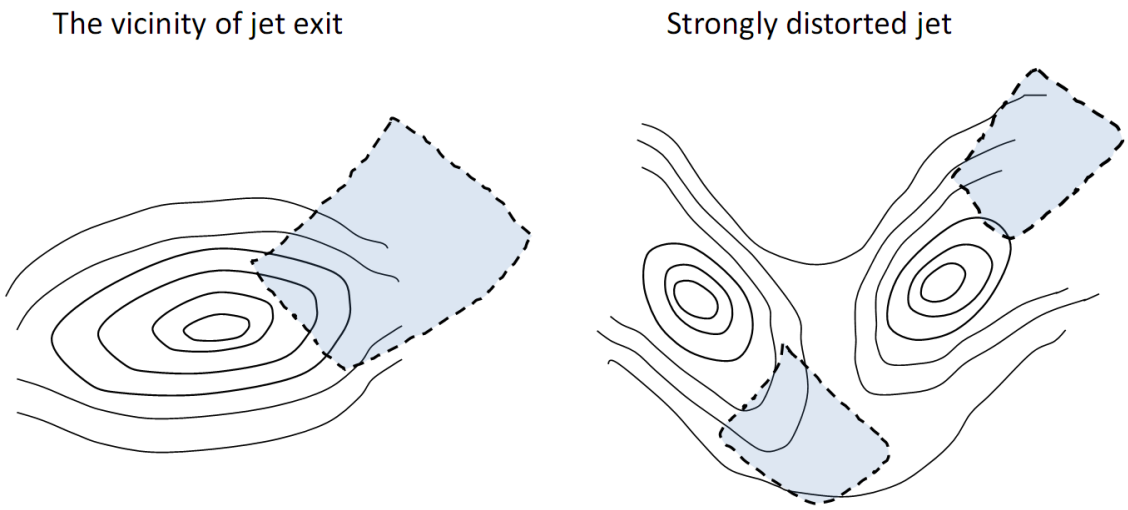

Figure 5.1: Schematic pictures showing the two situations of jet streaks, where solid lines are the isotachs, and dashed lines with light blue fill marked the favorable areas of high gravity wave activities. (Modified after Plougonven et al., 2003)

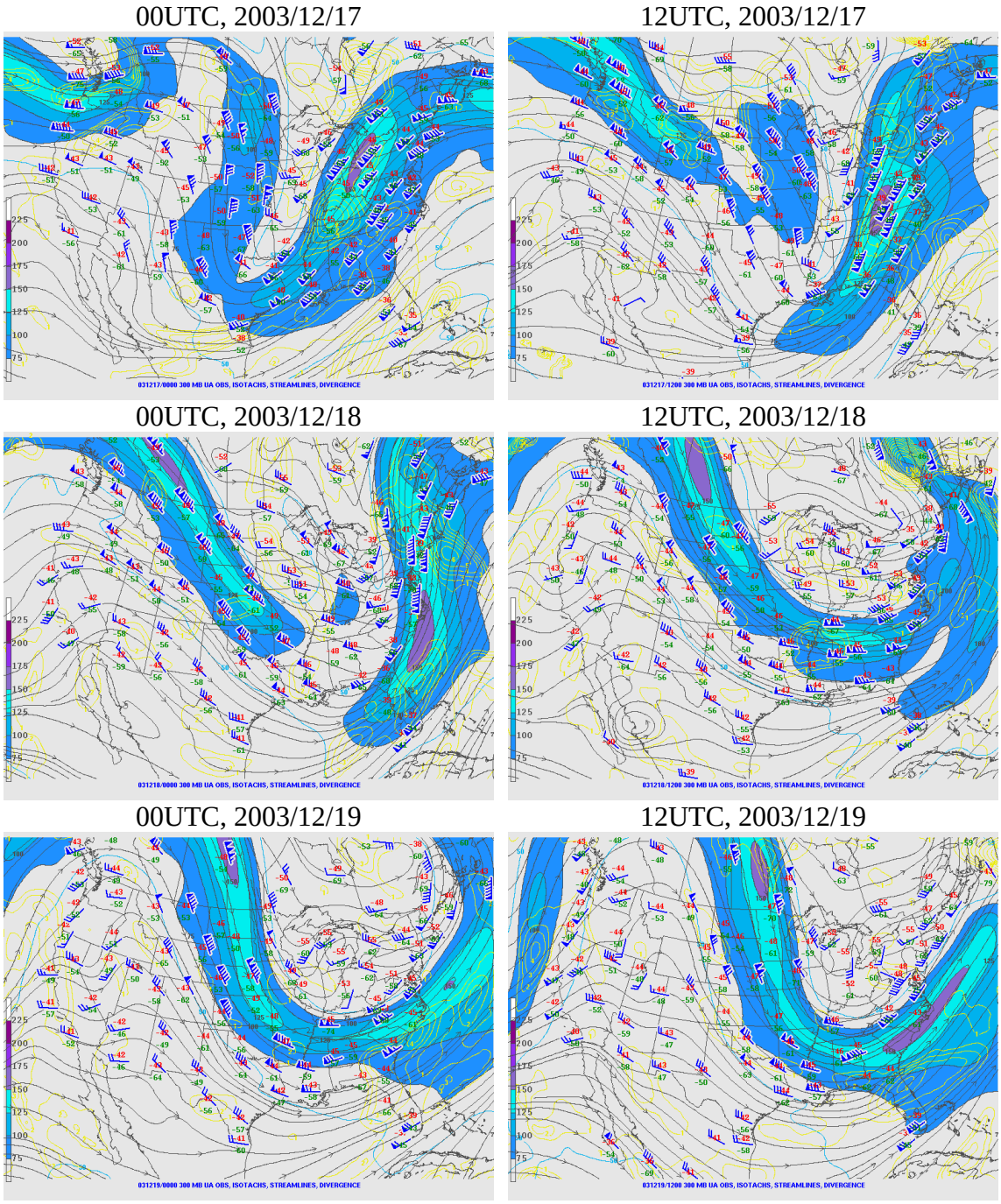

Figure 5.2: Synoptic maps at *300 hPa* (dates and times are labeled above each panel) with streamlines (black lines with arrows), divergence (yellow contours), isotachs (shaded) and observed wind vector. Wind speed increases from blue to light blue to purple. Graphs are taken from http://w1.spc.woc.noaa.gov/obswx/maps/ .

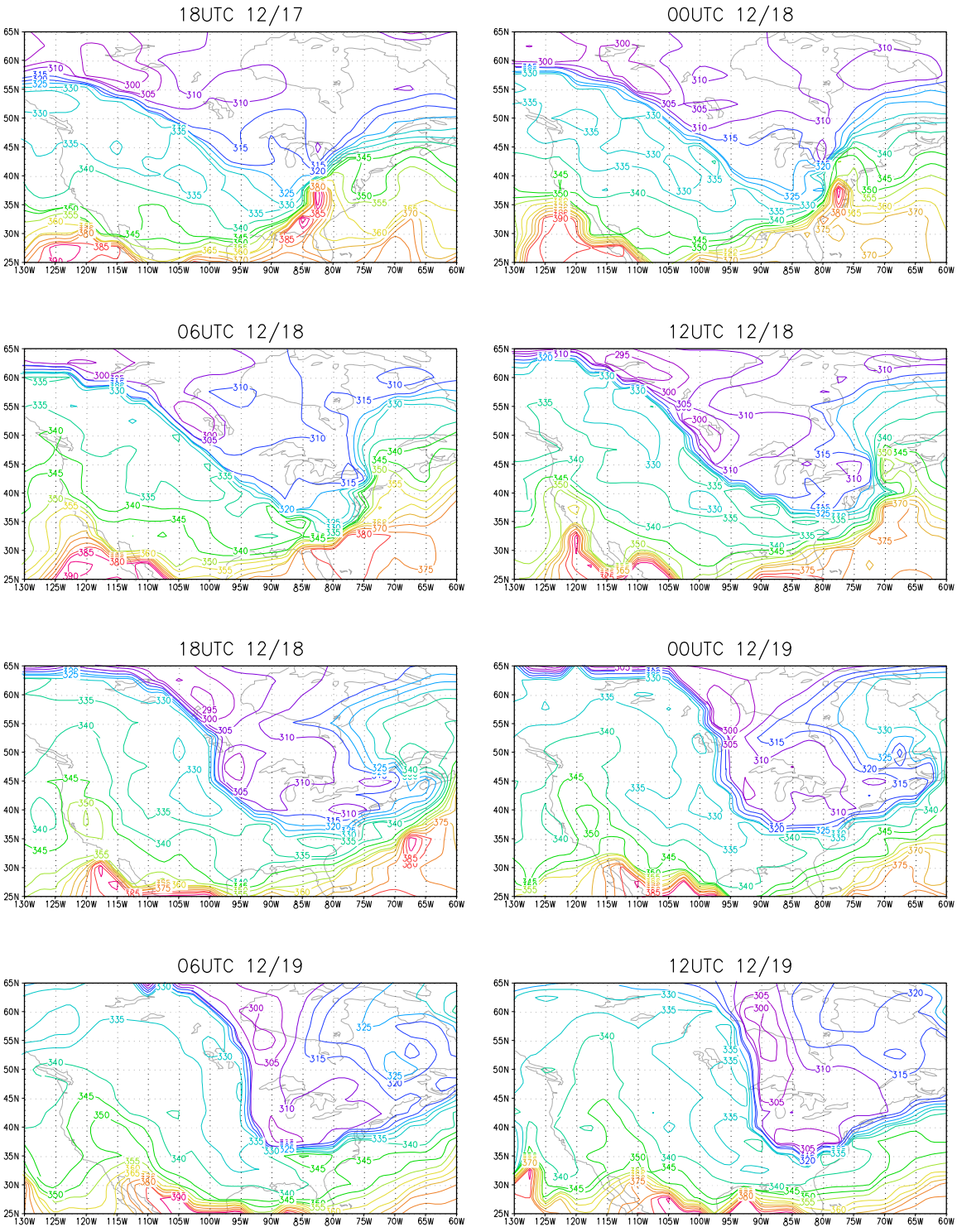

Figure 5.3: Isentropes at the tropopause evaluated from 4-times daily NCEP/NCAR reanalysis. The contour interval is $5K$.

(a) 00UTC, 12/18

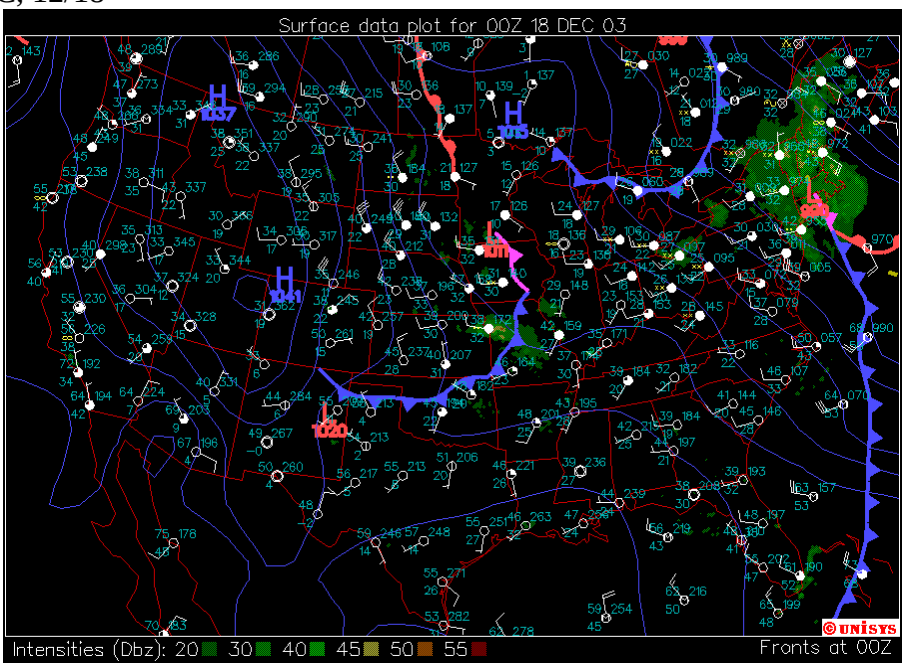

(b) 12UTC, 12/18

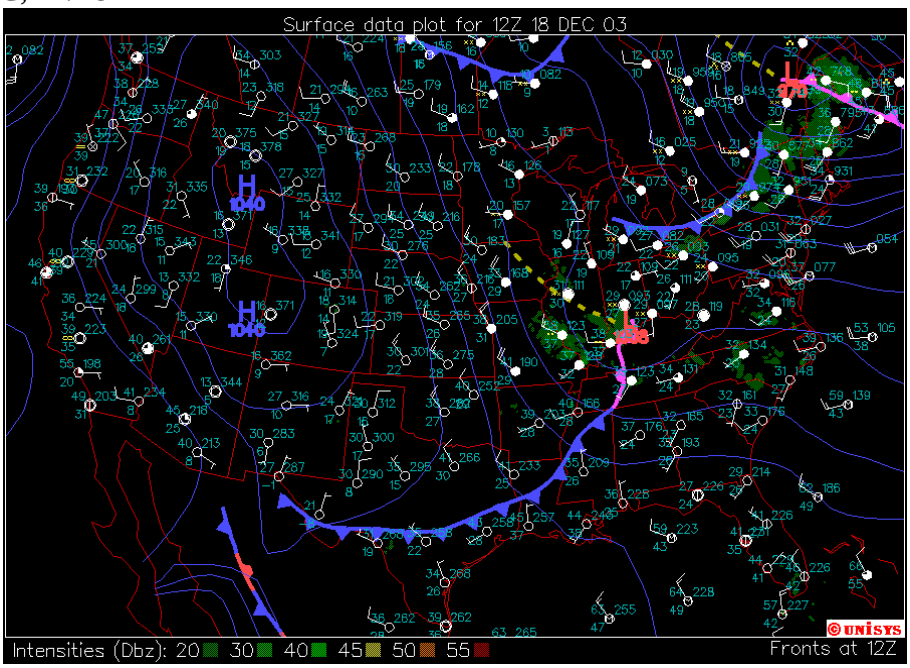

(c) 00UTC, 12/19

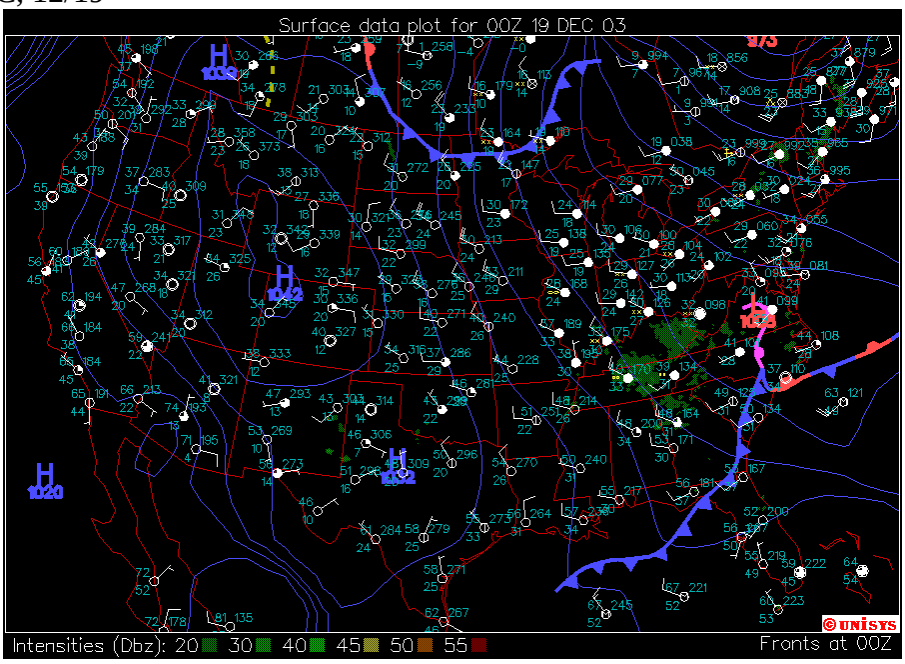

(d) 12UTC, 12/19

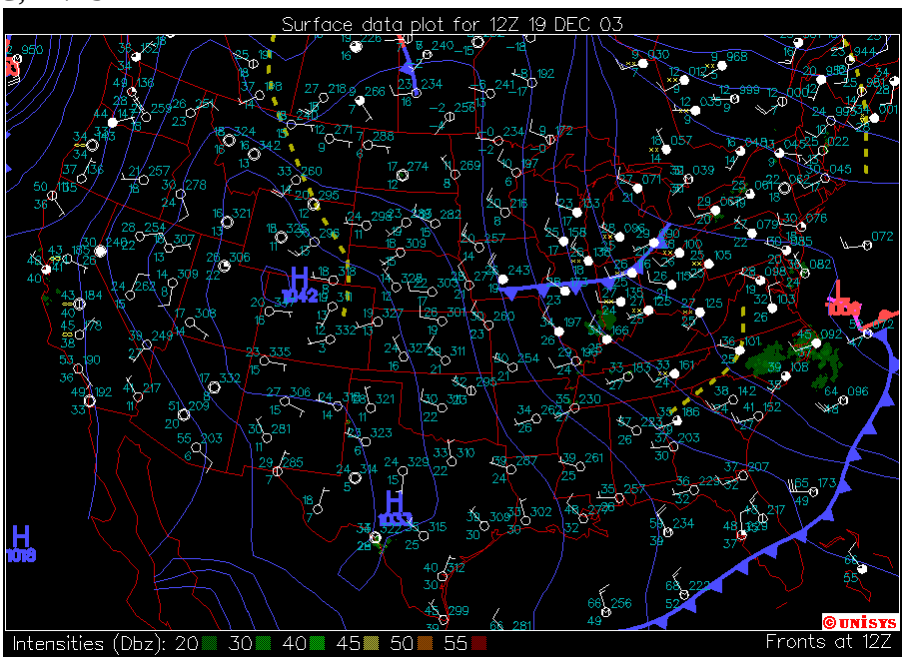

Figure 5.4: Surface analyses over CONUS for 00UTC, 18th (a), 12UTC, 18th (b), 00UTC, 19th (c) and 12UTC, 19th (d). Cold fronts, warm fronts, stationary fronts and dry lines are marked in blue lines with triangles, red lines with semicircles, blue and red lines with triangles and semicircles, and yellow dashed lines, respectively. Surface precipitation intensities (Dbz) are shaded. Maps are taken from http://weather.unisys.com/archive/sfc_map .

(a) 12UTC, 12/18 (d) 12UTC, 12/18

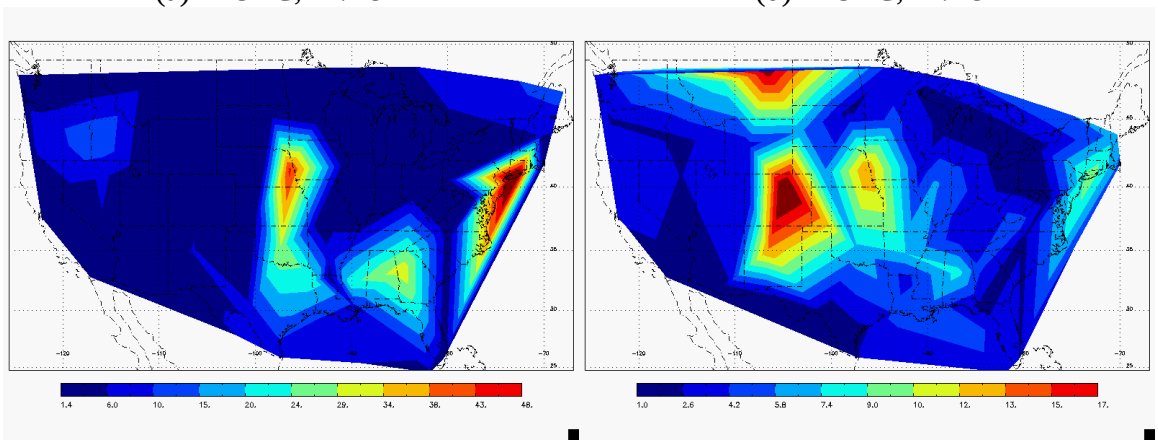

(b) 00UTC, 12/19 (e) 00UTC, 12/19

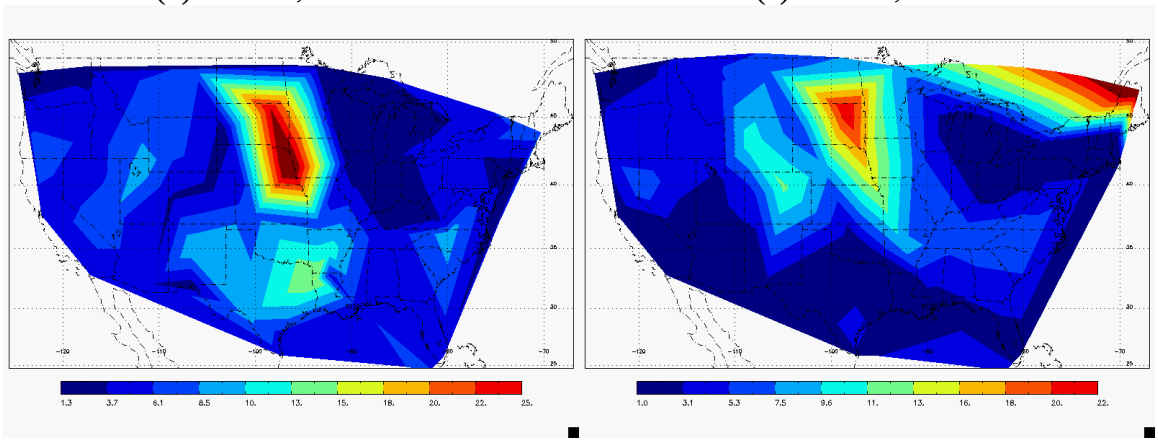

(c) 12UTC, 12/19 (f) 12UTC, 12/19

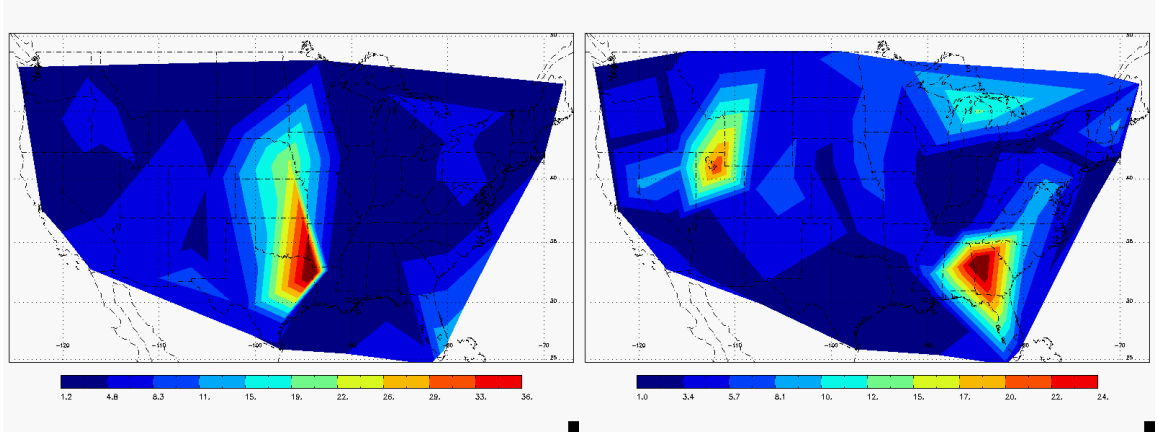

Figure 5.5: Spatial distribution of KE (J/kg) in the lower stratosphere (a) - (c), and the troposphere (d) - (f) derived from US high-vertical radiosonde data. The time is marked in the title of each panel.

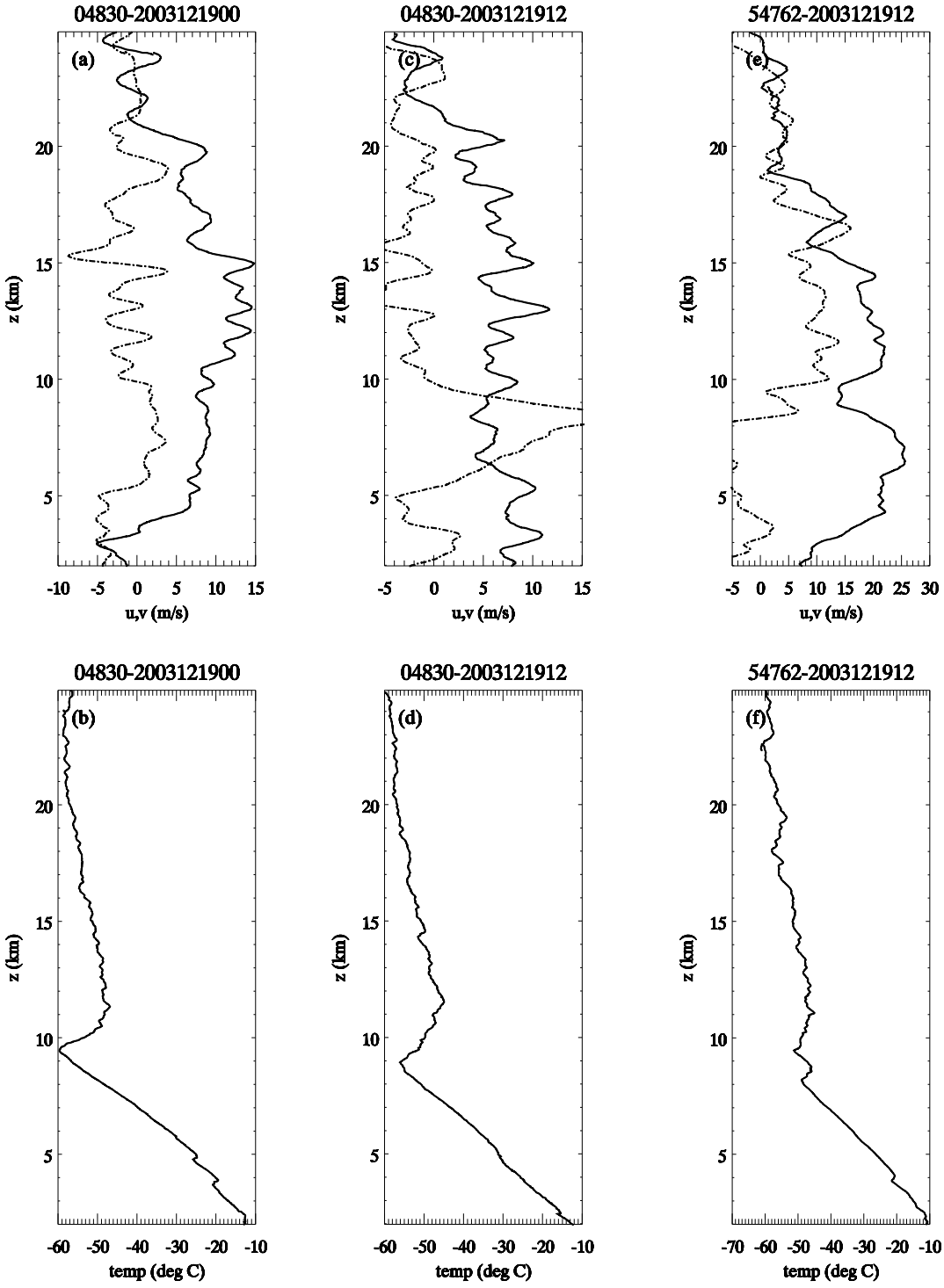

Figure 5.6: Vertical profiles of u (top, solid),v (top, dash-dot), and T (bottom, solid) for station 04830 (Detroit, MI [$42.7^\circ N$, $83.47^\circ W$], panels a-d) and 54762 (Grey, ME [$43.89^\circ N$, $70.25^\circ W$], panels e-f).

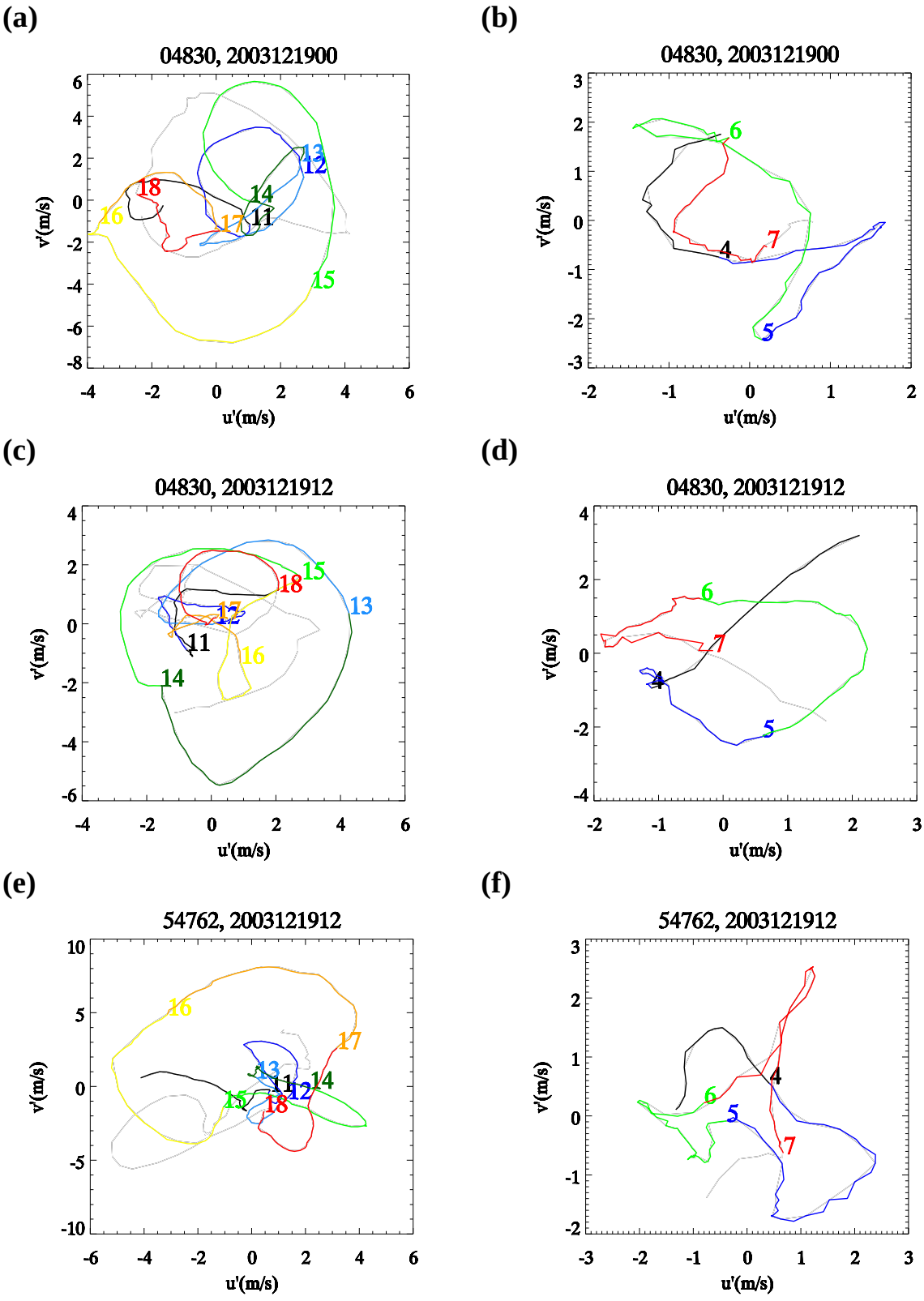
(a)
04830, 2003121900
v'(m/s)
u'(m/s)
(b)
04830, 2003121900
v'(m/s)
u'(m/s)
(c)
04830, 2003121912
v'(m/s)
u'(m/s)
(d)
04830, 2003121912
v'(m/s)
u'(m/s)
(e)
54762, 2003121912
v'(m/s)
u'(m/s)
(f)
54762, 2003121912
v'(m/s)
u'(m/s)

Figure 5.7: Hodographs from 10*km* to 18*km* (a) (c) and (e), and from 3*km* to 7*km* (b) (d) and (f) for station 04830 (Detroit, MI [$42.7^{\circ}N$, $83.47^{\circ}W$]) and 54762 (Grey, ME [$43.89^{\circ}N$, $70.25^{\circ}W$]). Time labels are the same as Fig. 5.6. The colors are in rainbow ascending order except the first 1*km* is marked in black. The corresponding altitudes (*km*) are marked with the same color.

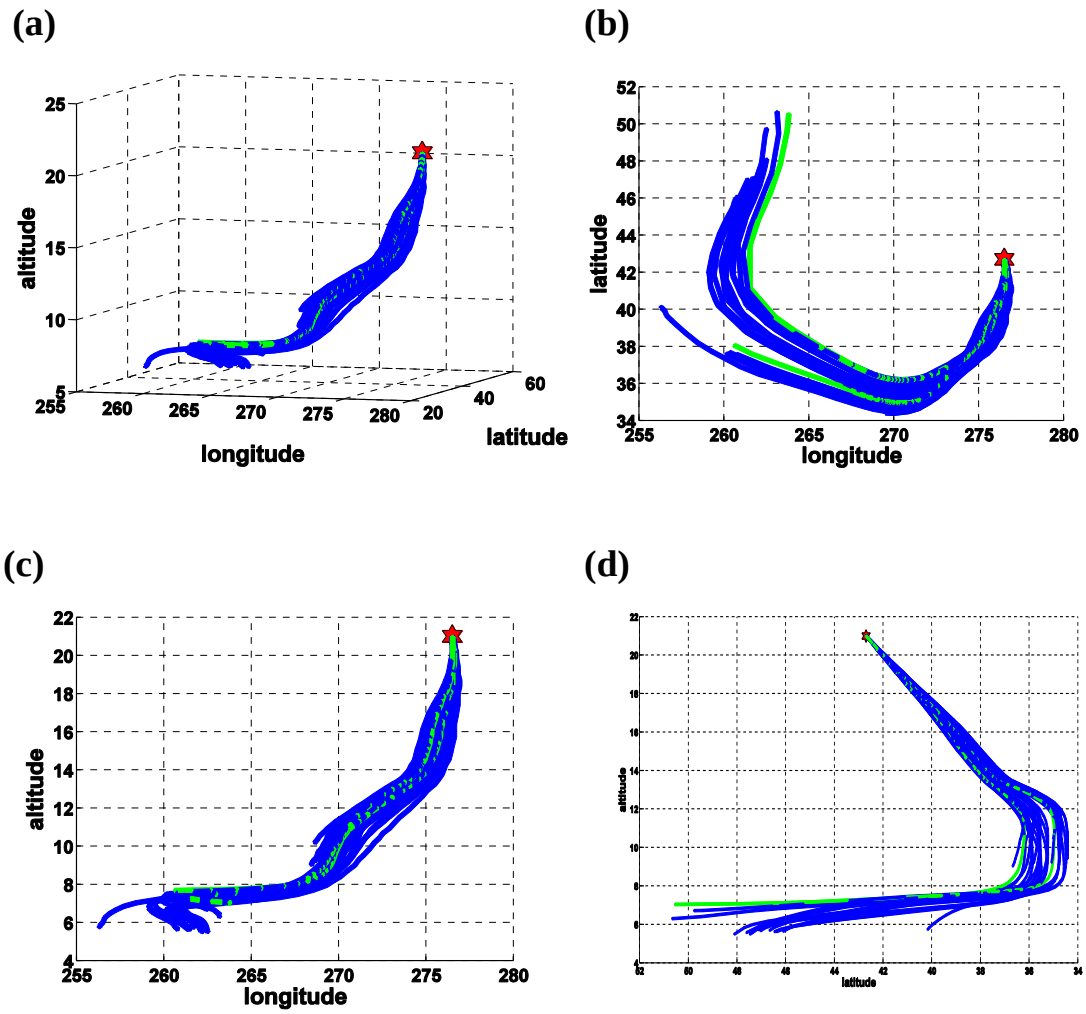

Figure 5.8: Rays released from 21 *km* over station 04830 (Detroit, MI) at 00UTC, 19th and their trajectories back in time. The blue rays break down because the WKB assumption is violated in z direction. The green rays are stalled vertically. Ray trajectories are viewed in different angles in three-dimensions (a), x-y (b), x-z (c) and y-z (d).

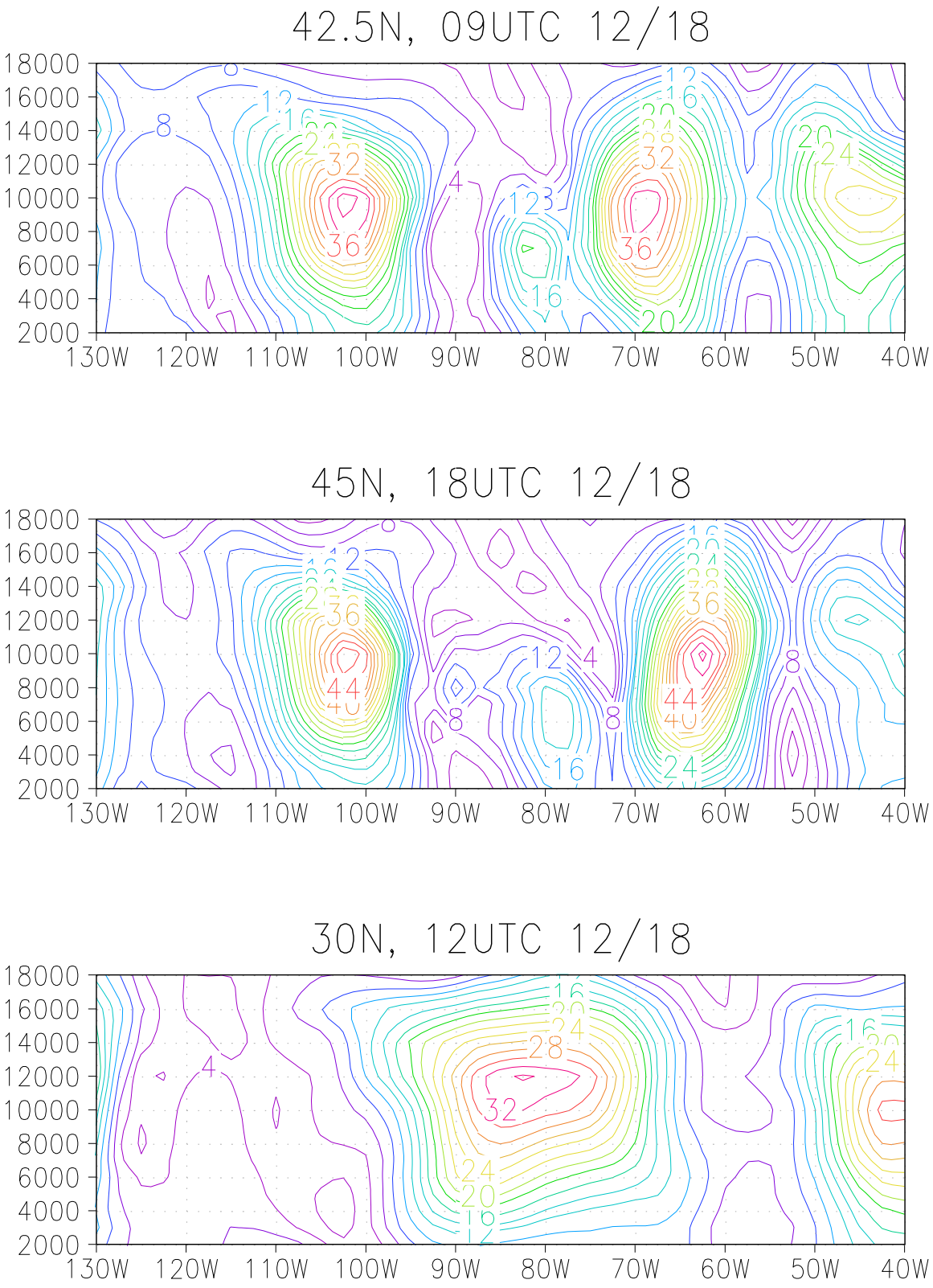

Figure 5.9: Cross section of jet centers (magnitude) at different latitudes and different time. The ordinate coordinate is the altitude (m). Contour interval is $2ms^{-1}$.

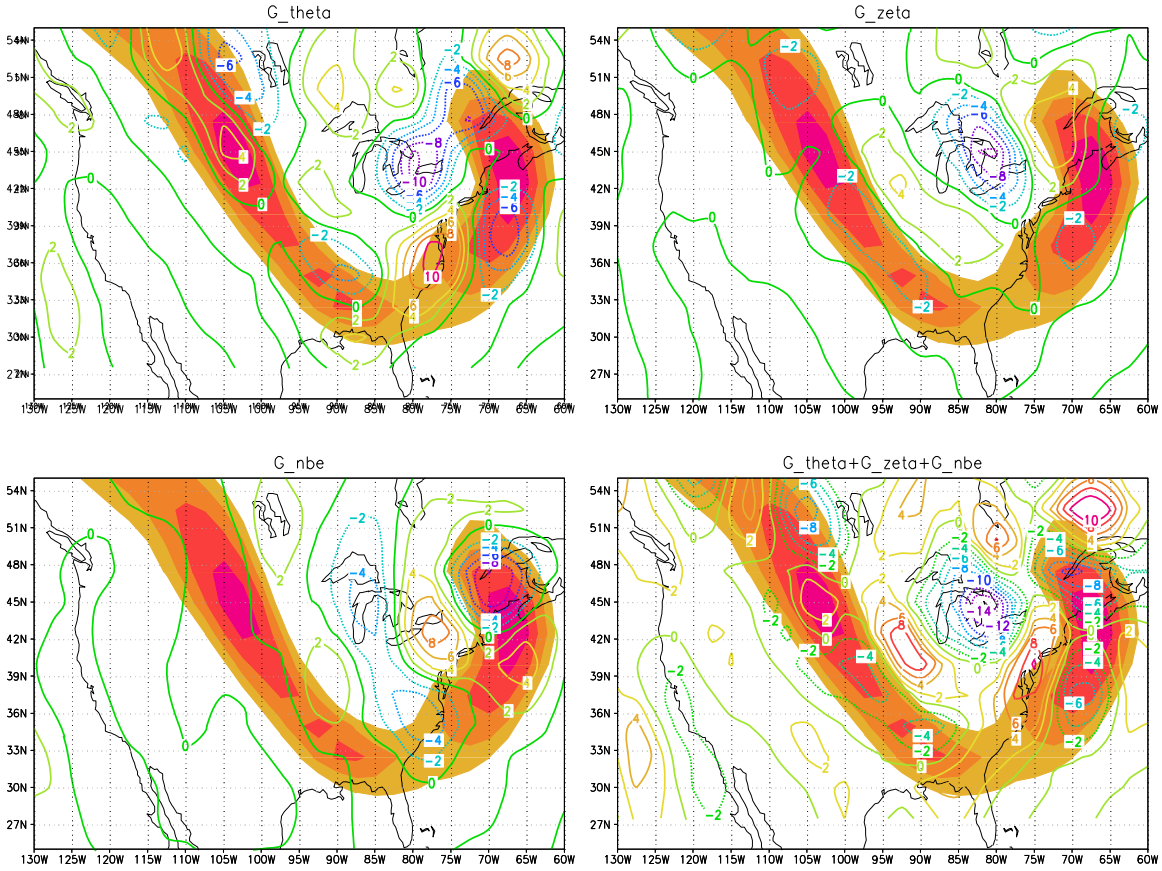

Figure 5.10: Spatial distributions of G_θ (top-left), G_ζ (top-right), G_δ (bottom-left) and the sum of the three (bottom-right) at 09UTC, 18th at 9 *km* (contours) overplotted on isotachs with wind velocities over $30 ms^{-1}$ being shaded. Contour values are multiplied by 1×10^{17} and the contour interval is $2\, m^{-1}s^{-3}$. Positive (negative) values are circles by solid (dotted) lines.

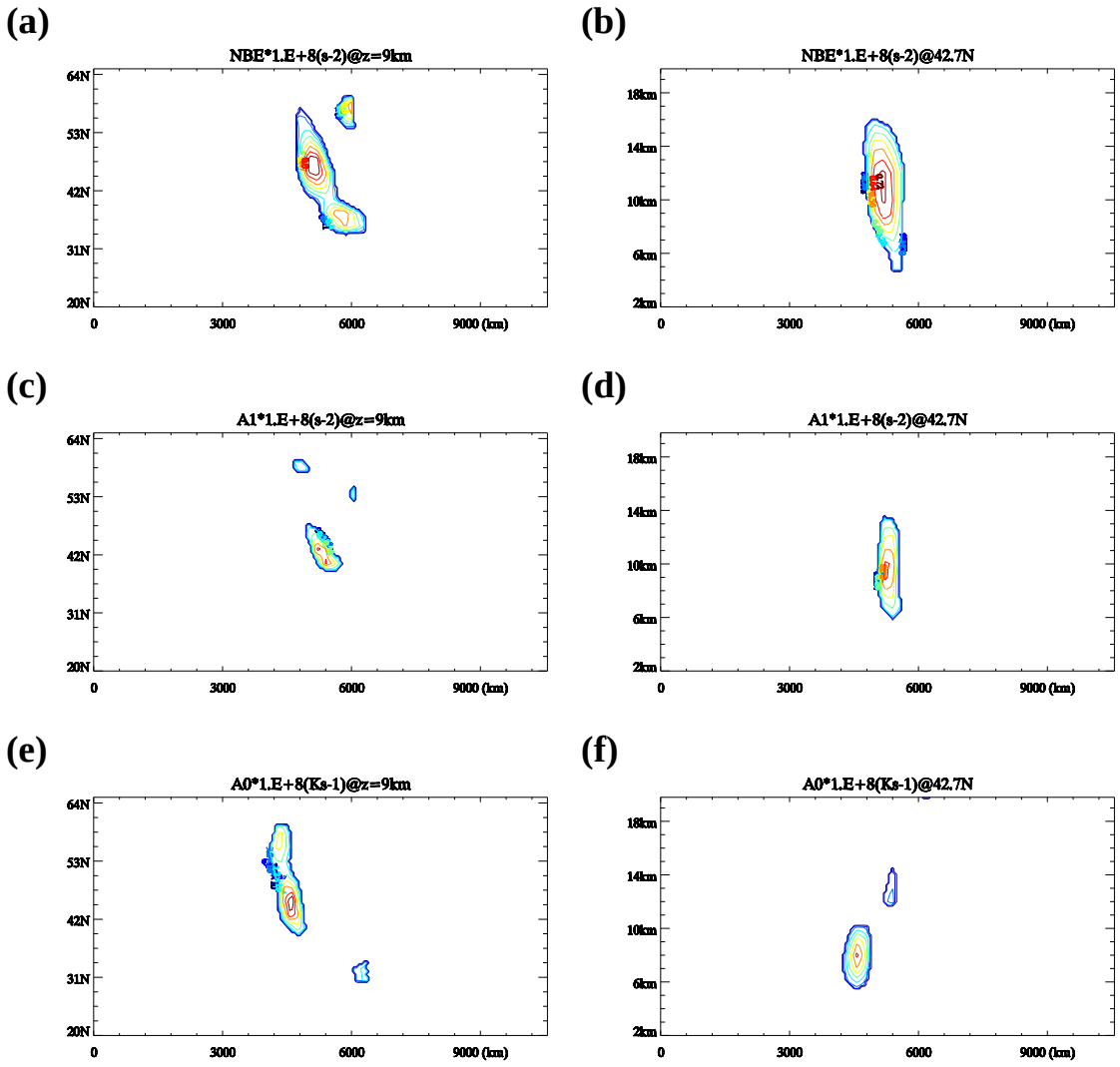

Figure 5.11: The solitary forcings of F_{δ} (a) (b), $A_{1,\zeta}$ (c) (d) and $A_{0,\theta}$ (e) (f) at 00UTC, 18th, viewing at z = 9 *km* (a, c, e) and cross-section at 42.7$^{\circ}N$ (b, d, f). All values are multiplied by 1×10^{8}.

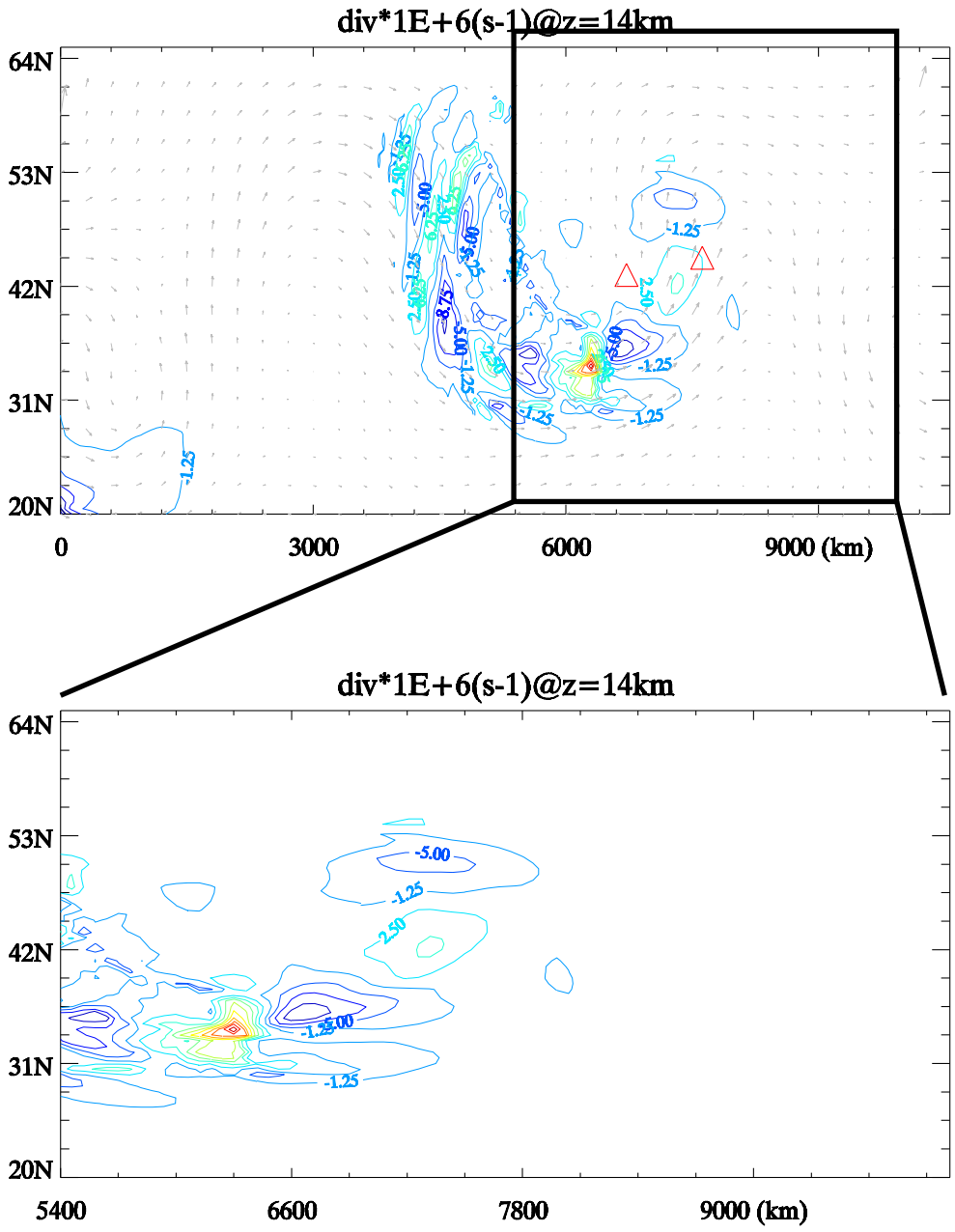

Figure 5.12: Horizontal distribution of the divergence field (s^{-1}) at $z = 14km$. The bottom panel is the enlarged view of the rectangle area in the top panel. All values are multiplied by 1×10^{6}. Stations 04830 (Detroit, MI) and 54762 (Grey, ME) are marked in red triangles in the top panel from left to right. The horizontal flow is overplotted also.

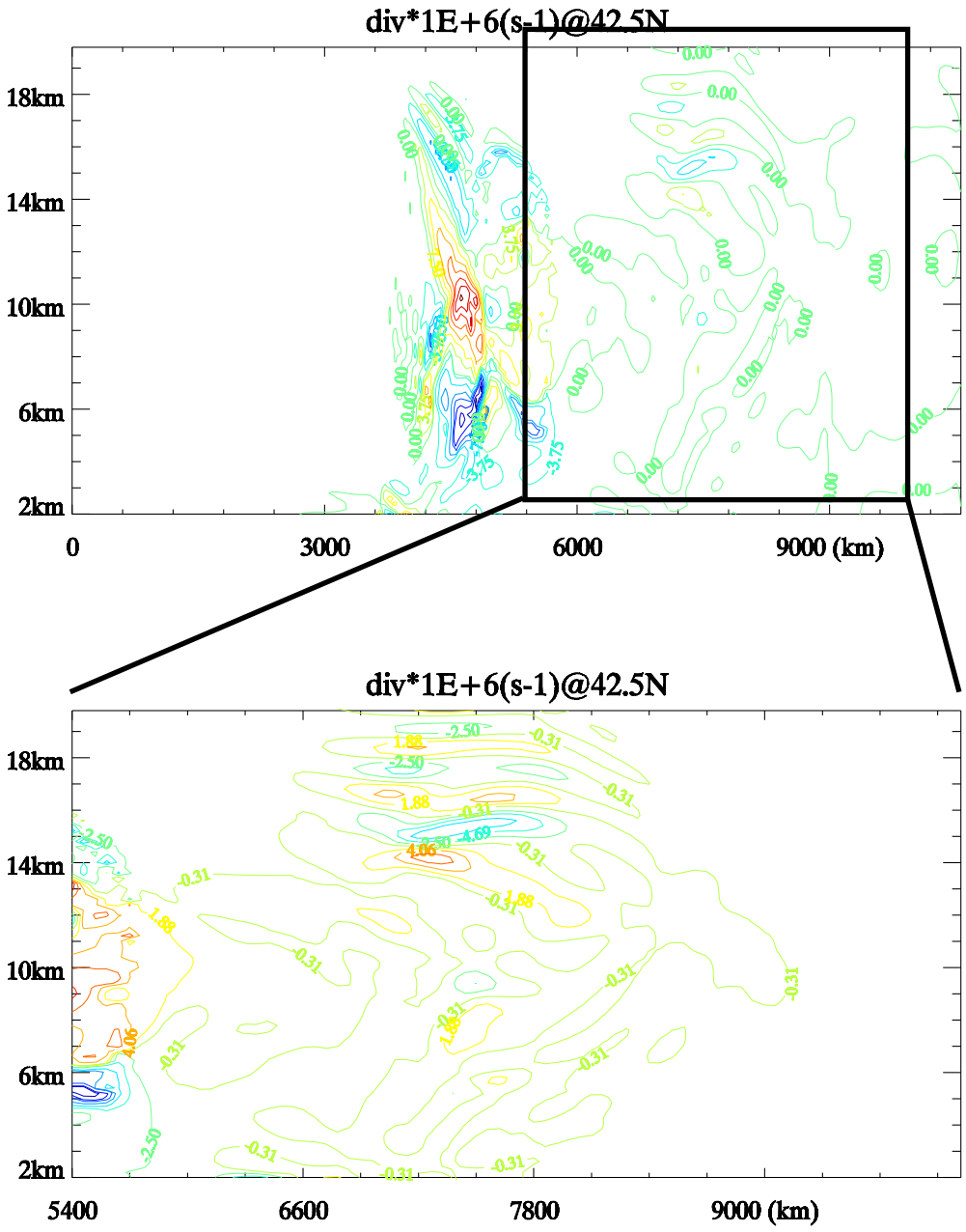

Figure 5.13: Same with Fig. 5.12, except for the cross-section taken at 42.5$^{\circ}N$.

(a)

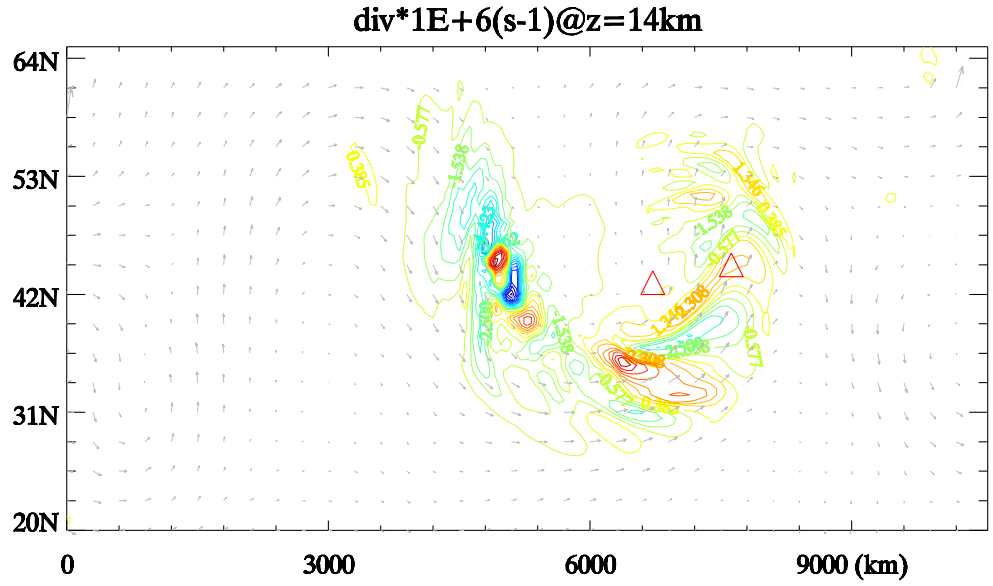

(b)

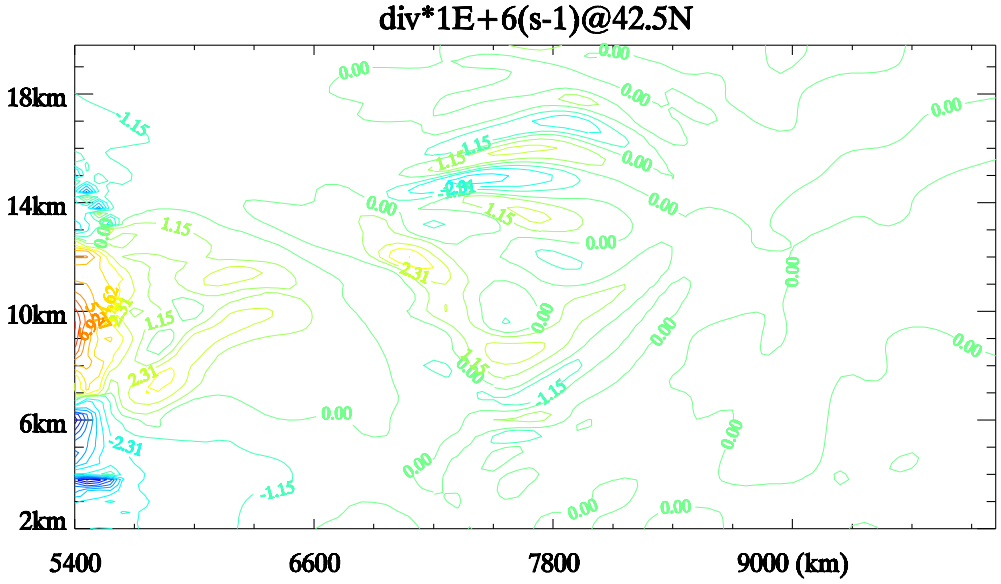

Figure 5.14: Horizontal map of the gravity wave field at $z = 14km$ (a) and the vertical cross-section taken at $42.5^{\circ}N$ to the east of 5400 *km* (b) for the "noA0" case. The station 04830 (Detroit, MI) is roughly located at 6700 *km*.

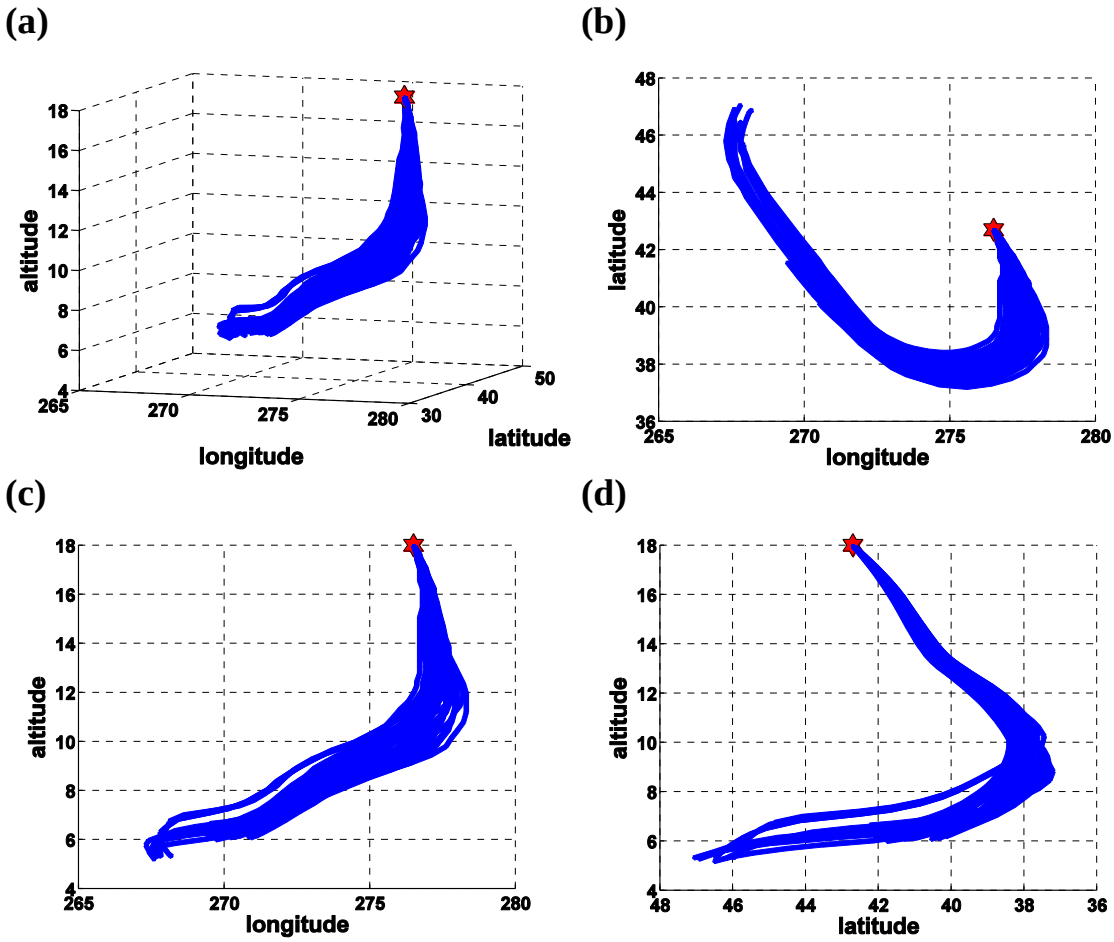

Figure 5.15: Same as Fig. 5.8, except for the rays are released at 12UTC, 19th at $z = 18km$.

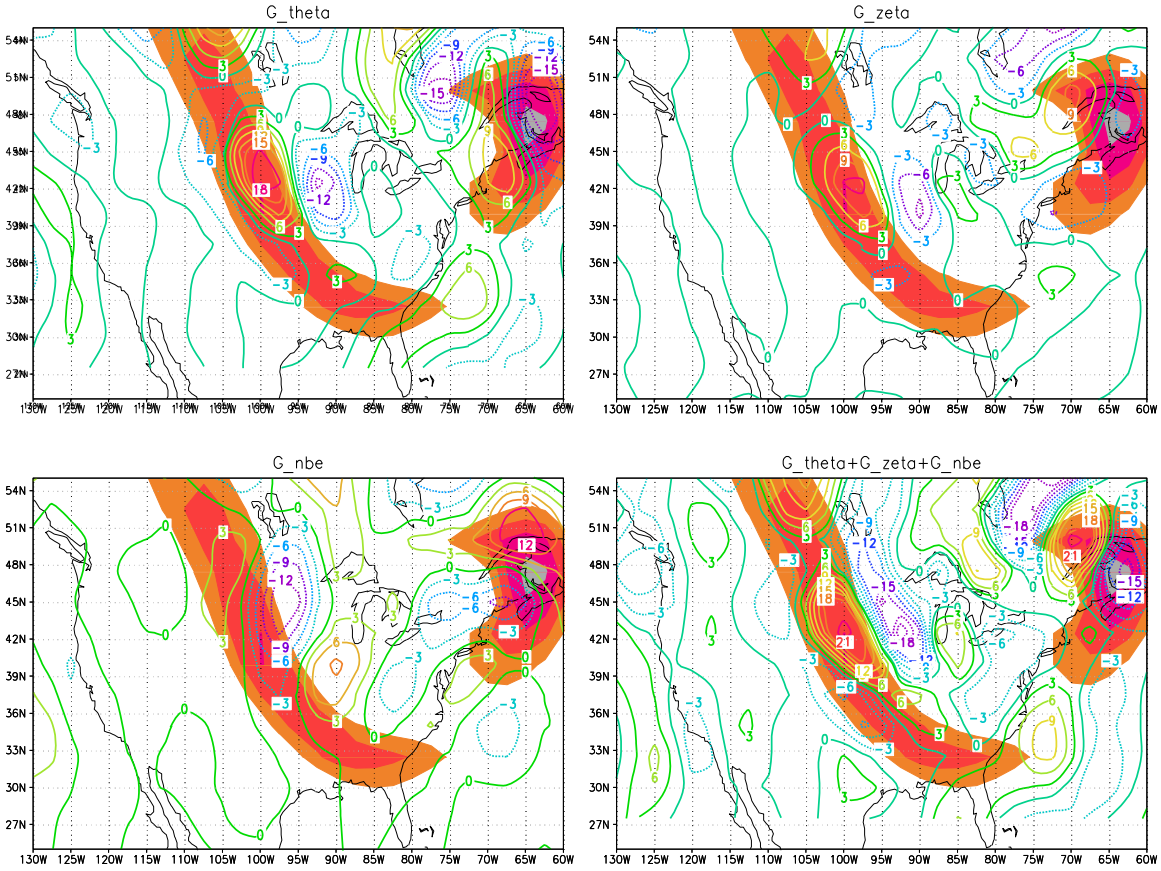

Figure 5.16: Same with Fig. 5.10, except at $z = 6km$ at 18UTC, 18th for the DIPOLE case. Wind velocities over $30ms^{-1}$ are shaded.

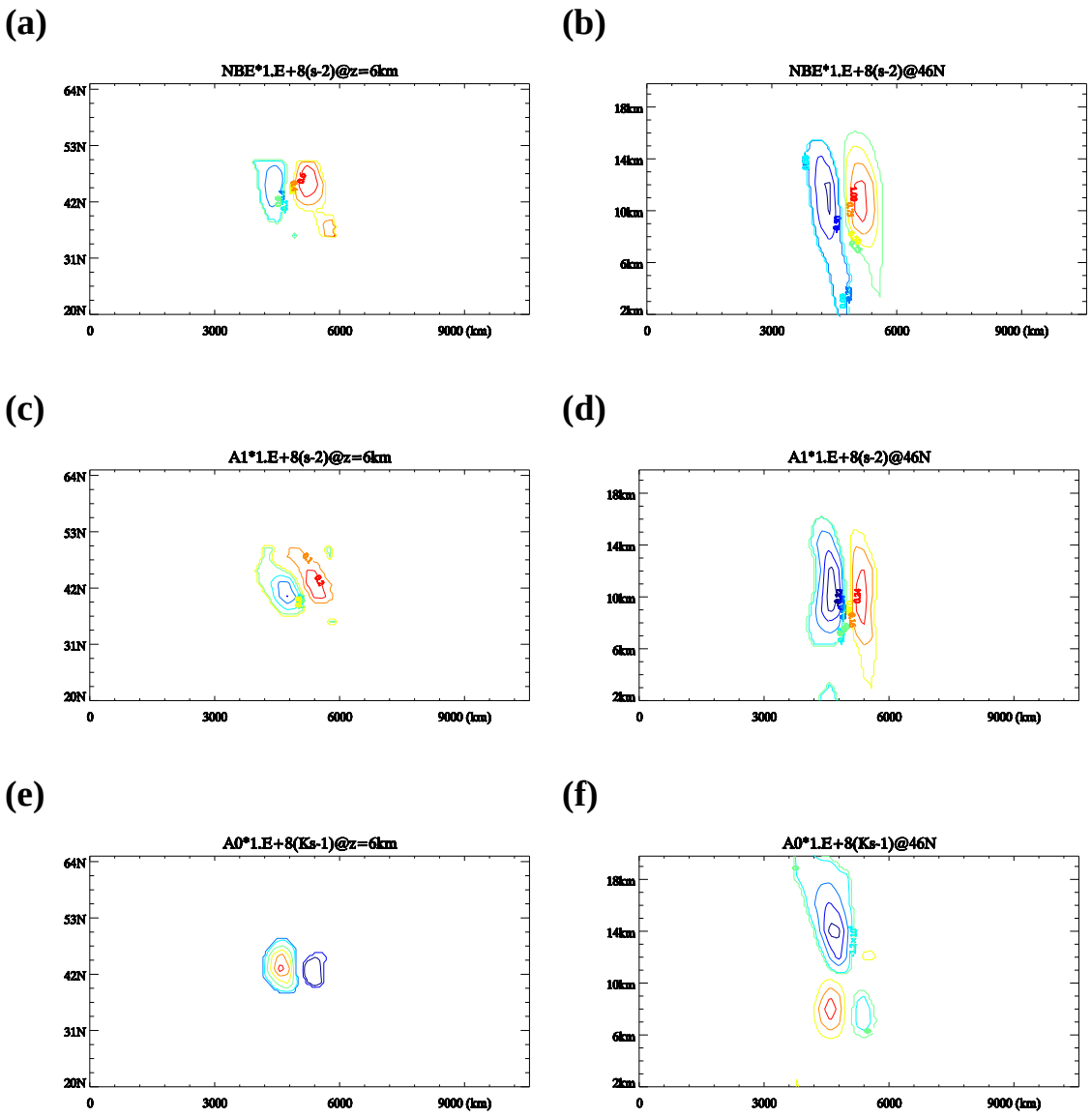

Figure 5.17: Same as Fig. 5.11, except the horizontal map is taken at $z = 6km$, and the vertical cross section is taken at $46^\circ N$ at 18UTC, 18^{th} for the DIPOLE case.

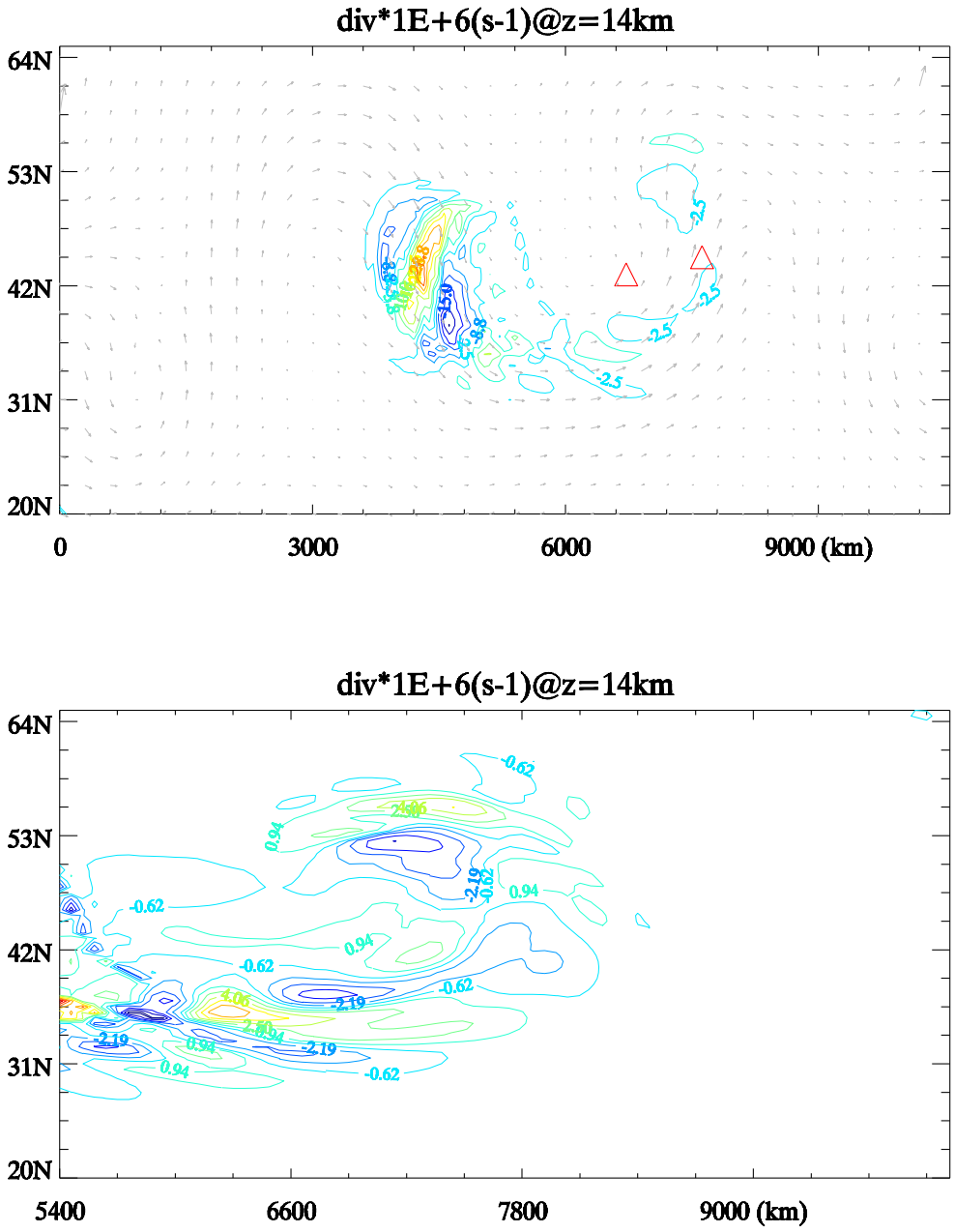

Figure 5.18: Same as Fig. 5.12, except for the DIPOLE case run.

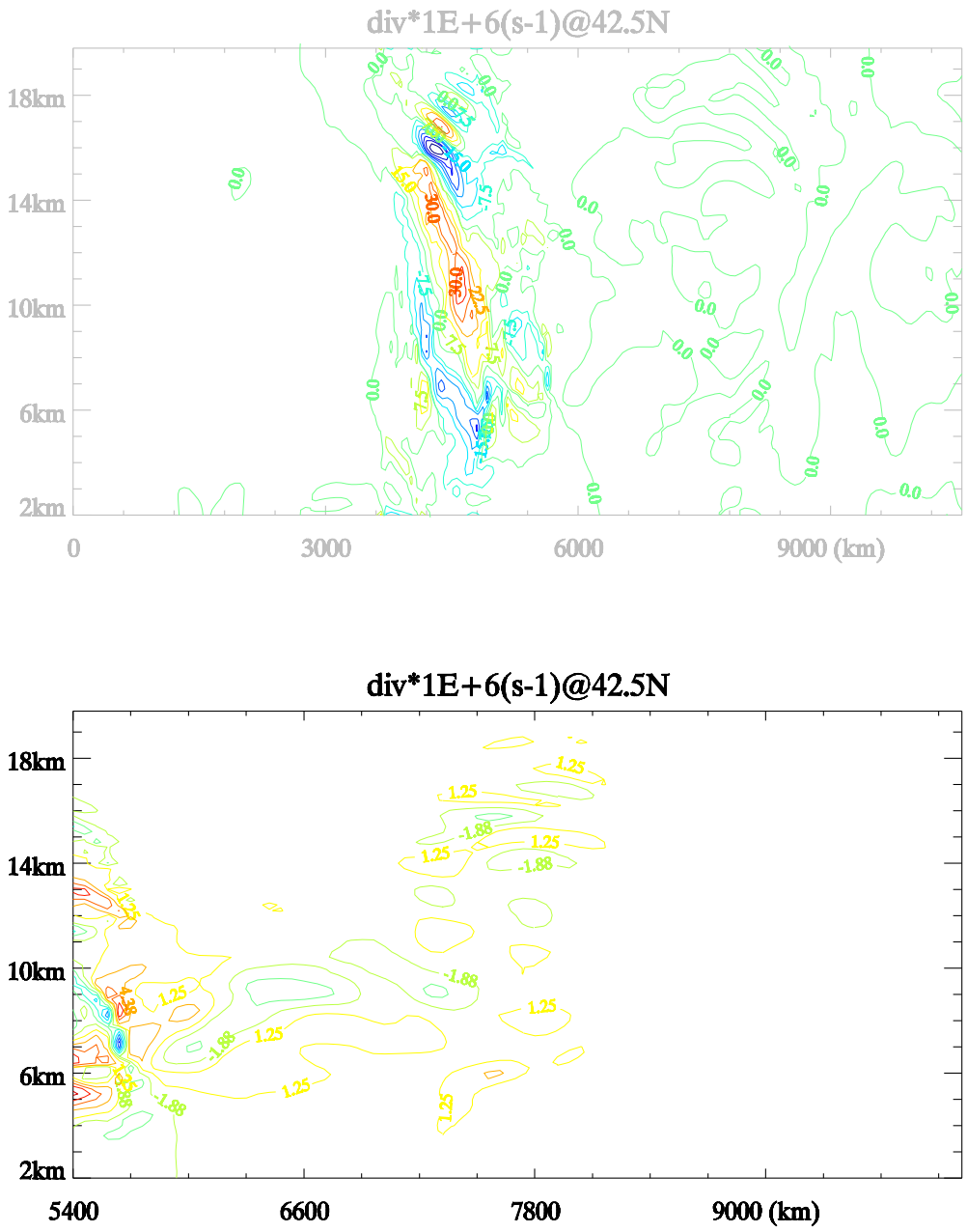

Figure 5.19: Same as Fig. 5.13, except for the DIPOLE case run.

(a)

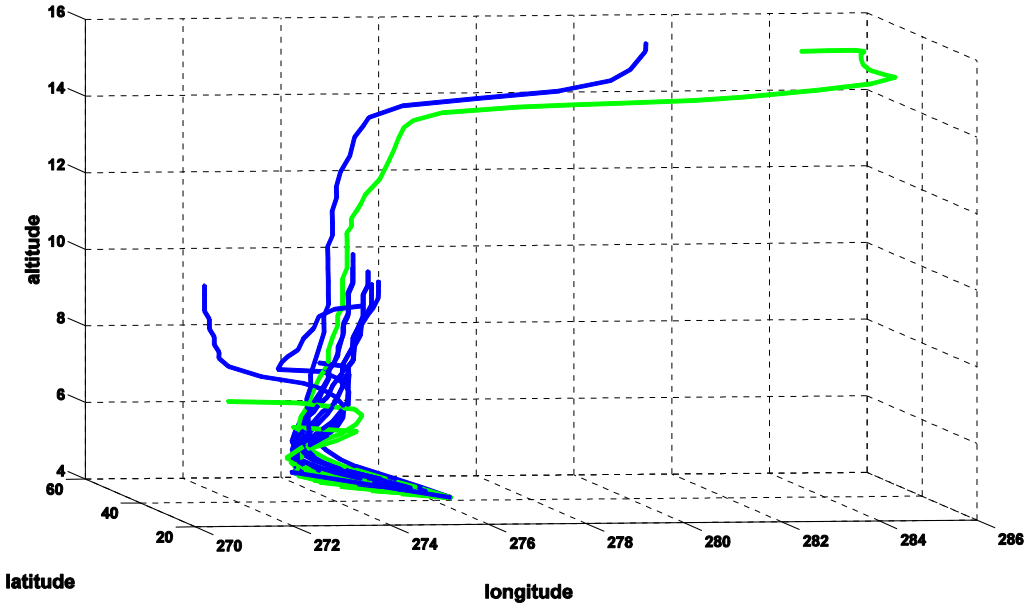

(b)

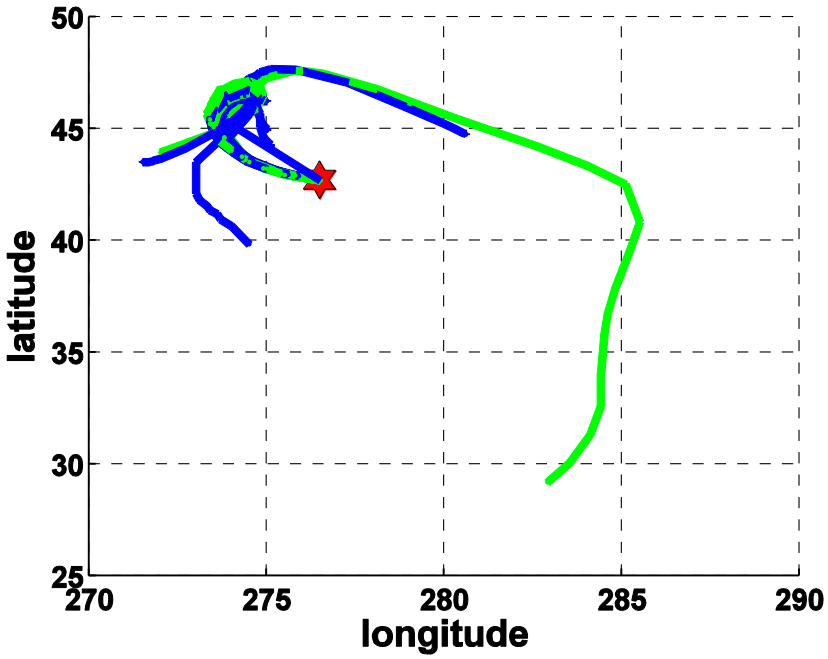

Figure 5.20: Three dimensional (a) and horizontal (b) map of the trajectories of the rays released from 4 km at 18UTC, 18th and traced back upward.

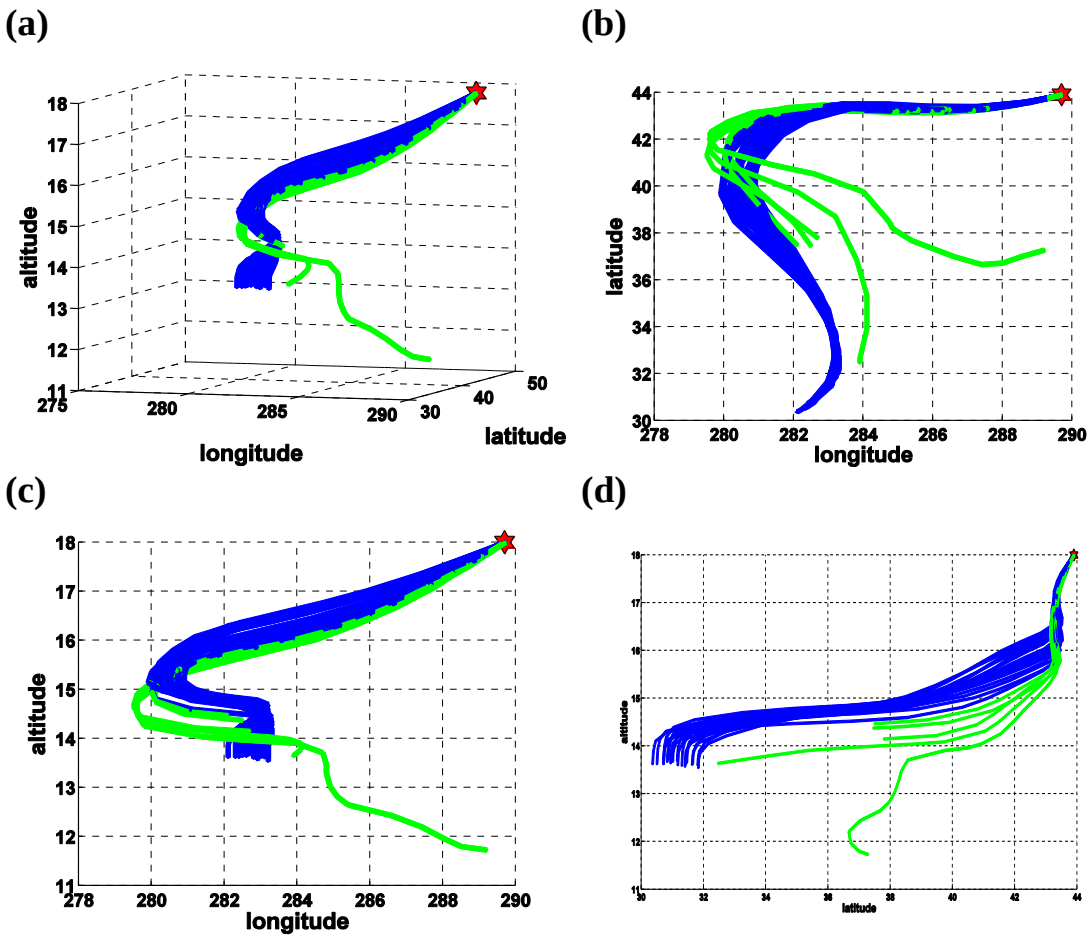

Figure 5.21: Same as Fig. 5.8, except for the rays are released at 12UTC, 19th at $z = 18km$ at station 54762 (Grey, ME).

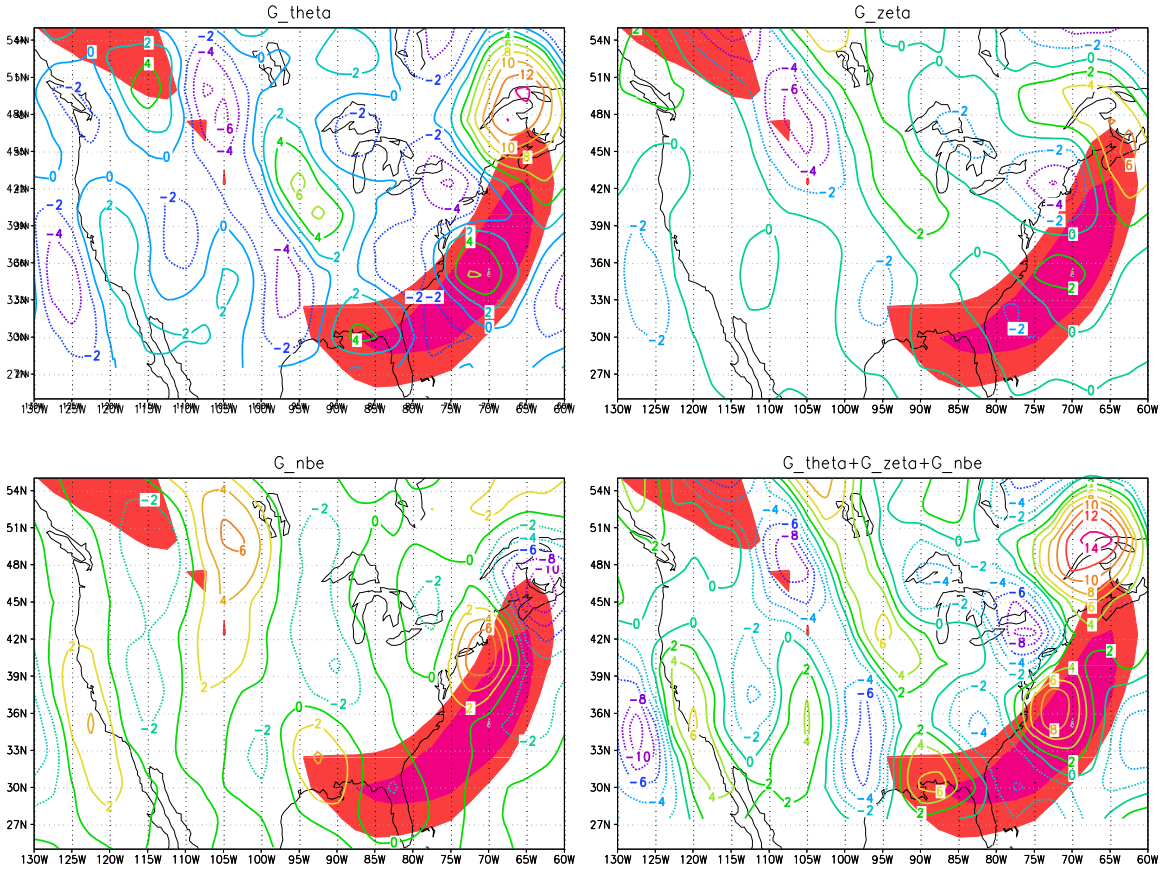

Figure 5.22: Same as Fig. 5.10, except at $z = 14km$ at 12UTC, 18th. Wind velocities over $25ms^{-1}$ are shaded.

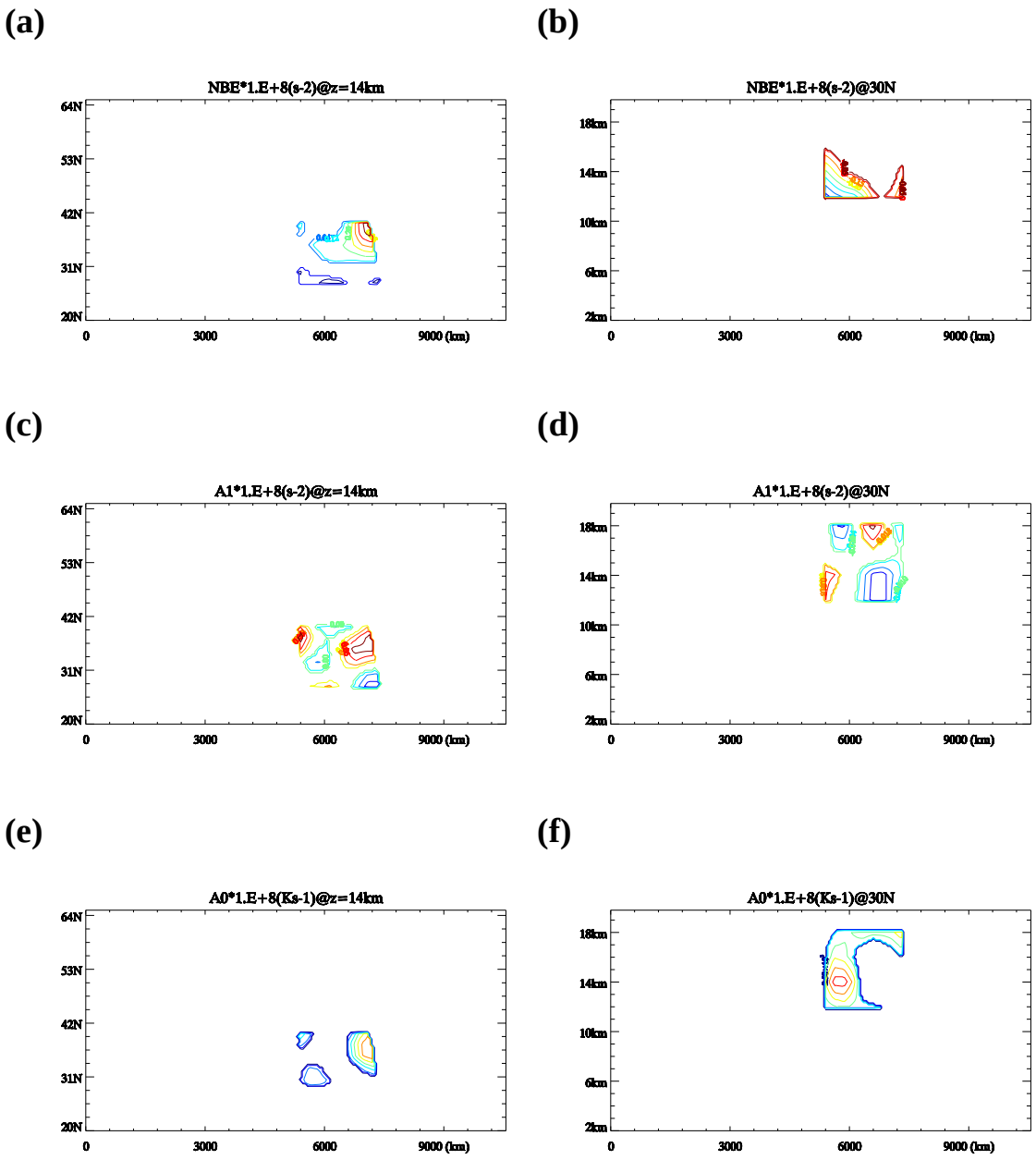

Figure 5.23: Same as Fig. 5.11, except that the horizontal map is taken at $z = 14km$, and the vertical cross section is taken at $30^\circ N$ at 12UTC, 18th for the CURVE case.

(a)

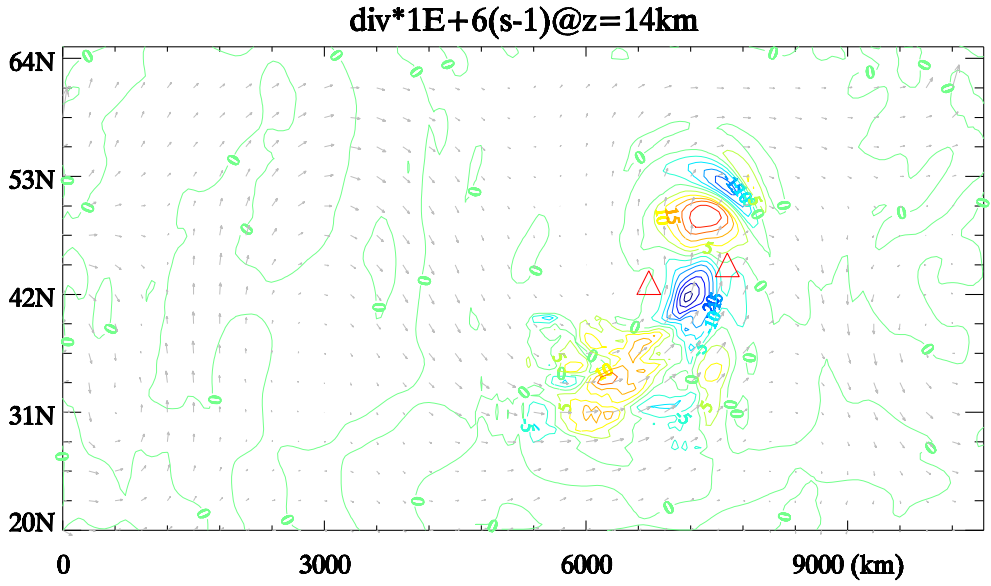

(b)

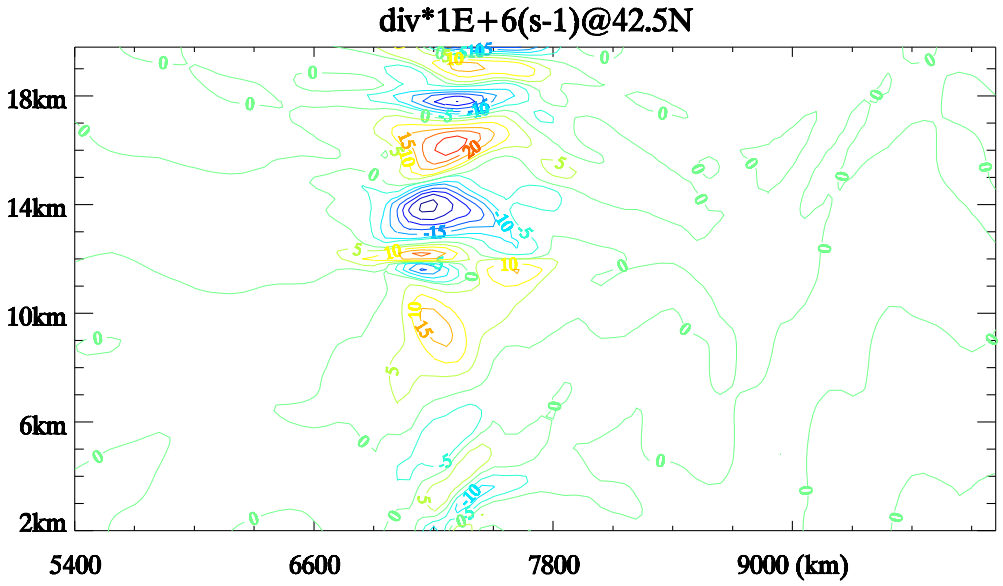

Figure 5.24: Same as Fig. 5.14, except for the CURVE case, starting from 12UTC, 18th.

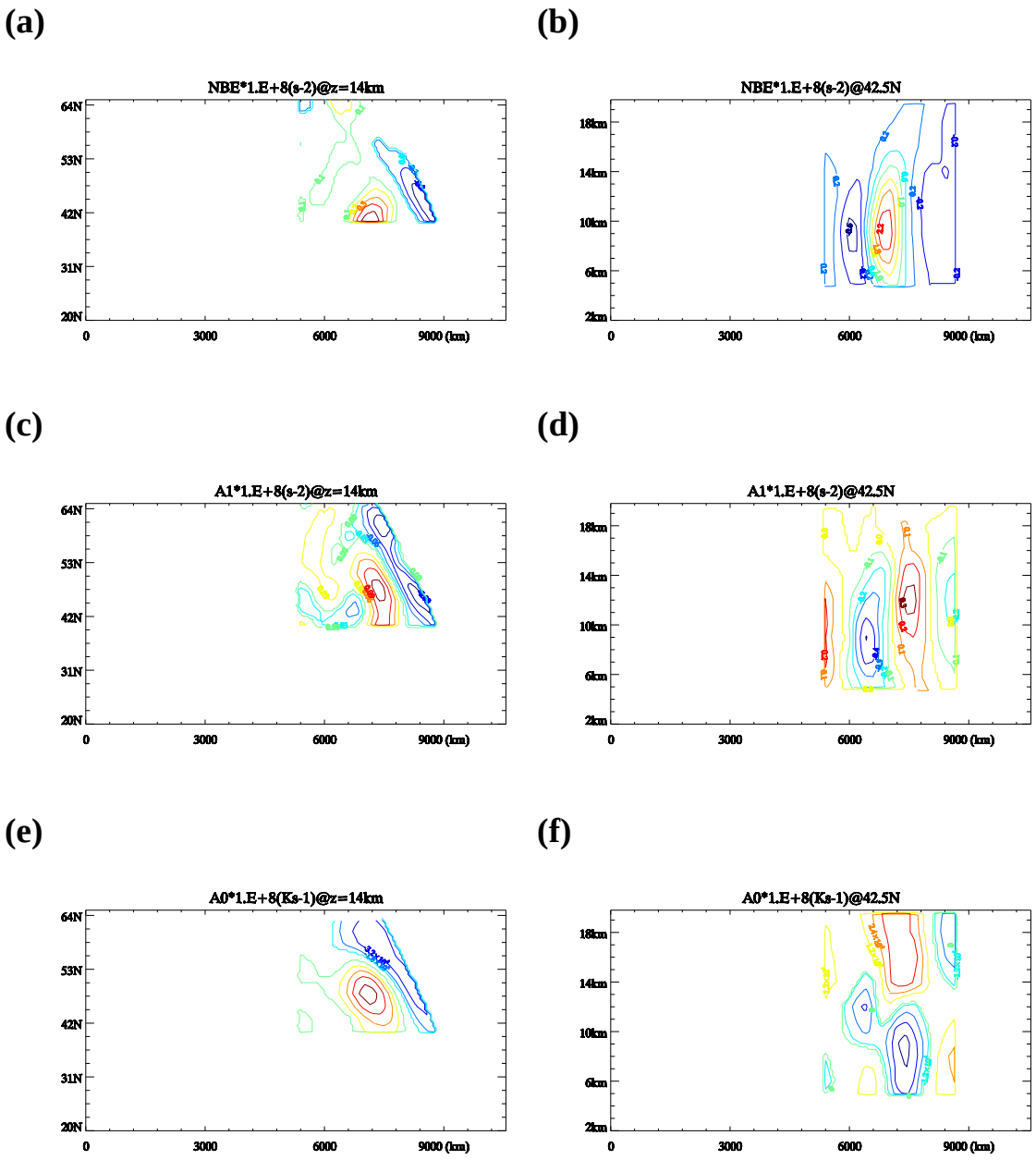

Figure 5.25: Same as Fig. 5.11, except the horizontal map is taken at $z = 14km$, and the vertical cross section is taken at $42.5^{\circ}N$ at 12UTC, 18th for the CYCLONE case.

(a)

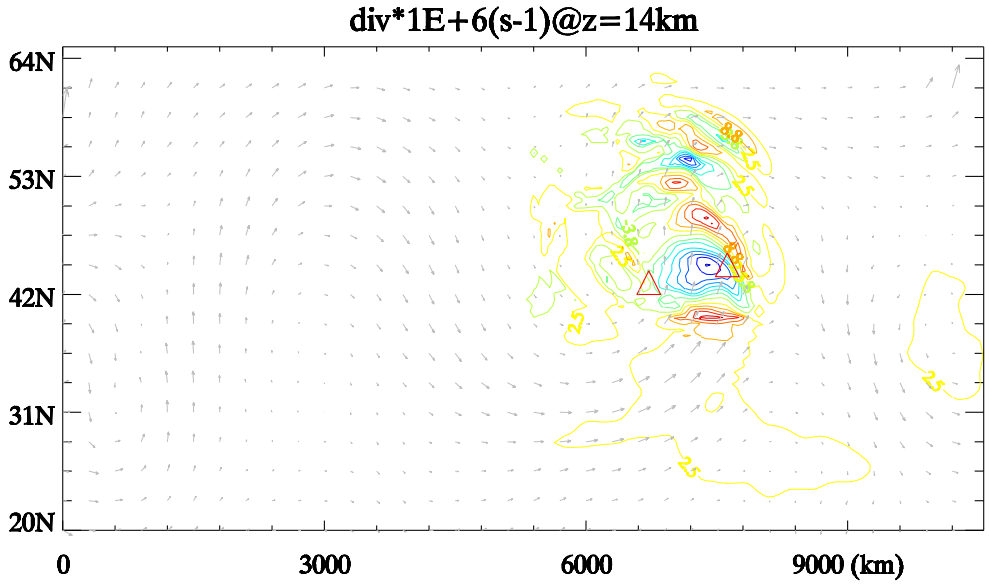

(b)

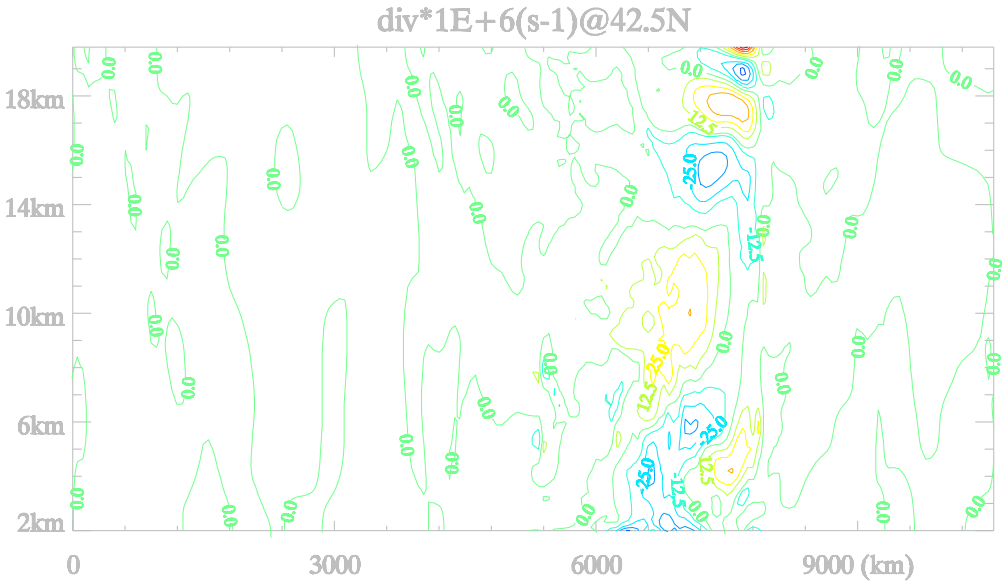

Figure 5.26: Same as Fig. 5.14, except for the CYCLONE case, starting from 12UTC, 18th.

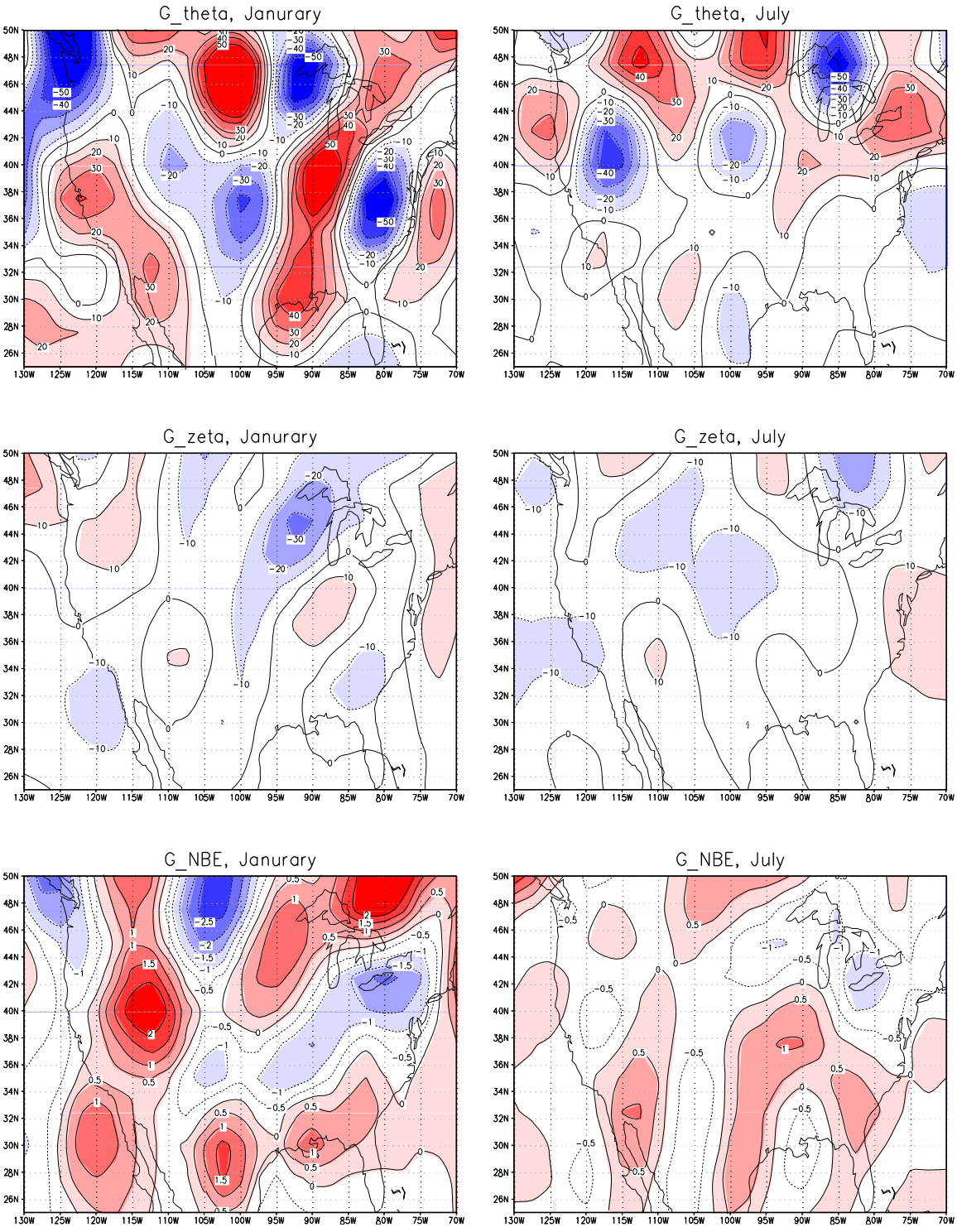

Figure 5.27: Nine-year (1998 - 2006) averaged G_θ (top), G_ζ (middle) and G_δ (bottom, G_{NBE}) of January (left) and July (right) over the contiguous US ($[70^\circ W - 130^\circ W, 25^\circ N - 50^\circ N]$). Values are multiplied by 1×10^{19}. The contour interval for the first two variables is $10 m^{-1}s^{-3}$, and is $0.5 m^{-1}s^{-3}$ for G_δ.

Chapter 6 Conclusions and Future Works

6.1 Conclusions

Understanding gravity wave sources is an essential path forward for improving general circulation models (GCMs) through properly including gravity wave effects. My Ph.D. work is to analyze, diagnose and simulate the source behaviors of gravity waves that are observed in the US high vertical-resolution radiosonde data. Two sources - convection and jet imbalance - are the gravity wave sources concentrated upon in this dissertation.

A ray-tracing gravity wave model GROGRAT is used to characterize the "mean" source spectrum of gravity waves in the lower stratosphere that are observed from US high vertical-resolution radiosonde profiles on a monthly scale. With a fixed source spectral function, one can get "best-fits" for most stations. A universal source function is found to be most powerful in capturing the major features of the variations, while another, which represents the convection source, works better for tropical stations.

The fluctuations in ascent rate profiles are likely to be representative of higher-frequency gravity waves that are generated from the convection sources during warm seasons. This provides the motivation to investigate radiosonde ascent rates in an analogous manner to previous investigations of radiosonde horizontal wind and temperature profiles.

GROGRAT and a linear forcing-response model are employed to study a baroclinic wave case, where the observed gravity wave characteristics generated from jet streaks

embedded at different locations are successfully modeled. The climatologies of the three forms of forcings that appear in this linear forcing-response model are also analyzed.

6.1.1 Gravity wave mean source spectra

The mean gravity wave source spectra constrained by observations in US high-vertical-resolution radiosonde data are studied on a monthly basis. Five forms of gravity wave source spectra that were used in *Alexander and Vincent (2000)* are implemented in the ray-tracing model GROGRAT over 85 US. stations where sufficient high vertical-resolution radiosonde data was available. Myriad combinations of wave parameters are tested one-by-one, and the simulated kinetic energy density *KE* and the zonal component of the vertical momentum flux *M* within the lower stratosphere section (18 - 24.9 *km*) are compared with those derived from observations. A set of "best-fit" criteria is specified, and we find a "best-fit" for 61 out of the total of 85 stations, using fixed source spectra throughout the eight-year (1998 - 2005) period.

The "best-fit" stations share some common characteristics. A high correlation between *KE* and *M* is almost always necessary to reach a "best-fit" solution. This is predicted by theory. The source must be just below the region of consideration. This is attributed to the climatological nature of both the representation of the physical sources and the wave propagation.

The "best-fit" source spectra are always anisotropic as long as the zonal wind at the source level is not zero. Moreover, most of the momentum flux is directed upstream of the dominant wind direction. We claim that the propagation effect below the source level is likely to be the main influence for shaping the anisotropic source spectra that are seen.

Having pointed out the importance of propagation effects, the "best-fit" source spectra still reveal some features that might be indicative of real physical sources. A source spectrum representing a "mean" convection source works better for most of the tropical-subtropical stations, while the most general source works better for mid-high latitude stations. The "best-fits" have difficulties in simulating the weak positive momentum flux during summer for the mid-latitudes, and it is also hard to find "best-fits" for the central US region, where organized mesoscale convective systems play an important role during summer. All of the above evidences suggest the necessity to apply different dominant sources for different seasons in GCMs, and also geographical differences should be taken into account. For example, the horizontal wavelength should be specified longer in the tropics and shorter in mid-high latitudes. An eastward anisotropic source spectrum is suggested in the tropics, and a westward anisotropic source spectrum is suggested for other latitudes. Recommended "best-fit" parameter sets for GCM modelers are provided for three regions.

This aspect of my dissertation research originated from extending the studies of *Alexander and Vincent (2000)*, and it reveals some very intriguing features. This is the first large-scale calculation of "best-fit" gravity wave source spectra for gravity waves observed in the high vertical-resolution radiosonde data in the lower stratosphere. Compared with other studies done to explicitly take into account individual sources of gravity waves (topography, convection, etc.), our techniques do not depend on the details of the specification of individual sources, yet provide a proper source spectrum beneath the layer of interest. This study also points out the importance of propagation effects. The idea is applicable to other types of observations.

One caveat for this aspect of this dissertation is that the gravity waves being observed and which provide the constraints on the source spectra are mainly long-period inertial gravity waves. These waves, however, likely play a significant role in the stratosphere.

6.1.2 Higher frequency gravity waves and convective sources

The fluctuations in the ascent rate profiles are analyzed for gravity waves. The newly defined variable, *VE* (essentially, the kinetic energy density due to the vertical velocity perturbations), as well as the apparent dominant vertical wavelength derived from the perturbation field of the ascent rate are analyzed on a climatological basis.

In the tropics, *VE* is closely correlated with convective clouds and precipitation in both the troposphere and the lower stratosphere, indicating the gravity waves in the ascent rate perturbation profiles are probably generated by local convection. The results agree well with *Lane et al. (2003)* in the lower stratosphere, while it is the first time that the coherence of *VE* and convective signals in the troposphere is discovered.

The diurnal variations of *VE* as well as the apparent dominant vertical wavelength peak at times when local convection is favored in the troposphere. They also show strong summer maxima in the mid-latitude troposphere, which is quite different from the winter maxima patterns of *KE* and *PE*. Both these bits of evidence suggest these waves are emitted from convective sources mainly during warm seasons. This is the first time that this type of study has been applied at mid-latitudes. The good correspondence between the geographical distribution of the diurnal variation of *VE* and those of local convection suggest the usefulness of the fluctuation in radiosonde ascent rate to study the behavior of the convective gravity wave source.

Given the high coherence of the diurnal variations in *VE* and local convection in the troposphere, it is interesting that the coherence between these patterns is much weaker in the lower stratosphere. A heuristic ray-tracing experiment using GROGRAT is carried out to investigate this difference between the tropics and the extratropics. The results of this suggest that most of the gravity wave rays forced by convection at a mid-latitude station either encounter critical-levels or are Doppler-shifted toward longer vertical wavelengths, in which case the waves are moved out of the "observational window" (i. e., the wavelength range being analyzed). This is not so likely to happen in the tropics due to the weak winds and wind shears there. This result has important implications for parameterizations of convective gravity wave sources in GCMs in that the convective source needs to be more carefully and more accurately parameterized in the tropics, while it may be a less important issue in mid-latitudes, since the mean flow there plays a more significant role in shaping the spectrum during wave propagation. This conclusion is consistent with our "best-fit" spectra work in that the convective source spectrum works better in the low latitudes, while a most general source spectrum, largely affected by the propagation factor, works the best for mid-high latitudes.

The seasonal variations of $\overline{KE}$ and $\overline{PE}$ are revisited (extending Wang's, 2003, work), but from a different perspective this time. The ratio between $\overline{KE}$ and $\overline{PE}$, and $\overline{VE}$ and $\overline{PE}$ are used to derive gravity wave intrinsic frequency information. After accounting for the effect of averaging processes, the derived intrinsic frequency from the ratio between $\overline{VE}$ and $\overline{PE}$ is significantly larger than that from the ratio between $\overline{KE}$ and $\overline{PE}$, and the former shows spatial and temporal patterns that largely coincide with convective activity, again demonstrating convection as an important source for the higher-frequency waves,

which are seen in the ascent rate perturbation field. This result is meaningful in that it points out the potential to extend the visibility of radiosonde soundings into higher frequencies and shorter horizontal wavelengths if we include information from fluctuations of the radiosonde ascent rates.

Moreover, a simple model is employed to simulate the correlations among three energy forms. The "best-fit" frequency spectra suggest a *p* value of 1.2 in the troposphere, and 2 in the lower stratosphere, agreeing well with what has been observed using the same dataset but using entirely different techniques (Wang, 2003) or other completely different datasets (VanZandt, 1987).

$\overline{VE}$ at high latitudes shows strong winter maxima in both the troposphere and the lower stratosphere, as well as in the mid-latitude lower stratosphere, where the summer peaks become secondary signals. Aside from propagation effects and/or variations in the background state, this can be attributed at least partly to the annual variation of the spontaneous emission source from jet imbalances.

6.1.3 Spontaneous emission from the jet imbalance source

Both the first and the second part of this work indicate that US high vertical-resolution radiosonde data may be sensitive to gravity waves that are emitted from jet imbalance sources, yet this is the least understood, and least studied, of the major gravity wave sources so far, compared with topography and convective sources. In the third part of my work, the spontaneous emission from jet streaks are studied using two complementary, but quite different approaches, for an observed baroclinic wave case.

Several ray-tracing experiments using GROGRAT and the wave parameters derived from observations are carried out back in time in the lower stratosphere. The rays are traced back to various jet streak sources, where the forcings resulting from the nonlinear balance residuals of the primary flow are the largest. A linear forcing-response model is then employed to study the spontaneous emission from these forcings.

Only the positive forcings and the dipole forcings associated with specific jet streaks are studied, and it is found that the positive forcing is the key component to generate the waves we observe. In general, the simulated gravity waves have the largest amplitudes at the exit region of the jet, but the wave field can extend a great distance downstream of the jet. The three components in the nonlinear balance residual forcings have different importance for different cases, but the forcing resulted from the divergence part of the residual of the nonlinear balanced equation is in general the smallest, and it tends to offset the effects from the other two forcings. Furthermore, the overall gravity wave field seems to be not too sensitive to the details of the forcings, as long as we are able to correctly prescribe the forcings associated with the designated jet streak. There is no evidence showing that the wave amplitude is proportional to the strength of the unbalanced forcings. The configuration of the forcings seems to be more closely related to the amplitude of the emitted gravity waves than the jet strength itself. However, the wave intrinsic frequency might be associated with the size of the forcing region, although many more experiments need to be carried out before we are confident about this point. Model simulations work well in the lower stratosphere, but not in the troposphere, at least for this specific case. We believe that other gravity wave sources might play more important roles there, such as surface fronts and convective activity along the front.

This case study is a new approach to bridge the gap between observations and numerical simulations of spontaneous emission from jet imbalance sources. It suggests the possibility of incorporating proper forcings associated with jets in GCMs to represent jet imbalance sources. The advantages of this include no need to specify the gravity wave launch level, and no need to tune the wave intermittency since it follows naturally. As a pilot investigation, however, it is far from perfect, and a lot of work needs to be done before practical applications into GCMs can be realized.

6.1.4 Summary of implications of GWD parameterization in GCMs

The primary goal of this research is to supply useful information for improving GWD parameterization in GCMs. In this setion, I'll summarize the major points in this regard that we have learned from this study.

Currently most state-of-the-art GCMs use uniform GWD parameterizations that vary neither with location nor with time. This simplification is unrealistic, and our study suggests that omitting the geographic variations or temporal variations could directly lead to the neglect of one or more important gravity wave sources.

Secondly, this research suggests that the wave source function specified in GCMs at a certain altitude is actually a representation of "wind shaped" physical sources. Since the wind/wind shear is typically smaller in the tropics than in the mid-latitudes, this conclusion also suggests that proper specification of the source spectrum is more crucial in the tropics than in mid-latitudes, and hence the modeler needs to be more careful when dealing with tropical GWD sources. It also implies the necessity to examine more observations in the tropics to constrain the source spectra.

Radiosondes contain more information than what has been commonly expected before to constrain the convective source. This investigation extends the coverage of radiosondes to include higher frequency waves that are closely associated with convective sources. Nevertheless, how to best utilize the information underlying in the ascent rate perturbations is a challenging topic.

Last but not the least, the specification of the jet imbalance source, which hasn't been seriously considered in any GCMs, can be approached through the three imbalance forcing terms. The wave generation is spontaneous in this way, and hence the wave intermittency is thus determined within the model. A stochastic approach may be combined with this method to determine the source spectrum (e.g., Dunkerton, 1982).

6.2 Future Works

I will present my observations of needed future research in this section. Some of them are rather straightforward extensions of my previous work, and some of them are long term goals.

- The mean source spectra simulations do not include considerations of the meridional wavenumber. As a matter of fact, the meridional component of the momentum flux is sometimes even larger than the zonal component, and negligence of this component of the momentum flux could cause failure of simulations. As shown in Fig. 6.1, the observed meridional component of the vertical momentum flux is greater than the zonal component at mid-latitudes in some years (compared with Fig. 3.10), and the simulations carried out south of $25^{\circ}N$ without considering meridional wavenumber

fails to capture the summer minimum of the meridional component of the momentum fluxes there. Therefore, it is necessary to take this factor into account.

- The combination of source spectra for different seasons (e. g., using the one representing convection in summer, and the most general one in the other three seasons) could solve the key issue that the observed positive zonal component of the momentum flux in mid-latitudes is not captured by the simulations. Other source spectra can also be tested. Also, we can apply our methods to other observations such as satellite measurements, etc..

- The difficulty of using only ascent rate profiles is that it is hard to determine all gravity wave parameters from single sounding. Cross wavelet analysis could be a potential way to solve this difficulty (Wang and Alexander, 2007). Introducing other observations, such as GPS temperature profiles might be another way, although one needs to be cautious about the "observational window" issue. Once a greater range of gravity wave parameters are obtained, they can be a large resource of observations that could constrain convective source parameterizations in GCMs.

- The third part of my work is quite encouraging, yet far from maturity. A comprehensive model run bears the brunt of priority using complicated non-hydrostatic and nonlinear models such as WRF or MM5. As a short time goal, a long-time run (e. g., about one month) of the linear forcing-response model can be carried out in order to realize real-time comparisons between simulations and observations. The background flows as well as the forcings need to be able to be updated constantly, or even to develop and interact with the generated gravity waves in the model. This requires a domain size as large as a half-hemisphere, and the geometry of the sphere

as well as the beta-effect need to be taken into account also. Other observational techniques, such as GPS, can be employed for better validations of the model results.

- Under a global warming scenario, storm tracks would shift their location, and their strengths would also likely change (Yin, 2005). How could this affect the global gravity wave source distributions? In turn, how would the GWD change impact the mean flow and the jet systems? These are interesting yet difficult questions to answer.

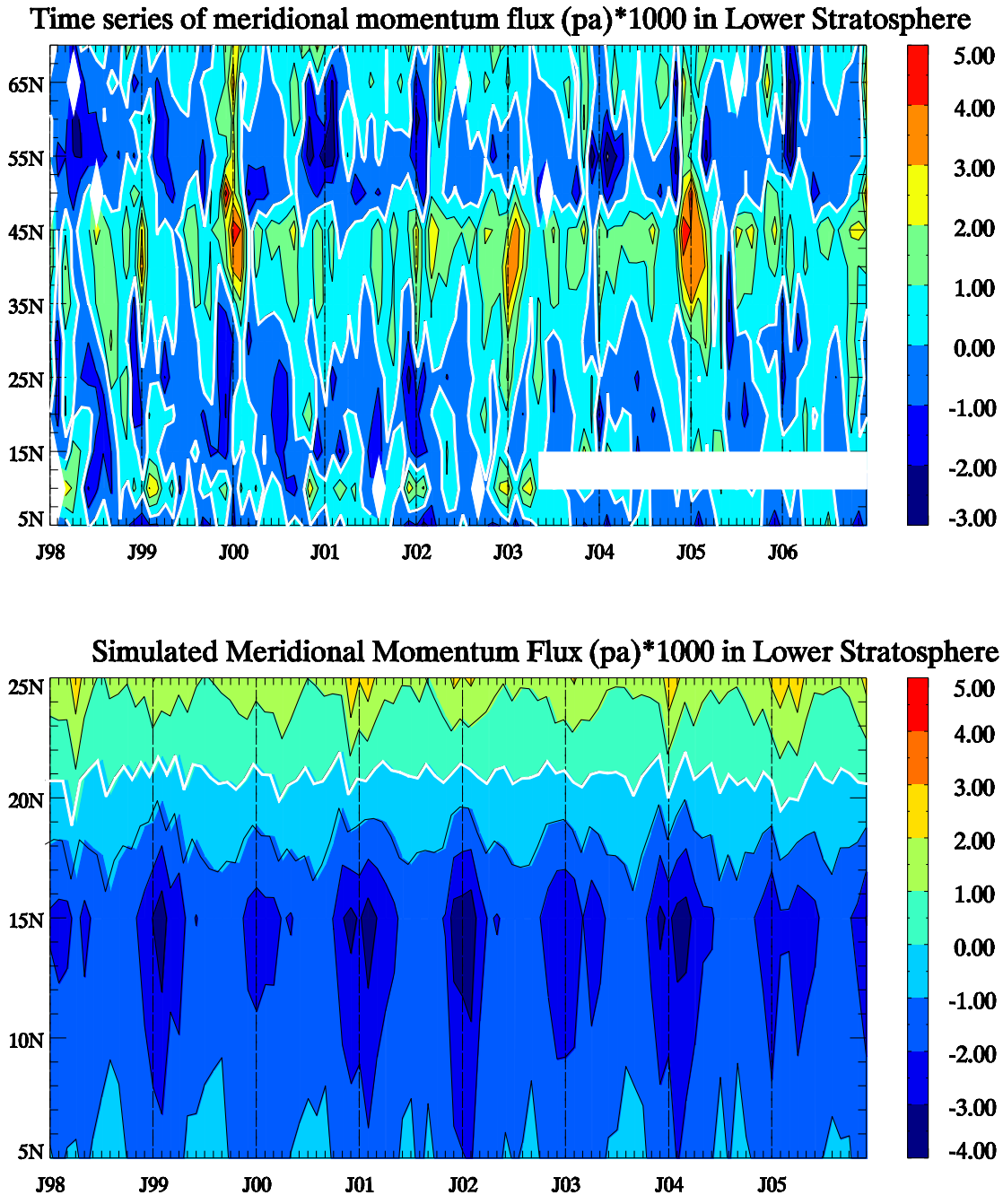

Figure 6.1: Meridional component of the vertical momentum flux (*mpa*) in the lower stratosphere from the observations (a) and the simulation (b), where simulation only takes place south of $25^{\circ}N$.

References

Alexander, M. J., J. R. Holton and D. R. Durran (1995), The gravity wave response above deep convection in a squall line simulation, J. Atmos. Sci., **52**, No. 12, 2212 – 2226

Alexander, M. J. and J. R. Holton (1997), A model study of zonal forcing in the equatorial stratosphere by convectively induced gravity waves, *J. Atmos. Sci.*, **54**, 408 - 419

Alexander, M. J. (1998), Interpretations of observed climatological patterns in stratospheric gravity wave variance, *J. Geophys. Res.*, **103**(D8), 8627–8640

Alexander, M. J. and T.J. Dunkerton (1999), A spectral parameterization of mean-flow forcing due to breaking gravity waves. *J. Atmos. Sci.*, **56**, 4167–4182

Alexander, M. J., J. H. Beres and L. Pfister (2000), Tropical stratospheric gravity wave activity and relationships to clouds, *J. Geophys. Res.*, **105**, 22,299 – 22,309

Alexander, M. J., and R. A. Vincent (2000), Gravity waves in the tropical lower stratosphere: A model study of seasonal and interannual variability, *J. Geophys. Res.*, **105**(D14), 17,983–17,993, doi:10.1029/2000JD900197

Alexander, M. J., T. Tsuda and R. A. Vincent (2002), Latitudinal variations observed in gravity waves with short vertical wavelengths, *J. Atmos. Sci.*, **59**, 1394 – 1404

Alexander, M. J., and C. Barnet (2007), Using Satellite observations to constrain parameterizations of gravity wave effects for global models, *J. Atmos. Sci.*, **64**, 1652 - 1665

Alexander, M. J., M. A. Geller, C. McLandress, S. Polavarapu, P. Preusse, F. Sassi, K. Sato, S. Eckermann, M. Ern, A. Herzog, Y. Kawatani, M. Pulido, T. Shaw, M. Sigmond, R. Vincent, S. Watanabe (2009), A review of recent development on gravity wave effects in climate models and the global distribution of gravity wave momentum flux, *Q. J. R. Meteorol. Soc.*, submitted

Allen, S. J., and R. A. Vincent (1995), Gravity wave activity in the lower atmosphere: Seasonal and latitudinal variations, *J. Geophys. Res.*, **100**(D1), 1327–1350

Andrews, D. G., J. R. Holton, C. B. Leovy (1987), Middle atmosphere dynamics, Academic press, ISBN 0-12-058575-8

Baldwin M. P., L. J. Gray, T. J. Dunkerton, K. Hamilton, P. H. Haynes, W. J. Randel, J. R. Holton, M. J. Alexander, I. Hirota, T. Horinouchi, D. B. A. Jones, J. S. Kinnersley, C. Marquardt, K. Sato and M. Takahashi (2001), The Quasi-Biennial Oscillation, *Rev. Geophys.*, **39**, 179–229

Bell, S. W. (2006), The climatology and synoptic behavior of the tropopause transition layer, Master Dissertation, Stony Brook University

Beres, J. H., M.J. Alexander and J. R. Holton (2004), A method of specifying the gravity wave spectrum above convection based on latent heating properties and background wind, *J. Atmos. Sci.*, **61**, 324 – 337

Beres, J. H. (2004), Gravity wave generation by a three-dimensional thermal forcing, *J. Atmos. Sci.*, **61**, 1805 – 1815

Beres, J. H., R. R. Garcia, B. A. Boville and F. Sassi (2005), Implementation of a gravity wave source spectrum parameterization dependent on the properties of convection in the whole atmosphere community climate model (WACCM), *J. Geophys. Res.*, **110**, D10108, doi:10.1029/2004JD005504

Berger, U. (2008), Modeling of middle atmosphere dynamics with LIMA, *J. Atmos. Sol. Terr. Phys.*, **70**, 1170–1200

Bosart, L. F. and J. G. J. Thomas (2005), The influence of the great lakes on warm season weather systems during BAMEX, *6th AMS Coastal Meteorology Conference*

Carslaw, K. S., M. Wirth, A. Tsias, B. P. Luo, A. Dörnbrack, M. Leutbecher, H. Volkert, W. Renger, J. T. Bacmeister, E. Reimer and Th. Peter (1998), Increased stratospheric ozone depletion due to mountain-induced atmospheric waves, *Nature*, **391**, 675-678

Chun, H.-Y. and J.-J. Baik (1998), Momentum flux by thermally induced internal gravity waves and its approximation for large-scale models. *J. Atmos. Sci.*, **55**, 3299 – 3310

Chun, H.-Y., M.-D. Song, J.-W. Kim and J.-J. Baik (2001), Effects of gravity wave drag induced by cumulus convection on the atmospheric general circulation, *J. Atmos. Sci.*, **58**, 302–319

Chun, H.Y., I.S. Song, and J.J. Baik (2006), Seasonal variations of gravity waves revealed in rawinsonde data at Pohang, Korea, *Meteorol Atmos Phys*, **93**, 255-273

Clark, T. L., W.D. Hall, R. M. Kerr, D. Middleton, L. Radke, F. M. Ralph, P. J. Neiman, and D. Levinson (2000), Origins of aircraft-damaging clear-air turbulence during the 9 December 1992 Colorado downslope windstorm: numerical simulations and comparison with observations, *J. Atmos. Sci.*, **57**, 8, 1105-1131

Colle, B. A., S. E. Yuter (2007), The impact of coastal boundaries and small hills on the precipitation distribution across southern Connecticut and Long Island, NY. *Mon. Wea. Rev.*, **135**, 933-954

Davis, C. A. and K. A. Emanuel (1991), Potential vorticity diagnostics of cyclogenesis. *Mon. Wea. Rev.*, **119**, 1929-1953

Dunkerton, T. J. (1982), Stochastic parameterization of gravity wave stresses, *J. Atmos. Sci.*, **39**, 1711-1725

Dunkerton, T. J. (1997), The role of gravity waves in the quasi-biennial oscillation, *J. Geophys. Res.*, **102**, 26053–26076

Easterling, D. R. and P. J. Robinson (1985), The diurnal variation of thunderstorm activity in the United States, *J. of Climate and Applied Meteorology*, **24**, 1048 – 1058

Eckermann, S. D., and W. K. Hocking (1989), Effect of superposition on measurements of atmospheric gravity waves: A cautionary note and some reinterpretations, *J. Geophys. Res.*, **94**, 6333–6339

Eckermann, S. D., and R. A. Vincent (1989), Falling sphere observations of anisotropic gravity wave motions in the upper stratosphere over Australia, *Pure Appl. Geophys.*, **130**, 509–532

Eckermann, S. D., and R. A. Vincent (1993), VHF radar observations of gravity-wave production by cold fronts over Southern Australia, *J. Atmos. Sci.*, **50**, 785–806

Eckermann, S.D. (1995), On the observed morphology of gravity-wave and equatorial-wave variance in the stratosphere, *J. Atmos. Terr. Phys.*, **57**, 105 – 134

Eckermann, S.D. (1996), Hodographic Analysis of Gravity Waves: Relationships among Stokes Parameters, Rotary Spectra, and Cross-spectral Methods, *J. Geophys. Res.*, **101**, 19,169-19,174

Eckermann, S. D., and C. J. Marks (1997), GROGRAT: A new model of the global propagation and dissipation of atmospheric gravity waves, *Adv. Space Res.*, **20**(6), 1253-1256

Eichler, T. and W. Higgins (2006), Climatology and ENSO-related variability of North American extratropical cyclone activity, *J. Clim.*, **19**, 2076 - 2093

Eliassen, A. and E. Palm (1960), On the transfer of energy in stationary mountain wave, *Geofis. Publ.*, **22**, 1 - 23

Fovell, R. G., D. Durran and J. R. Holton (1992), Numerical simulations of convectively generated stratospheric gravity waves, *J. Atmos. Sci.*, **49**, 1427 - 1442

Fritts, D. C., and R. A. Vincent (1985), Observations and a gravity wave-tidal interaction model, *J. Atmos. Sci.*, **44**, 605–619

Fritts, D.C. and R. A. Vincent (1987), A Climatology of Gravity Wave Motions in the Mesopause Region at Adelaide, Australia, *J. Atmos. Sci.*, **44**, 748 - 760

Fritts, D., and T. VanZandt (1987), Effects of Doppler Shifting on the Frequency Spectra of Atmospheric Gravity Waves, *J. Geophys. Res.*, **92**, 9723-9732

Fritts, D.C. and T.E. VanZandt(1993), Spectral estimates of gravity wave energy and momentum fluxes. Part I. Energy dissipation, acceleration, and constraints. *J. Atmos. Sci.*, **50**, 3685–3694.

Fritts, D.C., and M.J. Alexander (2003), Gravity Wave Dynamics and Effects in the Middle Atmosphere, *Review of Geophysics*, **41**, 1, doi: 10.1029/2001RG000106

Garcia, R.R. (1989), Dynamics, radiation and photochemistry in the mesosphere: implications for the formation of noctilucent clouds, *J. Geophys. Res.* **94**, 14,605–14,615

Garcia, R.R.(2000), The role of equatorial waves in the semiannual oscillation of the middle atmosphere. In: Atmospheric Science Across the Stratopause, *AGU Geophysical Monograph Series.*, **123**, 161–176

Geller, M. A. and J. Gong (2009), Gravity wave kinetic, potential and vertical fluctuation energies as indicators of different frequency gravity waves, *J. Geophys. Res.*, in revision

Gong, J., M. A. Geller, and L. Wang (2008), Source spectra information derived from U.S. high-resolution radiosonde data, *J. Geophys. Res.*, **113**, D10106, doi:10.1029/2007JD009252

Gong, J. and M. A. Geller (2009), Vertical fluctuation energy in US high vertical-resolution radiosonde data as an indicator of convective gravity wave sources, *J. Geophys. Res.*, in revision

Guest, F. M., M. J. Reeder, C. J. Marks and D. J. Karoly (2000), Inertia-gravity waves observed in the lower stratosphere over Macquarie Island, *J. Atmos. Sci.*, **57**, 737 - 752

Haag, W. and Karcher, B. (2004), The impact of aerosols and gravity waves on cirrus clouds at midlatitudes, *J. Geophys. Res.*, **109**, D12202

Hamilton, K., and R. A. Vincent (1995), High-resolution radiosonde data offer new prospects for research, *Eos*, **76**, 497

Hickey, M. P., M. J. Taylor, C. S. Gardner, and C. R. Gibbons (1998), Full-wave modeling of small-scale gravity waves using airborne lidar and observations of the Hawaiian airglow (ALOHA-93) O(1S) images and coincident Na wind/temperature lidar measurements, *J. Geophys. Res.*, **103**, 6,439 – 6,453

Hines, C. O. (1960), Internal atmospheric gravity waves at ionospheric heights, *Can. J. Physics*, **38**, 1441-1481

Hines, C.O. (1997a), Doppler-spread parameterization of gravity wave momentum deposition in the middle atmosphere. 1, Basic formulation, *J. Atmos. Sol.- Terr. Phys.*, **59**, 371–386.

Hines, C. O. (1997b), Doppler-spread parameterization of gravity wave momentum deposition in the middle atmosphere. 2, Broad and quasi-monochromatic spectra and implementation. *J. Atmos. Sol.-Terr. Phys.*, **59**, 387–400

Holton, J. R. (1982), The role of gravity wave induced drag and diffusion in the momentum budget of the mesosphere, *J. Atmos. Sci.*, **39**, 791-799

Holton, J. R. (2004), An introduction to dynamic meteorology, fourth edition, *Elsevier academic press*

Horinouchi., T., and T. Tsuda (2009), Spatial structures and statistics of atmospheric gravity waves derived using a heuristic vertical cross-section extraction from COSMIC GPS radio occultation data, *J. Geophys. Res.*, **114**(D16): D16110

Karoly, D. J., G. L. Roff and M. J. Reeder (1996), Gravity wave activity associated with tropical convection detected in TOGA COARE sounding data, *Geophys. Res. Lett.*, **23** (3), 261- 264

Keyser, D., B. D. Schmidt, and D. G. Duffy (1989), A technique for representing three-dimensional vertical circulations in baroclinic disturbances, *Mon. Wea. Rev.*, **117**, 2463 - 2494

Kim, Y.-J., S. D. Eckermann and H.-Y. Chun (2003), An overview of the past, present and future of gravity-wave drag parameterization for numerical climate and weather prediction models, Atmos.-Ocean, **41** (1), 65-98

Klemp, J. B., and R. B. Wilhelmson (1978), The simulation of three-dimensional convective storm dynamics, *J. Atmos. Sci.*, **35**, 1070–1096

Koch, S. E., and P. B. Dorian (1988), A mesoscale gravity wave event observed during CCOPE. part III: Wave environment and possible source mechanisms, *Mon. Weather Rev.*, **116**, 2570–2591

Lane, T. P., M. J. Reeder, B. R. Morton, and T. L. Clark (1999), Observations and numerical modelling of mountain waves over the Southern Alps of New Zealand, *Q. J. R. Meteorol. Soc.*, **126**, 2765-2788

Lane, T. P., M. J. Reeder and T. L. Clark (2001), Numerical modeling of gravity wave generation by deep tropical convection, *J. Atmos. Sci.*, **58**, 1249 - 1274

Lane, T. P., M. J. Reeder and F. M. Guest (2003), Convectively generated gravity waves observed from radiosonde data taken during MCTEX, *Q. J. R. Meteorol. Soc.*, **129**, 1731 – 1740

Lin, Y. and F. Zhang (2008), Tracing mesoscale gravity waves in baroclinic jet-front systems, *J. Atm. Sci.*, **65**, 2402 - 2415

Lindzen, R. S. (1981), Turbulence and stress owing to gravity wave and tidal break down, *J. Geophys. Res.*, **86** (C10), 9707-9714

Lindzen, R. S. (1990), Dynamics in Atmospheric Physics, *Cambridge Univ. Press*, New York, ISBN 0-521-36101-X

Luo, Z. G. and D. C. Fritts (1993), Gravity-wave excitation by geostrophic adjustment of the jet stream. Part II: three-dimensional forcing, *J. Atmos. Sci.*, **50**, 104 - 115

Liu, H.-L., and R. G. Roble (2002), A study of a self-generated stratospheric sudden warming and its mesospheric–lower thermospheric impacts using the coupled TIME-GCM/CCM3, *J. Geophys. Res.*, **107**(D23), 4695, doi: 10.1029/2001JD001533

Marks, C. J. and S. D. Eckermann (1995), A three-dimensional nonhydrostatic ray-tracing model for gravity waves: Formulation and preliminary results for the middle atmosphere, *J. Atmos. Sci.*, **52**, 1959-1984

McAnelly, R.L., and W.R. Cotton (1989), The Precipitation Life Cycle of Mesoscale Convective Complexes over the Central United States, *Monthly Weather Review*, **117** (4), 784-808

McFarlane, N. A. (1987), The effect of orographically excited wave drag on the general circulation of the lower stratosphere and troposphere, *J. Atmos. Sci.*, **44**, 1775–1800.

McLandress, C., and J. F. Scinocca (2005), The GCM response to current parameterizations of nonorographic gravity wave drag, *J. Atmos. Sci.*, **62**, 2394–2413, doi:10.1175/JAS3483.1

Morgan, M.C., J. W. Nielsen-gammon (1998), Using tropopause maps to diagnose midlatitude weather systems, *Mon. Wea. Rev.*, **126**, 2555-2579

Murayama, Y., T. Tsuda, and S. Fukao (1994), Seasonal variation of gravity wave activity in the lower atmosphere observed with the MU radar, *J. Geophys. Res.*, **99** (11), 23057-23070

NCDC (2002), National climatic data center: data documentation for dataset 6211 (DSI - 6211)

NWS (1991), Micro-ART observation and rework program technical document, NOAA

O'Sullivan, D. and T. J. Dunkerton (1995), Generation of inertia-gravity waves in simulated life cycle of baroclinic instability. *J. Atmos. Sci.*, **52**, 3695 - 3716

Palmer, T.N., G. J. Shutts, and R. Swinbank (1986), Alleviation of a systematic westerly bias in general circulation and numerical weather prediction models through a norgraphic gravity wave drag parameterization, *Q. J. R. Meteor. Soc.*, **112**, 1001 - 1039

Pfister, L., K. R. Chan, T. P. Bui, S. Bowen, M. Legg, B. Gary, K. Kelly, M. Proffitt and W. Starr (1993), gravity waves generated by a tropical cyclone during the STEP tropical field program: A case study. *J. Geophys. Res.*, **98**, 8611 - 8638

Plougonven, R., H. Teitelbaum, and V. Zeitlin (2003), Inertia gravity wave generation by the tropospheric midlatitude jet as given by the Fronts and Atlantic Storm-Track Experiment radio soundings. J. Geophys. Res., **108**, 4686, doi:10.1029/2003JD003535

Plougonven, R. and C. Snyder (2007), Inertia-gravity waves spontaneously generated by jets and fronts, *J. Atmos. Sci.*, **64**, 2502-2520

Plougonven, R. and F. Zhang (2007), On the forcing of inertia-gravity waves by synoptic scale flows, *J. Atmos. Sci.*, **64**, 1737-1742

Plumb, R. A. (2002), stratospheric transport, *J. Meteorol. Soc. Japan*, **80** (4B), 793 – 809

Pitteway, M. L. V., and C. O. Hines (1963), The viscous damping of atmospheric gravity waves, *Can. J. Phys.*, **41**, 1935-1948

Press, W. H., S. A. Teukolsky, W. T. Vetterling, and B. P. Flannery (1992), Numerical Recipes in Fortran 77, second edition, *Cambridge Univ. press*, 933

Preusse, P., S. D. Eckermann, and O. Dirk (2000), Comparison of global distributions of zonal-mean gravity wave variance inferred from different satellite instruments, *Geophys. Res. Lett.*, **27**, 3877-3880

Reeder, M. J., and M. Griffiths (1996), Stratospheric inertia-gravity waves generated in a numerical model of frontogenesis. Part II: Wave sources, generation mechanisms and momentum fluxes, *Q. J. Roy. Meteor. Soc.*, **122**, 1175–1195

Reeder, M. J., N. Adams and T. P. Lane (1999), Radiosonde observations of partially trapped lee waves over Tasmania, Australia, *J. Geophys. Res.*, **104** (D14), 16,719 – 16,727

Richter, J. H., F. Sassi, and R. R. Garcia (in print, 2009), Towards a physically based gravity wave source parameterization in a general circulation model, *J. Atmos. Sci.*, doi: 10.1175/2009JAS3112.1

Rind, D., R. Suozzo, N. K. Balachandran, A. Lacis, and G. Russel (1988), The GISS global climate global atmosphere model: Part I: Model structure and climatology, *J. Atmos. Sci.*, **45**, 329–370

Rossby, C. G. (1938), On the mutual adjustment of pressure and velocity distributions in simple current systems, *J. Mar. Res.*, **1,** 239–263

Sato, K. (1994), A statistical study of the structure, saturation and sources of inertia-gravity waves in the lower stratosphere observed with the MU radar, *J. Atmos. Terr. Phys.*, **56** (6), 755-774

Sato, K. and T.J. Dunkerton (1997), Estimates of momentum flux associated with equatorial Kelvin and gravity waves, *J. Geophys. Res.*, **102**, 26,247–26,262

Sato, K., D. J. O'Sullivan and T. J. Dunkerton (1997), Low-frequency inertia-gravity waves in the stratosphere revealed by three-week continuous observation with the MU radar, *Geophys. Res. Lett.*, **24**, 14, 1739-1742

Sato, K., T. Kumakura, and M, Takahashi (1999), Gravity waves appearing in a high-resolution GCM simulation, *J. Atmos. Sci.*, **56**, 8, 1005-1018

Sato, K., and M. Yoshiki (2008), Gravity wave generation around the polar vortex in the stratosphere revealed by 3-hourly radiosonde observations at Syowa station, *J. Atmos. Sci.*, **65**, 12, 3719-3735

Sawyer, J. S. (1961), Quasi-periodic wind variations with height in the lower stratosphere, *Q. J. R. Meteorol. Sc.*, **87**, 24-33

Shutts, G. J. (1992), Observations and numerical model simulation of a partially trapped lee wave over the Welsh Mountains, *Mon. Wea. Rev.*, **120**, 2056-2066

Shutts, G. J., Healey, P. and Mobbs, S. D. (1994), A multiple sounding technique for the study of gravity waves, *Q. J. R. Meteorol. Soc.*, **120**, 59-77

Skamarock, W. C., and J. B. Klemp (1992), The stability of time-split numerical methods for the hydrostatic and nonhydrostatic elastic equations, *Mon. Wea. Rev.*, **120**, 2109–2127

Skamarock, W.C., and J. B. Klemp (2008), A time-split nonhydrostatic atmospheric model for weather research and forecasting applications, *J. Comp. Phys.*, **227**, 3465-2485

Song, I. S. and H. Y. Chun (2003), Generation mechanisms of convectively forced internal gravity waves and their propagation to the stratosphere, *J. Atmos. Sci.*, **60**, 1960 – 1980

Song, I.-S. and H.-Y. Chun (2005), Momentum flux spectrum of convectively forced internal gravity waves and its application to gravity wave drag parameterization. Part I: theory, *J. Atmos. Sci.*, **62**, 107 - 124

Song, I.-S., H.-Y. Chun, R. R. Garcia and B. A. Boville (2007), Momentum flux spectrum of convectively forced internal gravity waves and its application to gravity wave drag parameterization. Part II: impacts in a GCM (WACCM), *J. Atmos. Sci.*, **64**, 2286 – 2308

Steiner, A. K. and G. Kirchengast (2000), Gravity wave spectra from GPS/MET occultation observations, *J. Atm. Ocn. Tech.*, **17**, 495 - 503

Thomas, S., C. Girard, G. Doms, and U. Schättler (2000), Semi-Implicit scheme for the DWD Lokal-Modell, *Meteorol. Atmos. Phys.*, **73**, 105-125

Tsuda, T., Y. Murayama, H. Wiryosumarto, S. W. B. Harijono and S. Kato (1994), Radiosonde observations of equatorial atmosphere dynamics over Indonesia, 2, Characteristics of gravity waves, *J. Geophys. Res.*, **99**, 10,507 – 10,516

Uccellini, L. W. and P. J. Kocin (1987), The Interaction of Jet Streak Circulations during Heavy Snow Events along the East Coast of the United States, *Weather and Forecasting*, **2**, 289 - 308

VanZandt, T. E. (1982), A universal spectrum of buoyancy waves in the atmosphere, *Geophys. Res. Lett.*, **9**, 575–578

Van Tuyl, A., and J. A. Young (1982), Numerical simulation of nonlinear jet streak adjustment, *Mon. Weather Rev.*, **110**, 2038–2054

Vincent, R. A. (1984), Gravity wave motions in the mesosphere, *J. Atmos. Terr. Phys.*, **46**, 119–128

Vincent, R. A., and D. C. Fritts (1987), A climatology of gravity wave motions in the mesopause region at Adelaide, Australia, *J. Atmos. Sci.*, **44**, 748–760

Vincent, R. A., S. J. Allen, and S. D. Eckermann (1997), Gravity wave parameters in the lower stratosphere, in Gravity Wave Processes: Their Parameterization in Global Climate Models, NATO ASI Ser., Ser. I, **50**, edited by K. Hamilton, 7–25, Springer, New York

Vincent, R. A., and M. J. Alexander (2000), Gravity waves in the tropical lower stratosphere: an observational study of seasonal and interannual variability, *J. Geophys. Res.*, **105**(D14), 17,971–17,982, doi:10.1029/2000JD900196

Vincent, R. A., A. Hertzog, G. Boccara, and F. Vial (2007), Quasi-lagrangian superpressure balloon measurements of gravity wave momentum fluxes in the polar stratosphere of both hemispheres, *Geophys. Res. Lett.*, **34**, doi: 10.1029/2007GL031072

Wallace, J.M. (1975), Diurnal variations in precipitation and thunderstorm frequency over the converminous United States, *Monthly Weather Review*, **103**, 406 - 419

Wang, L. (2003), Gravity wave analysis of four years of high vertical resolution U.S. radiosonde data, *Ph.D. dissertation*, State Univ. of New York at Stony Brook, Stony Brook.

Wang, L., and M. A. Geller (2003), Morphology of gravity wave energy as observed from four years (1998–2001) of high resolution U.S. radiosonde data, *J. Geophys. Res.*, **108**(D16), 4489, doi:10.1029/2002JD002786

Wang, L., M. A. Geller and M. J. Alexander (2005), Spatial and temporal variations of gravity wave parameters. Part I: Intrinsic frequency, wavelength, and vertical propagation direction, *J. Atmos. Sci.*, **62**, 125–142, doi:10.1175/JAS-3364.1

Wang, S. and F. Zhang (2007), Sensitivity of mesoscale gravity waves to the baroclinicity of jet-front systems. *Mon. Weather Rev.*, **135**, 670–688

Wang, S., F. Zhang, and C. Snyder (2009), Generation and Propagation of Inertia-Gravity Waves from Vortex Dipoles and Jets, *J. Atmos. Sci.*, **66** (5), 1294–1314

Weisman, M. L. and R. Rotunno (2004), "A theory for strong long-lived squall lines" revisited, *J. Atmos. Sci.*, **61** (4), 361 – 382

Wicker, L. J., and W.C. Skamarock (2002), Time splitting methods for elastic models using forward time schemes, *Mon. Wea. Rev.*, **130**, 2088–2097

Winkler, J. A., B. R. Skeeter and P. D. Yamamoto (1988), Seasonal variations in the diurnal characteristics of heavy hourly precipitation across the United States, *Monthly Weather Review*, **116**, 1641 – 1658

Williams, S. F., C. G. Wade, and C. Morel (1993), A comparison of high resolution radiosonde winds: 6-second Micro-ART winds versus 10-second CLASS LORAN winds. *preprints, Eighth Symp. On Meteorological Observations and Instrumentation, Anaheim, CA, Amer. Meteor. Soc.*, 60–65

Wu, D. L., P. Preusse, S. D. Eckermann, J. H. Jiang, M. T. Juarez, L. Coy, and D. Y. Wang (2006), Remote sounding of atmospheric gravity waves with satellite limb and nadir techniques, *Adv. Space Res.*, **37**, 2269-2277

Xu, J., A. K. Smith, and R. Ma (2003), A numerical study of the effect of gravity-wave propagation on minor species distributions in the mesopause region, *J. Geophys. Res.*, 108(D3), 4119, doi:10.1029/2001JD001570

Yang, M.-J. and R. A. Houze, Jr. (1995), Multicell squall-line structure as a manifestation of vertically trapped gravity waves, *Mon. Wea. Rev.*,**123**, 641-661

Zhang, F., S. E. Koch, C. A. Davis, and M. L. Kaplan (2000), A survey of unbalanced flow diagnostics and their application. *Adv. Atmos. Sci.*, **17**, 165–183

Zhang, F. Q. (2004), Generation of mesoscale gravity waves in upper-tropospheric jet–front systems, *J. Atmos. Sci.*, Vol. 61, 440 - 457

Zhang, F., S. Wang and R. Plougonven (2004), Uncertainties in using the hodograph method to retrieve gravity wave characteristics from individual soundings, *Geophys. Res. Lett.*, **31** (L11110), doi: 10.1029/2004GL019841

Zhu, X. (1993), Radiative damping revisited: parameterization of damping rate in the middle atmosphere, *J. Atmos. Sci.*, **50**, 3008-3021

Zink, F. and R. A. Vincent (2001a), wavelet analysis of stratospheric gravity wave packets over Macquarie Island, part1: wave parameters, *J. Geophys. Res.*, **106,** 10,275 – 10,288

Zink, F. and R. A. Vincent (2001b), wavelet analysis of stratospheric gravity wave packets over Macquarie Island, part1: intermittency and mean flow accelerations, *J. Geophys. Res.*, **106**, 10,289 – 10,297